Multiscale Simulations

for fracture prediction in composite materials: extension for anisotropic microstructures

Rubén Suárez Millán

Delft University of Technology

TU Delft

Multiscale Simulations

for fracture prediction in composite materials: extension for anisotropic microstructures

by

Rubén Suárez Millán

to obtain the degree of

Master of Science
in Aerospace Engineering

at the Delft University of Technology,
to be defended publicly on Thursday December 13, 2018 at 14:00.

Student number:	4229819	
Submitted on:	November 23, 2018	
Thesis committee:	Dr. S.R. Turteltaub,	TU Delft, supervisor
	Dr. B. Chen,	TU Delft
	Dr.ir. F.P. van der Meer,	TU Delft

An electronic version of this thesis is available at `http://repository.tudelft.nl/`.

TU Delft

Abstract

With a fast increasing use of composite materials in aerostructures, industry demands design tools capable of reducing experimental tests while providing reliable data. Multiscale simulations enable modeling and analysis of fracture processes at the microscale, thus delivering higher accuracy and fundamental information about crack processes which phenomenological models cannot capture.

In this thesis, the fracture processes developing in composite laminates are studied. Moreover, special focus is given to the influence of anisotropy in fracture simulations of microstructural domains and thus, their feasibility. To achieve this, the in-house multiscale framework by Turteltaub et al. [94] has been extended to account for multi-ply laminates. The framework features a pre-processing and post-processing which are performed in Python. Moreover, Abaqus is used to conduct the finite element analyses. A key characteristic of the framework is its intrinsic implementation, in which zero-thickness cohesive elements are inserted between all the solid elements of the domain. This approach enables to naturally model crack initiation and propagation in random directions, as well as crack coalescence and branching.

In the context of the in-house developed multiscale framework, several advances have been achieved towards obtaining Hill-Mandel compliant effective traction separation laws (ETSLs). A critical review of the previous homogenization relations was performed, and two alternative energy-consistent homogenization methods have been proposed: traction-based and opening-based homogenization. These alternative homogenization methods are key to comply with the Hill-Mandel condition and thus retain energy and power equilibrium between scales. Additionally, a new relation has been proposed for the calculation of geometrically accurate effective openings.

Furthermore, the framework's computational implementation has been renewed and several new features are presented raising the accuracy and control over the integrated quantities. For instance, crack-path integration has been corrected by properly re-orienting the crack elements' normal vectors. Consistency in the shear and mixed mode results has been achieved. Additionally, a crack recognition algorithm has been set, which allows to separate the fracture energy contributions when multiple main cracks propagate, and thus produce separate ETSLs for each crack autonomously.

Finally, the new methods were verified, and a convergence study was performed to study the influence of the mesh grid and the domain size. Moreover, it was found that periodic boundary conditions have an influence on the crack propagation upon localization, thus restricting the applicability of the multiscale framework.

Acknowledgments

This project represents the culmination of six years of higher education at Delft University of Technology. Along the way, and especially over the last months, there have been people who have been an essential support, and whom I am grateful for.

First, I am extremely grateful to my supervisor Dr. Sergio Turteltaub, whose door has always been open over the last months for any doubts and comments. His enthusiasm and feedback have been essential and I appreciate the extra-long meetings and insightful discussions we shared.

I am also very thankful to my friends and colleagues at the TU Delft. I would especially like to thank Mark and Daan, with whom I shared endless discussions and great moments over the past months. I would also like to thank Gijs, who helped me at the beginning of the project; and my colleague Philippe, with whom I had the pleasure to share debates about plenty of topics. Moreover, I would like to thank my long-lasting friends Baris, Dionisios, Jan and Thibault, who have always been there over the last years, and whose friendship is irreplaceable.

Finally, I would like to thank my family for their continuous and unwavering support. This thesis would not have been possible without them.

Rubén Suárez Millán

Contents

List of Figures xi

Nomenclature xv

1 Introduction 1

2 Literature Review 3

2.1 Fundamentals of Fracture Mechanics . . . 3

2.1.1 Linear Elastic Fracture Mechanics (LEFM) . . . 3

2.1.2 Elastic Plastic Fracture Mechanics (EPFM) . . . 6

2.2 Fracture of composite materials. . . . 7

2.2.1 Longitudinal tensile failure X_T . . . 8

2.2.2 Longitudinal compression failure X_C . . . 8

2.2.3 Transverse tensile failure Y_T . . . 9

2.2.4 Transverse compression failure Y_C . . . 9

2.2.5 In-plane shear failure S . . . 9

2.2.6 Failure modes interaction . . . 9

2.3 Cohesive Zone Models . . . 10

2.4 Multiscale methods . . . 11

2.4.1 Why multiscale? . . . 12

2.4.2 Classes of multiscale methods . . . 12

2.4.3 Representative Volume Element . . . 15

2.4.4 Homogenization . . . 16

2.4.5 Composite constituents modeling in RVEs . . . 17

3 Methodology 19

3.1 Overview . . . 19

3.2 Microstructure Volume Element . . . 19

3.3 Microstructural formulation . . . 20

3.4 Micro/macro scale coupling . . . 22
3.4.1 Homogenization of stresses and strains . . . 22
3.4.2 Power relations . . . 22
3.4.3 Hill-Mandel condition . . . 23
3.5 Effective quantities . . . 24
3.5.1 Old effective quantities . . . 24
3.5.2 New effective quantities . . . 24
3.5.3 Choice of new effective quantities . . . 26

4 Numerical Implementation: Pre-processing and Post-processing. 27

4.1 Overview . . . 27
4.2 Pre-processing . . . 28
4.2.1 Geometry generation . . . 28
4.2.2 Mesh generation . . . 30
4.2.3 Abaqus elements . . . 31
4.2.4 Embedding of cohesive elements . . . 31
4.2.5 Boundary Conditions . . . 31
4.2.6 Loading Modes . . . 33
4.2.7 Cohesive Material Model . . . 33
4.2.8 Materials . . . 35
4.2.9 Abaqus Numerical Artifacts . . . 35
4.2.10 Abaqus Input File . . . 36
4.3 Post-processing . . . 37
4.3.1 Bulk data extraction and homogenization . . . 37
4.3.2 Consistent reorientation of cohesive elements for data extraction . . . 38
4.3.3 Crack groups and threshold of damage . . . 44
4.3.4 Cohesive data extraction and rotation . . . 45
4.3.5 Cohesive data homogenization and crack quantities . . . 46
4.3.6 Handling of cohesive elements below the threshold of damage . . . 47
4.4 Computational implementation details . . . 47

5 Plots, Interpretation and Limitations. 51

5.1 Two effective quantity couples, two different effective materials . . . 51

5.2 Test tags and orientation conventions. . . . 52

5.3 Displacement curves . . . 53

5.4 Traction curves . . . 54

5.5 Power curves . . . 55

5.5.1 Discussion: comparison of the new/old Hill-Mandel decomposition . . . 55

5.5.2 Discussion: comparison of the new/old effective quantities . . . 56

5.6 Energy curves . . . 58

5.7 ETSLs . . . 59

5.8 Limitations . . . 60

5.8.1 Crack surfaces loss of contact and overlapping. . . . 60

5.8.2 Viscous dissipation . . . 61

5.8.3 Artificial compliance . . . 61

5.8.4 Post-processing limitations . . . 61

5.9 Lessons learned: Abaqus COH2D4 SDEG deviations due to high viscous regularization . . . 61

6 Verification 65

6.1 Hill-Mandel verification. . . . 65

6.2 Mesh convergence . . . 67

6.3 Geometry generation statistical convergence . . . 72

6.4 RVE convergence . . . 74

6.5 Energy comparison . . . 76

6.6 Multi-crack TSLs for biaxial loading . . . 79

6.7 Verification remarks. . . . 80

6.8 Multi-angle TSLs for uniaxial loading . . . 80

6.9 Crack orientation dependence on RVE dimensions and PBCs . . . 81

7 New Material Properties 87

7.1 New material parameters . . . 87

7.1.1 Carbon Fibers: HexTow IM7 . . . 87

7.1.2 Matrix: HexPly 8552 Epoxy Resin . . . 88

7.1.3 Interface: IM7/8552 88
7.2 Parametric study to determine E_{COH} and η 88
7.3 Discussion of the simulation results. 90

8 Conclusions and Recommendations **91**
8.1 Conclusions. 91
8.2 Recommendations 92

Bibliography **93**

A Analysis inputs **99**

B Gmsh .geo file structure **101**

C Gmsh PBC subroutine **103**

D Abaqus input .inp file structure **107**

List of Figures

2.1 Fracture modes [86] . . . 4

2.2 K-dominated zone [3] . . . 5

2.3 Irwin plastic zone correction diagram [3] . . . 6

2.4 Applicability of LEFM and EPFM [47] . . . 6

2.5 CTOD diagram [3] . . . 7

2.6 Failure mechanisms in unidirectional composite plies under different loading modes [67]. . . . 7

2.7 FRP composite longitudinal tension failure [14] . . . 8

2.8 FRP composite longitudinal compression failure [50] . . . 8

2.9 Transverse tensile failure. Diagram [66] and SEM image [91]. . . . 9

2.10 FRP composite transverse compression failure [33] . . . 9

2.11 Cohesive Zone Modeling idealization, FE implementation, and cohesive law . . . 10

2.12 Traction separation law examples [77] . . . 11

2.13 Multiscale bottom-top framework [57] . . . 12

2.14 Types of multiscale methods [83] . . . 13

2.15 Concurrent "embedded cell" model [8] . . . 14

2.16 Schematic operation of the FE^2 method [22] . . . 14

2.17 Periodic RVE [9] and first order homogenization scheme [53] . . . 15

2.18 Elasto-plastic matrix modeling [67] . . . 18

2.19 Matrix and interface modeling using cohesive elements [2] . . . 18

3.1 CFRP laminate microscope images and idealization . . . 20

3.2 Microstructural volume element. Nomenclature, domains and dimensions. . . . 21

3.3 Cracked micro-scale domains and effective macro-crack. . . . 25

4.1 Flow diagram of the computational implementation. . . . 27

4.2 Flow diagram of the pre-processing. . . . 28

4.3 Generated geometries for a [0,90,0] laminates with domain size of 100x100 μm, fiber volume fraction $V_f = 0.5$, and fiber diameters 10 μm (left) and 5.2 μm (right). . . . 28

4.4 C-Phase geometry . . . 29
4.5 T-Phase geometry. . . . 30
4.6 Meshing process using OpenCASCADE boolean operators. . . . 30
4.7 Abaqus CPE3 and COH2D4 nodes ordering and integration points . . . 31
4.8 Embedding of cohesive elements into the mesh. . . . 32
4.10 Assignment of PBCs at the domain edges [96] . . . 32
4.9 MVE boundary conditions and displacements of the dummy and corner nodes. . . . 33
4.11 Bilinear intrinsic TSL. . . . 34
4.12 Flow diagram of the post-processing . . . 37
4.13 MVE cohesive crack normals before and after reorientation . . . 38
4.14 Crack normals reorientation using projection of normals . . . 39
4.15 Crack normals reorientation using relative displacements. Definition of displacement vectors and static and moving faces. . . . 40
4.16 Crack normals reorientation using relative displacements. Flip process for generalized cracks. . . 41
4.17 Flow diagram of the crack identification and reorientation algorithm . . . 41
4.18 Basic operation of the multi crack identification and classification module (`multicrack.py`) . . 42
4.19 Multi-crack algorithm application in biaxial loading test (#42) . . . 43
4.20 Multi-crack algorithm application in pure shear loading test (#43) . . . 43
4.21 Multi-crack algorithm application in mixed loading test (#49) . . . 43
4.22 Multi-crack algorithm crack group identification. . . . 44
4.23 Cohesive element geometry (COH2D4) and vectors . . . 45
4.24 Flow diagram of the computational implementation. . . . 49

5.1 Test #38 fracture results . . . 51
5.2 Comparison between effective parameter pairs . . . 52
5.3 Test tags and conventions . . . 52
5.4 Displacement plot test #38 . . . 53
5.5 Traction plots tests #38 and #49 . . . 54
5.6 TSLs for UA1 and PS45 . . . 54
5.7 Power plot test #38. . . . 55
5.8 Power plot test #38. Comparison with old Hill-Mandel decomposition. . . . 56
5.9 Power plot test #1062. Comparison with old Hill-Mandel decomposition. . . . 56

5.10 Power plot test #38. Comparison with old effective quantities. 57

5.11 Power plot test #39. Comparison with old effective quantities. 57

5.12 Energy plot test #38 58

5.13 Energy control plots test #38 58

5.14 Energy plot test #39 59

5.15 Energy control plots test #39 59

5.16 ETSL test #38. Uniaxial loading. 60

5.17 ETSL test #49. Mixed loading case. 60

5.18 Crack surfaces overlap in shear 45° case, test #33. 61

5.19 Old ETSL test #38 with $\eta = 10^{-3}$. Uniaxial loading. 62

5.20 Damage variable deviation investigation plots. 62

5.21 ETSL test #21050 with $\eta = 10^{-5}$. Uniaxial loading. 63

6.1 Power plot, test #530, uniaxial tensile loading 0° with respect to $\boldsymbol{e}_1$ 65

6.2 Power plot, test #532, uniaxial tensile loading 45° with respect to $\boldsymbol{e}_1$ 66

6.3 Power plot, test #43, pure shear 45° 66

6.4 Power plot, test #49, mixed mode 66

6.5 Domain size: 25 x 25 μm. Gridsizes: 3, 2, 1, 0.5 μm 67

6.6 Domain size: 50 x 50 μm. Gridsizes: 3, 2, 1, 0.5 μm 67

6.7 Domain size: 75 x 75 μm. Gridsizes: 3, 2, 1 μm 67

6.8 Domain size: 100 x 100 μm. Gridsizes: 3, 2, 1 μm 67

6.9 Mesh convergence plot for domain size 25μm, gridsizes 0.5, 1, 2 and 3 μm. 68

6.10 Mesh convergence plot for domain size 50μm, gridsizes 0.5, 1, 2 and 3 μm. 69

6.11 Mesh convergence plot for domain size 75μm, gridsizes 1, 2 and 3 μm. 70

6.12 Mesh convergence plot for domain size 100μm, gridsizes 1, 2 and 3 μm. 71

6.13 Geometry generation statistical convergence tests # 21100, 21105, 21110, 21115. Domain size 25 μm, gridsize 1 μm. 72

6.14 Geometry generation statistical convergence tests # 21140, 21145, 21150, 21155. Domain size 75 μm, gridsize 1 μm. 73

6.15 Geometry generation statistical convergence tests # 2069, 2070, 2071. Domain size 75 μm, gridsize 1 μm. 73

6.16 RVE convergence plot for UA1 [0,90,0], domain sizes 25, 50, 75 and 100 μm, and gridsize 1 μm. . 74

6.17 RVE convergence plot for UA1 [0], domain sizes 50, 75 and 100 μm, and gridsize 1 μm. 75

6.18 Energy plot test #21120 (UA1V with domain size 50 μm, gridsize 1 μm). 76

6.19 Energy plot test #21160 (UA1V with domain size 100 μm, gridsize 1 μm). 77

6.20 Energy plot test #515 (UA1 with domain size 50 μm, gridsize 1 μm). 77

6.21 Energy plot test #550 (UA1 with domain size 100 μm, gridsize 1 μm). Analysis stop at $t = 0.29s$. . 78

6.22 Energy plot test #2067 (MATUA1 with domain size 50 μm, gridsize 1 μm). 78

6.23 Power plots test #42 (biaxial loading) 79

6.24 ETSLs test #42 (biaxial loading) 79

6.25 Multi-angle TSL 80

6.26 Uniaxial 22.5° tests #551, #556, #561, #566. Four repetitions with different fiber distributions are performed. 81

6.27 Uniaxial 22.5° tests with different RVE aspect ratios 82

6.28 Original and equivalent crack domains 83

7.1 Material TSL, with the undamaged G_f highlighted. 89

7.2 Abaqus energies and viscous dissipation for test #1046 90

7.3 Test #1046 fracture pattern and crack recognition 90

Nomenclature

Acronyms

BA	Biaxial
BC	Boundary Condition
BK	Benzeggagh-Kenane
CFRP	Carbon Fiber Reinforced Polymer
CG	Crack Group
CSR	Complete Spatial Random
CTOD	Crack Opening Tip Displacement
CZM	Cohesive Zone Model
DBT	Dummy node Bottom-Top
DLR	Dummy node Left-Right
EPFM	Elastic-Plastic Fracture Mechanics
ETSL	Effective Traction Separation Law
EVOL	Element Volume
FEA	Finite Element Analysis
FEM	Finite Element Method
FIB	Focused Ion Beam
FPZ	Fracture Process Zone
FRP	Fiber Reinforced Polymer
GLARE	Glass Reinforced Aluminum
HM	Hill-Mandel
LEFM	Linear Elastic Fracture Mechanics
MAAD	Macroscopic Atomistic Ab initio Dynamics
MAXS	Maximum Nominal Stress
MD	Molecular Dynamics
MVE	Microscopic Volume Element
MVE	Microstructural Volume Element
NNA	Nearest Neighbour Algorithm
PBC	Periodic Boundary Condition
PS	Pure Shear
QC	Quasicontinuum
QUADS	Quadratic nominal stress criterion
RVE	Representative Volume Element
SDEG	Stiffness degradation
SEM	Scanning Electron Microscope
SIF	Stress Intensity Factor
SSY	Small Scale Yielding
SVD	Singular Value Decomposition
TSL	Traction Separation Law
UA	Uniaxial
UD	Unidirectional
XFEM	eXtended Finite Element Method

Symbols

$()^{\mathrm{f}}$	Effective quantity
α	Traction calibration parameter
δ	Opening displacement
δ^f	Cohesive failure opening
δ^{max}	Maximum achieved opening
δ^o	Opening at damage initiation
δ_c	Cohesive characteristic length
ℓ	Scale characteristic size
$\bar{\boldsymbol{\varepsilon}}$	Macroscopic strain tensor
$\boldsymbol{\varepsilon}$	Microscopic strain tensor
η	Viscous regularization parameter
Γ	Crack domain
γ	Surface energy per unit area
γ_p	Surface energy per unit area (plastic)
γ_s	Surface energy per unit area (elastic)
Γ_{0m}	RVE boundary
ν	Poisson's ratio

Ω	Microstructural domain
$\partial\Omega$	Microstructural domain boundary
Π	Potential energy
Π_0	Potential energy of an uncracked plate
ρ	Density
σ, $\boldsymbol{\sigma}$	Stress
σ_{cr}	Critical stress
σ_{YS}	Yield stress
θ	Load angle
φ	Crack orientation
A	Area
a	Crack length
a_{eff}	Effective crack length
B	Plate thickness
b	Crack width
$\mathbf{C}$	Stiffness tensor
D, d, $\boldsymbol{\kappa}$	Damage variable
d_f	Critical displacement
d_f	Fiber diameter
d_v	Viscous stiffness degradation
E	Young's modulus
E'	Young's modulus modified in the case of plane strain
E_{COH}	Cohesive stiffness
f	Flip variable
$\mathbf{f}_{\mathrm{coh}}$	Cohesive response function
$\mathbf{F}$	Deformation gradient tensor
G	Energy release rate
G	Shear modulus
G_f	Strain energy release rate
${}^3\mathbf{G}_M$	Gradient of the deformation gradient tensor
K	Stress intensity factor
K_c	Fracture toughness
$\mathbf{l}$	Tangent vector
$\mathbf{m}$	Crack normal
$\mathbf{n}$	Normal vector
n_f	Fiber number
$\mathbf{P}$	First Piola-Kirchhoff stress tensor
$\mathbf{p}$	First Piola-Kirchhoff stress vector
P^{b}	Bulk power
P^{f}	Fracture power
P^{M}	Macroscopic power
P^{ext}	Externally applied power
R	Crack resistance
r	Distance from crack tip
r_p	Plastic zone size
r_y	Yielding zone size
S	Surface
S_D	Micro-cracks effective surface
t	Time
$\mathbf{T}$	Transformation matrix
$\mathbf{t}$	Traction vector
t^o	Maximum traction, traction at damage initiation
t_{ult}	Tensile strength
$[\![\mathbf{u}]\!]$	Crack opening
$\mathbf{u}$	Displacement vector
v	Volume
V_f	Fiber volume fraction
V_{0m}	RVE reference volume
$\mathbf{w}_m$	Microfluctuation field
W_s	Surface energy
X_C	Longitudinal compression failure strength
X_T	Longitudinal tension failure strength
Y_C	Transverse compression failure strength
Y_T	Transverse tension failure strength

Operators

$\mathrm{div}\,(\mathbf{A})$	$\nabla\cdot\mathbf{A}^T = \frac{\partial T_{ij}}{\partial x_j}$
$\mathrm{div}\,(\mathbf{a})$	$\nabla\cdot\mathbf{a} = \frac{\partial a_i}{\partial x_i}$
$\mathrm{grad}\,(\mathbf{A})$	$\nabla\mathbf{A} = \frac{\partial A_{ij}}{\partial x_k}$
$\mathrm{grad}\,(\mathbf{a})$	$\nabla\mathbf{a} = \frac{\partial a_i}{\partial x_j}$
$\mathbf{AB}$	$A_{ij}B_{jk}$
$\mathbf{Ab}$	$A_{ij}b_j$
$\mathbf{A}\cdot\mathbf{B}$	$A_{ij}B_{ij}$
$\mathbf{a}\otimes\mathbf{b}$	a_ib_j

1 Introduction

The massive introduction of composite materials in aerospace structures during the last decade has increased the demand for design tools able to partly replace the expensive structural tests required by certification authorities. In this context, advanced simulation methods provide a powerful approach to reduce experimental testing costs and shorten design cycle times [13, 59].

By implementing fundamental modeling, multiscale simulations capture fracture processes at the microscopic level (μm). This is crucial for composite materials in which fracture entails highly complex nonlinear processes developing at the micro level. Furthermore, thorough understanding of fracture processes is essential to realize the full potential of advanced materials in structural applications. For instance, micro-structural modeling enables researchers and engineers to virtually tailor composite materials, paving the road for microstructural modification [74]. The success of these approaches will result in more accurate simulations, more efficient designs and subsequently, reduction of costs, material and weight savings, and environmental benefits.

In this context, an in-house multiscale simulation framework [94] has been developed to predict fracture initiation and propagation in composite materials. The framework presents a novel approach to extract effective traction-separation laws (ETSLs) based on Hill-Mandel compliant post-processing for both bulk and fracture regions. However, there is a need to expand the capabilities of the framework and to improve its predicting performance, particularly when dealing with complex loading modes and multi-crack propagation [39]. With this aim, a new computational implementation is required to allow for flexible multi-phase mesh generation and finite element analysis (FEA) results post-processing.

This project aims to extend the current theory and computational implementation with three main objectives. First, to extend the framework to simulate fracture in multi-directional composite laminates, accounting for combined failure mechanisms. Second, to refine the theory presented in [94] in order to solve known implementation problems and improve the fracture predictions. Third, to study the impact of anisotropy in the obtention of effective quantities using the developed framework. Hence, the project objective can be defined as follows:

The **research objective** of this project is to contribute to the development of accurate fracture prediction methods, focusing on the study of the influence of anisotropy on the fracture behavior of micro-structural composite models. This objective is achieved by extending and applying a multiscale framework to simulate fracture initiation and propagation in idealized multi-directional laminates, and by solving known theoretical and computational hurdles reported by previous researchers.

The document is structured as follows: in chapter §2 a literature review is provided. The methodology is explained in chapter §3. Then, the numerical implementation is addressed in chapters §4 and §5. The verification of the results is presented in chapter §6. A review on the application of newly found material properties is studied in chapter §7. Finally, conclusions and recommendations are given in §8.

2

Literature Review

This literature review aims to provide a foundation to define research questions and give a clear overview of the state of the art in the field. The subject of this proposal encompasses several fields within structural mechanics, making it highly multidisciplinary. Thus, fundamental fracture mechanics, failure criteria, advanced finite element modelling implementations for fracture simulation, and the most up-to-date research in multiscale simulations is covered.

2.1. Fundamentals of Fracture Mechanics

Fracture mechanics is the branch of engineering science that studies failure in solids due to crack initiation and propagation and is nowadays one of the key topics in engineering. Since the invention of the first tools, fracture has been a problem for humankind. However, it gained special importance during the Industrial Revolution due to the massive introduction of steel products and structures. Back then, the poor understanding of fracture phenomena lead to unexpected failures at sub-critical operation stresses, and engineers were forced to use large safety factors. Thus, small cracks were set aside as inevitable annoyances in structures. However, this changed during the World War II as the spectacular fractures of the Liberty ships due to cold embrittlement brought great attention to the study of fracture.

In parallel, the fast development of aviation and the occurrence of tragic accidents also demanded an urgent need for fracture understanding and new design tools. As a consequence, since the 50s there has been an incredible progress in this branch of engineering sciences. The work lead by Irwin (based on the pioneering works of Griffith and Westergaard) and many others contributed to the development of the methods we use today. Nevertheless, the increasing introduction of composites into the aerospace industry demands further research. Overall, the failure mechanics of composite materials pose a a great challenge and their complex fracture patterns and microscopic failure behavior demand a new set of methods able to predict failure onset and propagation.

2.1.1. Linear Elastic Fracture Mechanics (LEFM)

Linear Elastic Fracture Mechanics (LEFM) describes crack propagation in bodies based on the assumption that the solid shows linear elastic deformation. Thus, LEFM is only applicable in those cases in which plastic deformations are small compared with the crack size, or in other words, under small-scale Yielding (SSY). However, several extensions from LEFM have been developed to deal with non-linear material behaviors under certain circumstances. One of the most noticeable characteristics of LEFM is the prediction of an inverse square-root singularity at crack tip [86]. As a consequence, stress values in the proximity of crack tips approach infinity providing unrealistic results.

Griffith criteria

The work of Griffith [34] represents the beginning of fracture mechanics as an engineering science. Motivated by the discrepancy between the theoretical and the real strength of solids, Griffith postulated the existence

of microscopic flaws in solids, and argued that failure was the product of their growth and propagation. By applying the principle of minimum potential energy to the fracture of solids, Griffith formulated that the cracks would propagate if the internal energy release $\frac{d\Pi}{dA}$ during crack growth overcame the required energy to create new crack surfaces $\frac{dW_s}{dA}$.

$$\frac{d\Pi}{dA} + \frac{dW_s}{dA} \leq 0 \tag{2.1}$$

Years before, Inglis [43] had already described the stress concentration due to elliptical holes in elastic plates under tension (2.2). However, infinite stresses are predicted for sharp cracks ($b = 0$), no matter how small the applied load. In reality, the discrete nature of atomic distances and the appearance of plasticity hinder this behavior. In order to circumvent the limitations of Inglis solution, Griffith determined the energy release of a crack in an elastic plate which, combined with his minimum potential energy formulation yield the Griffith fracture criteria for plane stress and plane strain (2.3).

$$\sigma_{\text{peak}} = \sigma\left(1 + 2\frac{a}{b}\right) \tag{2.2}$$

$$\sigma_{\text{cr,planestress}} = \sqrt{\frac{2E\gamma}{\pi a}} \quad ; \quad \sigma_{\text{cr,planestrain}} = \sqrt{\frac{2E\gamma}{\pi\left(1-\nu^2\right)a}} \tag{2.3}$$

The Griffith criterion is accurate when predicting the strength of brittle materials. However, large inaccuracies raise when applied to ductile materials since the plastic work encompassed by the new crack surfaces creation is neglected. In order to correct this issue, Orowan [75] and Irwin [44] introduced the plastic work involved in the creation of crack surfaces γ_p, so that $\gamma = \gamma_s + \gamma_p$.

Energy Release Rate

On the basis of Griffith's work, Irwin [45] introduced the energy release rate G, defined as the available energy per increment of crack surface dA. Analogously to Griffith's theory, a crack would propagate if the energy release rate surpasses the crack resistance R, defined as the energy required for an increment of crack length. Thus, crack extension takes place when $G \geq R$. The critical value of G at which fracture occurs is defined as fracture toughness G_c.

$$G = -\frac{d\Pi}{dA} \tag{2.4}$$

Stress Intensity Factor Approach

Alternatively, Westergaard developed stress field solutions for cracked infinite plates under external forces [103]. On the grounds of his work, Irwin [46] introduced the stress intensity factors (SIF) for the three fracture modes K_I,K_{II},K_{III}. The fracture modes can be seen in Figure 2.1. The general form of the stress field is shown in eq. (2.5), where f_{ij} represents a dimensionless θ function describing the stress field with respect to the orientation. The stress singularity $1/\sqrt{r}$ can be observed.

$$\sigma_{ij} = \frac{K}{\sqrt{2\pi r}} f_{ij}(\theta) \tag{2.5}$$

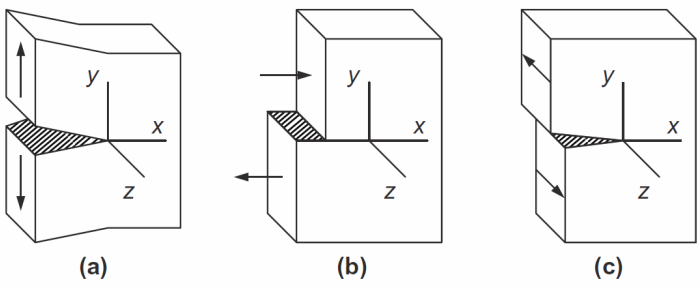

Figure 2.1: Fracture modes a) Mode I: opening, b) Mode II: in-plane shear, c) Mode III: out-of-plane shear [86]

The stress intensity factor K is used as failure criteria. When the SIF reaches the critical value K_c, the crack propagates. Moreover, K_c is also known as fracture toughness. One of the main benefits of using stress intensity factors in engineering applications is the possibility of obtaining the stress field of arbitrary load conditions by superposition of basic solutions [86].

Furthermore, the stress field in an elastic cracked body may be divided into two differentiated components: the singularity and non-singular terms. While in the vicinity of the crack edge the stress field is mainly described by the singularity, in the regions far from the crack tip, the stresses are governed by the edge boundary conditions [3] (see Figure 2.2). When using SIFs, only the singularity component of the stress is captured. Thus, SIFs can only be accurately used in the region close to the crack tip. This region is named K-dominance zone or fracture process zone.

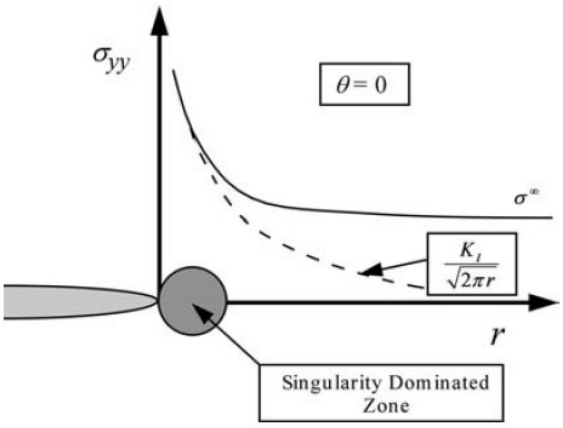

Figure 2.2: Crack front displaying the singularity dominated zone or K-dominated zone, the stress curve predicted by K_I and the actual stress field σ^{∞}. Extracted from [3].

G-K Relation

Both the energy release rate G and the stress intensity factor K are related by eq. (2.6), or in the case of mixed modes by eq. (2.7), assuming selfsimilar crack growth [3]. E' represents the modified Young's modulus in case of plane strain conditions.

$$G = \frac{K_I^2}{E'} \tag{2.6}$$

$$G = \frac{K_I^2}{E'} + \frac{K_{II}^2}{E'} + \frac{K_{III}^2}{2\mu} \tag{2.7}$$

Irwin plastic zone correction

Previously, it has been mentioned the importance of the crack tip stress singularity within LEFM, which predicts infinite stresses at the tip of the crack growth. However, in reality, crack tip radii are finite and thus the stresses are finite as well. Moreover, experimental practice shows a variety of mechanisms such as plasticity or crazing providing stress relaxation [3].

In order to account for this phenomenon, Irwin developed a method to estimate the size of the plastic zone based on the stress redistribution of those areas where the yield stress is exceeded. This method allows applying LEFM with a small correction in materials displaying small-scale yielding. Equation (2.8) describes Irwin's redistribution, where r_p is the size of the plastic zone and σ_{YS} is the yield stress.

$$\sigma_{YS} r_p = \int_0^{r_y} \sigma_{yy} dr = \int_0^{r_y} \frac{K_I}{\sqrt{2\pi r}} dr \quad \rightarrow \quad r_p = \frac{1}{\pi}\left(\frac{K_I}{\sigma_{YS}}\right)^2 \tag{2.8}$$

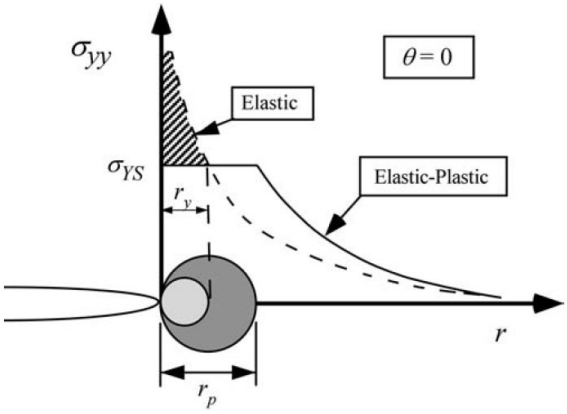

Figure 2.3: Irwin plastic zone correction diagram. Extracted from [3]

As the stresses in the plastic zone are lower than in the elastic model, Irwin proposed to compensate for this phenomenon with an effective crack length $a_{eff} = a + r_y$

2.1.2. Elastic Plastic Fracture Mechanics (EPFM)

Linear Elastic Fracture Mechanics are applicable when the crack tip plasticity is small in comparison to the crack size. An additional requirement is that the cracked entity must still comply with the elastic deformation precepts. For those cases in which these conditions are not applicable, the problem shall be addressed via an elastic-plastic analysis [47].

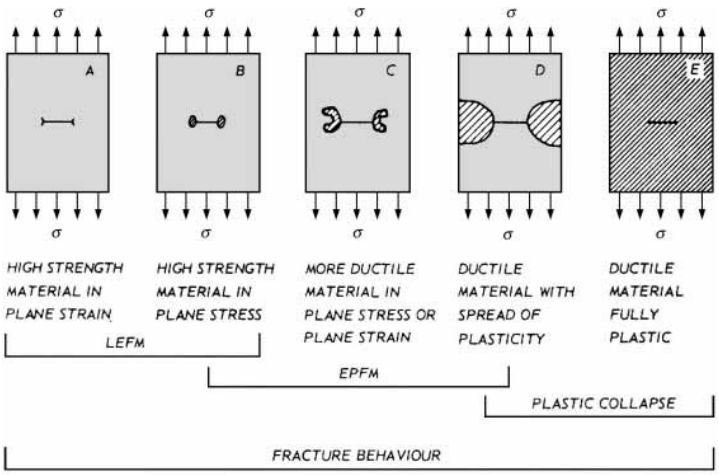

Figure 2.4: Range of applicability of LEFM and EPFM in function of the level of ductility and plastic deformation. Extracted from [47].

Several methods have been developed in order to predict fracture behavior under these conditions. While adaptations of LEFM theory exist for small plastic zones (e.g. Irwin effective crack length), Elastic-Plastic Fracture Mechanics (EPFM) covers cases with a broader extent of the plastic damage. Among EPFM methods they can be found Crack Tip Opening Displacement (CTOD), the J contour integral, K-resistance curves or Cohesive Zone Modelling.

Crack Tip Opening Displacement

Crack Tip Opening Displacement (CTOD) was introduced by Wells as a fracture parameter related to the fracture toughness [101]. Wells realized that due to plasticity, the crack tip blunts. This bluntness can be char-

acterized by the CTOD (see figure 2.5). Thus, it is possible to correlate CTOD with the stress intensity factors while considering plasticity. While several definitions have been proposed [3], Wells suggested calculating the CTOD at the limit of SSY. CTOD (δ) is generally expressed in terms of the energy release rate G.

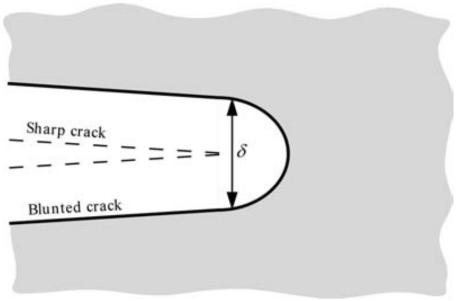

Figure 2.5: CTOD diagram. δ represent the crack tip opening displacement. Extracted from [3]

$$\delta = \frac{4}{\pi}\frac{G}{\sigma_{YS}} \tag{2.9}$$

J Integral

The J-integral was introduced by Rice [80] as a replacement for G. It represents energy release of the material as the crack grows. However, unlike G, the J-integral considers a part of the deformation energy absorbed by the elasto-plastic material as non-recoverable. This work is associated with irreversible plastic deformation. Moreover, the J parameter can also be used to describe the stresses and strains in the crack front (HRR singularity solutions). Similarly to LEFM, resistance R-curves can be drawn for elasto-plastic fracture from J-integral calculations.

2.2. Fracture of composite materials

Failure of composites is a highly complex phenomenon involving several mechanisms at the micro-scale and mesoscale. What it would seem a crack at the macro scale is, in reality, the consequence of several processes at different scales. Moreover, the inherent heterogeneous of composite materials and its associated anisotropy makes failure analysis of these materials extremely complex. In fiber reinforced polymer composites (CFRP), the mechanisms of failure are dependent on the loading mode exerted and the characteristics of the constituents of the composite, as seen in Figure 2.6. Next, the different failure modes of CFRP are covered.

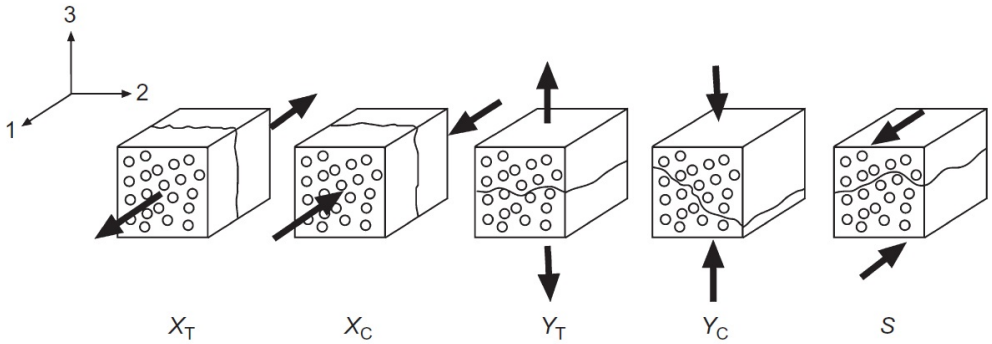

Figure 2.6: Failure mechanisms in unidirectional composite plies under different loading modes [67].

2.2.1. Longitudinal tensile failure X_T

In the case of fiber reinforced composites under longitudinal load, the failure is mainly controlled by the brittle fracture of the fibers [67]. However, failure does not occur simultaneously. Instead, firstly isolated fiber cracks occur at weak spots leading to the development of non-uniform stress fields in the vicinity of these breaks (figure 2.7). Moreover, there is an increase in the normal and interfacial shear stresses of the adjacent fibers. As a result of these local stress concentrations, other failure features follow: transverse matrix cracking (in composites with brittle matrix and strong interfaces), fiber-matrix debonding (in composites with weak interfaces and/or high fiber failure stain) and conical shear fractures in the matrix (in the case of composites with ductile matrix) [14]. Moreover, as the load is increased, the density of these single fiber failures raises until the failures start interacting with each other and eventually coalesce producing general fiber break, fiber pull-out and thus catastrophic failure [14, 61].

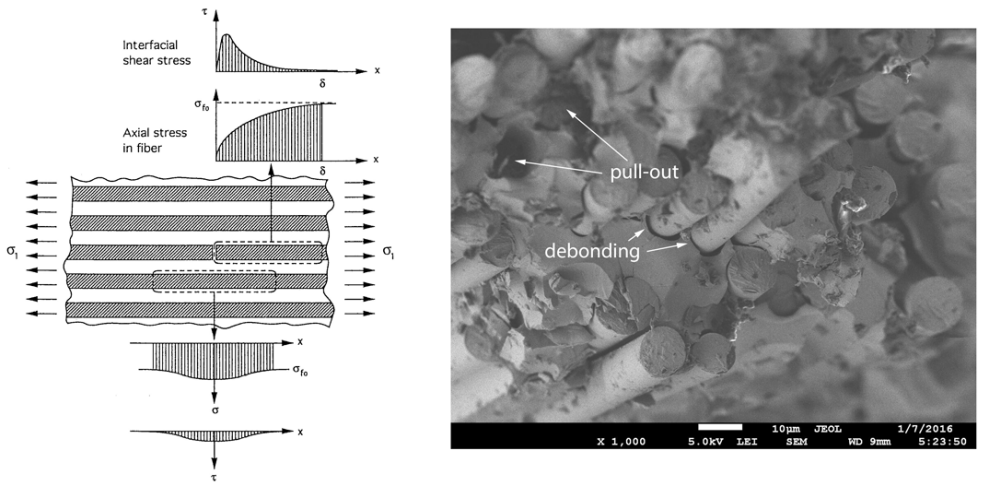

Figure 2.7: Left: Stress distribution in a UD composite laminate under longitudinal tension [14]. Right: SEM FRP composite tensile failure features.

2.2.2. Longitudinal compression failure X_C

Compressive failure of laminates under longitudinal compression occurs due to the collapse of the fibers under microbuckling or kinking [14]. Depending on the fiber volume fraction of the laminate, the out-of-phase/extensional mode (low fiber volume fraction V_f) or the in-phase/shear mode (high V_f) of micro-buckling occurs. Kinking is associated with an initial misalignment of the fibers. It induces local stresses that rotate the fibers, increasing even more the stress and resulting in the fracture of the material. For high V_f laminates with highly aligned fibers, pure compressive failure occurs, governed by the shear failure of the fibers.

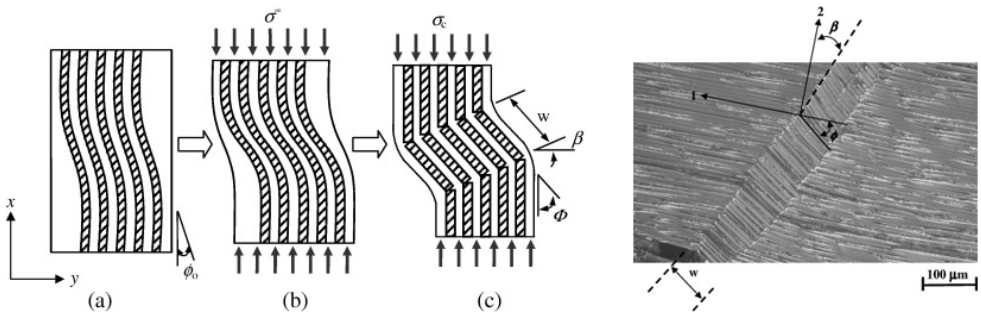

Figure 2.8: Left: kinking process. Right: SEM CFRP compression failure under kinking [50].

2.2.3. Transverse tensile failure Y_T

Transverse tensile strength is governed by the matrix and interface failure. This loading state creates stress concentrations in the matrix and the interface [14]. The most critical ones appear at the fiber-matrix interface, leading to interfacial debonding. As the load increases, the density of interfacial debonding locations increases, eventually coalescing into a crack perpendicular to the tensile axis.

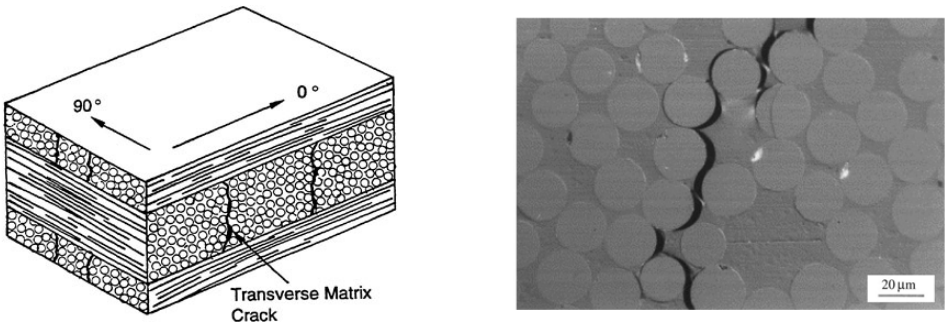

Figure 2.9: Transverse tensile failure. Diagram [66] and SEM image [91].

2.2.4. Transverse compression failure Y_C

Transverse compression failure is governed by the shear failure of the matrix and interface decohesion. This leads to the creation of a shear band due to the plastic deformation of the matrix. This band generally has an orientation in the range of $50-56°$ with respect to the loading direction [33].

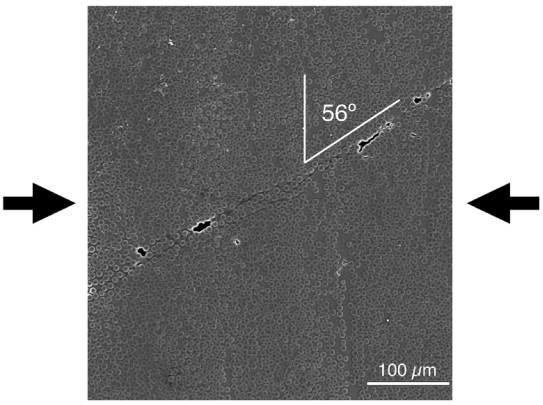

Figure 2.10: SEM image of AS4-epoxy under transverse compression [33].

2.2.5. In-plane shear failure S

In-plane shear loading leads to high shear stress concentrations at fiber-matrix interface. This can provoke shear failure of the matrix or fiber-matrix interface debonding [14].

2.2.6. Failure modes interaction

Moreover, there are interactions between the different failure modes. Shear and compression are reported to have a strong interaction on the strength of the composite ply [6, 100].

2.3. Cohesive Zone Models

Introduced by Barenblatt [5] and Dugdale [20], Cohesive Zone Models (CZM) describe non-linear progressive fracture processes while avoiding the stress singularity predicted by LEFM. By assuming the failure zone locates into a narrow strip ahead of the crack (see figure 2.11), the interaction between crack faces is idealized by establishing a cohesive law, also referred as traction separation law (TSL) . The TSL characterizes the relationship between the opening displacement δ and the cohesive traction t [49]. These laws are generally constructed using experimental data or micromechanical models [21] and can be used for both the initiation and the propagation of damage [7], thus avoiding the use of complex nucleation criteria.

A generic TSL is represented in relation (2.10), where $\sigma_{\max}$ is the peak cohesive traction, and δ_c a characteristic length. Furthermore, δ_c is often replaced by specific characteristic lengths for the normal δ_n and tangential directions δ_t. In addition, the history variable D is commonly used to account for the irreversibility of the damage. Moreover, the required work to separate the faces is the area below the TSL curve, described by (2.11), where δ^{f} is the complete failure opening.

$$\sigma = \sigma_{\max} f(\delta/\delta_c) \tag{2.10}$$

$$G_c = \int_0^{\delta^{\mathrm{f}}} \sigma(\delta)\, d\delta \tag{2.11}$$

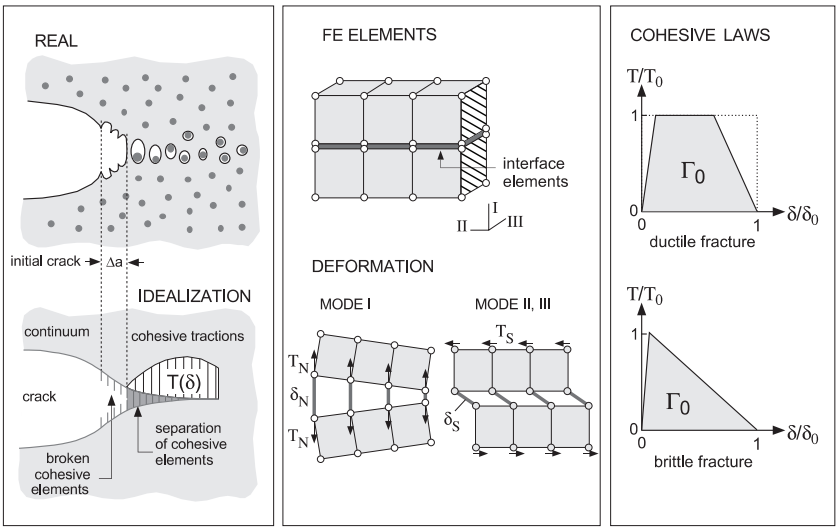

Figure 2.11: Cohesive Zone Modeling idealization, FE implementation, and cohesive law. Extracted from [12]

.

The effectiveness of CZM is dictated by the quality and representative of its TSL. Since the softening curve is considered a material property, several models have been proposed with different adjusting parameters. Park and Paulino [77] distinguish between potential and nonpotential TSLs. While non-potential are easier to develop and are obtained through a phenomenological approach, potential-based TSLs are derived from a potential function governing the fracture process and the tractions and constitutive relations follow naturally from the derivatives of the potential function. Bi-linear TSLs are frequently used [7, 11, 48, 57, 85], however many other TSLs have been established to address the unequal failure behavior of different materials (see figure 2.12) [77]. Overall, two large groups of TSLs can be distinguished: displacement-based and potential-based.

Within **displacement-based** TSLs, Tvergaard and Hutchinson [95] introduced a trapezoidal TSL together with a potential-based model to study elasto-plastic materials. Ortiz and Pandolfi [76] introduced a free energy density dependant traction force. Moreover, after comparing bi-linear (linear softening) and exponential (Smith-Ferrante envelope) TSLs, it was concluded that bi-linear TSLs are preferable due to time-step inte-

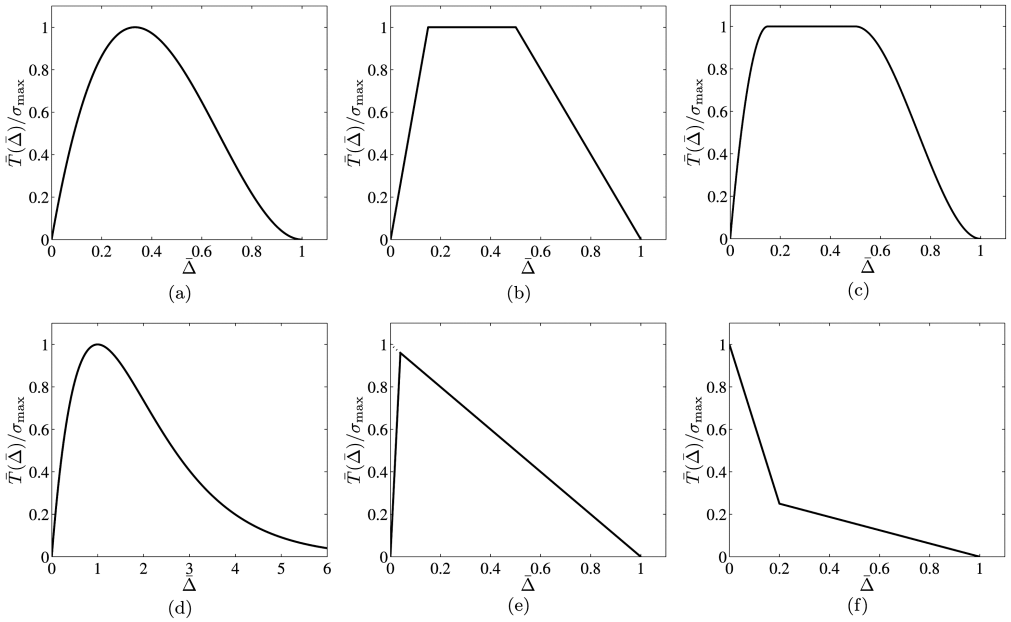

Figure 2.12: Traction separation law examples. a) Cubic b) Trapezoidal c) Smoothed trapezoidal d) Exponential e) Bi-linear f) Bi-linear softening. Adapted from [77]

gration considerations during explicit analysis. The model by Geubelle and Baylor [28] presents a bi-linear cohesive model but incorporates and internal damage variable d governing the reloading and failure.

Potential-based TSLs were developed to cope with some of the weaknesses of 1D non-potential TSLs. For instance, potential-based TSLs are able to provide positive stiffness during the softening phase under tangential deformation or different fracture energies for each fracture mode [77]. These methods use a potential function dependent on the normal and tangential displacements (δ_n,δ_t). Needleman [69] proposed a polynomial potential function dependent on the interfacial separation components δ_n,δ_t. A known drawback is the incorrect prediction of tangential tractions when large shear loads are applied [77]. Several models based on the universal binding energy between atoms have also been developed: the exponential-periodic model, the generalized exponential-periodic model, and the exponential-exponential model. Details can be found in [77].

Moreover, it is important to differentiate between **intrinsic** and **extrinsic** models. While this classification has major implications for FEM implementation, it also has an influence on the shape of the TSLs. While intrinsic laws embody the constitutive model of the material and the failure process in the same curve, extrinsic laws require of an external activation component, generally a critical value. Thus, the cohesive law, in this case, is only active once the failure has started.

The relative simplicity of CZMs with respect to other methods has fostered its implementation within FEM and its use in diverse fields. One of the main applications is the simulation of damage at interfaces (generally adhesive) between two solids. A thorough review of applications can be consulted in [77].

2.4. Multiscale methods

In this section, multiscale theory and applications are introduced. First, the field of multiscale methods is introduced in §2.4.1. Next, the different types of multiscale methods are addressed in §2.4.2, together with a detailed exposition of state of the art research and industrial applications. Moreover, Representative Volume Elements are explained in §2.4.3 and homogenization methods are unraveled in §2.4.4, together with a mathematical excerpt of the first-order computational homogenization scheme. Finally, the computational modeling of the composites' internal phases is discussed in §2.4.5.

2.4.1. Why multiscale?

In engineering practice, the use of different scales for the analysis of engineering products is globally accepted. In the case of the aerospace industry, due to its strict certification requirements, this reality is even more obvious. When analyzing a composite structure it is common to perform a series of uncoupled stress analysis at different length scales i.e. structural level, joint level, and microstructure level, each feeding the next one [24, 59]. This is known as top-down or global-local multiscale approach. While this practice has enabled great developments over the last years, there is a need for a new class of methods able to provide high-fidelity physics-based predictions of composites behavior [24].

Formally, multiscale modeling focuses on providing properties or solutions for each relevant scale (micro, meso, macro) by making use of information provided from other larger or smaller scales [27]. Thus, these methods allow bridging the macroscale analysis with the microscale at which the mechanisms governing the body occur. This allows substituting phenomenological models by constitutive laws derived at the scale at which the physics laws governing the material are better understood [23]. This is especially interesting for composite materials, whose damage mechanisms are not accurately modeled in macroscopic simulations. Moreover, multiscale simulations for composites also open the door to gain knowledge about the impact of composition, orientation and damage evolution of the constituents at the microstructural level have on the macroscopic behavior [74]. Another popular application is the study of damage progression with microscopic resolution.

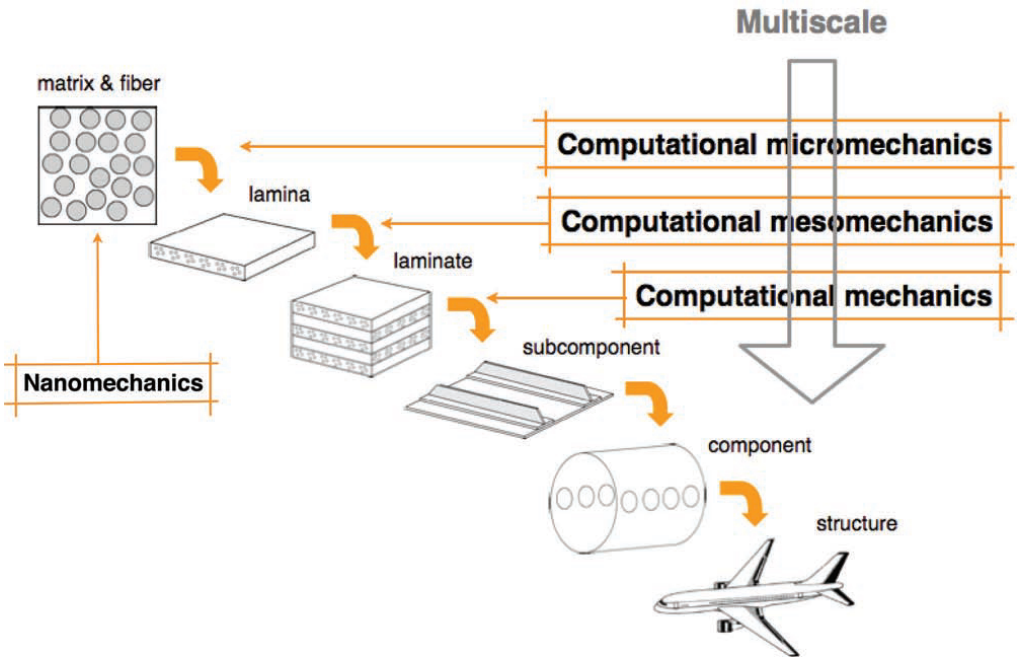

Figure 2.13: Multiscale bottom-top framework for the application of fundamental modeling into the development of composite structures. Obtained from [57].

2.4.2. Classes of multiscale methods

Multiscale methods can be classified into three categories depending on the way the different scales are coupled: hierarchical, concurrent and semi-concurrent [105]. A diagram with all three types and their underlying concept is presented in figure 2.14. In the next sections, each category is explained and applications from the literature are reviewed.

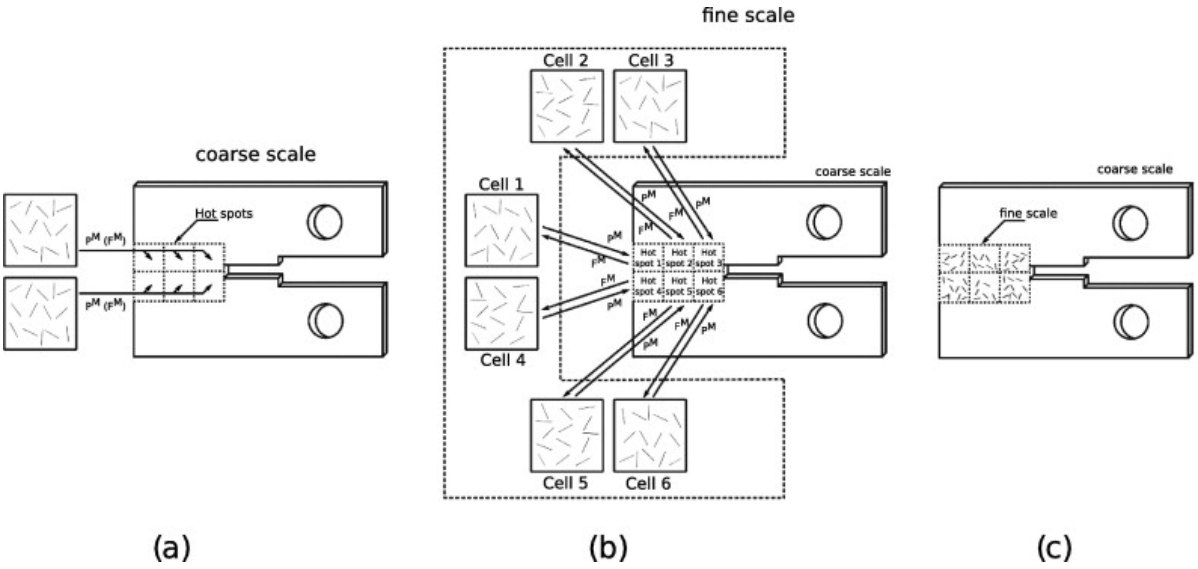

Figure 2.14: Types of multiscale methods. a) Hierarchical b) Semiconcurrent c) Concurrent. Obtained from [83]

Hierarchical methods

Hierarchical methods make use of a fine-scale model in order to derive constitutive laws. This is done by evaluating the response of a Representative Volume Element (RVE) to different inputs. Then, the created constitutive law is applied in the coarse-macro scale. Hierarchical schemes are considered computationally more efficient than semi-concurrent and concurrent methods [89]. However, in the case of problems showing localization (e.g. crack propagation), several authors claim RVE cannot be used due to the loss in statistical homogeneity of the material [31, 57, 105].

Applications of hierarchical methods in composite fracture mechanics are numerous. With the objective of performing high fidelity virtual tests for the screening of composite materials, LLorca and coworkers devised a bottom-up hierarchical multiscale approach [57, 59, 67]. UD plies are simulated at the microscale to characterize their properties and failure initiation locus. Above the fracture initiation point, cracks and/or shear bands are created across the RVE as result of damage localization and the actual behavior is argued to depend on the actual orientation of the crack or shear band [67]. With a similar micromodel, Vaughan and McCarthy [98] studied the impact of intra-ply properties and thermal residual stresses in the shear deformation of a carbon-epoxy composite.

Alfaro et al. [2] performed microscale uniaxial tensile simulations to study the failure of glass-epoxy composites like the ones used in GLARE. Through homogenization, a mesoscopic TSL response was derived from the microscale analysis. Among other topics, the influence of the volume fraction and imperfections on the failure behavior of the material was analyzed.

Concurrent methods

In the case of **concurrent methods**, the fine scale is embedded into the coarse level, coupling both scales at the interface, where the information is exchanged and compatibility and momentum balance are controlled [105]. It is common to make use of an overlapping region "handshake domain", where there is a scale transition from the coarse to the fine model. However, it must be remarked that the coupling between the fine and coarse regions poses difficulties. There are numerical problems associated to the transition between length scales, such as ill-conditioned equilibrium equations and spurious reflections of the interface [104, 105]. Several coupling methods have been developed to reduce these problems [90, 104]. Moreover, due to their computational cost, concurrent models are generally restricted to situations where the refined region is small in comparison to the global domain [105].

Concurrent schemes are quite popular in atomistic simulations. Abraham et al. [1] developed macro-

scopic atomistic ab initio dynamics (MAAD), a methodology to simulate fracture combining ab initio quantum analysis, molecular dynamics (MD) and FEM. Other atomistic-continuum coupling methods have been developed [81], such as the quasicontinuum (QC) method [88] or the Bridging Domain Method [104]. In the field of fracture, Loehnert and Belytschko [58] proposed a concurrent multiscale model for macro- and microcracks simulations using XFEM and developed coupling formulations. Schemes combining XFEM with molecular dynamics have also been used to study fracture propagation [90].

In the field of composite materials, concurrent multiscale simulations have become popular to investigate processes showing localization such as fracture, in which due to the path dependency and the crack size, hierarchical and semi-concurrent schemes are considered invalid by some authors [30]. González and LLorca [32] simulated the fracture behavior of a notched specimen made of SiC fiber reinforced Ti matrix. In a later paper, a notched E-glass/epoxy UD laminate was simulated for fracture prediction under a virtual three-point bend test to investigate fracture toughness properties [8]. Braided composites have been simulated concurrently by Šmilauer et al. [84] to investigate the fracture energy of braided composites under a three-point bending test.

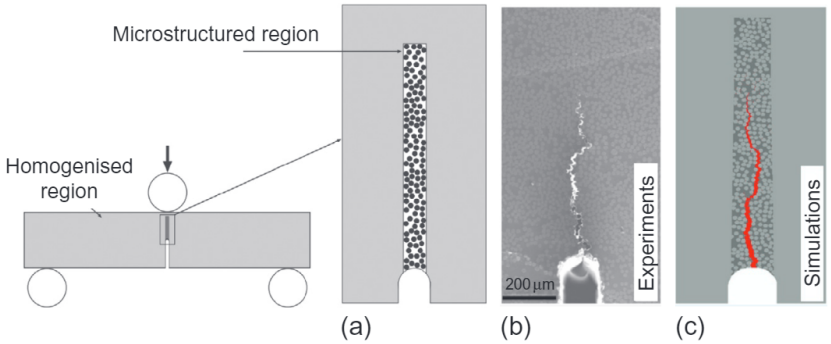

Figure 2.15: Concurrent "embedded cell" model to calculate the fracture toughness of a composite specimen. Extracted from [8].

Semi-concurrent methods

Semi-concurrent methods simultaneously simulate/calculate the coarse and fine scales without a direct coupling between both scales. This is performed by simulating both regions separately. The main advantage is the flexibility of using specific methods/software for each region and also to avoid the numerical problems of concurrent methods [89]. However, they are computationally expensive and, like hierarchical methods, several sources argue that they are not suitable to model localized problems.

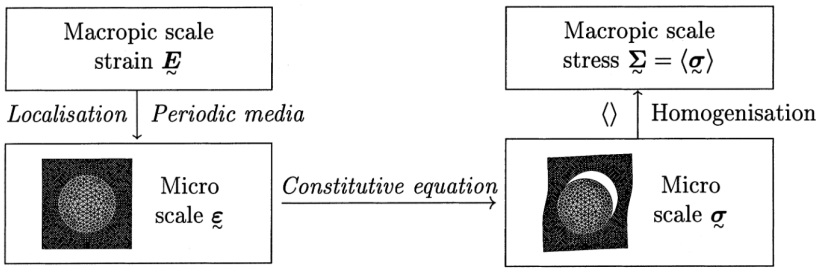

Figure 2.16: Schematic operation of the FE^2 method. Extracted from [22]

One of the most popular examples of semi-concurrent methods in computational mechanics is the FE^2 method developed by Feyel and Chaboche [22]. FE^2 uses a multiscale approach to substitute phenomenological models by micropscopic-level constitutive equations. The method is performed in three steps. First, the macroscopic strains are localized into the microscopic scale, by imposing periodic displacement boundary conditions to the cell. Secondly, a FEM analysis of microscopic cell is performed. Finally, the calculated stresses are homogenized and transferred to the macroscopic level. An analogous procedure is adopted by

Kouznetsova et al. [52] to model large deformations in heterogeneous materials. Later, this model was extended by the use of a higher order method able to transfer the deformation gradient into the microscopic model to increase accuracy [26, 53, 54]. The use of cohesive models for thin layers fracture prediction has been studied relating the cohesive law with failure phenomena occurring at the microscopic level [62]. Verhoosel et al. [99] and Nguyen et al. [71] obtained traction-separation laws for fracture in quasi-brittle solids using a FE^2 setting. The FE^2 method has also been used to model concrete failure [73].

2.4.3. Representative Volume Element

The notion of Representative Volume Element (RVE) is essential in multiscale analysis. Overall, RVEs are smaller instances of the structure used to analyze its behavior with reduced computational effort. RVEs are generally as small as possible, but sufficiently large to be representative of the physical behavior. RVEs shall be big enough to embody the statistical description of the microstructure and to guarantee the independence of its properties with respect to size and location [56]. Several formal definitions have been proposed [31]. Two definitions for RVEs were given by Drugan and Willis [19]: 1) the smallest volume statistically representative of the microstructure 2) is the smallest volume of the heterogeneous material whose behavior accurately represents the actual macroscopic behavior. Proper application of RVEs relies in separation of scales: the microstructure scale ℓ_μ shall be smaller than the RVE size ℓ_m, and much smaller than the characteristic size at the macroscale ℓ_M [25].

$$\ell_\mu < \ell_m \ll \ell_M \tag{2.12}$$

Due to its impact on the simulation time, the determination of the critical RVE size is important. Generally, the critical dimension is found numerically for each different heterogeneous material. Convergence to the exact result shall be obtained by increasing the size of the RVE [31, 51]. Note that tools such as cohesive elements can induce an artificial compliance which impedes convergence when increasing the RVE size or refining the mesh. Moreover, if second-order homogenization is used (see 2.4.4), an additional upper bound to the RVE size is required, which cannot exceed the macroscopic length characterizing the linear variations of the strain field [26]. In the case of composite structures, critical sizes in the order of 30 fibers have been reported to provide good predictions (few percentage error) [33, 38]. In [87, 93] a RVE length to fiber radius $L/R = 50$ is proposed. However, each material has a different critical RVE size dependant on its own constituents properties.

The construction of *statistically representive* RVEs for composite materials is generally performed by randomization of the fibers position within the volume (e.g. [2, 31, 57, 98, 99]). In addition. due to the application of periodic boundary conditions, special care is taken in producing a geometrically periodic pattern. This is, when a fiber is cut at boundary it shall appear at the opposite side (no wall effect). This can be observed in figure 2.17a. Several algorithms have been devised for this purpose (e.g. Nearest Neighbour Algorithm [97], VIPER [42]).

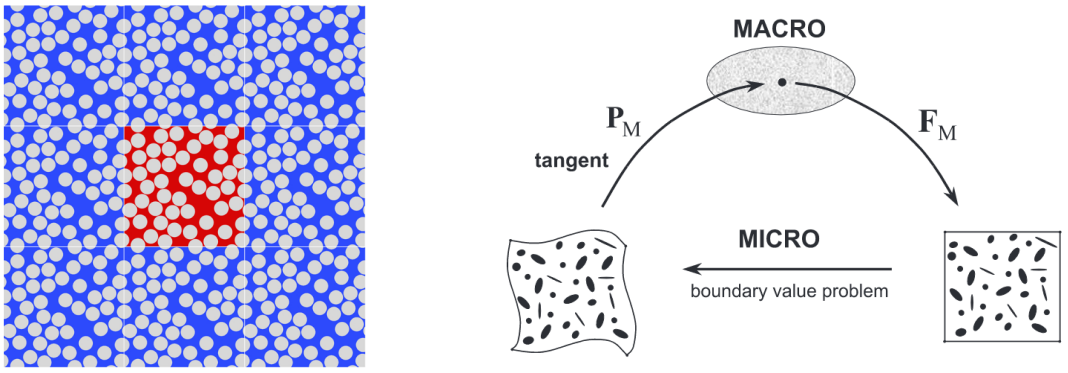

(a) (b)

Figure 2.17: (a) RVE with periodic boundary conditions. Extracted from [9]. (b) First order homogenization scheme. Extracted from [53].

2.4.4. Homogenization

For non-linear processes, homogenization processes are generally used to perform the scale transition and provide useful data from the RVE (microscale) to the macro-level. In this section, the main focus is in computational homogenization. A historical review on homogenization methods can be found at [25].

Overall, microstructural computational homogenization has two main advantages with respect to classic homogenization [33]. Firstly, it allows to accurately model the geometry and the phases. For example in the case of composites the fibers' spatial distribution, size, and shape can be modeled, and voids and inclusions can be taken into account too. This leads to more accurate results. Moreover, the resolution of the boundary value problem at the microscale provides detailed data about the stress and strain distributions inside the RVE. This information can be used to study the damage and failure mechanisms for different loading cases and configurations without conducting extensive laboratory experimentation.

First-order computational homogenization

The most extended scheme is **first-order homogenization**. In this method, the material vector in current configuration of the micro-scale problem $\Delta\mathbf{x}_m$, is related to its counterpart in the reference configuration $\Delta\mathbf{X}_m$ by a first order Taylor expansion (see equation (2.13)). In (2.13), $\mathbf{F}_M$ is the macroscale deformation gradient tensor and $\mathbf{w}_m$ the microfluctuation field. Moreover, a general view of the first-order computational homogenization by [53] can be seen in figure 2.17, where $\mathbf{P}_M$ represents the macroscopic stress tensor.

$$\Delta\mathbf{x}_m = \mathbf{F}_M \Delta\mathbf{X}_m + \mathbf{w}_m \tag{2.13}$$

Overall, the multiscale framework can be derived from kinematic homogenization and the Hill-Mandel principle [18, 25]. Kinematic homogenization obtains the macroscopic strain tensor $\mathbf{F}_M$ by averaging $\mathbf{F}_m$ over the RVE volume. However, in order for the problem to be kinematically admissible, the fluctuations $\mathbf{w}_m$ in the RVE's underformed boundary Γ_{0m} have to be prescribed such that $\int_{\Gamma_{0m}} \mathbf{w}_m \otimes \mathbf{n}_m \, d\Gamma_{0m} = 0$, where $\mathbf{n}_m$ represent the normal vector of the undeformed boundary.

The Hill-Mandel principle safeguards energy conservation through scale transitions, and is the keystone of hierarchical multiscale simulations. Basically, it dictates that the RVE-volume average of the work increment at the micro-scale must equal the local work increment at the macroscale. This can be seen in equation (2.14). If the Hill-Mandel principle holds, the macroscopic stress can be obtained from the volume average of the microscopic stress tensor.

$$\frac{1}{V_{0m}} \int_{V_{0m}} \mathbf{P}_m \cdot \delta\mathbf{F}_m \, dV_{0m} = \mathbf{P}_M \cdot \delta\mathbf{F}_M \tag{2.14}$$

The application of kinematic homogenization and the Hill-Mandel principle imposes two conditions that the RVE boundary conditions must comply with. These conditions are noted in equation (2.15).

$$\int_{\Gamma_{0m}} \mathbf{p}_m \delta\mathbf{w}_m \, d\Gamma_{0m} = 0 \quad ; \quad \int_{\Gamma_{0m}} \mathbf{w}_m \otimes \mathbf{n}_m \, d\Gamma_{0m} = 0 \tag{2.15}$$

Generally, periodic boundary conditions (PBCs) are enforced when working with RVE. These boundary conditions have been reported to provide better estimations of the properties (e.g. effective moduli) [25], to converge faster and to eliminate border effects. When enforcing periodic boundary conditions, a geometrically periodic RVE (such as in figure 2.17a) is used and the microscale fluctuation field is set as periodic at the boundaries of the RVE, such that $\mathbf{w}_m^+ = \mathbf{w}_m^-$.

While PBCs are the most popular, alternative boundary conditions have been proposed [25, 78]:

- Taylor-Voigt: no fluctuations in the RVE are allowed. $\mathbf{w}_m = \mathbf{0}$, for $\forall \mathbf{X}_m \in V_{0m}$
- Uniform displacement: no fluctuations at the RVE boundary are allowed. $\mathbf{w}_m = \mathbf{0}$, for $\forall \mathbf{X}_m \in \Gamma_{0m}$

- Minimal kinematic boundary condition. $\int_{\Gamma_{0m}} \mathbf{w}_m \otimes \mathbf{n}_m \, d\Gamma_{0m} = 0$

Although periodic boundary conditions are considered superior, there are discrepancies about if their use within a concurrent scheme is adequate for the simulation of fracture processes [30, 67, 94]. Thus, the suitability of their use will be assessed in this project.

Alternative homogenization schemes

While the first-order homogenization scheme is popular and its implementation and operation are well understood, it presents limitations when simulating certain problems [26]. Thus, several additions to the first-order homogenization scheme have been proposed [25] such as higher order computational homogenization, continuous-discontinuous homogenization-localization, multiscale interfaces-cohesive cracks and many others.

Second-order computational homogenization is similar to the first-order but the correlation of the current configuration to the reference configuration is performed using a second order Taylor expansion, where ${}^3\mathbf{G}_M$ is the gradient of the deformation gradient tensor $\mathbf{F}_M$ (see equation (2.16). This scheme has some advantages over first-order homogenization [26]. For example, it allows modeling geometrical size effects by introducing a length scale. Moreover, it allows to deal with large deformation gradients and to capture the bending failure mode. However, first-order homogenization is still recommended for applications with a clear separation of scales and small gradients [53].

$$\Delta\mathbf{x}_m = \mathbf{F}_M \Delta\mathbf{X}_m + \frac{1}{2}\Delta\mathbf{X}_m {}^3\mathbf{G}_M \Delta\mathbf{X}_m + \mathbf{w}_m \tag{2.16}$$

Continuous-discontinuous homogenization is mainly oriented to incorporate localized properties of the microscale (such as fracture or damage) in the macroscale without homogenization. Also interesting is the use of multiscale simulations at adhesive/cohesive interfaces [62, 72, 99]. This approach uses microscopic inter-facial RVEs to extract the TSL parameters controlling the macroscopic cohesive zones.

2.4.5. Composite constituents modeling in RVEs

When used for composite multiscale simulations, RVEs are a representation of the microstructure of the material. Thus, all phases are present in the analysis: matrix, fibers and sometimes inclusions and voids. While at the microscale phenomenological models are not required anymore, it is necessary to use constitutive models for the fibers, the matrix and the interface between them. Several methods have been proposed to model the phases of the material. A summary of the approaches found in the literature is shown below.

Fibers

Fibers are generally modeled as linear elastic transversely isotropic solids (in the case of glass fibers, fully isotropic) [67, 98]. In [98], a domain similar to the one in figure 2.17a is modeled, but fiber failure is assumed to be exclusively transverse and thus is not implemented in its 2D model. In 3D models, tensile failure is modeled by inserting several interface elements (serving as fracture planes) in the longitudinal direction of the fiber [67]. The resistance of these interfaces is extracted from fiber strength experimental data. Moreover, in 3D models, compression loading can be studied with undulation models in order to capture the kinking phenomena. In the model used by [79, 96], cohesive elements are inserted between all bulk elements, including fibers. Different TSLs and cohesive properties are used for each of the phases.

Matrix

Several authors model the matrix as an isotropic elasto-plastic solid. Under tension, epoxy matrices are known to fail in a brittle manner. However, in compression and shear they show substantial plastic deformation [107]. The elasto-plastic model determines the yield envelope of the matrix using a modified Drucker-Prager yield criteria, based on the models developed by [60] and [55]. The post-yielding behavior is modeled

differently for tension and compression. Under tensile stress, the damage is accounted using a linear softening law. In compression, a different law is used to account for the plastic deformation before failure. How these models are implemented in FE is not clear. However, Abaqus includes these models for the simulation of concrete under the denomination "damaged plasticity model for concrete and other quasi-brittle materials" [15]. Other authors [63, 85, 98] make use of the Mohr-Coulomb yield criteria with Menétrey and William flow potential function. In [108], the Mohr-Coulomb criteria is used to set the failure value for shear stress. Although there are computational issues regarding the use of these models, they can be alleviated by the use of the crack band model or viscoplastic regularization [15].

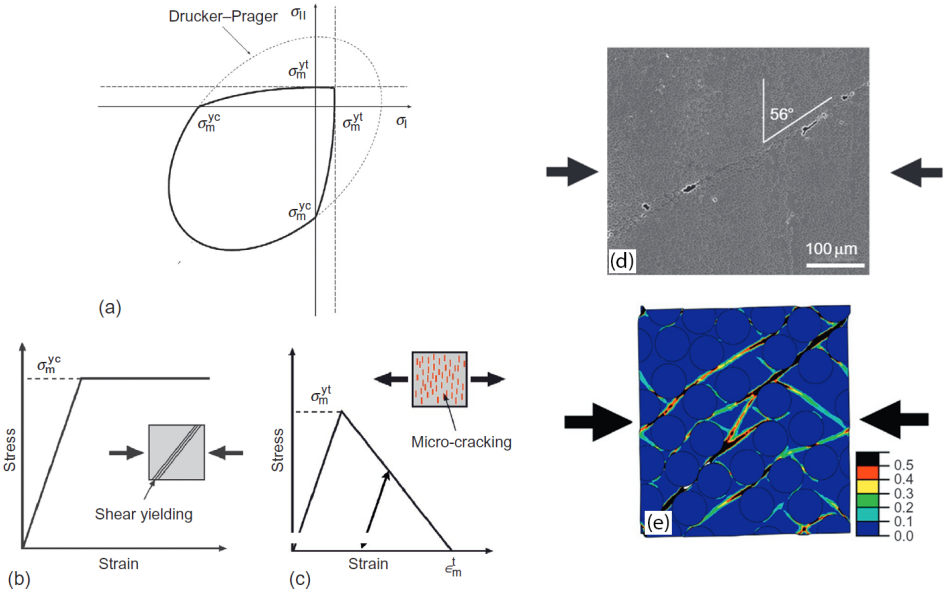

Figure 2.18: Elasto-plastic matrix modeling. a) Epoxy matrix yield envelope under plane stress. b) Post-yield stress-strain curve under compression. c) Post-yield stress-strain curve under tension. d) Microscope image of the composite failure under compression. e) RVE simulation of the composite failure under compression. Adapted from [67].

An alternative way to model the matrix fracture relies on the insertion of zero-thickness cohesive elements in all the interfaces between the matrix solid elements (see figure 2.19) [2, 70, 79, 96]. This approach is based on the work by Xu and Needleman [106]. Since the fracture paths are limited to the interfaces between elements, triangular unstructured meshes are generally used to increase the possible crack propagation directions. In this way, the mesh bias associated with the implementation of cohesive elements within FEM [16] is reduced and the artificially induced fracture energy is minimized (although not completely eliminated).

Fiber-matrix Interface

The fiber-matrix interface is modeled using cohesive laws in most of the reviewed literature dealing with multiscale simulations of composites. However, obtaining experimentally-based cohesive parameters is very challenging. Thus, certain cohesive parameters (e.g., mode I interface fracture energy G_{Ic}) are assumed [68].

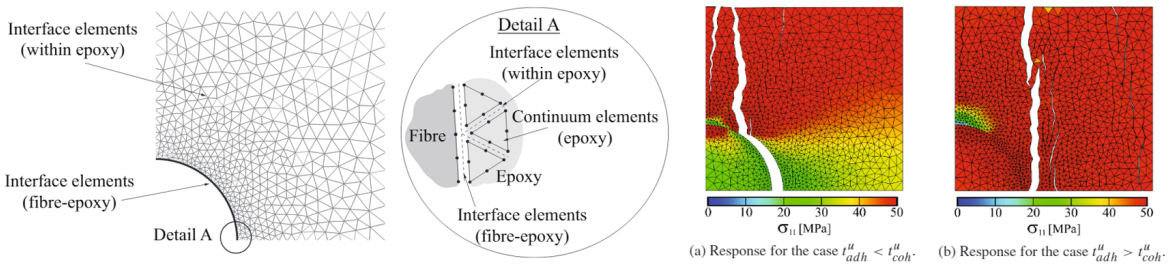

(a) Response for the case $t^u_{adh} < t^u_{coh}$. (b) Response for the case $t^u_{adh} > t^u_{coh}$.

Figure 2.19: Matrix and interface modeling using cohesive elements. Extracted from [2].

3
Methodology

This chapter unfolds the key points of this thesis and the theory upon which is based. First an overview of the thesis methodology is covered in section §3.1. This is followed by a description of the microstructure volume element in section §3.2 and its microstructural formulation in §3.3. Then, the transition relations together with the Hill Mandel principles are covered in §3.4. Effective quantities and their homogenization are discussed in §3.5.

3.1. Overview

This thesis features a framework based on a consistent kinematical analysis which translates micro-cracked domains into one or two effective macro-cracks while complying with the Hill-Mandel condition of energy conservation for both the bulk and crack regions. By homogenizing micro-domain quantities, the effective strength, the fracture energy, and other parameters are obtained for composite materials based on the constituent material's properties and their arrangement. Numerically discontinuous algorithms featuring crack identification and segregation of their energy contributions are used to achieve this. The framework applies periodic boundary conditions and can handle arbitrary loading conditions and geometries.

Building upon the multiscale framework by Turteltaub et al. [94], this thesis deepens the understanding of crack homogenization in highly isotropic domains and paves the way of multi-crack Effective Traction Separation Laws (ETSLs) in multiple-ply domains by setting accurate, numerically consistent new micro-scale homogenization relations. These relations are verified and compared with previous methods. Experimental validation is not performed, as this proof of concept cannot yet provide quantitatively comparable results.

One of the main objectives of the framework is the generation of Effective Traction Separation Laws (ETSLs). These laws derive from the homogenization of the stresses inside a microstructural RVE. ETSLs can be used in macroscopic Cohesive Zone Models (CZMs) to increase the accuracy of coarse models. Moreover, ETSLs can also serve to draw comparisons about the fracture behaviour under different geometric and material configurations.

However, the use of the multiscale framework by Turteltaub et al. [94] to study the fracture behaviour of multi-ply CFRP composite laminates (e.g. [0/90/0]) is subjected to the unlocking of several ongoing and newly identified critical technical issues (e.g. SVD information loss, α factor homogenization, artificial compliance handling, effect of high anisotropy in the simulations, multi-crack identification, enforcing realistic material properties and convergence problems). The identification, assessment, and resolution of this problems represent as well a core part of this thesis.

3.2. Microstructure Volume Element

The Microstructure Volume Element (MVE) represents the foundation of the framework, as it embodies all the features of the CFRP microstructure (e.g., fibers, matrix, interfaces, imperfections) to be analyzed. When using MVE, we refer to any geometric domain featuring the microstructure of the material. The term RVE

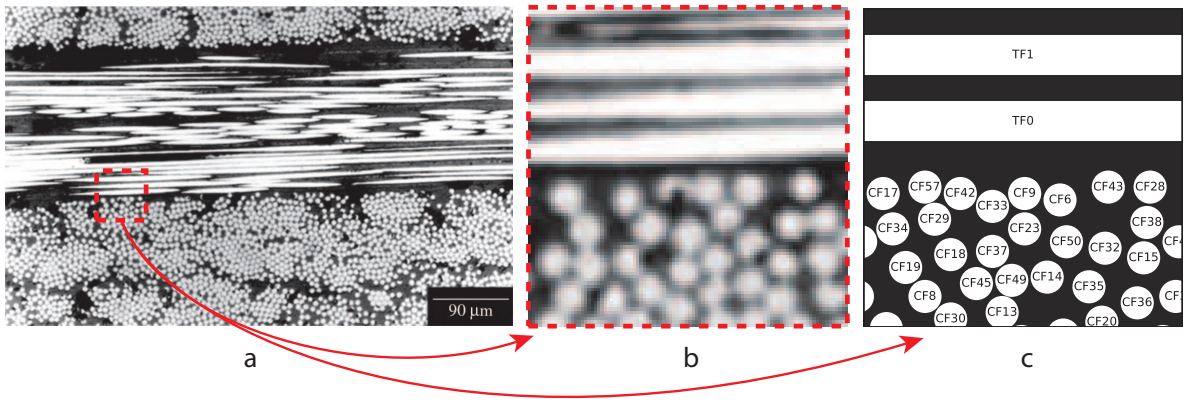

Figure 3.1: CFRP laminate microscope images (*a* and *b*) [92] and idealization *c*.

refers to those MVEs whose ETSLs have shown convergence. The definition of an RVE is discussed in 2.4.3. The convergence studies for determining the minimum RVE size are carried in section §6.4.

The MVEs hereby used simplify the chosen multi-ply laminate (e.g., [0/90], [0/90/0]) to 2D geometries (see figure 3.1). This requires a great idealization of the [90] phase, in which the fibers are sectioned in half along their longitude. While using a 2D simplified model for this case may not be optimal to study the entire complexity of the fracture process, this approach portrays a proof of concept, and its limitations are acknowledged. Nevertheless, this project represents a logical step towards the larger goal of developing a 3D-capable industry-ready application able to feed FEM simulations with accurate fracture parameters based on fundamental modeling at a fraction of the current cost.

The MVEs used in this project model the fibers in the [0] and [90] plies, the matrix holding them together, and the interface between both. Voids, inclusions and imperfections are not modeled.

3.3. Microstructural formulation

Before diving into the scale transition and homogenization equations, it is necessary to properly define the microstructural domain and its constitutive relations. The microstructural domain can be seen in figure 3.2. The domain is labeled as Ω and its boundary as $\partial\Omega$. Each individual edge of the domain is denoted by Ω_i, with $i \in [1,4]$ pointing at the bottom, right, top and left edges respectively. The normals to these edges are referred as $\mathbf{n}_i$, $i \in [1,4]$. Moreover, the global cartesian system is defined by $\mathbf{e}_1$ and $\mathbf{e}_2$, representing the horizontal and vertical directions respectively.

The crack domain is denoted by Γ. In the case of several independent cracks being present, these are represented by Γ_i. The crack's normal is denoted as $\mathbf{m}$. Each crack surface has its normal pointing outwards of the domain. Thus $\mathbf{m} = \mathbf{m}^+$ for the + side, and vice-versa [1]. Moreover, the normals are equals but opposite in direction $\mathbf{m}^+ = -\mathbf{m}^-$. Figure 3.2 also displays the periodicity of the cracks, which seemingly continue over the edges of the domain due to the application of periodic boundary conditions. While other boundary conditions can be applied [25, 78] (see section 2.4.4), in this derivation periodic boundary conditions (PBCs) are applied from the start for simplicity.

The boundary value problem (BVP) governing the MVE is described hereafter. The complete and detailed derivation can be found in [94]. Similarly to other works [39, 96, 102], the fracture process is simulated as a quasi-static process in absence of body forces. This is represented in (3.1), with $\boldsymbol{\sigma}$ being the stress tensor, $\mathbf{x}$ the reference coordinates, and t time. Moreover, the continuity of tractions along crack sides is denoted in (3.2).

$$\operatorname{div} \boldsymbol{\sigma}(\mathbf{x}, t) = \mathbf{0} \qquad \mathbf{x} \in \Omega \backslash \Gamma \tag{3.1}$$

$$\mathbf{t}^+\left(\mathbf{x}^+, t\right) = -\mathbf{t}^-\left(\mathbf{x}^-, t\right) \qquad \mathbf{x} \in \Gamma \tag{3.2}$$

[1] More details on the convention of the normals can be found at §4.3.2

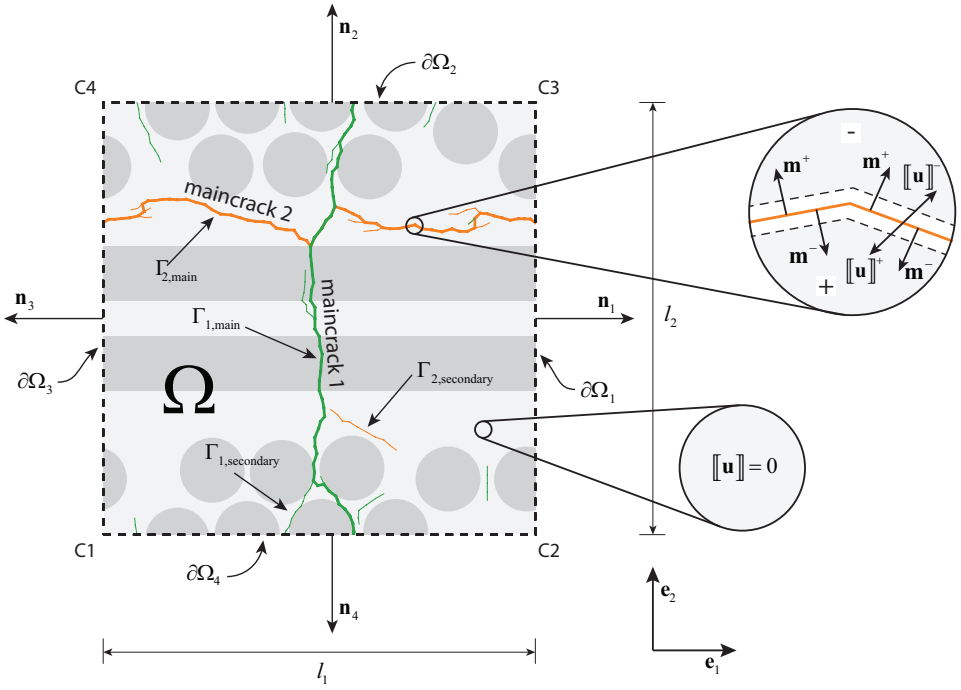

Figure 3.2: Microstructural volume element. Nomenclature, domains and dimensions.

As mentioned before, PBCs are enforced on the domain both for displacements $\mathbf{u}$ and tractions $\mathbf{t}$ (see equations (3.3a) and (3.3b), with $\bar{\boldsymbol{\varepsilon}}$ being the macroscopic strain tensor). Moreover, the present framework includes specific conditions for those crack regions crossing through the domain (periodic) boundaries. This is denoted in (3.3c) and (3.3d).

$$\begin{aligned}&\mathbf{u}(\mathbf{x}+l_1\mathbf{e}_1,t)-\mathbf{u}(\mathbf{x},t)=l_1\bar{\boldsymbol{\varepsilon}}(t)\,\mathbf{e}_1\\&\mathbf{t}(\mathbf{x}+l_1\mathbf{e}_1,t)=-\mathbf{t}(\mathbf{x},t)\end{aligned}\qquad \mathbf{x}\in\partial\Omega_3\backslash\Gamma \tag{3.3a}$$

$$\begin{aligned}&\mathbf{u}(\mathbf{x}+l_2\mathbf{e}_2,t)-\mathbf{u}(\mathbf{x},t)=l_2\bar{\boldsymbol{\varepsilon}}(t)\,\mathbf{e}_2\\&\mathbf{t}(\mathbf{x}+l_2\mathbf{e}_2,t)=-\mathbf{t}(\mathbf{x},t)\end{aligned}\qquad \mathbf{x}\in\partial\Omega_4\backslash\Gamma \tag{3.3b}$$

$$\begin{aligned}&\mathbf{u}^{\pm}\left(\mathbf{x}^{\pm}+l_1\mathbf{e}_1,t\right)-\mathbf{u}^{\pm}\left(\mathbf{x}^{\pm},t\right)=l_1\bar{\boldsymbol{\varepsilon}}(t)\,\mathbf{e}_1\\&\mathbf{t}^{\pm}\left(\mathbf{x}^{\pm}+l_1\mathbf{e}_1,t\right)=-\mathbf{t}^{\pm}\left(\mathbf{x}^{\pm},t\right)\end{aligned}\qquad \mathbf{x}\in\partial\Omega_3\cap\Gamma \tag{3.3c}$$

$$\begin{aligned}&\mathbf{u}^{\pm}\left(\mathbf{x}^{\pm}+l_2\mathbf{e}_2,t\right)-\mathbf{u}^{\pm}\left(\mathbf{x}^{\pm},t\right)=l_2\bar{\boldsymbol{\varepsilon}}(t)\,\mathbf{e}_1\\&\mathbf{t}^{\pm}\left(\mathbf{x}^{\pm}+l_2\mathbf{e}_2,t\right)=-\mathbf{t}^{\pm}\left(\mathbf{x}^{\pm},t\right)\end{aligned}\qquad \mathbf{x}\in\partial\Omega_4\cap\Gamma \tag{3.3d}$$

The micro-scale strain field is considered as (3.4) for all points excluding those in the crack surface. It is important to remark that currently the displacement loading is calculated using small strains.

$$\boldsymbol{\varepsilon}=\frac{1}{2}\left(\nabla\mathbf{u}+\nabla\mathbf{u}^T\right)\qquad \mathbf{x}\in\Omega\backslash\Gamma \tag{3.4}$$

The constitutive behavior of the composite constituents is governed by the elastic relation (3.5), with $\mathbb{C}$ being the stiffness. Moreover, the crack surfaces' constitutive relation is dictated by a cohesive law (3.6). Thus, the tractions $\mathbf{t}$ are governed by the cohesive relation $\mathbf{f}_{\text{coh}}$ being dependent on the crack surface opening $[\![\mathbf{u}]\!]$, the damage variable κ (also noted as D) and the normal vector $\mathbf{m}=\mathbf{m}^+$.

$$\boldsymbol{\sigma}=\mathbb{C}\boldsymbol{\varepsilon}\qquad \mathbf{x}\in\Omega\backslash\Gamma \tag{3.5}$$

$$\mathbf{t}=\mathbf{f}_{\text{coh}}\left([\![\mathbf{u}]\!],\kappa,\mathbf{m}\right)\qquad \mathbf{x}\in\Gamma \tag{3.6}$$

The crack opening $[\![\mathbf{u}]\!]$ is considered as in (3.7). Furthermore, the crack openings are also subjected to the application of the periodic boundary conditions. This yields in relation (3.8).

$$[\![\mathbf{u}]\!]=\mathbf{u}^--\mathbf{u}^+\qquad \mathbf{x}\in\Gamma \tag{3.7}$$

$$\begin{aligned} [[\mathbf{u}(\mathbf{x},t)]] &= [[\mathbf{u}(\mathbf{x}+l_1\mathbf{e}_1,t)]] \qquad \mathbf{x}\in\partial\Omega_3\cap\Gamma \\ [[\mathbf{u}(\mathbf{x},t)]] &= [[\mathbf{u}(\mathbf{x}+l_2\mathbf{e}_2,t)]] \qquad \mathbf{x}\in\partial\Omega_4\cap\Gamma \end{aligned} \tag{3.8}$$

3.4. Micro/macro scale coupling

The scale transition is one of the most critical steps. In the present work, the coupling is performed by homogenization of microscale quantities into the macroscopic quantities. The keystone of this process is the Hill-Mandel condition, which dictates that the power and energy dissipated across scales shall be equivalent.

3.4.1. Homogenization of stresses and strains

Thus, the volumetric average $\langle\boldsymbol{\varepsilon}\rangle_\Omega$ of the microscopic strain field $\boldsymbol{\varepsilon}$ is defined as (3.9). By applying the divergence theorem, $\langle\boldsymbol{\varepsilon}\rangle_\Omega$ and be subdivided in the component integrated around the domain external boundaries $\partial\Omega$, and the component integrated in the crack path Γ. Moreover, by applying the periodic boundary conditions on the integral over the MVE boundary, it is possible to identify the applied strain $\bar{\boldsymbol{\varepsilon}}$ (3.10). The integral in the crack path can be simplified into a *fracture* strain $\boldsymbol{\varepsilon}^{\mathrm{f}}$, defined as (3.11).

$$\langle\boldsymbol{\varepsilon}\rangle_\Omega := \frac{1}{|\Omega|}\int_\Omega \boldsymbol{\varepsilon}\,dv = \frac{1}{|\Omega|}\int_\Omega [\nabla\mathbf{u}]_{\mathrm{sym}}\,dv = \frac{1}{|\Omega|}\int_{\partial\Omega}[\mathbf{u}\otimes\mathbf{n}]_{\mathrm{sym}}\,ds - \frac{1}{|\Omega|}\int_\Gamma [[[\mathbf{u}]]\otimes\mathbf{n}]_{\mathrm{sym}}\,ds \tag{3.9}$$

$$\frac{1}{|\Omega|}\int_{\partial\Omega}[\mathbf{u}\otimes\mathbf{n}]_{\mathrm{sym}}\,ds = [\bar{\boldsymbol{\varepsilon}}\mathbf{e}_1\otimes\mathbf{e}_1]_{\mathrm{sym}} + [\bar{\boldsymbol{\varepsilon}}\mathbf{e}_2\otimes\mathbf{e}_2]_{\mathrm{sym}} = \bar{\boldsymbol{\varepsilon}} \tag{3.10}$$

$$\boldsymbol{\varepsilon}^{\mathrm{f}} = \frac{1}{|\Omega|}\int_\Gamma [[[\mathbf{u}]]\otimes\mathbf{n}]_{\mathrm{sym}}\,ds \tag{3.11}$$

By rewritting the previous relations, the applied strain can be defined as (3.12).

$$\bar{\boldsymbol{\varepsilon}} = \langle\boldsymbol{\varepsilon}\rangle_\Omega + \boldsymbol{\varepsilon}^{\mathrm{f}} \tag{3.12}$$

Furthermore, the macroscopic stress is obtained by stress homogenization as shown in (3.13). For the squared/rectangular MVE geometry, and with the application of periodic boundary conditions, the macroscopic stress simplifies to (3.14). The averaged edge tractions $\bar{\mathbf{t}}_i$ are defined as (3.15).

$$\langle\boldsymbol{\sigma}\rangle_\Omega := \frac{1}{|\Omega|}\int_\Omega \boldsymbol{\sigma}\,dv = \frac{1}{|\Omega|}\int_{\partial\Omega}\mathbf{t}\otimes\mathbf{x}\,ds \tag{3.13}$$

$$\langle\boldsymbol{\sigma}\rangle_\Omega = \bar{\mathbf{t}}_1\otimes\mathbf{e}_1 + \bar{\mathbf{t}}_2\otimes\mathbf{e}_2 \tag{3.14}$$

$$\bar{\mathbf{t}}_i = \frac{1}{|\partial\Omega_i|}\int_{\partial\Omega_i}\mathbf{t}\,ds \tag{3.15}$$

3.4.2. Power relations

The externally applied power P^{ext} done on the MVE by the displacement conditions is described by the line integral over the MVE edges (3.16). The time here considered is the simulation time. Moreover, the power performed by the bulk P^{b} is defined in (3.17). The hereby stated powers are expressed per unit area and unit depth.

$$P^{\mathrm{ext}} := \frac{1}{|\Omega|}\int_{\partial\Omega}\mathbf{t}\cdot\dot{\mathbf{u}}\,ds \tag{3.16}$$

$$P^{\mathrm{b}} := \frac{1}{|\Omega|}\int_\Omega \boldsymbol{\sigma}\cdot\dot{\boldsymbol{\varepsilon}}\,dv \tag{3.17}$$

Moreover, by applying (3.18), the bulk power can be developed into (3.19). By comparing (3.19) and (3.16), it is possible to define a *fracture* power (3.20). Moreover, the externally applied power can linked to the bulk and fracture power (3.21).

$$\operatorname{div}\left(\boldsymbol{\sigma}^T\dot{\mathbf{u}}\right) = \operatorname{div}\boldsymbol{\sigma}\cdot\dot{\boldsymbol{u}} + \boldsymbol{\sigma}\cdot\nabla\dot{\mathbf{u}} = \boldsymbol{\sigma}\cdot\dot{\boldsymbol{\varepsilon}} \tag{3.18}$$

$$P^{\mathrm{b}} := \frac{1}{|\Omega|}\int_{\Omega}\operatorname{div}\left(\boldsymbol{\sigma}^T\dot{\mathbf{u}}\right)dv = \frac{1}{|\Omega|}\int_{\partial\Omega}\mathbf{t}\cdot\dot{\mathbf{u}}\,ds - \frac{1}{|\Omega|}\int_{\Gamma}\mathbf{t}\cdot[\![\dot{\mathbf{u}}]\!]\,ds \tag{3.19}$$

$$P^{\mathrm{f}} = \frac{1}{|\Omega|}\int_{\Gamma}\mathbf{t}\cdot[\![\dot{\mathbf{u}}]\!]\,ds \tag{3.20}$$

$$P^{\mathrm{ext}} = P^{\mathrm{b}} + P^{\mathrm{f}} \tag{3.21}$$

The macroscopic power is defined as the product of the homogenized stress and the applied strain rate (3.22).

$$P^{\mathrm{M}} = \langle\boldsymbol{\sigma}\rangle_{\Omega}\cdot\dot{\bar{\boldsymbol{\varepsilon}}} \tag{3.22}$$

3.4.3. Hill-Mandel condition

The Hill-Mandel principle safeguards power and energy conservation through scale transitions. This is done by considering that the RVE-volume average of the rate of work at the micro-scale must equal the local rate of work at the macroscale. This is expressed in equation (3.23).

$$P^{\mathrm{M}} = P^{\mathrm{ext}} \tag{3.23}$$

By using the previously derived homogenization scheme, and applying periodic boundary conditions, it can be shown that the Hill Mandel is satisfied (3.25). In the expression (3.25), the displacement at the edges $\mathbf{u}$ is substituted by its equivalent in terms of the applied strain rate $\dot{\bar{\boldsymbol{\varepsilon}}}$, its position coordinates $\mathbf{x}$ and the micro-scale fluctuation $\delta\mathbf{w}$. By ruling out the contribution of the microfluctuations around the boundaries due to the periodic boundary conditions, it is possible to obtain the Hill-Mandel condition with the bulk and crack contributions (3.26) and (3.24).

$$\langle\boldsymbol{\sigma}\rangle_{\Omega}\cdot\dot{\bar{\boldsymbol{\varepsilon}}} = \frac{1}{|\Omega|}\int_{\partial\Omega}\mathbf{t}\cdot\dot{\mathbf{u}}\,ds \tag{3.24}$$

$$\frac{1}{|\Omega|}\int_{\partial\Omega}\mathbf{t}\cdot\dot{\mathbf{u}}\,ds = \frac{1}{|\Omega|}\int_{\partial\Omega}\mathbf{t}\cdot\left(\dot{\bar{\boldsymbol{\varepsilon}}}\cdot\mathbf{x}+\delta\dot{\mathbf{w}}\right)ds = \underbrace{\left(\frac{1}{|\Omega|}\int_{\partial\Omega}\mathbf{t}\otimes\mathbf{x}\,ds\right)}_{\langle\boldsymbol{\sigma}\rangle_{\Omega}}\cdot\dot{\bar{\boldsymbol{\varepsilon}}} + \underbrace{\frac{1}{|\Omega|}\int_{\partial\Omega}\mathbf{t}\cdot\delta\dot{\mathbf{w}}\,ds}_{\text{0 due to PBC}} \tag{3.25}$$

$$\langle\boldsymbol{\sigma}\rangle_{\Omega}\cdot\dot{\bar{\boldsymbol{\varepsilon}}} = \frac{1}{|\Omega|}\int_{\Omega}\boldsymbol{\sigma}\cdot\dot{\boldsymbol{\varepsilon}}\,dv + \frac{1}{|\Omega|}\int_{\Gamma}\mathbf{t}\cdot[\![\dot{\boldsymbol{u}}]\!]\,ds \tag{3.26}$$

In the past, by considering the applied strain as the mutual contribution of the bulk and fracture strains, the macroscopic power was unfolded into (3.27). Similarly, the microscale power was subdivided into bulk and crack contributions. Moreover, two Hill Mandel sub-relations for the bulk and the crack regions (see equation (3.29)) were hypothesized provided the condition in (3.30). As it will be seen later on, results in §5.5.1) show that the condition in the right side of (3.29) does not hold with generality, especially in cases with anisotropy, at least when the quantities are homogenized as they are in this framework.

$$P^{\mathrm{M}} = \langle\boldsymbol{\sigma}\rangle_{\Omega}\cdot\dot{\bar{\boldsymbol{\varepsilon}}} = \langle\boldsymbol{\sigma}\rangle_{\Omega}\cdot\langle\dot{\boldsymbol{\varepsilon}}\rangle_{\Omega} + \langle\boldsymbol{\sigma}\rangle_{\Omega}\cdot\dot{\boldsymbol{\varepsilon}}^{\mathrm{f}} \tag{3.27}$$

$$\langle\boldsymbol{\sigma}\rangle_{\Omega}\cdot\langle\dot{\boldsymbol{\varepsilon}}\rangle_{\Omega} + \langle\boldsymbol{\sigma}\rangle_{\Omega}\cdot\dot{\boldsymbol{\varepsilon}}^{\mathrm{f}} = \frac{1}{|\Omega|}\int_{\Omega}\boldsymbol{\sigma}\cdot\dot{\boldsymbol{\varepsilon}}\,dv + \frac{1}{|\Omega|}\int_{\Gamma}\mathbf{t}\cdot[\![\dot{\boldsymbol{u}}]\!]\,ds \tag{3.28}$$

$$\begin{aligned}\langle\boldsymbol{\sigma}\rangle_{\Omega}\cdot\langle\dot{\boldsymbol{\varepsilon}}\rangle_{\Omega} &\stackrel{?}{=} \tfrac{1}{|\Omega|}\textstyle\int_{\Omega}\boldsymbol{\sigma}\cdot\dot{\boldsymbol{\varepsilon}}\,dv\\ \langle\boldsymbol{\sigma}\rangle_{\Omega}\cdot\dot{\boldsymbol{\varepsilon}}^{\mathrm{f}} &\stackrel{?}{=} \tfrac{1}{|\Omega|}\textstyle\int_{\Gamma}\mathbf{t}\cdot[\![\dot{\boldsymbol{u}}]\!]\,ds\end{aligned} \tag{3.29}$$

$$\frac{1}{|\Omega|}\int_{\Gamma}(\langle\boldsymbol{\sigma}\rangle_{\Omega}\mathbf{m}-\mathbf{t})\cdot[\![\dot{\boldsymbol{u}}]\!]\,ds = 0 \tag{3.30}$$

With the power used by the crack, it is possible to define the macroscopic (or effective) quantities that will be used to generate the ETSLs. The macroscopic cohesive TSL is governed by three parameters: the effective crack opening $[\![\mathbf{u}]\!]^{\mathrm{f}}$, the effective normal of the crack $\mathbf{m}^{\mathrm{f}}$ and the applied strain $\bar{\boldsymbol{\varepsilon}}$. Therefore, the effective traction can be expressed as a function of the previous parameters (3.31). For our effective properties to be Hill-Mandel compliant, they would need to satisfy (3.32). The definition of the effective quantities is given in the next section.

$$\mathbf{t}^{\mathrm{f}} = \mathbf{f}_{\mathrm{coh}}\left([\![\dot{\mathbf{u}}]\!]^{\mathrm{f}}, \mathbf{m}^{\mathrm{f}}, \bar{\boldsymbol{\varepsilon}}\right) \tag{3.31}$$

$$\frac{\Gamma^{\mathrm{f}}}{|\Omega|}\mathbf{t}^{\mathrm{f}} \cdot [\![\dot{\mathbf{u}}]\!]^{\mathrm{f}} = \frac{1}{|\Omega|}\int \mathbf{t} \cdot [\![\dot{\mathbf{u}}]\!]\, ds \tag{3.32}$$

3.5. Effective quantities

In the previous section, the Hill Mandel has been satisfied for the global domain, and the Hill-Mandel sub-condition for the crack domain has been set as (3.32). Unfortunately, determining the effective quantities in the crack domain is a more complex process.

3.5.1. Old effective quantities

In previous works, the homogenization had been done via effective quantities defined as the average of tractions (3.33), and the scaled average of displacements (3.36). However, during this thesis, this has been identified to be a source of errors, especially in the case of anisotropic models. The product of averages leads to the combination of the high tractions on non-opened fibers with the large displacements in the almost non-loaded matrix. Overall, and particularly in highly anisotropic domains, it is not possible to consider that the sum of products (integral) equals the product of sums (product of effective quantities). This effect was previously camouflaged due to the cracking of only one phase, or two with similar material properties (matrix, interface).

Additionally, the use of the previously developed α relation (3.33) is dropped. Enforcing the Hill Mandel condition based on a weighted average of $\mathbf{t}^{\mathrm{f}}_{\Gamma}$ and $\mathbf{t}^{\mathrm{f}}_{\Omega}$ should not be used for two reasons. Firstly, it does not guarantee full complying with the Hill Mandel relation. Secondly, because by proper oriented integration of the tractions along the crack, the values of $\mathbf{t}^{\mathrm{f}}_{\Gamma}$ and $\mathbf{t}^{\mathrm{f}}_{\Omega}$ are equal for single fully periodic cracks, and very similar in the case of multiple cracks; thus α is not playing a role. This correlation between $\mathbf{t}^{\mathrm{f}}_{\Gamma}$ and $\mathbf{t}^{\mathrm{f}}_{\Omega}$ can be seen in the results presented in §5.5.2.

$$\mathbf{t}^{\mathrm{f,old}} = \alpha\mathbf{t}^{\mathrm{f}}_{\Gamma} + (1-\alpha)\,\mathbf{t}^{\mathrm{f}}_{\Omega} \tag{3.33}$$

$$\mathbf{t}^{\mathrm{f}}_{\Gamma} = \langle \mathbf{t} \rangle_{\Gamma} = \frac{1}{|\Gamma|}\int_{\Gamma} \mathbf{t}\, ds \tag{3.34}$$

$$\mathbf{t}^{\mathrm{f},}_{\Omega} = \langle \boldsymbol{\sigma} \rangle_{\Omega}\mathbf{m}^{\mathrm{f}} = \frac{1}{|\Omega|}\int_{\Omega} \boldsymbol{\sigma}\, dv \int_{\Gamma} \mathbf{m}\, ds \tag{3.35}$$

$$[\![\dot{\mathbf{u}}]\!]^{\mathrm{f,old}} := \frac{|\Gamma|}{|\Gamma|^{f}}\int_{\Gamma} [\![\dot{\mathbf{u}}]\!]\, ds \tag{3.36}$$

3.5.2. New effective quantities

Thus, a new series of effective quantities are presented. Since up-to-now it has not been possible to devise energy-consistent effective values based on averages for both $[\![\dot{\mathbf{u}}]\!]^{\mathrm{f}}$ and $\mathbf{t}^{\mathrm{f}}$, a new approach is taken. Taking one of the effective quantities as correct, the other effective quantity is recalculated. Using this approach, the effective quantities are Hill-Mandel compliant by definition. Thus, two pairs of effective quantities can be obtained: $\left[\mathbf{t}^{\mathrm{f,calc}},\ [\![\dot{\mathbf{u}}]\!]^{\mathrm{f}}\right]$ and $\left[\mathbf{t}^{\mathrm{f}},\ [\![\dot{\mathbf{u}}]\!]^{\mathrm{f,calc}}\right]$. In the next paragraphs, these quantities are defined.

Effective traction

The effective traction is defined as the average of the tractions along the main crack (3.37). The tractions over the secondary cracks and branches are not integrated.

$$\mathbf{t}^{\mathrm{f}} = \mathbf{t}^{\mathrm{f}}_{\Gamma} = \frac{1}{|\Gamma|}\int_{\Gamma_{\mathrm{main}}} \mathbf{t}\, ds \tag{3.37}$$

Alternatively, secondary effective tractions are defined as (3.38) and (3.39). These tractions are later used in the implementation for checks, and also as the effective traction when the characteristics of the analysis lead to an ill-calculated $\mathbf{t}^{\mathrm{f}}_{\Gamma}$.

$$\mathbf{t}^{\mathrm{f}}_{\Omega} = \langle \boldsymbol{\sigma} \rangle_{\Omega} \mathbf{m}^{\mathrm{f}} \tag{3.38}$$

$$\mathbf{t}^{\mathrm{f}}_{\partial\Omega} = \langle \boldsymbol{\sigma} \rangle_{\partial\Omega} \mathbf{m}^{\mathrm{f}} \tag{3.39}$$

Effective opening rate

The effective opening and the effective opening rate have been reformulated. Averaging and scaling, as used in [17], does not provide an accurate representation of the actual opening of the RVE. Instead, projections are used (3.42), where $[\![\mathbf{u}]\!]_{\mathrm{elem}}$ is the opening of each element, and Γ_{proj} the projection of the element length over the effective crack. This projection is calculated as in (3.41), where $\hat{\mathbf{l}}_{\mathrm{elem}}$ and $\hat{\mathbf{l}}_{\mathrm{CG}}$ are the tangent vectors of the element and the effective (macro) crack group, respectively.

The use of projections allows leveling the contributions of the non-parallel crack segments, particularly the perpendicular ones. For example, in figure 3.3a the old formula (3.40) would account for the displacements marked in red (tangential sliding) while still keeping Γ^{f} as in 3.3c. This would result in an overestimation of the actual opening. An additional advantage of using projections is that it is possible to add the opening contributions of secondary cracks and branches in a general way, such as the ones displayed in figure 3.3b. A comparison between effective opening displacements is given in §5.3.

The effective opening rate $[\![\dot{\mathbf{u}}]\!]^{\mathrm{f}}$ is obtained by differentiation of $[\![\mathbf{u}]\!]^{\mathrm{f}}$

$$[\![\mathbf{u}]\!]^{\mathrm{f,old}} = \frac{\Gamma}{\Gamma^{\mathrm{f}}} \frac{\int_{\Gamma} [\![\mathbf{u}]\!]\, ds}{\Gamma} \tag{3.40}$$

$$\Gamma_{\mathrm{proj}} = \left| \Gamma_{\mathrm{elem}} \hat{\mathbf{l}}_{\mathrm{CG}} \right| \tag{3.41}$$

$$[\![\mathbf{u}]\!]^{\mathrm{f}} = \frac{\sum [\![\mathbf{u}]\!]_{\mathrm{elem}} \Gamma_{\mathrm{proj}}}{\Gamma^{\mathrm{f}}} \tag{3.42}$$

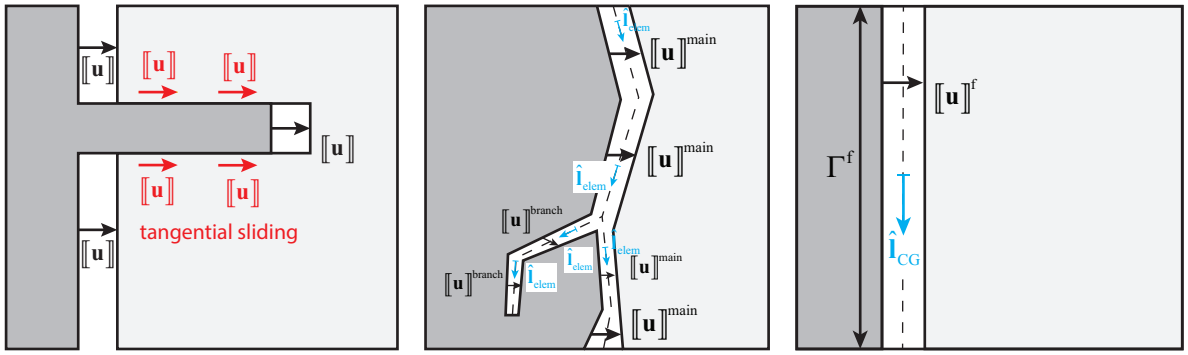

Figure 3.3: Cracked micro-scale domains and effective macro-crack.

Effective traction calculated ($\mathbf{t}^{\mathrm{f,calc}}$)

The recalculated traction is obtained from the Hill Mandel condition for the crack domain (3.43). By multiplying both sides in the right by $\mathbf{t}^{\mathrm{f}}$, it is possible to solve for $\mathbf{t}^{\mathrm{f,calc}}$ (3.45).

$$\frac{1}{\Gamma^{\mathrm{f}}}\int \mathbf{t}\cdot[\![\dot{\mathbf{u}}]\!]\,ds = \mathbf{t}^{\mathrm{f,calc}}\cdot[\![\dot{\mathbf{u}}]\!]^{\mathrm{f}} \tag{3.43}$$

$$\frac{1}{\Gamma^{\mathrm{f}}}\int \mathbf{t}\cdot[\![\dot{\mathbf{u}}]\!]\,ds\,\mathbf{t}^{\mathrm{f}} = \mathbf{t}^{\mathrm{f,calc}}\cdot[\![\dot{\mathbf{u}}]\!]^{\mathrm{f}}\cdot\mathbf{t}^{\mathrm{f}} \tag{3.44}$$

$$\mathbf{t}^{\mathrm{f,calc}} = \frac{\frac{1}{\Gamma^{\mathrm{f}}}\int \mathbf{t}\cdot[\![\dot{\mathbf{u}}]\!]\,ds\,\mathbf{t}^{\mathrm{f}}}{[\![\dot{\mathbf{u}}]\!]^{\mathrm{f}}\cdot\mathbf{t}^{\mathrm{f}}} \tag{3.45}$$

Effective displacement rate calculated ($[\![\dot{\mathbf{u}}]\!]^{\mathrm{f,calc}}$)

A similar procedure is used to calculate effective opening rate (3.47). In this case both sides are multiplied in the left by $[\![\dot{\mathbf{u}}]\!]^{\mathrm{f}}$.

$$\frac{1}{\Gamma^{\mathrm{f}}}\int \mathbf{t}\cdot[\![\dot{\mathbf{u}}]\!]\,ds = \mathbf{t}^{\mathrm{f}}\cdot[\![\dot{\mathbf{u}}]\!]^{\mathrm{f,calc}} \tag{3.46}$$

$$[\![\dot{\mathbf{u}}]\!]^{\mathrm{f,calc}} = \frac{[\![\dot{\mathbf{u}}]\!]^{\mathrm{f}}\,\frac{1}{\Gamma^{\mathrm{f}}}\int \mathbf{t}\cdot[\![\dot{\mathbf{u}}]\!]\,ds}{[\![\dot{\mathbf{u}}]\!]^{\mathrm{f}}\cdot\mathbf{t}^{\mathrm{f}}} \tag{3.47}$$

The calculated opening $[\![\mathbf{u}]\!]^{\mathrm{f,calc}}$ is obtained via integration of $[\![\dot{\mathbf{u}}]\!]^{\mathrm{f,calc}}$

3.5.3. Choice of new effective quantities

The choice of calculating the traction $\left[\mathbf{t}^{\mathrm{f,calc}},\ [\![\mathbf{u}]\!]^{\mathrm{f}}\right]$ (3.45) or the displacement $\left[\mathbf{t}^{\mathrm{f}},\ [\![\mathbf{u}]\!]^{\mathrm{f,calc}}\right]$ (3.47) has a big impact on the traction separation law obtained. While both pairs of parameters yield in Hill-Mandel compliant ETSLs, their shape is different and their interpretation as well. Details on this matter are given in §5.1.

4

Numerical Implementation: Pre-processing and Post-processing.

This chapter covers the pre-processing and post-processing stages of the numerical implementation. First, an overview of the whole process and its main characteristics is given in section §4.1. Then the pre-processing stage is introduced in section §4.2 and the post-processing in §4.3. Moreover, details on the storage, data transfer, and automatization of the process are given in §4.4. The generation of plots and ETSLs and their interpretation are covered in chapter §5.

4.1. Overview

The numerical implementation of the methodology described in chapter §3 is rather complex and involves several steps. A simplified flow diagram of the implementation is presented in figure 4.1. The computational implementation is structured in three main phases: pre-processing, which generates the analysis; the processing, handled by Abaqus; and the post-processing, where the methodology relations are applied, and valuable relations and plots are produced.

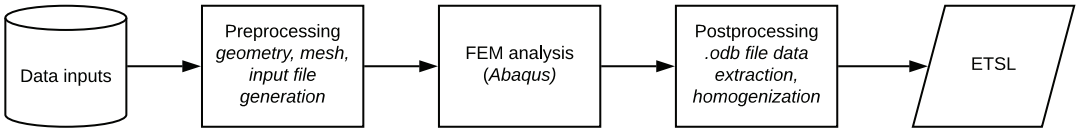

Figure 4.1: Flow diagram of the computational implementation.

The implementation adopts an off-the-shelf approach, where existing solid and cohesive elements in Abaqus are used to simulate the failure and post-failure behavior of the material. Then, advanced post-processing algorithms extract and calculate the relevant quantities. A randomized mesh of solid triangular elements is used to model the domain. In the mesh, cohesive elements are inserted in between all the contact faces of the triangles to model the potential crack paths, allowing crack growth in quasi-arbitrary directions. This enables to circumvent several limitations associated with XFEM, such as crack branching and coalescence. However, the present method shows also several limitations, such as mesh dependency, severe analysis convergence problems, numerical instabilities and loss of contact between crack surfaces, among others.

As part of this thesis, a new implementation has been written to model and process multi-ply composite laminates and perfect the control over the crack domains and their effective displacements, tractions, and powers. Building on the previous works by van Hoorn [96], Westbroek [102] and Hirsch [39], all modules have been rewritten to enable multi-ply object-oriented geometry generation, crack identification and grouping, enhanced multi-crack post-processing, automatic workflow management, and plotting of the outputs. The new implementation increases the efficiency and accuracy of the method, corrects previous errors and, in general, provides a more natural and transparent way to generate, interpret, troubleshoot and present the results.

4.2. Pre-processing

The pre-processing comprises all the steps from the definition of the simulation parameters, the generation of the MVE geometry, its meshing and the creation of the Abaqus input file (see diagram 4.2). In the next chapters, the details of each step are explained. Moreover, a table summarizing all the test and database inputs can be consulted in Appendix A.

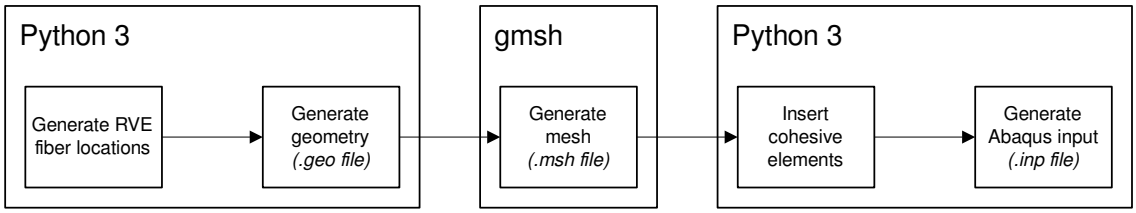

Figure 4.2: Flow diagram of the pre-processing.

4.2.1. Geometry generation

The process starts with the inputs definition and the generation of the geometry. In the study, several geometries are studied, however, the most used geometry is a [0,90,0] laminate[1]. While in the past separate codes had been written to generate cross-sectional [102] and longitudinal phases [39], the nature and differences among the codes made them extremely cumbersome to combine and extend. Thus, an entirely new geometry generation module has been implemented. Overall, the system is capable of generating [0°] and [90°] composite multilayer RVEs, with and without periodicity, with fiber volume fractions from 0% up to approximately 56%, constrained by algorithm limitations.

The new pre-processing module has an object-oriented architecture and defines the RVE at 3 levels: basic features (fibers - in the future voids, inclusions, and so forth could be added), phases (made of basic features) and RVE (made of phases). Each object contains essential information about itself (ID, position, dimensions, periodicity) and methods to, for instance, generate its mesh or draw itself, making debugging and further developments (e.g., the addition of new phases, 3D extension, and so forth) much more manageable. The three main entities of the module (RVE, C-Phase and T-Phase) are now covered.

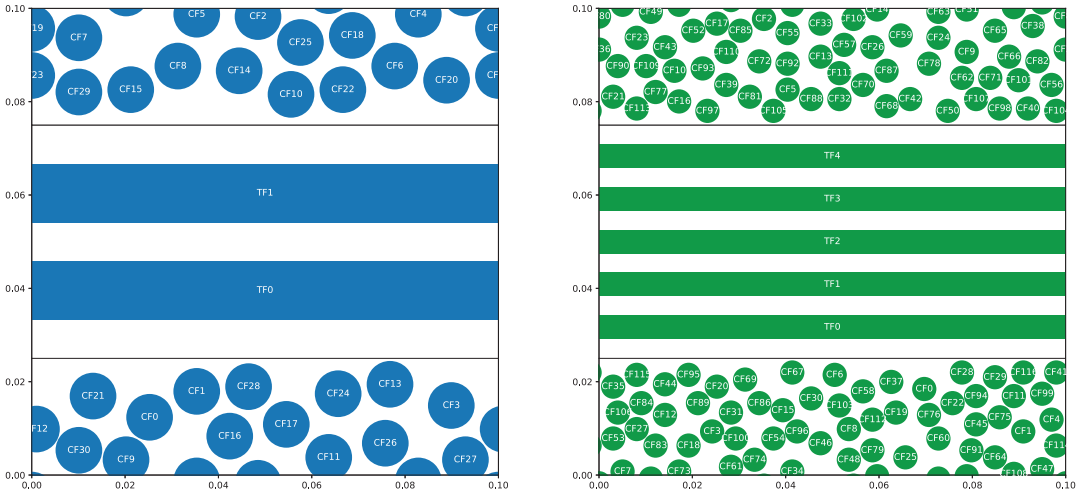

Figure 4.3: Generated geometries for a [0,90,0] laminates with domain size of 100x100 μm, fiber volume fraction $V_f = 0.5$, and fiber diameters 10 μm (left) and 5.2 μm (right).

[1] The [0,90,0] laminate geometries here presented can be considered a [0,90] laminate due to the periodicity. The [0,90,0] notation is preferred.

RVE

The RVE-object is the top entity and embodies information about the dimensions, the boundary conditions and contains the phases that form the simulation domain. The RVE-object has three functions: first, to assemble and generate the phases consistently. Second, to apply the domain boundary conditions to the phases, and the internal boundary conditions to the interfaces between phases. Third, it has the main mesh generation method, which calls the mesh generation method of each element present in the phases.

Cross section phase [0°] (C-Phase)

The cross section phase [0°] generator is based on the algorithm used in [102] and is of Complete Spatial Random (CSR) type. Fibers are randomly positioned within a grid of points. Each time a fiber is placed in one of the randomly selected grid points, those points within the area delimited by the circumference with center at x, y and radius $r_{\text{fibre}} + l_{\text{exclusive}}$ are deleted. If the generation process finishes without allocating all fibers within the domain (i.e., there are no more grid points available for allocation), the process is restarted. Moreover, grid points can also be deleted due to boundary conditions (e.g., wall boundary conditions). If periodicity is enforced, clones of the positioned fiber are created in the opposite sides of the domain.

Although this algorithm is relatively easy to implement, it shows deficiencies when scaling up the problem. The time of generation increases substantially for larger domains and volume fractions above 56%, and the algorithm is not able to find a fiber arrangement with the desired fiber volume fraction in a reasonable time. Other more elaborated algorithms are available in the literature (NNA, shaking methods, etc.) tackling this issue.

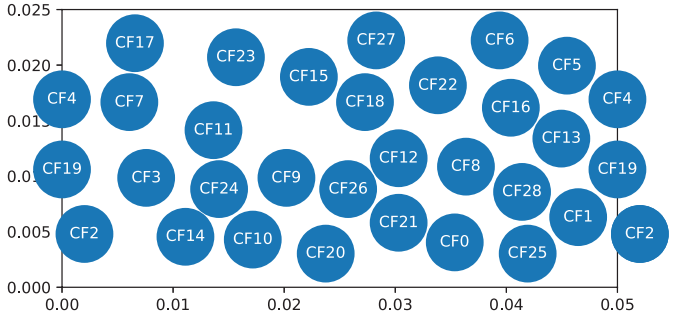

Figure 4.4: C-Phase geometry. Fibers are uncut to showcase periodicity. The characters inside the fibers stand for their identifier.

Transveral phase [90°] (T-Phase)

The generation algorithm for the transversal phase is more straightforward, as it allocates n_f parallel fibers equally spaced over the thickness of the ply. The number of fibers is adapted to satisfy the desired volume fraction (4.1). Alternatively, the number of fibers can be fixed and their diameter changed to satisfy the prescribed V_f.

Several remarks must be made concerning the simplifications of this phase. Firstly, the analysis is conducted in 2D, and thus the transversal phase is idealized. This poses a limitation towards the representativeness and validity of the analysis within the T-Phase, as the microstructure is greatly simplified. Secondly, no random fiber allocation is considered, since the aim of this phase is not to provide true representative (limited by the aforementioned reasons), but to explore and develop the theory when dealing with anisotropy inside the microstructural domain. Furthermore, the fibers are modeled perfectly parallel to each other, and to the top and bottom domain edges. Finally, the imperfections of the fibers are not modeled, and neither are matrix voids nor other inclusions.

$$n_f = \text{round}\left(\frac{V_f \cdot h}{d_f}\right) \tag{4.1}$$

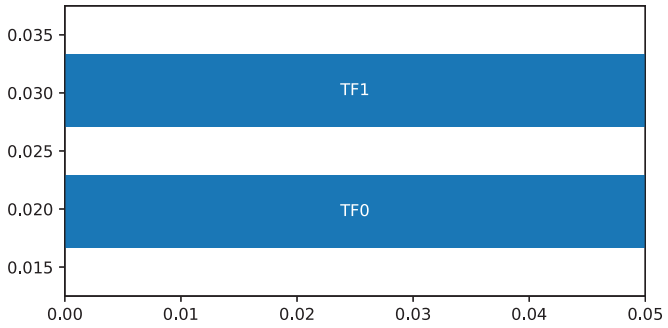

Figure 4.5: T-Phase geometry.

4.2.2. Mesh generation

The mesh is created using using Gmsh [29]. A non-structured triangular mesh is created using Delaunay triangulation. The Delaunay algorithm yields a random distribution of triangles. This randomness is important to reduce the influence of the mesh on the result, achieved by performing repetitions of the test with different meshes. Moreover, a triangular mesh provides more routes for the crack to propagate than quadrilaterals. Although other random algorithms are available, the Delaunay generation algorithm is selected as it is deemed to be the robust and efficient [29].

Furthermore, new methods have been implemented to provide a structured and flexible approach to generate the mesh of the RVE microstructure. The module now makes use of the kernel OpenCASCADE and its boolean capacities to generate the mesh. Using boolean operators has great advantages, as the geometry can be described using simple entities (`Circle` and `Rectangle`, see figure 4.6a), which are later cut by the external RVE rectangular domain (figure 4.6b) and meshed (figure 4.6c). This avoids the cumbersome process of calculating all intersections between the fibers and the domain and defining the geometry on a per-segment basis. Additionally, this new approach allows each fiber/feature object within the `Python` environment to generate its Gmsh geometry code independently. This object-oriented environment is helpful when generating geometries with multiple kinds of elements (differently shaped fibers, and in the future voids, inclusions, and so forth). Additionally, this new implementation closes the gap with any future 3D extension, as 3D boolean operations can also be performed.

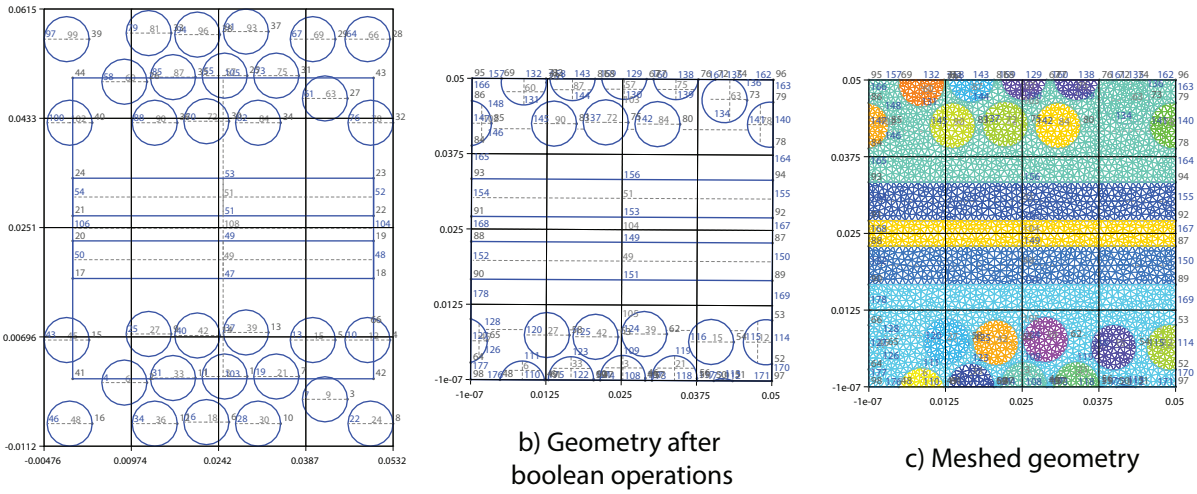

Figure 4.6: Meshing process using OpenCASCADE boolean operators.

While the use of higher geometry entities such as `Circle` and `Rectangle` together with boolean intersections provide advantages, it has the drawback of not having direct control over the naming of the domain's contour segments. Thus, to enforce periodicity in the RVE edges, it is required to identify and couple the opposite boundary segment pairs. This has been achieved by writing a subroutine in Gmsh code which

automatically detects and couples the boundary edges based on the coordinates of their endpoints. This subroutine is presented and commented on appendix C.

Prior to the mesh generation in Gmsh, the python RVE-object generates the `.geo` file containing the geometry of the MVE and the mesh instructions for Gmsh. Additionally, the following parameters were used during the generation of the mesh. The number of mesh smoothing steps set to 10, the minimum and maximum characteristic length are set to half the grid size and the grid size, respectively. The coherence mesh option is enabled. A brief exposition of the `.geo` file structure and these parameters is given in appendix B

4.2.3. Abaqus elements

Within Abaqus, the bulk material is modeled using CPE3 elements, a 3-node, linear, plane strain element. The crack interfaces are modeled using COH2D4 elements, a 4-node two-dimensional cohesive element, with the default thickness set to zero. Figure 4.7 shows the node ordering and the integration points (marked with a cross) for both elements. Special attention must be paid to the counterclockwise node ordering convention, critical during the definition of the element, and explained in the next section.

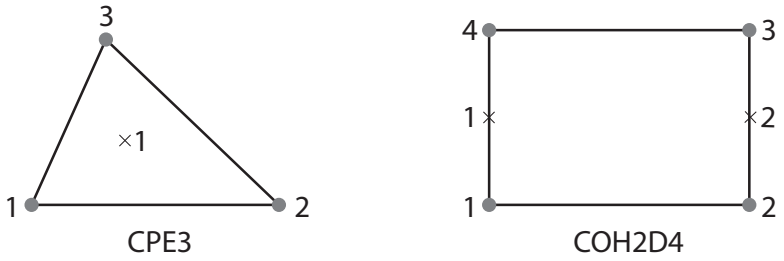

Figure 4.7: Abaqus CPE3 and COH2D4 node ordering (•) and integration points (marked with ×) [15]

4.2.4. Embedding of cohesive elements

Once Gmsh generates the mesh, the `.inp` file generator script inserts cohesive elements between all the elements' faces. The cohesive element embedding process starts by importing the mesh file and finding the shared faces between the triangular elements. The nodes are then duplicated in such a way each of the triangular elements has its individual nodes. The node identifiers are kept and saved together in an array with the shared faces, now composed of 4 nodes.

The next step is the generation of the cohesive elements in all the faces between the elements. For each common face, a cohesive element is inserted. It is **critical** to respect the Abaqus counterclockwise node numbering convention. This is enforced by altering the node sequence of the cohesive element according to condition (4.2), where **a** is the vector from the element centre C_A to N_1 (see figure 4.8) and **b** the vector from the element centre C_A to the cohesive centre F. Moreover, by definition $N_{1,\text{COPY}}$ and $N_{2,\text{COPY}}$ are the duplicates of N_1 and N_2 respectively.

$$\text{Cohesive Element Nodes List} = \begin{cases} \{N_1,\, N_2,\, N_{2,\text{COPY}},\, N_{1,\text{COPY}}\} & \text{if} \quad (\mathbf{a}\times\mathbf{b})_z < 0 \\ \{N_2,\, N_1,\, N_{1,\text{COPY}},\, N_{2,\text{COPY}}\} & \text{if} \quad (\mathbf{a}\times\mathbf{b})_z > 0 \end{cases} \tag{4.2}$$

4.2.5. Boundary Conditions

The implementation of the periodic boundary conditions was introduced in the framework by van Hoorn [96]. The same scheme, with small variations, has been used in the current work.

The mathematical description of the PBCs is given in §3.3, equations (3.3a) to (3.3d). However, Abaqus multi-point constraints only allows that a linear combination of nodal variables are equal to zero [15]. This

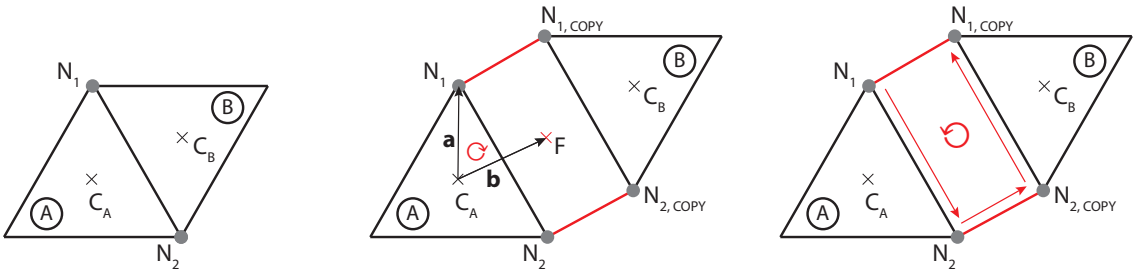

(a) Case 1: z component of the product $\mathbf{a} \times \mathbf{b}$ is negative.

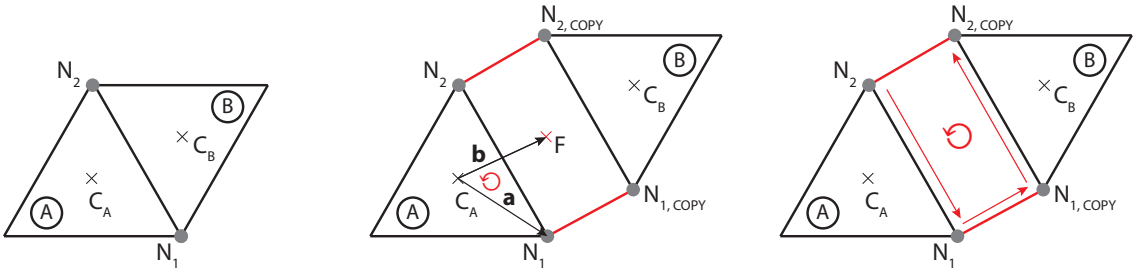

(b) Case 2: z component of the product $\mathbf{a} \times \mathbf{b}$ is positive.

Figure 4.8: Embedding of cohesive elements into the mesh.

can be circumvented by rewriting the periodic boundary condition equations as in equation (4.3), where the non-homogeneous terms ($\bar{\varepsilon}_{11}w$, $\bar{\varepsilon}_{21}w$, $\bar{\varepsilon}_{21}h$, $\bar{\varepsilon}_{22}h$) are accounted for through dummy node displacements (u_1^{DLR}, u_2^{DLR}, u_1^{DBT}, u_2^{DBT}). For each periodic node pair, two equations are imposed, one for each direction.

$$\begin{array}{l} u_1^{\mathrm{R}} - u_1^{\mathrm{L}} = \bar{\varepsilon}_{11}w \\ u_2^{\mathrm{R}} - u_2^{\mathrm{L}} = \bar{\varepsilon}_{21}w \\ u_1^{\mathrm{T}} - u_1^{\mathrm{B}} = \bar{\varepsilon}_{21}h \\ u_2^{\mathrm{T}} - u_2^{\mathrm{B}} = \bar{\varepsilon}_{22}h \end{array} \rightarrow \begin{array}{l} u_1^{\mathrm{R}} - u_1^{\mathrm{L}} - \bar{\varepsilon}_{11}w = 0 \\ u_2^{\mathrm{R}} - u_2^{\mathrm{L}} - \bar{\varepsilon}_{21}w = 0 \\ u_1^{\mathrm{T}} - u_1^{\mathrm{B}} - \bar{\varepsilon}_{21}h = 0 \\ u_2^{\mathrm{T}} - u_2^{\mathrm{B}} - \bar{\varepsilon}_{22}h = 0 \end{array} \rightarrow \begin{array}{l} u_1^{\mathrm{R}} - u_1^{\mathrm{L}} - u_1^{\mathrm{DLR}} = 0 \\ u_2^{\mathrm{R}} - u_2^{\mathrm{L}} - u_2^{\mathrm{DLR}} = 0 \\ u_1^{\mathrm{T}} - u_1^{\mathrm{B}} - u_1^{\mathrm{DBT}} = 0 \\ u_2^{\mathrm{T}} - u_2^{\mathrm{B}} - u_2^{\mathrm{DBT}} = 0 \end{array} \tag{4.3}$$

In figure 4.9, the displacements imposed to the dummies DBT and DLR are shown. These displacements increase monotonically over the simulation time. Moreover, corner C1 is pinned. Although the displacements of nodes C2, C3 and C4 are displayed, no specific boundary conditions are imposed. Their displacements fall naturally from the application of PBCs and dummy displacements.

A vital remark made in [96] on the implementation of the PBCs is the correct selection of node pairs after the duplication of nodes. Only those nodes belonging to elements with at least one face at the edge shall be coupled. The correct coupling of nodes is shown in figure 4.10, wherein the left, top and bottom edges of the mesh are drawn, and the red lines display the periodic couplings.

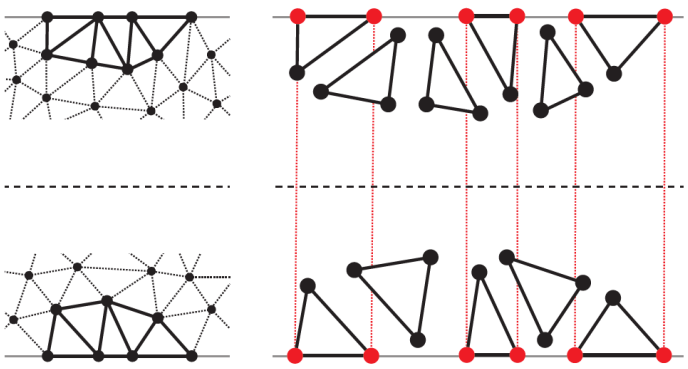

Figure 4.10: Assignment of PBCs at the domain edges. Obtained from [96].

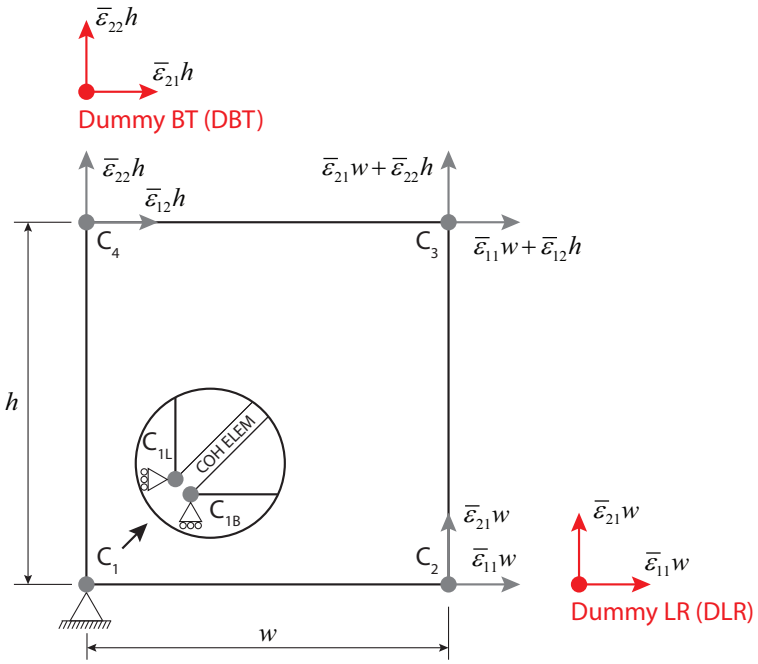

Figure 4.9: MVE boundary conditions and displacements of the dummy and corner nodes.

4.2.6. Loading Modes

Most of the tests performed are uniaxial loading (UA) simulations under different angles θ. However, biaxial tension (BA), pure shear (PS) and mixed loading cases have also been studied. The selected loading modes are introduced through the strain tensor $\bar{\boldsymbol{\varepsilon}}$ and can be seen in table 4.1. The magnitude of the strain tensor is chosen such that it is large enough to produce a full periodic crack.

Table 4.1: Loading strain tensors

Uniaxial	Biaxial	Pure Shear	Mixed
$\boldsymbol{\varepsilon}_{\text{UA},0^\circ} = \begin{pmatrix} \lambda & 0 \\ 0 & 0 \end{pmatrix}$	$\boldsymbol{\varepsilon}_{\text{BA}} = \begin{pmatrix} \lambda & 0 \\ 0 & \lambda \end{pmatrix}$	$\boldsymbol{\varepsilon}_{\text{PS},0^\circ} = \begin{pmatrix} 0 & \lambda \\ \lambda & 0 \end{pmatrix}$	$\boldsymbol{\varepsilon}_{\text{Mixed}} = \begin{pmatrix} \lambda & \lambda \\ \lambda & \lambda \end{pmatrix}$
$\boldsymbol{\varepsilon}_{\text{UA},\theta} = \mathbf{T}(\theta)\ \boldsymbol{\varepsilon}_{\text{UA},0^\circ}\ \mathbf{T}(\theta)^T$		$\boldsymbol{\varepsilon}_{\text{PS},45^\circ} = \begin{pmatrix} \lambda & 0 \\ 0 & -\lambda \end{pmatrix}$	

$$\mathbf{T}(\theta) = \begin{pmatrix} \cos(\theta) & \sin(\theta) \\ -\sin(\theta) & \cos(\theta) \end{pmatrix} \tag{4.4}$$

4.2.7. Cohesive Material Model

Intrinsic Traction Separation Laws (TSLs), introduced in §2.3, are used to model the constitutive response of the crack within the fiber, matrix and interface material.

The damage initiation, indicating the start of material degradation, is modeled using the Maximum Nominal Stress (MAXS) damage initiation criteria, where t_n^o, t_s^o and t_t^o are the maximum values of the nominal stress for purely normal to the interface direction, and purely normal to the two tangential directions[2] [15]. $\langle t_n \rangle$, t_s and t_t are the tractions in the normal and two tangential directions respectively, and the Macaulay bracket $\langle\,\rangle$ indicates that pure compressive stress does not contribute towards damage initiation.

[2]Being the model 2D plane strain, there would not be necessity for the second tangential direction, however it has been implemented in the database/pre-processing to ease future 3D extension.

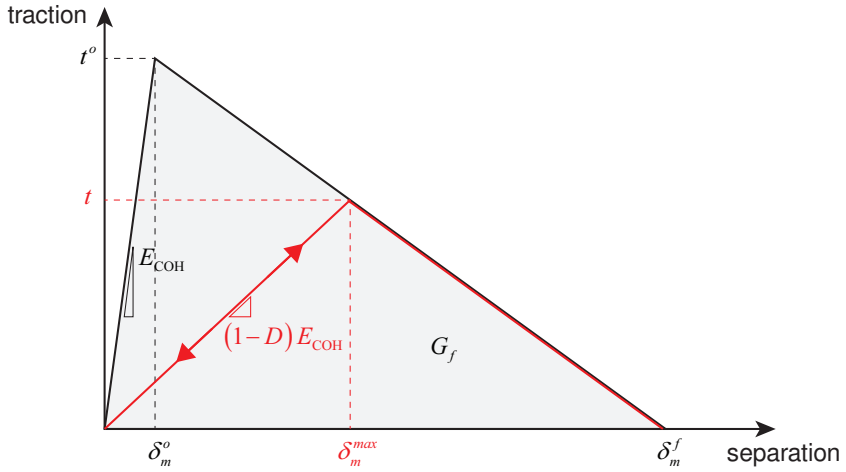

Figure 4.11: Bilinear intrinsic TSL.

$$\max\left\{\frac{\langle t_n\rangle}{t_n^o}, \frac{t_s}{t_s^o}, \frac{t_t}{t_t^o}\right\} = 1 \tag{4.5}$$

Damage evolution, describing the degradation progress of the material stiffness, is modeled using a linear damage evolution law based on energy. The traction response is degraded due to the damage variable $D \in [0,1]$, as indicated in (4.6). In the normal direction, the compression stiffness is not degraded. Moreover, the damage evolution is modeled as mode independent.

$$\begin{aligned} t_n &= \begin{cases} (1-D)\,E_{\text{COH}}\delta_n & \text{for} \quad E_{\text{COH}}\delta_n \geq 0 \\ E_{\text{COH}}\delta_n & \text{otherwise (no damage in compression)} \end{cases} \\ t_s &= (1-D)\,E_{\text{COH}}\delta_s \end{aligned} \tag{4.6}$$

The damage variable D is governed by equation (4.7) by Camanho and Davila [7], where δ^o is the opening at the damage initiation, δ^f the displacement at complete failure and δ^{max} the maximum achieved opening in the history of the cohesive element. Moreover, δ^f can be calculated from the fracture energy G_f and the maximum traction t^o by (4.8).

$$D = \frac{\delta^f\,(\delta^{max} - \delta^o)}{\delta^{max}\left(\delta^f - \delta^o\right)} \tag{4.7}$$

$$\delta^f = \frac{2G_f}{t^o} \tag{4.8}$$

While damage and evolution can be modeled with other relations which may be considered more physically sound (eg. QUADS, BK-law mode mix), in this thesis the emphasis is put on the development of a robust post-processing and homogenization. Using the same material modeling as in the past [39, 96, 102] eases comparing results. While some work has been done in updating the material properties (see 7), it is left as a recommendation to explore in-depth other material and damage modeling possibilities.

One particular consequence of the use of intrinsic TSLs is artificial compliance. This issue, covered in the literature review §2.4.3 can be minimized by the use of very high cohesive stiffness ($E_{\text{COH}} \geq 10^8$ MPa), which has no physical basis and required by the intrinsic, off-the-shelf approach. This value can be even higher if different material properties are used (see chapter §7). The use of such high E_{COH} values drives the damage variable D very fast to values close to one. However, D should not be interpreted as a direct indicator of the level of damage, this is, D = 0.99 indicates a 99% degradation of the initial E_{COH} but, due to the very high ($E_{\text{COH}} = 10^8$ MPa), even D = 0.99 results in large tractions in the cohesive element.

4.2.8. Materials

The materials chosen for the study are HexTow IM7 carbon fibers and HexPly 8552 epoxy matrix. This combination, used in [39] and similar to the one used in [17, 94], is chosen as it is a common combination in aerospace. Thus, material and experimental data are readily available in the literature. The material parameters used are obtained from the theses of Hirsch [39], and de Jong [17]; and the paper by Turteltaub et al. [94]. Please note that matrix void nucleation and plasticity are not modeled.

Table 4.2: **IM7 fiber properties**. Obtained from [39], [17], [94]

ρ (g/cm^3)	E_1 (GPa)	E_2 (GPa)	E_3 (GPa)	ν_{12}	ν_{13}	ν_{23}	G_{12} (GPa)	G_{13} (GPa)	G_{23} (GPa)
1.78	275	20	20	0.2	0.2	0.333	27.5	27.5	7.5

$\varnothing$ (µm)	t_{ult} (MPa)	G_f (J/m^2)	d_f (mm)	E_{coh} (GPa)
10	5000	7500	1.5×10^{-3}	1×10^8

Table 4.3: **HexPly 8552 properties**. Obtained from [39]

ρ (g/cm^3)	E (GPa)	ν	t_{ult} (MPa)	G_f (J/m^2)	d_f (mm)	E_{coh} (GPa)
1.3	4000	0.35	80	200	5×10^{-3}	1×10^8

Table 4.4: **Interface IM7/8552 properties**. Obtained from [39].

t_{ult} (MPa)	G_f (J/m^2)	d_f (mm)	E_{coh} (GPa)
85	200	5×10^{-3}	1×10^8

In a late stage of this thesis, it was detected several of the inherited parameters lacked strong experimentation support. Moreover, several parameters such as the fracture strain energy release rate of the fibers $G_{f,\text{fiber}}$ deviated from the values reported in the literature. Therefore, in an attempt to raise the confidence level of the micromechanical parameters, a new literature review on material properties was conducted. A detailed view of the new material parameters can be found in chapter §7.

4.2.9. Abaqus Numerical Artifacts

Several elements must be taken into consideration while performing the numerical simulations. The sudden change in stiffness after the bilinear law peak and the subsequent softening creates serious convergence problems. These issues are alleviated using automatic stabilization and viscous regularization.

Automatic Stabilization

Automatic stabilization is allowed to help Abaqus converge. The ratio of viscous stabilization energy to strain energy is kept at 5%. In the analyses outputs, its contribution is shown in `ALLSD`.

Viscous regularization

Overall, it is a challenge to reach a converged result without the use of numerical artifacts while performing complex simulations involving a great number of cohesive elements. The stiffness degradation, together with the sudden failure of multiple cohesive elements leads to convergence difficulties, in the form of a negative tangent stiffness matrix. Viscous regularization alleviates this issue by introducing an artificial contribution

into the tangent stiffness matrix, thus making it positive. The regularization is performed by introducing the viscous stiffness degradation d_v, which is ruled by (4.9) [15], with η as the viscous parameter. The viscous regularization contribution is reflected in the output `ALLCD`.

$$\dot{d}_v = \frac{1}{\eta}(d - d_v) \tag{4.9}$$

The value of parameter η is selected on the basis of a parametric study and literature research. After performing several tests in order to compare the contribution of η and compare it to commonly used values, η was set as:

$$\eta = 1e-5 \tag{4.10}$$

From an implementation point of view, it is important to remark this parameter must be implemented through `*SECTION CONTROLS` instead of `*DAMAGE STABILIZATION` as traction-separation laws are used.

When using these numerical artifacts, it is required to check the viscous energy contribution to determine the validity of the results. Within this study, results are considered to convey quantitative information within the 0 to 5% ratio of viscous energy to total energy. However, simulation convergence is still desired after that point to run the crack identification algorithm. During the last stages of the analysis, which feature viscous energy ratios over 20% in most cases, the crack branches coalesce thus forming the main cracks. The formation of clear cracks helps the correct functioning of the crack identification/classification/integration algorithms developed as part of this thesis.

4.2.10. Abaqus Input File

After generating the mesh, the final step before the test processing is to create the input file (`.inp` file). The input file contains all the information required for the Abaqus analysis: geometry, elements, sets, boundary conditions, material properties, load steps, and so forth. The input file is hard-coded automatically, and the whole process is performed outside of the Abaqus Graphical User Interface (GUI) application to avoid the use of the limited Abaqus CAE licenses (and the potential waiting time if all are in use). Once the input file is written, it is submitted to the solver to perform the FEA analysis. A detailed explanation of the structure of the input file is given in appendix D.

4.3. Post-processing

The post-processing encompasses all the operations from the end of the finite element analysis to obtaining the ETSLs. This involves the extraction of the analysis results, their post-processing and plotting. The new post-processing has several differences with respect to previous versions by Westbroek [102] and Hirsch [39], adding two extra steps into the work-flow (see figure 4.12) and heavily modifying the rest.

Over the next pages, the procedures associated to the data extraction and homogenization of the bulk elements (§4.3.1), crack identification and grouping (§4.3.2, §4.3.3), data processing of the cohesive elements (§4.3.4, §4.3.5) and TSLs generation (§5.7) are covered.

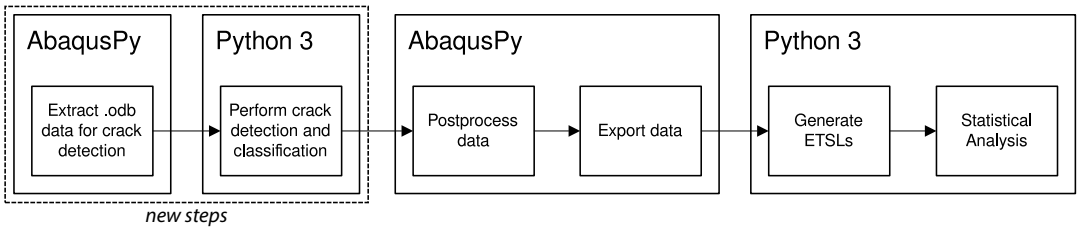

Figure 4.12: Flow diagram of the post-processing

4.3.1. Bulk data extraction and homogenization

As explained in the methodology (chapter §3) and in the overview of the current chapter, one of the key aspects of the current framework is the segregation of the bulk and crack properties. In this section, the procedures used to extract and homogenize the bulk microscopic quantities are explained.

The element stress tensor $\boldsymbol{\sigma}_{\text{elem}}$ can be defined by reshaping the Abaqus stress array `S`.

$$\boldsymbol{\sigma}_{\text{elem}} = \begin{pmatrix} \texttt{S11} & \texttt{S12} \\ \texttt{S12} & \texttt{S22} \end{pmatrix} \tag{4.11}$$

The extraction of the element strain tensor $\boldsymbol{\varepsilon}_{\text{elem}}$ has to be performed carefully, since Abaqus always reports the shear strain $\texttt{E}_{12}$ as engineering strain $\gamma_{12} = 2\,\varepsilon_{12}$. This detail had been overlooked in previous works, creating power and energy inconsistencies in simulations displaying large amounts of shear.

$$\boldsymbol{\varepsilon}_{\text{elem}} = \begin{pmatrix} \texttt{E11} & \frac{\texttt{E12}}{2} \\ \frac{\texttt{E12}}{2} & \texttt{E22} \end{pmatrix} \tag{4.12}$$

Moreover, the volume v of the element is extracted through the `EVOL` output field (4.13). The total domain volume $|\Omega|$ is calculated as (4.14)

$$v_{\text{elem}} = \texttt{EVOL}_{\texttt{elem}} \tag{4.13}$$

$$|\Omega| = \sum_{\text{elem} \in \Omega} v_{\text{elem}} \tag{4.14}$$

The stress and strain quantities can be homogenized in the bulk domain as (4.15) and (4.16) respectively. These relations correspond to equations (3.13) and (3.9).

$$\boldsymbol{\sigma}^{\text{M}}_{\Omega} = \frac{\sum_{\text{elem} \in \Omega} \boldsymbol{\sigma}_{\text{elem}}\, v_{\text{elem}}}{|\Omega|} \tag{4.15}$$

$$\boldsymbol{\varepsilon}^{\text{M}}_{\Omega} = \frac{\sum_{\text{elem} \in \Omega} \boldsymbol{\varepsilon}_{\text{elem}}\, v_{\text{elem}}}{|\Omega|} \tag{4.16}$$

As shown in equation (3.13), the macroscopic stress tensor can also be obtained from the boundary tractions using the divergence theorem. This is implemented as in equation (4.17), where $\mathrm{TF}_{\mathrm{DUMMY\_LR}}$ and $\mathrm{TF}_{\mathrm{DUMMY\_BT}}$ are the traction forces at the dummy nodes, w the MVE width, h the MVE height and e_1, e_2 the global coordinate basis vectors.

$$\boldsymbol{\sigma}^{\mathrm{M}}_{\partial\Omega} = \frac{\mathrm{TF}_{\mathrm{DUMMY\_LR}}}{\mathrm{w}} \otimes \mathrm{e}_1 + \frac{\mathrm{TF}_{\mathrm{DUMMY\_BT}}}{\mathrm{h}} \otimes \mathrm{e}_2 \tag{4.17}$$

The micro-level integrated bulk power is calculated as the sum of each bulk element power contribution (4.18).

$$P_{\mathrm{B}} = \frac{1}{|\Omega|} \sum_{\mathrm{elem} \in \Omega} \boldsymbol{\sigma}_{\mathrm{elem}} \cdot \dot{\boldsymbol{\varepsilon}}_{\mathrm{elem}} v_{\mathrm{elem}} \tag{4.18}$$

4.3.2. Consistent reorientation of cohesive elements for data extraction

The insertion of the cohesive element in Abaqus works randomly. While the consistency of the nodal counterclockwise convention is enforced during the creation of the cohesive elements (see section §4.2.4), the orientation of the normals remains random (see figure 4.13, left). This raises a challenge since during the extraction of data from the cohesive elements it is crucial to maintain control over their normal vectors **m** definition.

Previous methods to perform this control were the use of Singular Value Decomposition (SVD) [94], and the projection of normals by Hirsch [39]. However, both of these methods present deficiencies. In this section, the characteristics of the methods mentioned above are covered, together with the new ones created to tackle the problem: the reorientation by relative displacement, and the algorithm-based reorientation.

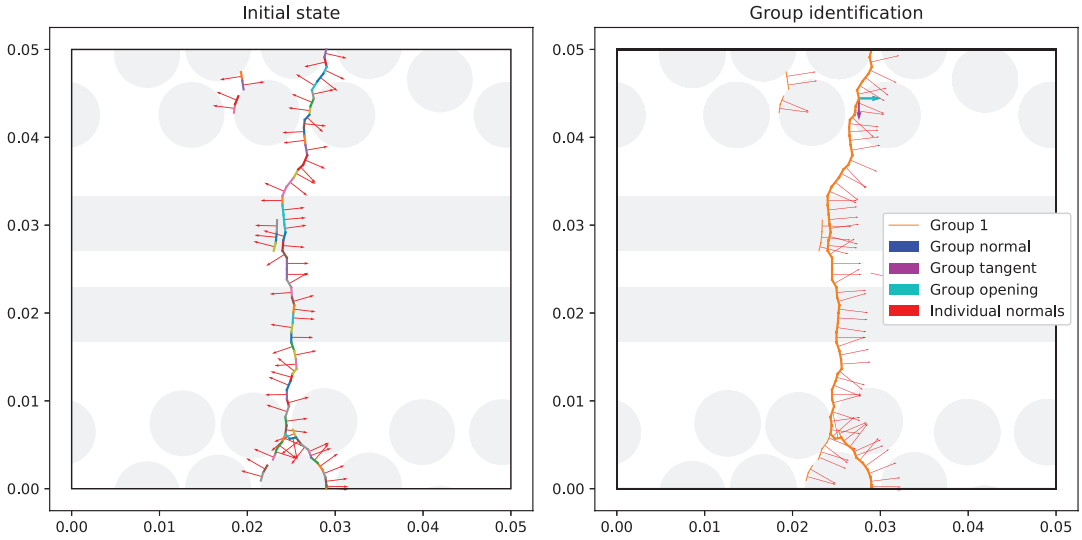

Figure 4.13: Left: element normal vectors **m** across the cohesive crack. Right: element normal vectors **m** across the cohesive crack after applying the reorientation algorithm. (REF38).

Singular Value Decomposition (SVD) method

The use of Singular Value Decomposition tackles the inherent randomness of the normals by defining a quantity invariant with respect to the orientation for each element $|\Gamma| \langle [\![\mathbf{u}]\!]_F \otimes \mathbf{m} \rangle_\Gamma$. This quantity is integrated along the crack path. In a later stage, the effective normal and the effective opening are obtained by performing a SVD decomposition of the orientation-invariant tensor product.

However, the use of this approximation results in a loss of information and precision, which worsens under high anisotropy. In his thesis, Hirsch [39] thoroughly explains the potential information loss processes,

namely during the integration of the invariant tensor product $\langle [\![\mathbf{u}]\!]_F \otimes \mathbf{m} \rangle_\Gamma$ and due to the use of only a part of the SVD decomposition. Moreover, the latter one makes SVD unsuitable for the homogenization of domains displaying two main cracks.

Method of projection of normals

The method of projection of normals by Hirsch [39], reformulated by de Jong [17], represents the first attempt to reorientate the elements' normals in a consistent manner with the opening vector of the crack. The operative principle of the method is as follows: the normals of the cohesive elements $\mathbf{m}$ are projected on the vector $\mathbf{e}_1 = (1,0)$ and divided by the module of the product to obtain a sign depending on their relative orientations. A second projection over $\mathbf{e}_2 = (0,1)$ can be introduced for those cases where the first projection yields zero. The oriented quantities are marked by $(^*)$, and shown below.

$$[\![\mathbf{u}]\!]^* = \frac{\mathbf{m}\cdot\mathbf{e}_1}{|\mathbf{m}\cdot\mathbf{e}_1|}[\![\mathbf{u}]\!] \tag{4.19}$$

$$\mathbf{m}^* = \frac{\mathbf{m}\cdot\mathbf{e}_1}{|\mathbf{m}\cdot\mathbf{e}_1|}\mathbf{m} \tag{4.20}$$

$$\mathbf{t}^* = \frac{\mathbf{m}\cdot\mathbf{e}_1}{|\mathbf{m}\cdot\mathbf{e}_1|}\mathbf{t} \tag{4.21}$$

However, within this thesis it was found that the applicability of the projection of normals is restricted to simple vertical cracks such as the ones featured by uniaxial loading. Thus, the method fails when applying the method to arbitrary-path cracks. This is shown in figure 4.14, where for each orientation the consistent and inconsistent orientations are drawn. The diagram shows how the method misses a flip, and how it incorrectly performs another one.

A consequence of this phenomena is, for example, the wrong calculation of $\boldsymbol{t}_\Gamma$. The incorrect orientation of the crack normals leads to the canceling out of the integrated terms, and a lower $\boldsymbol{t}_\Gamma$ value. Moreover, this leads to a divergence between the crack integrated traction $\boldsymbol{t}_\Gamma$ and the projected traction $\boldsymbol{t}_\Omega$.

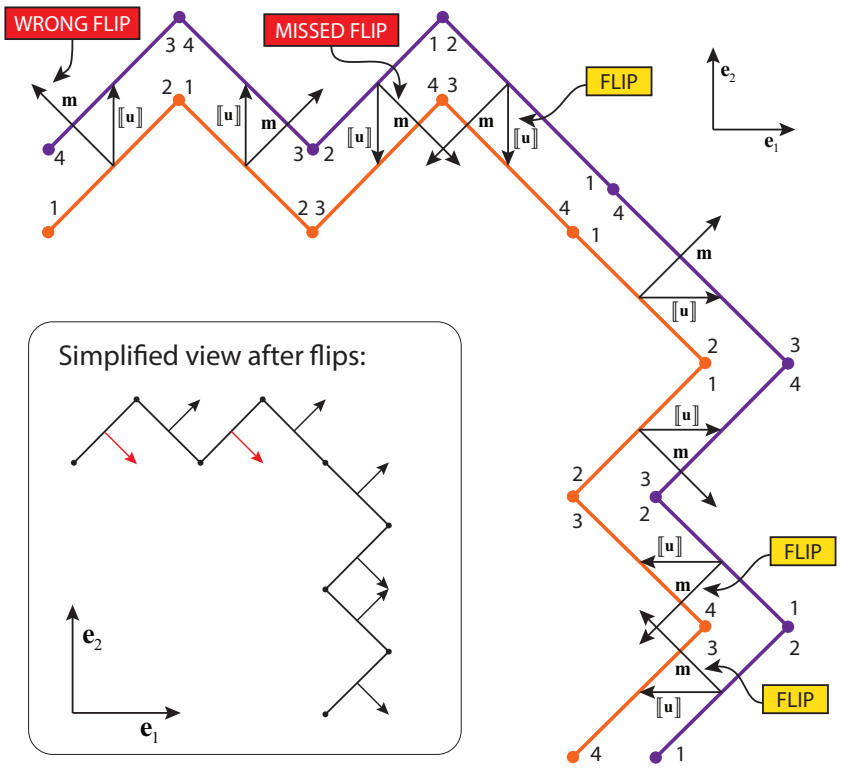

Figure 4.14: Crack normals reorientation using **projection of normals**.

Normal reorientation by relative displacement

The proposed method consistently reorientates the normals of the cohesive elements at the crack interface by comparing the displacements of each of the crack faces.

Within a cohesive crack, it is possible to establish for each cohesive element two faces F12 and F34, each connecting the cohesive element nodes 1 and 2, and 3 and 4, respectively (see figure 4.15, where the two possible nodal orderings are present). The average displacement of the crack faces in the cohesive element can be calculated at timestep t_i as in (4.22).

$$\begin{aligned} \mathbf{u}_{\mathrm{F12}}(t_i) &= \tfrac{1}{2}\left(\mathbf{u}_{\mathrm{N1}}(t_i) + \mathbf{u}_{\mathrm{N2}}(t_i)\right) \\ \mathbf{u}_{\mathrm{F34}}(t_i) &= \tfrac{1}{2}\left(\mathbf{u}_{\mathrm{N3}}(t_i) + \mathbf{u}_{\mathrm{N4}}(t_i)\right) \end{aligned} \tag{4.22}$$

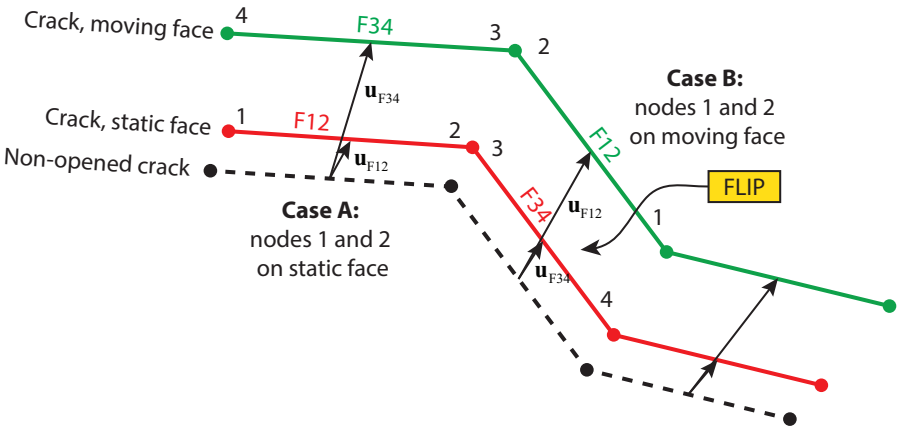

Figure 4.15: Crack normals reorientation using **relative displacements**. Definition of displacement vectors and static and moving faces.

Moreover, a static and a moving face can be defined in the crack interface. The moving face features a larger absolute displacement than the static face. Moreover, by convention the crack interface normals shall point from the static domain outwards. This effectively implies that the face F12 shall be the static face, and the F34 the moving one. If this assignment is inverted (figure 4.15, case B), the cohesive element is considered not to be oriented correctly and its normal, tangent and opening vectors are flipped. The flip condition is expressed in equation 4.23. Moreover, if the crack is closed, this is $|\mathbf{u}_{\mathrm{F12}}| = |\mathbf{u}_{\mathrm{F34}}|$ the flip condition is indeterminate. This limitation can be tackled by executing the reorientation algorithm over the load history.

$$f(t_i) = \begin{cases} 1 & |\mathbf{u}_{\mathrm{F12}}| > |\mathbf{u}_{\mathrm{F34}}| \\ -1 & |\mathbf{u}_{\mathrm{F12}}| < |\mathbf{u}_{\mathrm{F34}}| \\ \mathrm{ind} & |\mathbf{u}_{\mathrm{F12}}| = |\mathbf{u}_{\mathrm{F34}}| \end{cases} \tag{4.23}$$

The result is a correct normal reorientation, as seen in figure 4.16, which surpasses the limitations of previous methods (see figure 4.14).

Algorithm-based crack identification and reorientation

While the method of reorientation by relative displacement provides an accurate fix for the integration of crack quantities, additional problems arise when having to deal with multiple independent cracks in the domain. In these cases, it is required to detect and isolate the contributions of each crack group. This capability requires the implementation of a more sophisticated algorithm.

The developed solution performs identification of crack segments, classification into crack groups and consistent reorientation of their cohesive elements. Moreover, it extracts independent TSLs for each of the cracks in case of multi-crack propagation. These split TSLs enable to differentiate the fracture dissipated

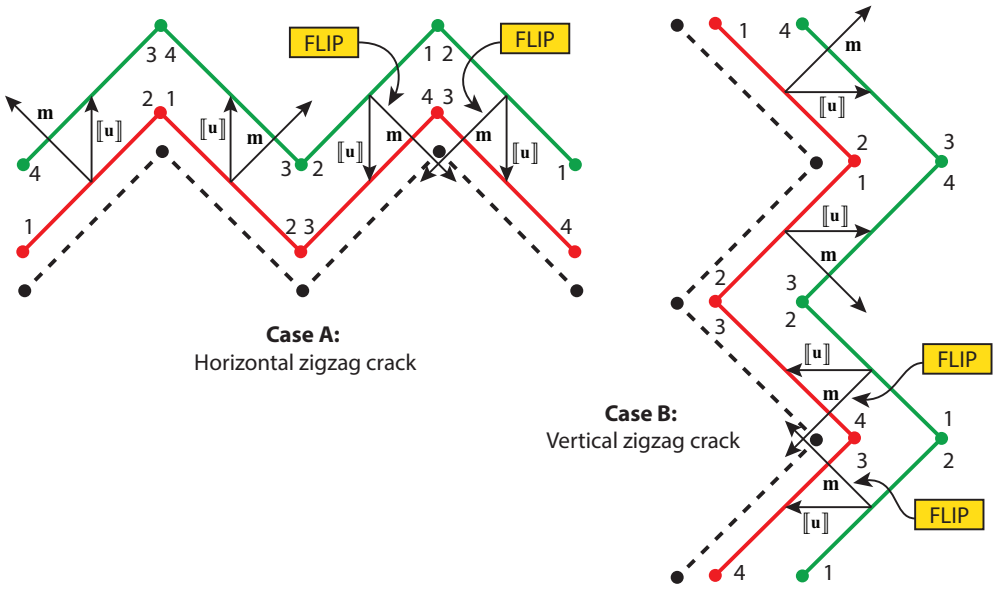

Figure 4.16: Crack normals reorientation using **relative displacements**. Flip process for generalized cracks.

energy between the cracks and the compliance. An overview of the operation of the code can be seen in figure 4.18.

Examples of the output can be seen for biaxial, shear and mixed loading modes in figures 4.19 to 4.21. In these last figures, the thick lines represent the main opened crack, while the thin lines represent secondary damaged surfaces. Moreover, the circles indicate junctions of three or more individual segments. The figures in the left column showcase the segment identification, this is, the continuous crack path in between junctions. The figures in the right column show the segments already grouped. It must be noted that the pre-reorientation normals in all these cases look similar to the previously presented figure 4.13.

This algorithm accounts for the two new added steps in the process, requiring a preliminary `.odb` extraction to record the nodal and element information needed by `multicrack.py` to detect the cracks and be able to group the elements in crack groups. The new steps highlighted in figure 4.12 are expanded in figure 4.17, where the main processes and the inputs and outputs are drawn.

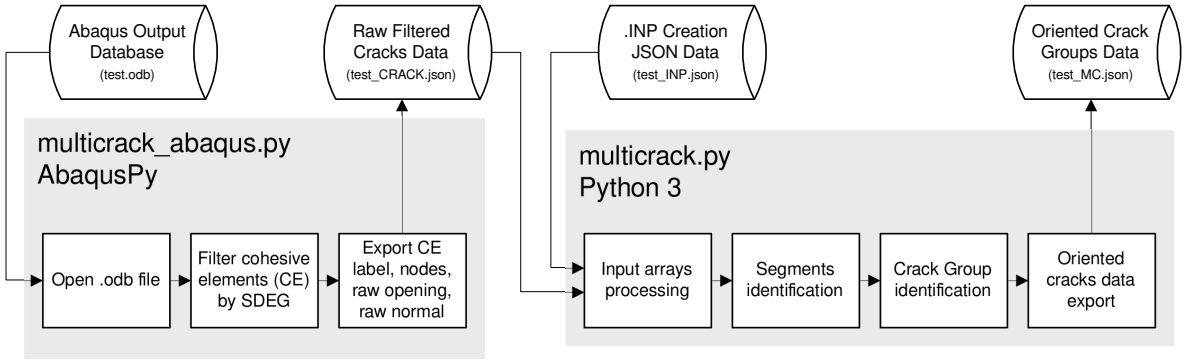

Figure 4.17: Flow diagram of the **crack identification and reorientation algorithm.**

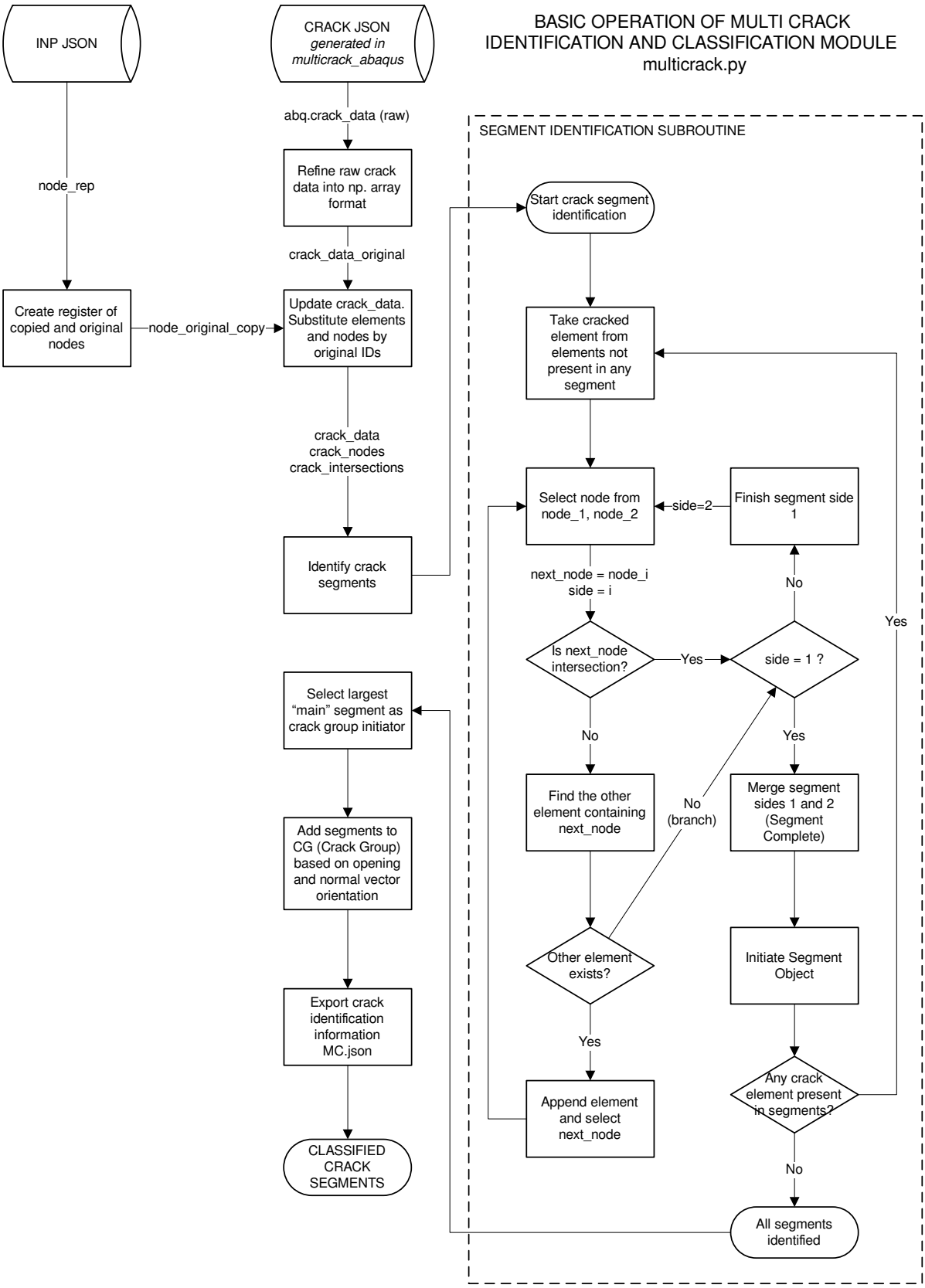

Figure 4.18: Basic operation of the multi crack identification and classification module (`multicrack.py`)

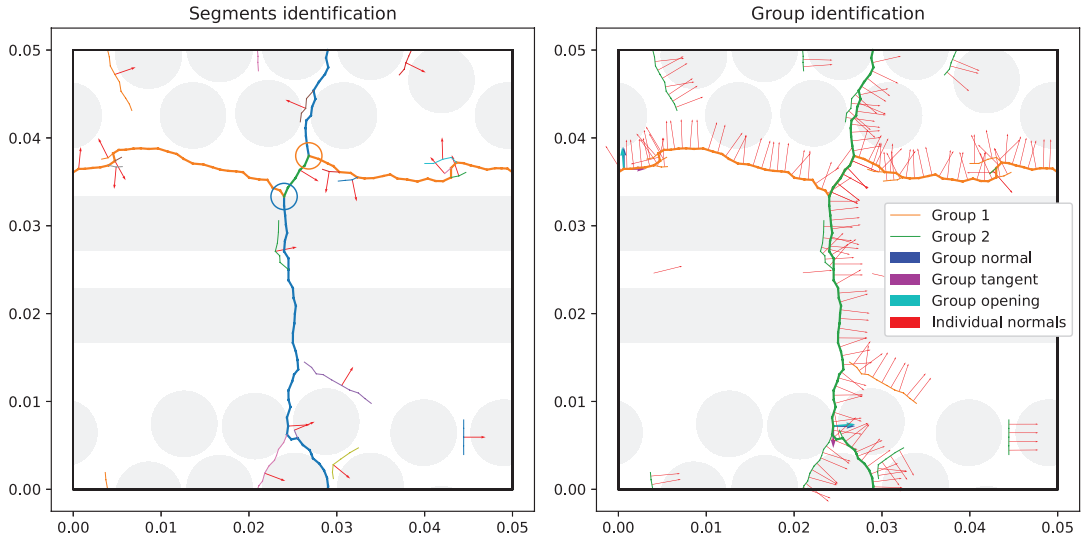

Figure 4.19: Multi-crack algorithm application in biaxial loading test (#42)

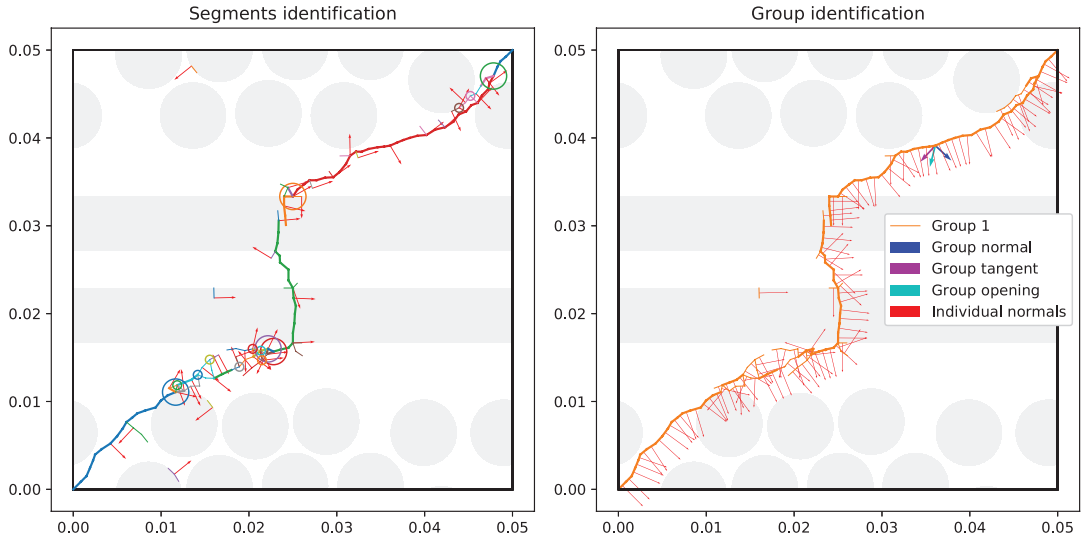

Figure 4.20: Multi-crack algorithm application in pure shear loading test (#43)

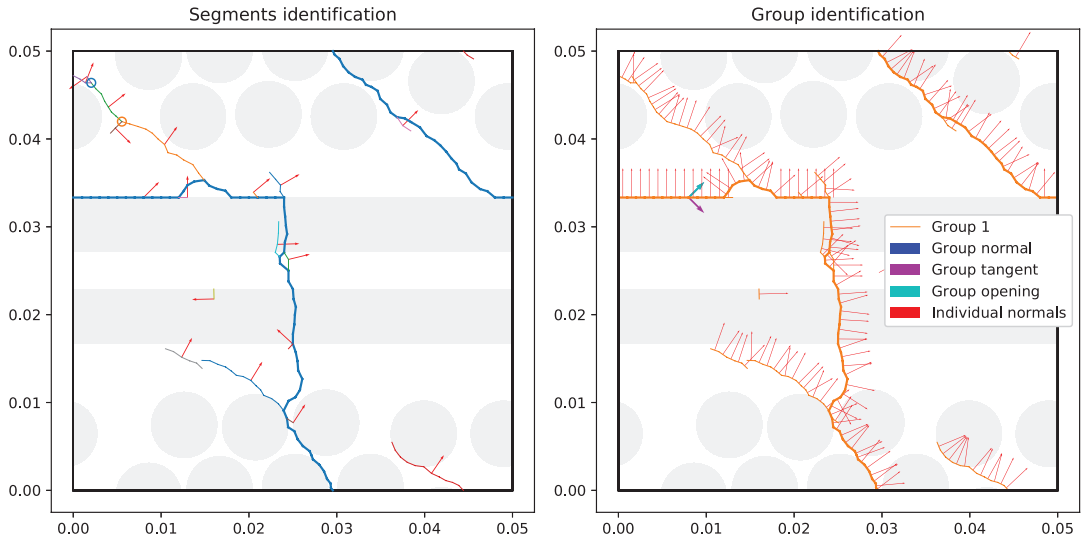

Figure 4.21: Multi-crack algorithm application in mixed loading test (#49)

4.3.3. Crack groups and threshold of damage

The crack identification algorithm described in the previous section results in two or three main groups depending on the characteristics of the fracture pattern. These groups are key during the homogenization process, as they separate the damage and enable to assess the fracture energy of each crack. In this section, a review of these cracks groups is done, and a discussion about the threshold of damage is given.

- **Crack Group 0 (CG0):** contains all the cohesive elements below the threshold of damage for the multi-crack identification. Apart from the non-damaged elements, this group also includes those elements lightly damaged, which cause artificial compliance. Moreover, CG0 includes two subdivisions (CG0-1 and CG0-2) to associate the compliance damage to the corresponding crack process (see section §4.3.6). This group is also referred as *compliance* or *auxiliary*.
- **Crack Groups 1 and 2 (CG1 and CG2):** comprise the cohesive elements forming the cracks. Two groups are set, as a maximum of two main cracks propagate in different directions in the simulated domains. For example, in figure 4.22 the Crack Group 1 (CG1) is marked in orange and the Crack Group 2 (CG2) in green.

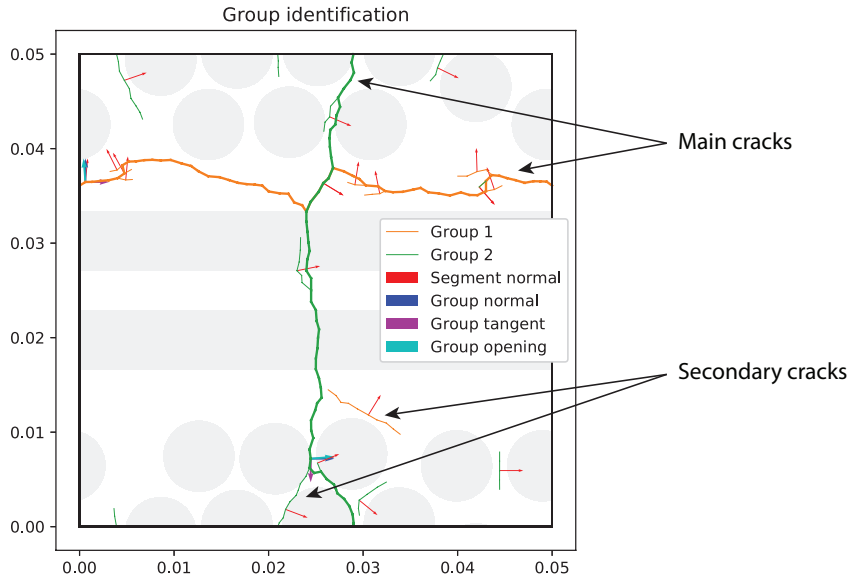

Figure 4.22: Multi-crack algorithm crack group identification.

The threshold of damage `sdeg_cut_off` is set to discriminate between those damaged elements forming the crack and damaged elements accounting for the artificial compliance. Previous sections (§4.2.7) addressed that the Abaqus damage variable `SDEG` did not offer a clear indication of the degree of damage present in the material. Thus, the cutoff is defined in function of the maximum traction attainable at the damage state.

The choice of the threshold of damage is subjective, but still motivated by several factors. The threshold should be such that the main crack is included, but also secondary cracks. These secondary cracks, which dissipate energy during their fracture process, may not fully propagate and close due to their residual stiffness after the main crack opening. These secondary cracks can only be accounted for by setting the threshold to a lower level of damage. Nevertheless, lowering the threshold raises the complexity of multi-crack identification: more segments have to be processed, and the grouping becomes more complicated.

In the past, values between 10-20% of the ultimate traction have been used to set the threshold of damage. This relatively low threshold choice simplifies certain operations, as only the main crack is above the threshold. However, it also disregards the bifurcations and other segments contributing to the process. The new algorithm enables to raise the threshold to 90%, thus capturing secondary cracks and providing a more accurate understanding of the process.

4.3.4. Cohesive data extraction and rotation

Once the crack elements' normals are under control, it is possible to extract and post-process the cohesive crack data. In this section, the extraction of cohesive crack data and its transformations are discussed.

The tangent vector $\mathbf{l}$ of the element is defined as the product of the flip function and the vector from edge midpoint M14 to edge midpoint M23 (4.25). The positions of the edge midpoints M14 and M23 are defined as (4.24). The normalized tangent vector $\hat{\mathbf{l}}$ is defined in equation (4.26), with f being the flip function defined in (4.23).

$$\begin{aligned} \mathbf{x}_{\mathrm{M14}} &= \tfrac{1}{2}\left(\mathbf{x}_{\mathrm{N1}} + \mathbf{x}_{\mathrm{N4}}\right) \\ \mathbf{x}_{\mathrm{M23}} &= \tfrac{1}{2}\left(\mathbf{x}_{\mathrm{N2}} + \mathbf{x}_{\mathrm{N3}}\right) 5 \end{aligned} \tag{4.24}$$

$$\mathbf{l} = f \cdot \left(\mathbf{x}_{\mathrm{M23}} - \mathbf{x}_{\mathrm{M14}}\right) \tag{4.25}$$

$$\hat{\mathbf{l}} = \frac{\mathbf{l}}{\|\mathbf{l}\|} \tag{4.26}$$

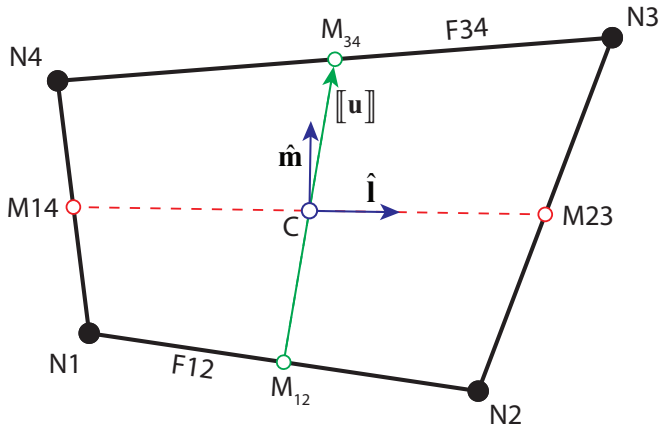

Figure 4.23: Cohesive element geometry (COH2D4) and vectors

Once the tangent vector is correctly defined, the normal can be easily obtained by creating the local orthonormal frame of the element $\{\hat{\mathbf{l}}, \hat{\mathbf{m}}, \hat{\mathbf{e}}_3\}$ with the out of plane unit vector $\hat{\mathbf{e}}_3 = [0, 0, 1]$ (equation 4.27).

$$\hat{\mathbf{m}} = \hat{\mathbf{e}}_3 \times \hat{\mathbf{l}} \tag{4.27}$$

Alternatively, if using the algorithm-based cracked reorientation (see section §4.3.2), the oriented normals $\hat{\mathbf{m}}$ are available. Thus, the tangent $\hat{\mathbf{l}}$ is obtained as in (4.28). Additionally, the flip function f would be defined as (4.29).

$$\hat{\mathbf{l}} = \hat{\mathbf{m}} \times \hat{\mathbf{e}}_3 \tag{4.28}$$

$$f\left(t_i\right) = \begin{cases} 1 & \hat{\mathbf{l}} \cdot \left(\mathbf{x}_{\mathrm{M23}} - \mathbf{x}_{\mathrm{M14}}\right) > 0 \\ -1 & \hat{\mathbf{l}} \cdot \left(\mathbf{x}_{\mathrm{M23}} - \mathbf{x}_{\mathrm{M14}}\right) < 0 \end{cases} \tag{4.29}$$

For both methods, the opening vector $[\![\mathbf{u}]\!]$ of the cohesive element is defined as (4.30), where $\mathbf{u}_{\mathrm{F12}}$ and $\mathbf{u}_{\mathrm{F34}}$ represent the displacements of face F12 and face F34.

$$[\![\mathbf{u}]\!] = f \cdot \left(\mathbf{u}_{\mathrm{F34}} - \mathbf{u}_{\mathrm{F12}}\right) \tag{4.30}$$

Moreover, the opening rate, required to calculate the element power contribution (see equation (3.26)), can be easily calculated by performing numerical differentiation.

$$[\![\dot{\mathbf{u}}]\!]\left(t_i\right) = \frac{[\![\mathbf{u}]\!]\left(t_i\right) - [\![\mathbf{u}]\!]\left(t_{i-1}\right)}{t_i - t_{i-1}} \tag{4.31}$$

The element traction vector $\mathbf{t}_{\text{local}}$ is obtained by extracting the $\mathtt{S}_{12}$ and $\mathtt{S}_{22}$ components of the element's stress tensor output of Abaqus S (4.32). However, the element traction vector values are defined in the local element coordinate basis $\{\hat{\mathbf{l}}, \hat{\mathbf{m}}, \hat{\mathbf{e}}_3\}$ and thus needs to be transformed to global coordinates. The traction vector in global coordinates can be obtained by defining a transformation matrix $\mathbf{T}$ (4.33) and performing the transformation (4.34).

$$\mathbf{t}_{\text{local}} = \begin{pmatrix} \mathtt{S}_{12} & \mathtt{S}_{22} \end{pmatrix} \tag{4.32}$$

$$\mathbf{T} = \begin{pmatrix} \hat{\mathbf{l}}_1 & \hat{\mathbf{m}}_1 \\ \hat{\mathbf{l}}_2 & \hat{\mathbf{m}}_2 \end{pmatrix}^T \tag{4.33}$$

$$\mathbf{t}_{\text{global}} = \mathbf{T}\,\mathbf{t}_{\text{local}} \tag{4.34}$$

The length of the cohesive element $|\Gamma_{\text{elem}}|$ is given by the module of the tangent vector $\mathbf{l}$ (4.35)

$$|\Gamma_{\text{elem}}| = |\mathbf{l}| \tag{4.35}$$

4.3.5. Cohesive data homogenization and crack quantities

With the individual element properties set (see section §4.3.4), it is possible to calculate the cohesive effective macroscopic quantities: the effective crack normal $\hat{\mathbf{m}}^{\text{f}}$, the effective crack length $\left|\Gamma^{\text{f}}\right|$ and other effective integrated quantities.

Effective normal

The effective normal of each crack group is calculated by the crack identification algorithm (`multicrack.py`). For each main crack $\Gamma_{\text{i,main}}$, an effective tangent vector $\mathbf{l}^{\text{f}}$ can be calculated (4.36). Then, the effective normal $\mathbf{m}^{\text{f}}$ can be calculated as (4.37) and normalized (4.38).

$$\mathbf{l}^{\text{f}} = \sum_{\text{elem} \in \Gamma_{\text{i,main}}} \mathbf{l}_{\text{elem}} \tag{4.36}$$

$$\mathbf{m}^{\text{f}} = \hat{\mathbf{e}}_3 \times \mathbf{l}^{\text{f}} \tag{4.37}$$

$$\hat{\mathbf{m}}^{\text{f}} = \frac{\mathbf{m}^{\text{f}}}{\left|\mathbf{m}^{\text{f}}\right|} \tag{4.38}$$

Effective crack length

An additional advantage of using the crack-identification algorithm is being able to calculate the effective length of the crack $\left|\Gamma^{\text{f}}\right|$ at every timestep, even when not fully propagated. This can be done by taking the module of the sum of all main segments (4.39).

$$\left|\Gamma^{\text{f}}\right| = \left|\mathbf{l}^{\text{f}}\right| \tag{4.39}$$

Moreover, the crack effective length is also computed with the previous established method (described in equations (4.40) and (4.41) [94]), which is robust, and serves well for most of the cases. Moreover, the combination of both methods helps to detect errors in the crack detection.

$$\left|\Gamma^{\text{f}}_{\text{min}}\right| := \min\left(\frac{l_1}{\left|\mathbf{n}_2 \cdot \mathbf{m}^{\text{f}}\right|}, \frac{l_2}{\left|\mathbf{n}_1 \cdot \mathbf{m}^{\text{f}}\right|}\right) \qquad \left|\Gamma^{\text{f}}_{\text{max}}\right| := \max\left(\frac{l_1}{\left|\mathbf{n}_2 \cdot \mathbf{m}^{\text{f}}\right|}, \frac{l_2}{\left|\mathbf{n}_1 \cdot \mathbf{m}^{\text{f}}\right|}\right) \qquad r := \frac{\left|\Gamma^{\text{f}}_{\text{max}}\right|}{\left|\Gamma^{\text{f}}_{\text{min}}\right|} \tag{4.40}$$

$$\left|\Gamma^{\text{f}}\right| := \begin{cases} \left|\Gamma^{\text{f}}_{\text{min}}\right| & \text{if} \quad r \geq r_{\text{max}} \\ \left|\Gamma^{\text{f}}_{\text{max}}\right| & \text{if} \quad r < r_{\text{max}} \end{cases} \tag{4.41}$$

Integrated quantities

The power dissipated by the crack through the fracture process can be calculated as (4.42) for the different cracks Γ_i. This quantity is calculated for each crack group Γ_i. Moreover, the homogenized effective tractions $\mathbf{t}^{\mathrm{f}}_{\Gamma}$, $\mathbf{t}^{\mathrm{f,calc}}$, $\mathbf{t}^{\mathrm{f}}_{\Omega}$, $\mathbf{t}^{\mathrm{f}}_{\partial\Omega}$ and displacements $[\![\mathbf{u}]\!]^{\mathrm{f}}$, $[\![\mathbf{u}]\!]^{\mathrm{f,calc}}$ are calculated according to the procedures covered in §3.5.2.

$$\int_{\Gamma_i} \mathbf{t}\cdot[\![\dot{\mathbf{u}}]\!]\,ds = \sum_{\mathrm{elem}\in\Gamma_i} \mathbf{t}_{\mathrm{elem}}\cdot[\![\dot{\mathbf{u}}]\!]_{\mathrm{elem}}\,|\Gamma_{\mathrm{elem}}| \tag{4.42}$$

4.3.6. Handling of cohesive elements below the threshold of damage

A large number of cohesive elements fall below the damage threshold required to be classified by the multi-crack identification process. However, these elements have a contribution to the power dissipation during the crack initiation and the very first stage of the damage propagation. While their contribution is small, it has to be taken into account that before the main crack opens, every cohesive element within the RVE domain experience small-opening before damage due to the intrinsic implementation (artificial compliance). This issue, as explained in section §4.2.7, is minimized by the use of a high cohesive stiffness. When the main crack finally appears, these elements relax.

A method has been established to adscribe the opening and power dissipation contribution to the main crack groups ($\mathrm{CG_{i,aux}}$, $\Gamma_{\mathrm{i,aux}}$, where aux stands for auxiliary, and i indicates the crack group). When only one maincrack propagates, the process is straightforward as all the opening and power dissipation of the compliance cohesive elements (CE) goes to crack group 1 (CG1). However, in the case with two cracks propagating, the process is slightly more complex. The classification is based on the similarity of the cohesive element opening vector with the main crack opening vectors. This is determined by decomposing the cohesive element opening into the non-orthogonal basis formed by the opening direction vectors of crack groups 1 and 2.

$$[\![\mathbf{u}]\!]_{\mathrm{CE}} = h[\![\hat{\mathbf{u}}]\!]_{\mathrm{CG1}} + k[\![\hat{\mathbf{u}}]\!]_{\mathrm{CG2}} \tag{4.43}$$

$$\begin{cases} h[\![\hat{\mathbf{u}}]\!]_{\mathrm{CG1}}[\![\hat{\mathbf{u}}]\!]_{\mathrm{CG1}} + k[\![\hat{\mathbf{u}}]\!]_{\mathrm{CG2}}[\![\hat{\mathbf{u}}]\!]_{\mathrm{CG1}} = [\![\mathbf{u}]\!]_{\mathrm{CE}}[\![\hat{\mathbf{u}}]\!]_{\mathrm{CG1}} \\ h[\![\hat{\mathbf{u}}]\!]_{\mathrm{CG1}}[\![\hat{\mathbf{u}}]\!]_{\mathrm{CG2}} + k[\![\hat{\mathbf{u}}]\!]_{\mathrm{CG2}}[\![\hat{\mathbf{u}}]\!]_{\mathrm{CG2}} = [\![\mathbf{u}]\!]_{\mathrm{CE}}[\![\hat{\mathbf{u}}]\!]_{\mathrm{CG2}} \end{cases} \tag{4.44}$$

By solving the linear system for h and k, it is possible to assess the relative contribution of each basis vector. The classification of the cohesive element into a crack group is performed attending to this relative contribution.

$$\begin{array}{l} \mathrm{CCE} \in \mathrm{CG1} \quad \text{if} \quad |h| \geq |k| \\ \mathrm{CCE} \in \mathrm{CG2} \quad \text{if} \quad |h| < |k| \end{array} \tag{4.45}$$

It must be noted that the derived TSLs exclude the power generated by the compliance / auxiliary group. However, the above-classified method is useful to assess the effect of artificial compliance on each of the cracks.

4.4. Computational implementation details

This section aims to shed some light on newly implemented features and the main changes with respect to previous implementations. Firstly, the bookkeeping and traceability of the tests has been significantly improved. A SQL database was set up, which keeps track of all the jobs and their parameters. This had been previously done in Excel, but it gave many problems when automating the process and having to deal with concurrent read/write operations. Moreover, the SQL database can be seamlessly integrated within the Python environment.

Moreover, the workload required to start and process the analyses has been significantly reduced by the creation and use of an automatic test manager (`auto.py`). The manager autonomously executes the different operations require over the whole process (see figure 4.24). Moreover, it checks the number of Abaqus tokens and starts jobs according to the cluster usage regulations, and other rational usage guidelines.

Regarding the storage of the results and other data, the previously used `Pickle` files have been replaced by `JSON` files. This has many benefits, starting by being able to read the data directly from the file. Moreover, interoperability is an important consideration, since the `JSON` standard is widely used among different software.

Furthermore, access to the Abaqus output database (`.odb` files) is performed via the Abaqus Scripting Interface, thus bypassing the Abaqus GUI interface. This has the benefit of not requiring either Abaqus/CAE licenses nor tokens. The scripting environment works with a customized version of Python2.7, with modules and utilities to create, process and read Abaqus analysis. By avoiding the use of `"from abaqus import *"`, the post-processing can be run outside of the Abaqus kernel process.

While the scripting interface is structured and well documented, it has the drawback of not allowing to add external libraries or update the current ones. Thus, plotting within the environment is not possible. Moreover, the distributed Abaqus Python development environment (PDE) is quite impractical when debugging and performing code checks. This issue is circumvented by exporting the data in `JSON` files and alternating between AbaqusPy and Python3.

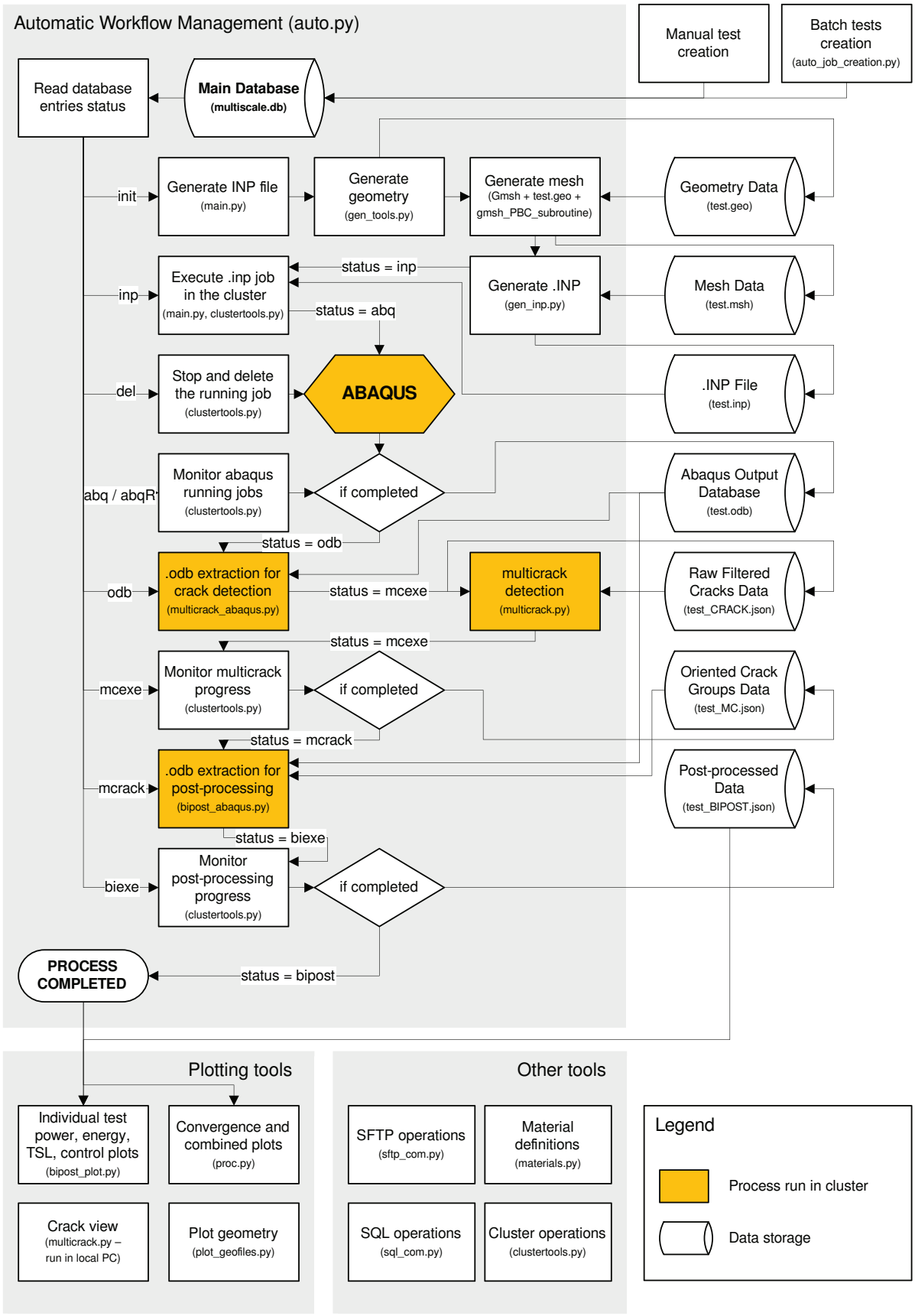

Figure 4.24: Flow diagram of the computational implementation.

5

Plots, Interpretation and Limitations.

This chapter showcases the generated plots and provides insight into their interpretation. Moreover, the results motivating several of the discussions provided in chapter §3 are presented. The chapter starts by offering a discussion on the different interpretation of the two effective quantity couples (§5.1). Then, the displacement (§5.3), traction (§5.4), power (§5.5), energy (§5.6) and ETSL (§5.7) curves are described, highlighting their relevant aspects. The limitations of the implementation are addressed in section §5.8.

As a tool to explain these results, test #38 is chosen. Test #38 features uniaxial loading applied in the horizontal axis, and presents a relatively simple fracture process and crack geometry. The crack geometry and the fracture process for #38 are given in figure 5.1. The material properties used for these tests are listed in section §4.2.8.

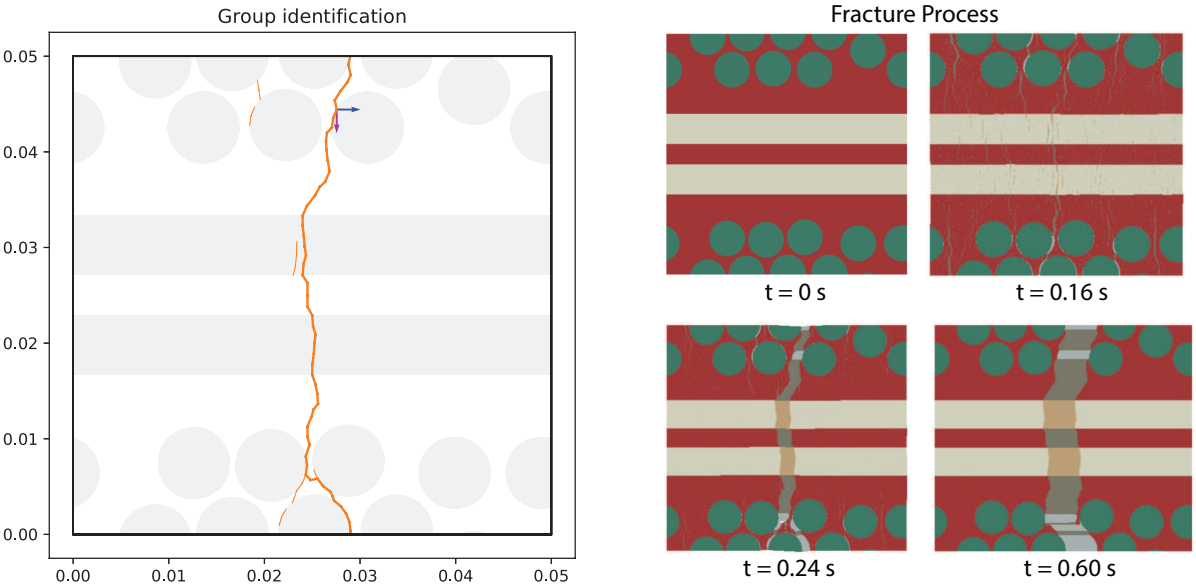

Figure 5.1: Test #38 fracture results. Left: crack geometry. Right: fracture process.

5.1. Two effective quantity couples, two different effective materials

The choice of effective quantity couple ($\left[\mathbf{t}^{\mathrm{f,calc}},\ [\![\mathbf{u}]\!]^{\mathrm{f}}\right]$ or $\left[\mathbf{t}^{\mathrm{f}},\ [\![\mathbf{u}]\!]^{\mathrm{f,calc}}\right]$) influences the way damage is modeled at the macroscale. Thus, neither TSLs, displacement curves or traction curves are expected to coincide for both effective pairs. However, what is common for both couples is that the power and energy exchanged by the macroscopic quantities always remain equal to the ones on the microscopic domain.

If we take, for example, the opening-based homogenization couple $\left[\mathbf{t}^{\mathrm{f,calc}},\ [\![\mathbf{u}]\!]^{\mathrm{f}}\right]$, we are modeling two blocks with a cohesive law which fully respects the geometric opening, and adapts the traction. Thus, when

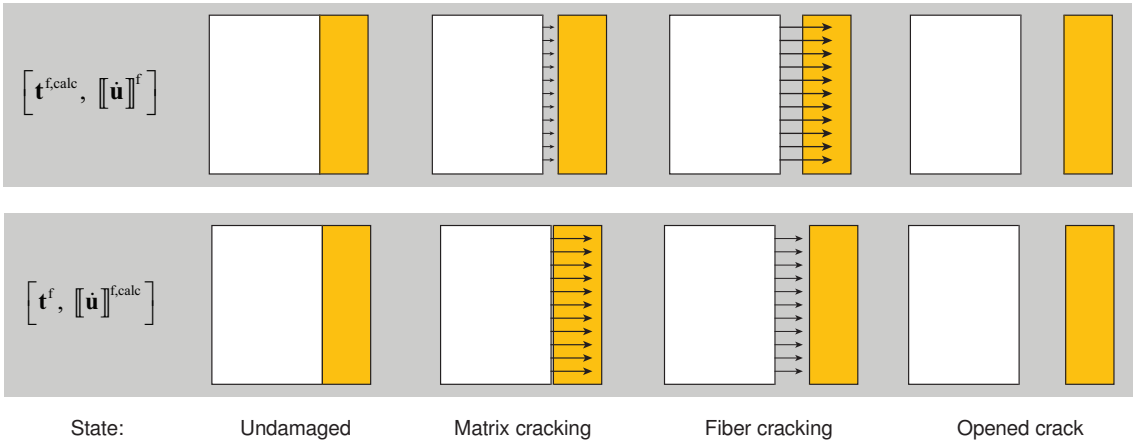

Figure 5.2: Comparison between effective parameter pairs $\left[\mathbf{t}^{\mathrm{f,calc}},\ [\![\mathbf{u}]\!]^{\mathrm{f}}\right]$ and $\left[\mathbf{t}^{\mathrm{f}},\ [\![\mathbf{u}]\!]^{\mathrm{f,calc}}\right]$.

the matrix cracks there would be a moderate opening, but as the energy dissipated by the matrix cracks is low, the traction will be very small. However, when the fibers break the caculated tractions are large (even over the theoretical σ_{ult}), due to the immense energy dissipated.

If we analyze the behavior of the traction-based effective quantities $\left[\mathbf{t}^{\mathrm{f}},\ [\![\mathbf{u}]\!]^{\mathrm{f,calc}}\right]$, we can observe that during the matrix cracking the tractions are already high and the effective opening is minimal, since the dissipated energy is very small. Moreover, during the fiber cracking, the effective tractions drop as result of the damage in the material, and the opening is slightly larger than the geometrically accurate one to compensate for the simplified crack path, smaller than the actual one in the micro-structure. In this way, the Hill-Mandel condition is kept.

Over the next sections, the impact of the choice of $\left[\mathbf{t}^{\mathrm{f,calc}},\ [\![\mathbf{u}]\!]^{\mathrm{f}}\right]$ or $\left[\mathbf{t}^{\mathrm{f}},\ [\![\mathbf{u}]\!]^{\mathrm{f,calc}}\right]$ on the displacements, tractions and TSLs will be covered. Moreover, it will be shown that, although both curves are valid from a Hill-Mandel point of view, $\left[\mathbf{t}^{\mathrm{f,calc}},\ [\![\mathbf{u}]\!]^{\mathrm{f}}\right]$ is more prone to numerical instabilities, and is more sensitive to the artificial compliance effects.

5.2. Test tags and orientation conventions

In many cases, the test reference is followed by a descriptive tag. This tag contains information about the test group, loading mode, domain size, grid size and angle of application of the load. Moreover the cracks' orientation φ is given as the difference between the crack normal $\mathbf{m}^{\mathrm{f}}$ and $\mathbf{e_1}$. Similarly, the load angle θ, especially relevant for the uniaxial cases with a load not applied in the principal directions, defines the rotation of the applied deformation tensor $\bar{\boldsymbol{\varepsilon}}$ from $\mathbf{e_1}$.

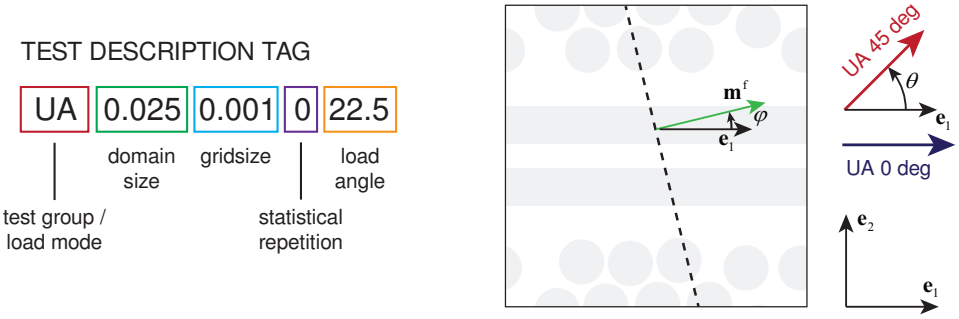

Figure 5.3: Left: test tag description. Right: Crack and load angle convention.

5.3. Displacement curves

One of the main ingredients to extract TSLs are displacements. However, as seen in §3.5, there are various approaches to determine the effective displacements. Moreover, the existence of artificial compliance makes the interpretation more complex.

In figure 5.4, the norms of several of the effective displacement vectors are plotted. It can be seen how the old effective opening $[\![\mathbf{u}]\!]^{\mathrm{f}}_{\mathrm{mc,old}}$ is larger than the applied displacement boundary conditions, as explained in §3.5.2 (scaling vs projection). Using the new projection-based formula $[\![\mathbf{u}]\!]^{\mathrm{f}}_{\mathrm{mc}}$ yields perfect coincidence after the opening of the main crack. Moreover, before the opening of the crack, the applied displacement is equivalent to the sum of the elastic deformation of the body, the opening of the crack $[\![\mathbf{u}]\!]^{\mathrm{f}}_{\mathrm{mc}}$, and the opening of the compliance elements $[\![\mathbf{u}]\!]^{\mathrm{f}}_{\mathrm{aux}}$. Furthermore, the $[\![\mathbf{u}]\!]^{\mathrm{f}}_{\mathrm{mc}}$ between $t = 0.025$ and $t = 0.1$ represents the opening of the matrix. This interval is of great importance to justify the behavior of the ETSL covered later on.

The calculated effective opening $[\![\mathbf{u}]\!]^{\mathrm{f,calc}}$, as seen in figure 5.4, does not coincide with the applied displacement. However, this is not intended, as explained in section §5.1, since it depends on the power dissipated and the traction present in the maincrack. On the interval $t \in [0.04, 0.12]$, for example, $[\![\mathbf{u}]\!]^{\mathrm{f,calc}}$ is close to zero, since very little energy is dissipated, and high tractions are already present in the (future) crack path.

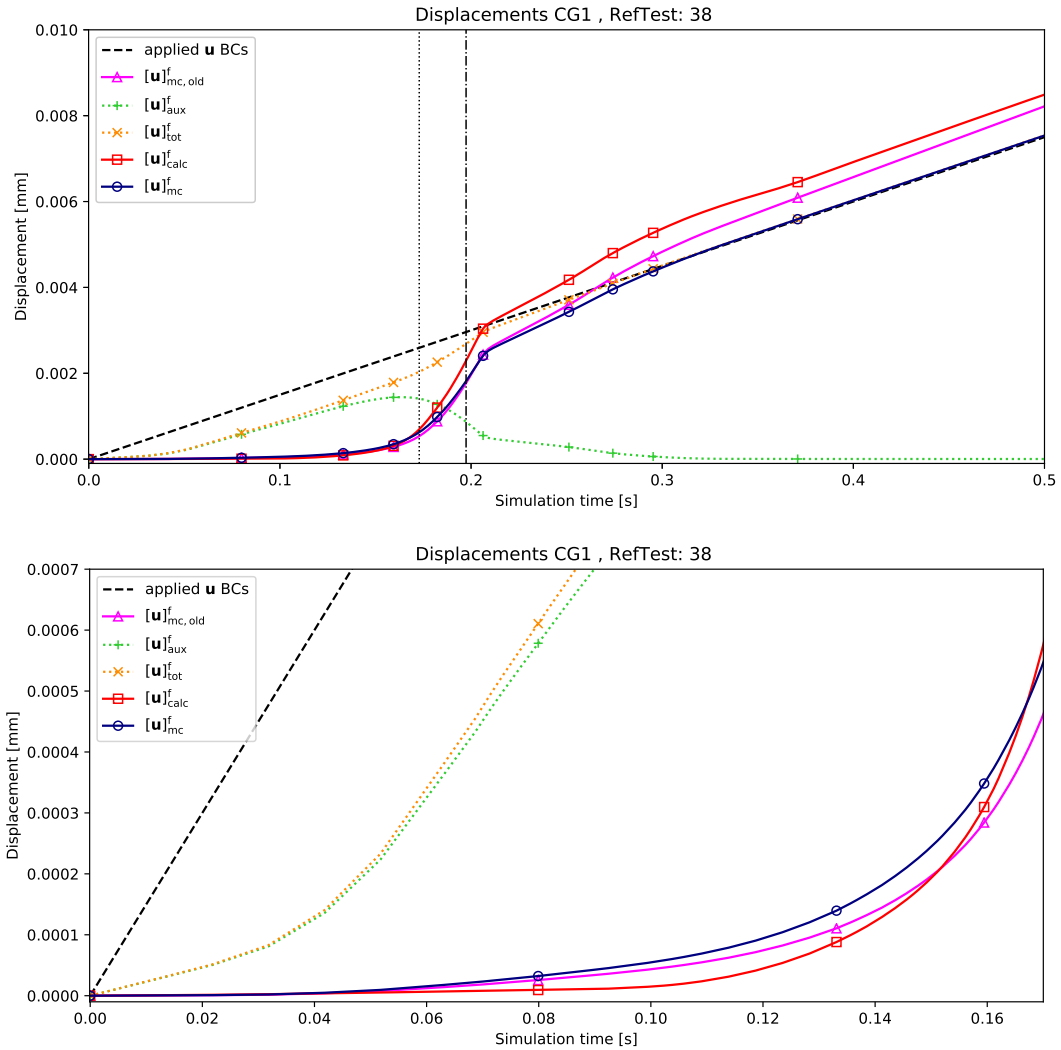

Figure 5.4: Displacement plot test #38 (). Top: overall view. Bottom: magnification simulation time interval $t \in [0, 0.17]$.

5.4. Traction curves

Tractions, calculated using the equations in §3.5, are hereby plotted against the simulation time. Figure 5.5 shows the tractions evolution for uniaxial loading (left) and mixed mode loading (right).

One of the most relevant aspects present in the plot is the behavior of the calculated traction $\mathbf{t}^{\mathrm{f}}_{\mathrm{calc}}$ curve. Due to the way this parameter is calculated, $\mathbf{t}^{\mathrm{f}}_{\mathrm{calc}}$ focuses more on elements and time periods in which cracks are dissipating energy. The first traction peak at $t = 0.025s$ is linked to the opening of matrix cracks. This is followed by lower effective tractions until $t = 0.09s$, driven by little energy dissipated and moderate openings ($[\![\mathbf{u}]\!]^{\mathrm{f}} > [\![\mathbf{u}]\!]^{\mathrm{f,calc}}$ in that interval). From $t = 0.09s$ to $t = 0.18s$ the failure of the longitudinal fibers and the great amount of dissipated energy raises the calculated traction. As a result, the calculated effective traction $\mathbf{t}^{\mathrm{f,calc}}$ can even surpass the ultimate traction that would be expected from classic homogenization formulas. Again, this is a consequence of the geometry simplification that comes with homogenization (see §5.1).

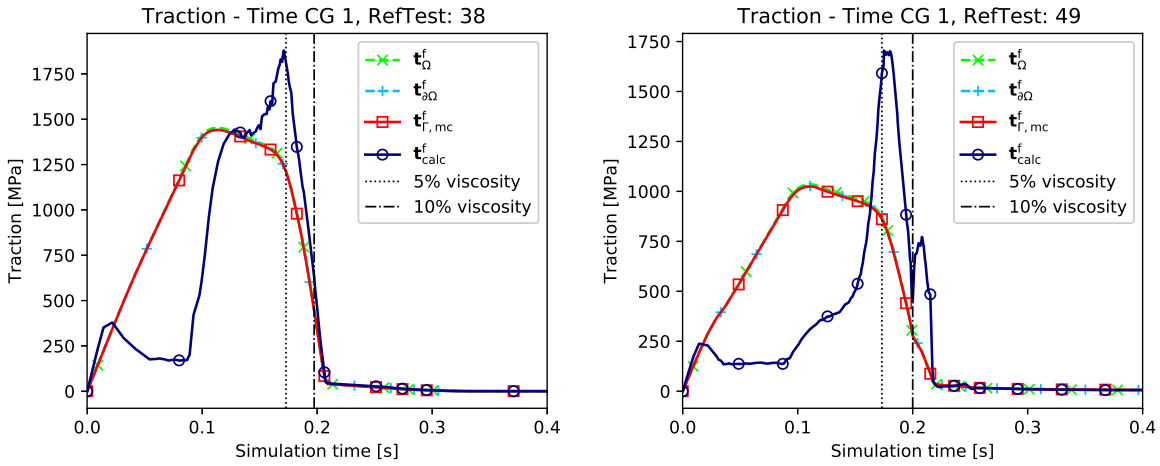

Figure 5.5: Left: Traction plot test #38 (UA1). Right: Traction plot test #49 (mixed loading).

Moreover, in section §4.3.2, it was noted that a defect in the orientation of the normals could make $\mathbf{t}^{\mathrm{f}}_{\Gamma}$ and $\mathbf{t}^{\mathrm{f}}_{\Omega}$ curves diverge. This can be seen in the TSLs from [17] given in figure 5.6. The uniaxial case (vertical crack with no normal vectors reorientation problems) 5.6a shows a perfect match. However, when applying 45° shear loading (irregular crack path in 45°, faulty normal vectors), the tractions lead to the aforementioned divergence. Using the new algorithms, it is possible to obtain a match between $\mathbf{t}^{\mathrm{f}}_{\Gamma}$ and $\mathbf{t}^{\mathrm{f}}_{\Omega}$ in shear and mixed modes (figure 5.5R). Small discrepancies can occur as the algorithm troubles to process simulations suffering from compression and loss of contact. This problem is explained later on in section §5.8.

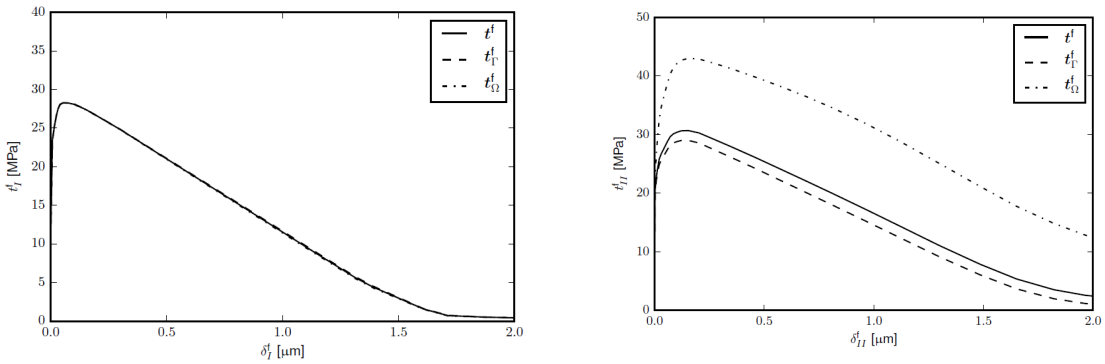

(a) Uniaxial loading in horizontal direction

(b) 45° pure shear loading

Figure 5.6: TSLs for UA1 and PS45 loading modes in a [90] RVE. Obtained from [17].

5.5. Power curves

Power curves are, together with the ETSLs, the primary output of the thesis, as they convey crucial information about the crack progress and the compliance to the Hill-Mandel condition. The curves presented in this section are normalized results by the domain surface area $|\Omega|$.

Figure 5.7 depicts the power contributions of the bulk and crack, and the power calculated from the effective quantities. The black lines represent the total power. P_{ALLIE} is the time derivative of the Abaqus total strain energy history output[1]. Moreover, the total power is also calculated as the sum of the microscale bulk and crack powers (P_{total}), and as the product of the macroscopic homogenized stress and strain ($P^{\text{M}}_{\text{total}}$). The compliance of the global Hill-Mandel condition can be observed as $P_{\text{total}} = P^{\text{M}}_{\text{total}}$.

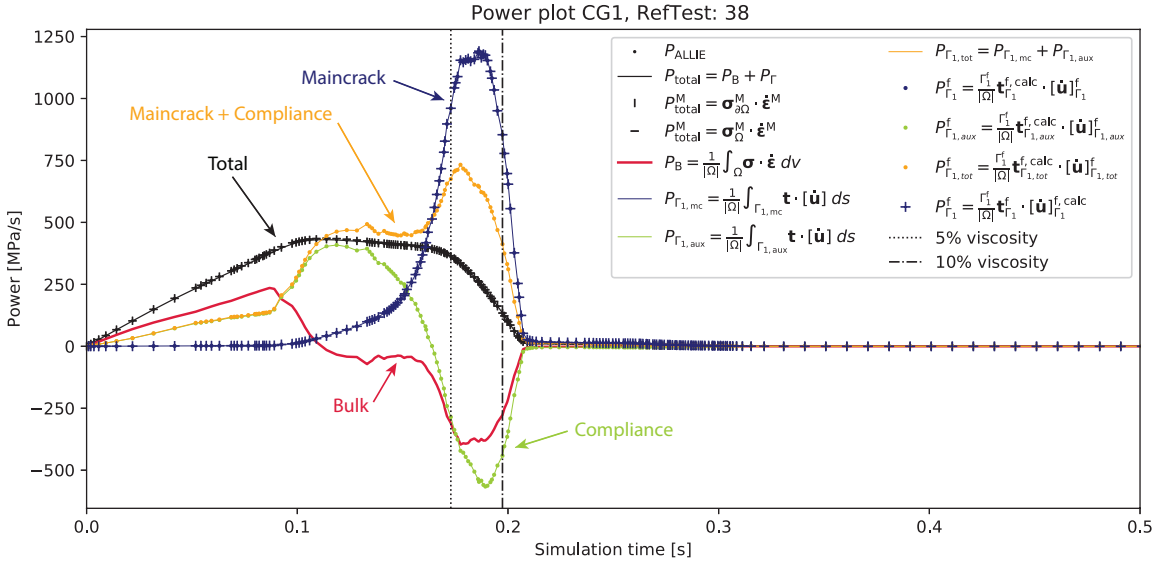

Figure 5.7: Power plot test #38.

Moreover, it can also be seen how the power calculated from the crack effective quantities $P^{\text{f}}_{\Gamma_1}$ matches the crack power curve obtained by integration of the power contributions of the crack's elements P_{Γ_1}. Thus, the Hill Mandel condition for the crack domain (3.32) is satisfied too.

Careful observation of figure 5.7 provide insight on the behavior of the simulation. It can be seen how at the start of the simulation power is done on the bulk, which stores elastic strain energy. Around point $t = 0.1s$, the bulk power goes to zero, reaching its maximum stored elastic strain energy. Instead, the cohesive elements suffer from artificial compliance, which reflects on the compliance power increasing. Finally, at the point $t = 0.18s$ the crack forms (thus the peak in P_{Γ_1}), and power is released from the bulk elements and the non-cracked cohesive elements.

5.5.1. Discussion: comparison of the new/old Hill-Mandel decomposition

In section §3.4.3, the non-conformity of the previous Hill-Mandel decomposition was presented. The results supporting this argumentation are shown in figure 5.8, where it can be seen how the power exchanged by the old homogenized quantities (discontinuous lines, calculated using equation (3.29)), diverges from the integrated power quantities (continuous lines) and the new effective quantities (markers).

Moreover, the impact of anisotropy can be seen when compared with figure 5.9. While figure 5.8 represents the power of the [90,0,90] geometry described in §4.2.1, figure 5.9 represents the previous cross sectional phase [90] analysed in previous works. Cracking in this domain has a more homogeneous behavior

[1] `ALLIE = ALLSE + ALLPD + ALLCD + ALLAE + ALLQB + ALLEE + ALLDMD`

since fracture originates and propagates exclusively through the matrix and interfaces. Moreover, the material properties used for the matrix and the interfaces were very similar in previous studies. The sum of all this effects make the product of averages $\langle \boldsymbol{\sigma} \rangle_\Omega \cdot \langle \dot{\boldsymbol{\varepsilon}} \rangle^{\mathrm{f,mc}}$ to be more similar to the actual integrated power $P_{\Gamma_{1,\mathrm{mc}}}$.

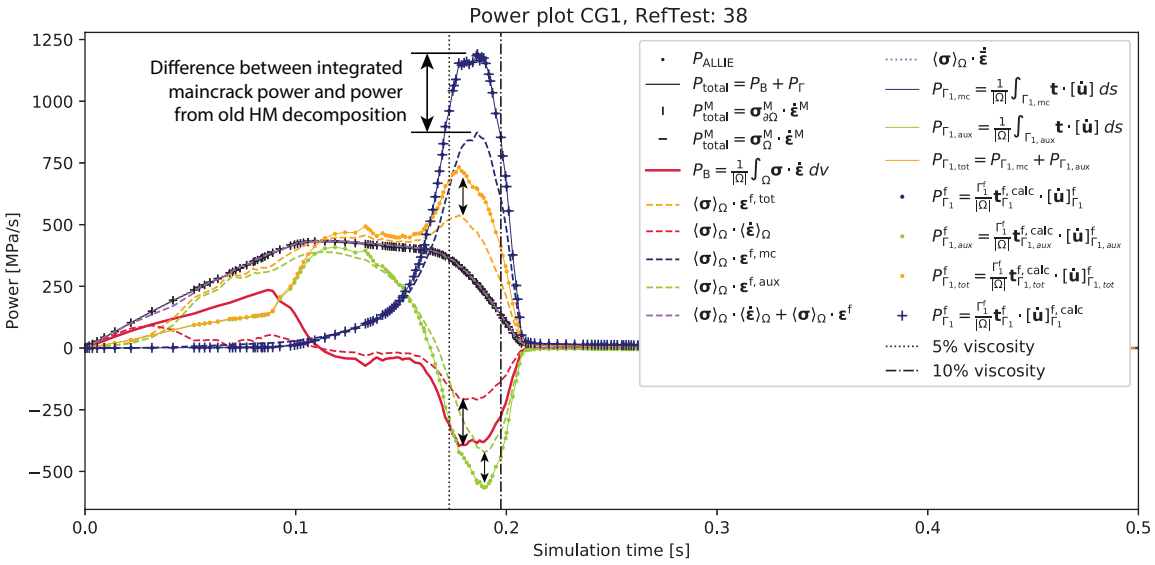

Figure 5.8: Power plot test #38. Comparison with old Hill-Mandel decomposition.

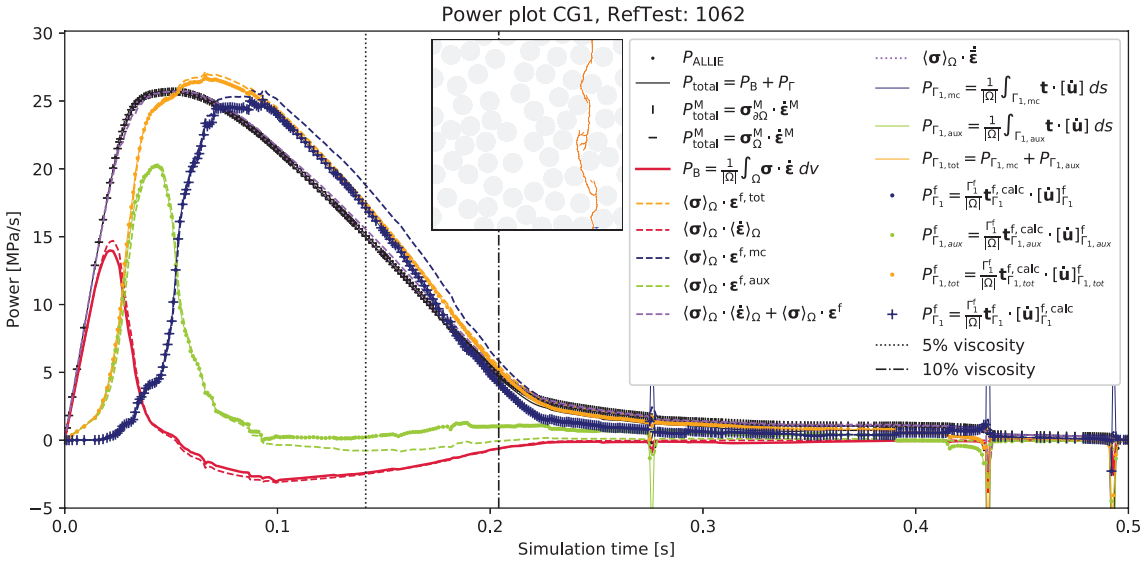

Figure 5.9: Power plot test #1062. Comparison with old Hill-Mandel decomposition.

5.5.2. Discussion: comparison of the new/old effective quantities

The old effective quantities shown in §3.5.1 were also revised as simulations showed disagreement between the effective power and the integrated one. These differences can be seen in figure 5.10, where the old effective power $P^{\mathrm{f,old}}_{\Gamma_1}$, calculated with $\mathbf{t}^{\mathrm{f}}_{\Gamma_1}$ (3.34), is plotted. This offset (A) is consistent for all loading cases involving rupture of the fibers. The lower power levels of the old and non-calculated curves are explained by the reduction of the effective traction due to the already cracked matrix. This leads to an effective power smaller than the one generated by the breaking of the fibers, featuring very high tensile stresses and displacement rates.

In simulations displaying fracture propagation through a single type of material, this offset reduces (e.g., figure 5.11, featuring axial loading in the vertical direction, with a crack propagating exclusively through the matrix). In previous studies, the offset was approximately in between the two cases presented as fracture propagated through the matrix and the interface. The use of new effective properties with no recalculation also results in an offset (B).

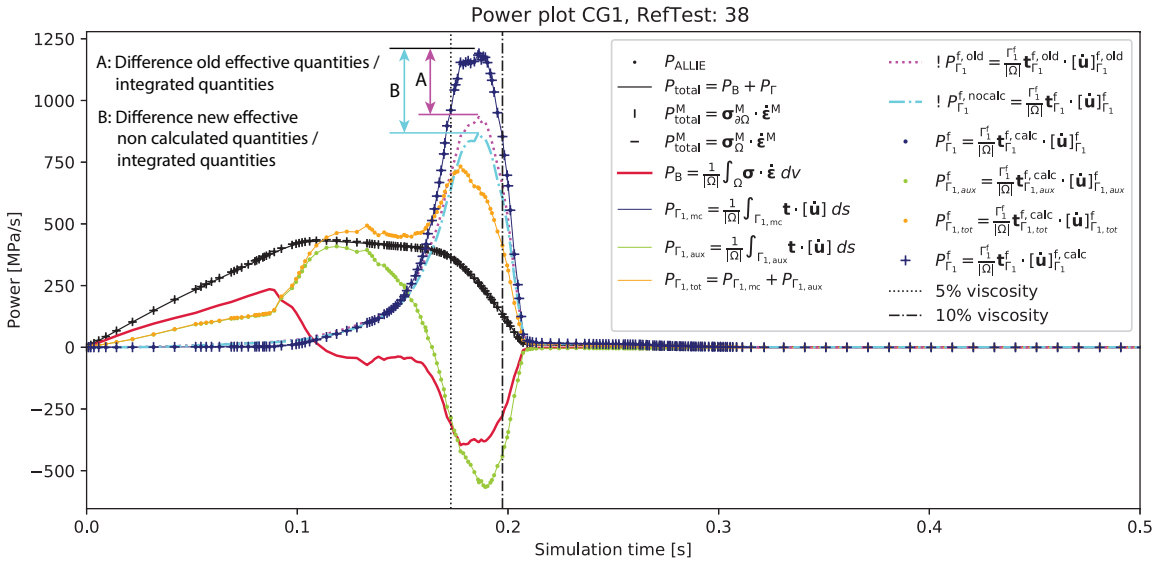

Figure 5.10: Power plot test #38. Comparison with old effective quantities.

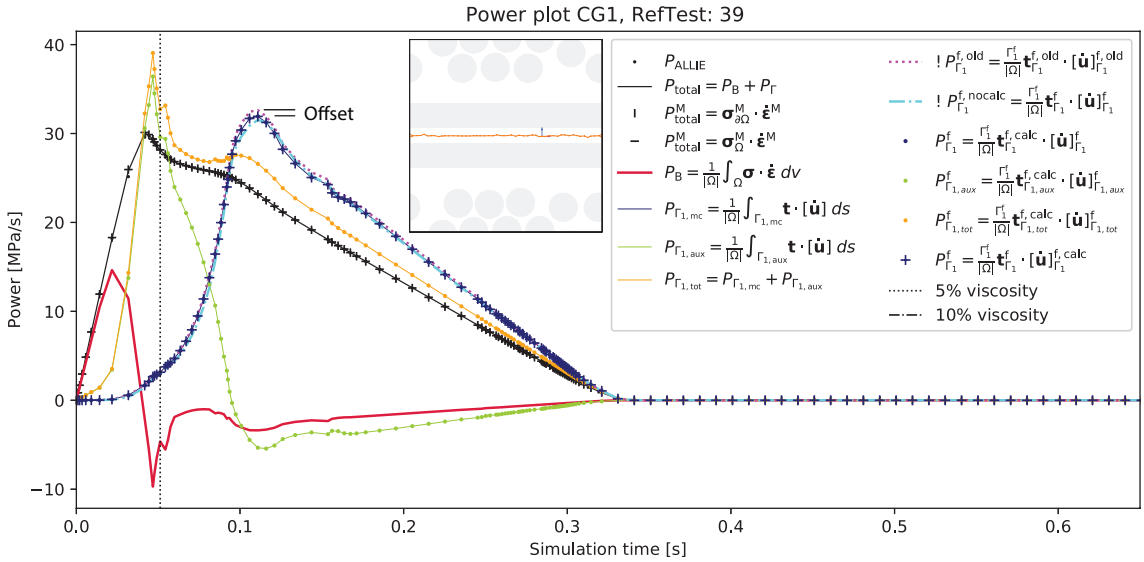

Figure 5.11: Power plot test #39. Comparison with old effective quantities.

5.6. Energy curves

The integration of the previously presented power curves results in the energy curves presented in figure 5.12. Additional curves are plotted, such as ALLDMD (energy dissipated by cohesive damage), ALLCD (approximate amount of energy associated with viscous regularization) and ALLSD (energy dissipated by automatic stabilization - especially critical in contact cases). The curves are normalized with respect to the domain surface $|\Omega|$.

It can be observed how the final energy dissipated by all cohesive elements $E_{\Gamma_{1,\text{tot}}}$ is higher than $E_{\texttt{ALLDMD}}$. This is due to the viscous energy generated by the viscous regularization $E_{\texttt{ALLCD}}$. This component cannot be directly decoupled from the main crack energy E_{Γ_1}, and thus results obtained over the 5% viscosity limit should be treated carefully. Additionally, the difference between the crack energy E_{Γ_1} and the old effective energy $E_{\Gamma_1}^{\text{f,old}}$ can be clearly appreciated. Similarly to the previous section, this difference becomes negligible when the crack entirely propagates through the same phase (e.g., figure 5.14).

Moreover, energy control plots are produced to study the evolution of the different energy components and the viscous dissipation percentage (see figures 5.13 and 5.15).

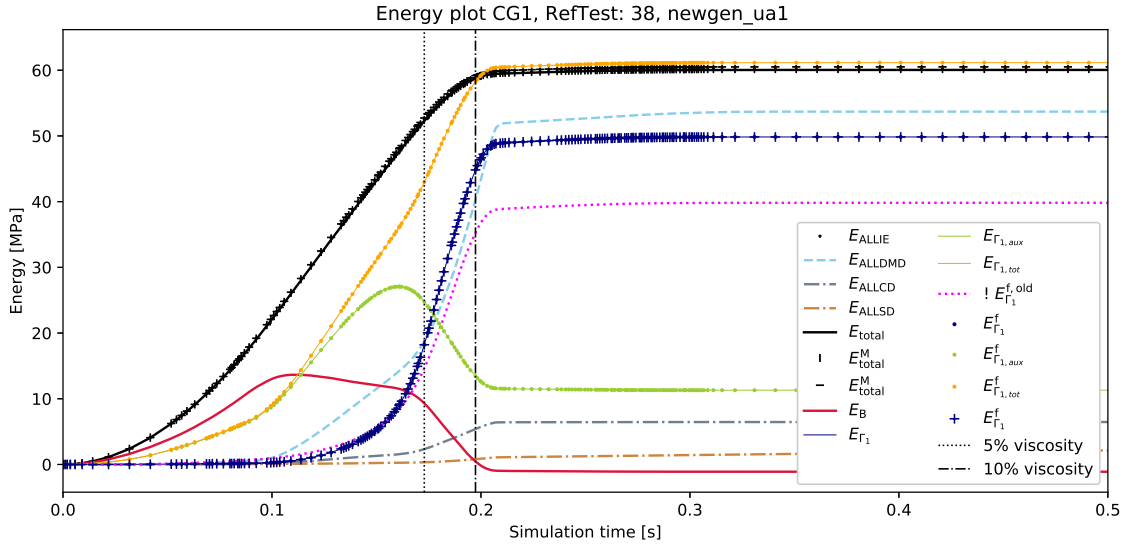

Figure 5.12: Energy plot test #38

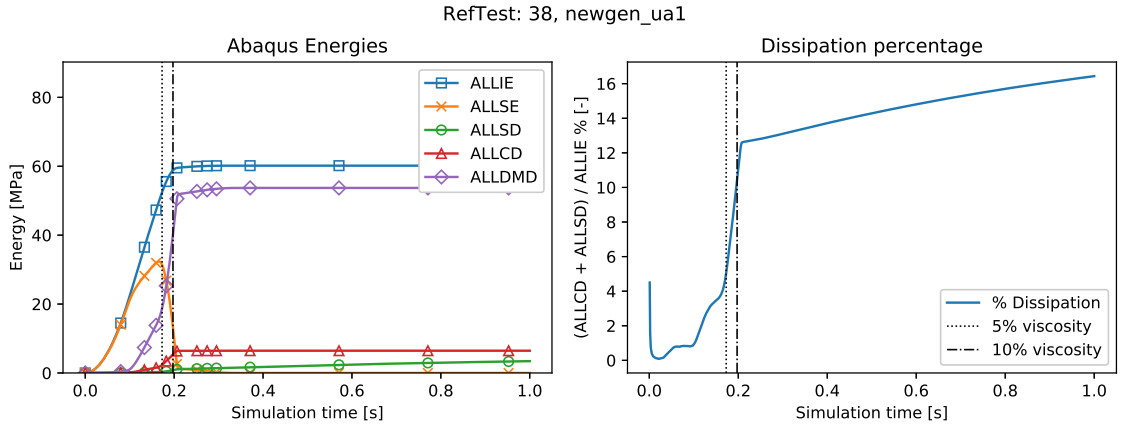

Figure 5.13: Energy control plots test #38

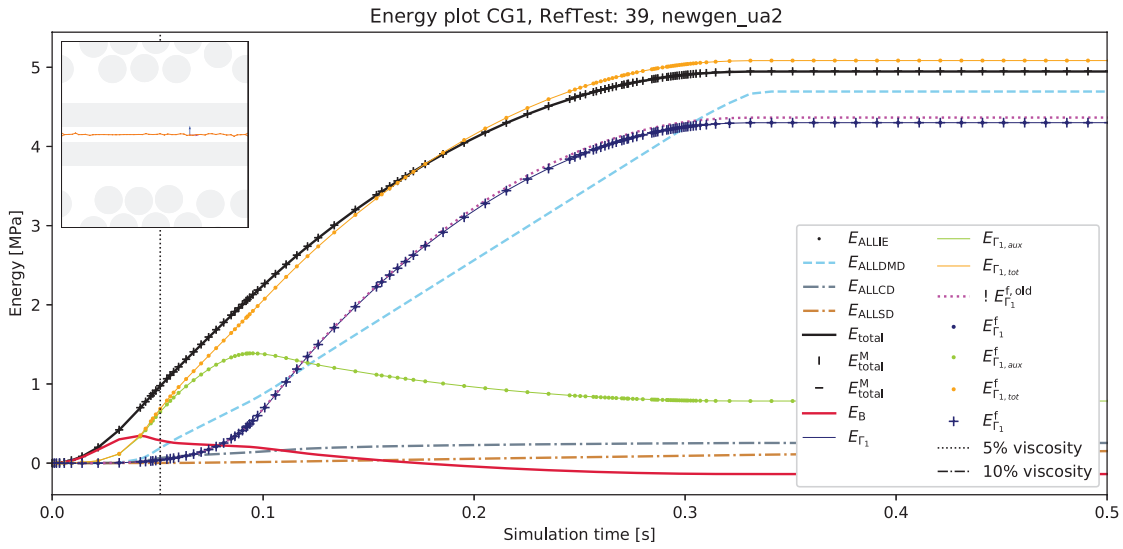

Figure 5.14: Energy plot test #39

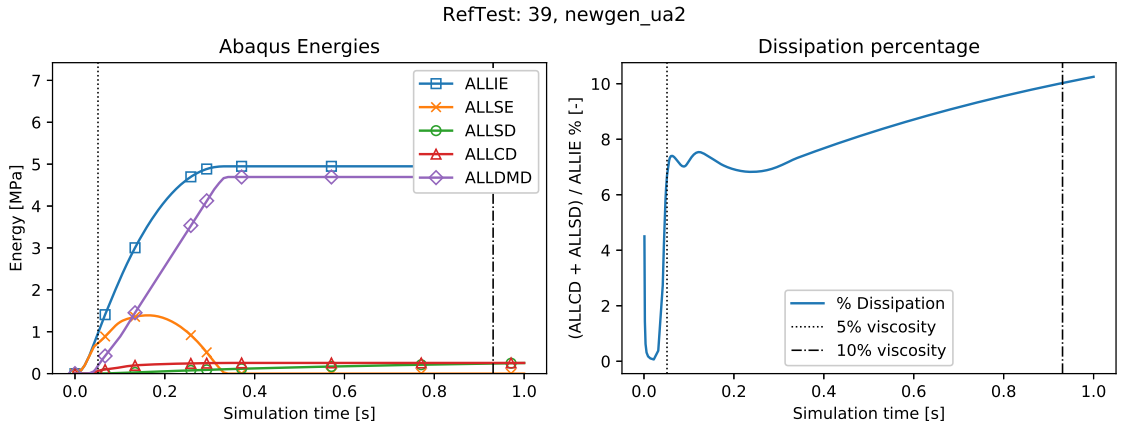

Figure 5.15: Energy control plots test #39

5.7. ETSLs

Finally, using the effective tractions and displacements previously presented, and having the power and energy balances on check, it is possible to generate the Effective Traction Separation Laws (ETSLs). As it was previously mentioned, depending on the choice of the effective quantities (i.e., $\left[\mathbf{t}^{\mathrm{f,calc}},\ [\![\mathbf{u}]\!]^{\mathrm{f}}\right]$ or $\left[\mathbf{t}^{\mathrm{f}},\ [\![\mathbf{u}]\!]^{\mathrm{f,calc}}\right]$) the resultant ETSL will be different. This can be observed in figure 5.16.

On the one hand, the set $\left[\mathbf{t}^{\mathrm{f}},\ [\![\mathbf{u}]\!]^{\mathrm{f,calc}}\right]$ approximately[2] respects the peak stress of the material predicted by classic relations. On the other hand $\left[\mathbf{t}^{\mathrm{f,calc}},\ [\![\mathbf{u}]\!]^{\mathrm{f}}\right]$ shows traction values which are far above what would be expected. However, when displacement boundary conditions are imposed and a consistent effective opening is desired, these traction levels would be the only guarantee of satisfying Hill-Mandel.

It is also interesting to observe the behavior of the other effective quantity pairs, which have reasonable shape but fail to dissipate the energy of the crack. Although in figure 5.16 the general shape of $\left[\mathbf{t}^{\mathrm{f}},\ [\![\dot{\mathbf{u}}]\!]^{\mathrm{f}}\right]$ and $\left[\mathbf{t}^{\mathrm{f,old}},\ [\![\dot{\mathbf{u}}]\!]^{\mathrm{f,old}}\right]$ are similar to the one of $\left[\mathbf{t}^{\mathrm{f}},\ [\![\dot{\mathbf{u}}]\!]^{\mathrm{f,calc}}\right]$, this is not always the case (e.g., figure 5.17).

[2] Numerical problems associated with the cohesive elements cause a deviation, see §5.9

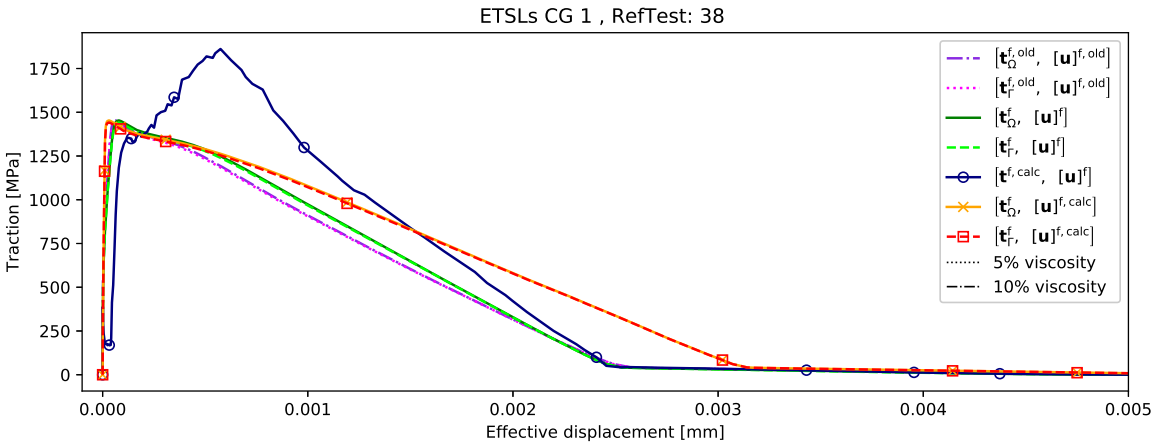

Figure 5.16: ETSL test #38. Uniaxial loading.

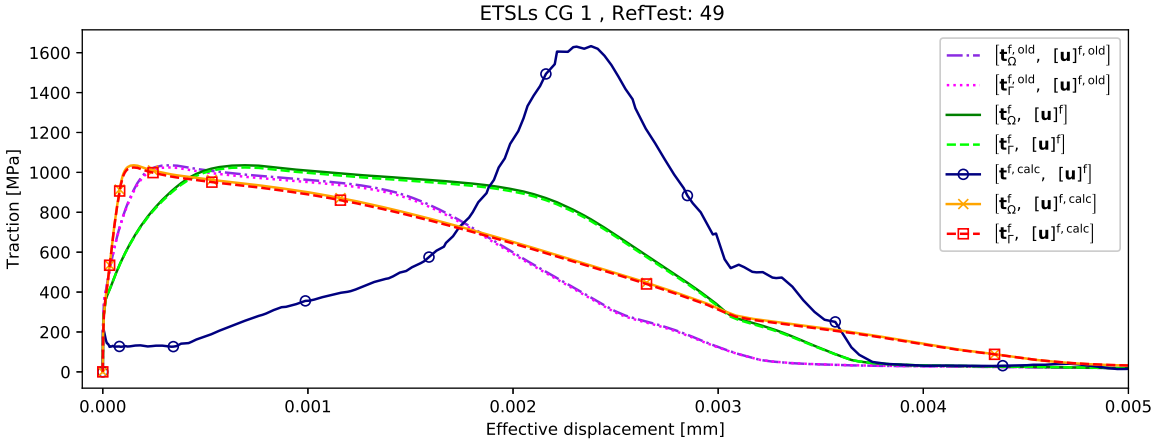

Figure 5.17: ETSL test #49. Mixed loading case.

5.8. Limitations

While this computational implementation represents a great advance regarding control, precision, and consistency, several limitations must be considered.

5.8.1. Crack surfaces loss of contact and overlapping

In shear and compression simulations, the cohesive elements often loose contact between their crack faces. Although cohesive elements are programmed to retain their compression resistance, large tangential displacements loosen the cohesive faces contact relation. This issue, acknowledged by Abaqus as a software limitation [15], results in interpenetration between the crack faces (see figure 5.18).

Solving this problem may require the creation of an internal Abaqus subroutine able to define on the fly the crack surfaces and add contact relations. Moreover, the subroutine could also be used to implement friction forces between crack surfaces (currently neglected). This action is added as a recommendation.

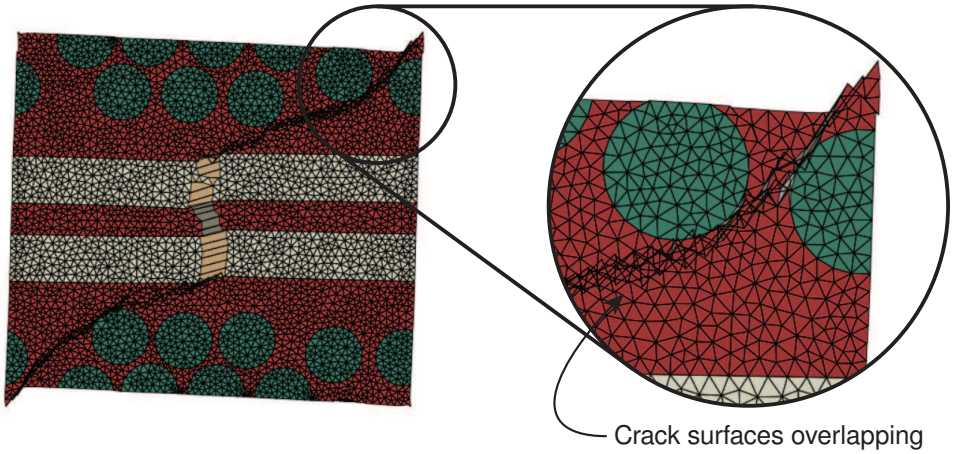

Figure 5.18: Crack surfaces overlap in shear 45° case, test #33.

5.8.2. Viscous dissipation

The implementation of the longitudinal [0°] fiber phase entails a much more violent and unstable fracture behavior. This forces Abaqus to use viscous regularization and automatic stabilization. While the use of these numerical artifacts is common practice (both in this kind of simulations and others), the quick rise above the safety levels (5% viscous dissipation with respect to the total strain energy) voids the quantitative significance of the results above this limit. The most immediate solution, reducing the viscous regularization parameter, cannot be taken as it results in an inability to converge the job.

5.8.3. Artificial compliance

Artificial compliance is observable, both in displacement (figure 5.4) and power curves (figure 5.7). Artificial compliance effectively softens the material, delaying the aperture of the crack. Besides, there is a percentage of energy dissipated through artificial compliance. For example, for test #38, this quantity represents 18% of the total energy at the end of the analysis.

5.8.4. Post-processing limitations

While substantial efforts have been performed to raise the robustness of the code, non-completed fracture simulations displaying opened branches can pose problems to the multi-crack recognition script. This may compromise the quantities that are integrated through the crack path. Moreover, cases displaying loss of contact and overlapping can also be problematic, as the erratic displacements difficult the crack identification. Finally, errors can occur in the detection of multiple propagating cracks with sudden changes in direction. The identification of each crack in complex multi-crack patterns has not been achieved with the desired robustness and generality. The use of artificial intelligence techniques for this purpose is recommended.

5.9. Lessons learned: Abaqus COH2D4 SDEG deviations due to high viscous regularization

While comparing the TSL of the uniaxial test #38 (figure 5.19) against classical formulas such as (5.1) [14], it was found that the ETSL peak was higher (≈ 10%) than the calculated one (5.2). This triggered a root-cause investigation. Possible post-processing effects related with the effective crack length were accounted for by using factors in equation (5.3), but their contribution was found to be small.

$$F_{1t} \cong F_{ft}\left(V_f + V_m \frac{E_m}{E_f}\right) \tag{5.1}$$

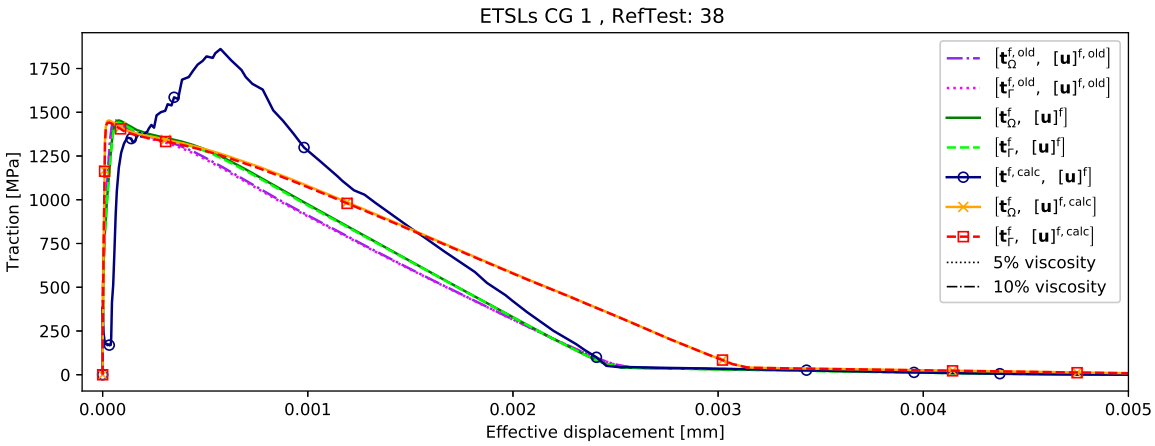

Figure 5.19: Old ETSL test #38 with $\eta = 10^{-3}$. Uniaxial loading.

$$F_{1t} \cong 5000\left(0.25 + 0.75\frac{4000}{275000}\right) = 1304\ \text{MPa} \tag{5.2}$$

$$F_{1t} \cong 5000\left(0.25\cdot 1.01 + 0.75\frac{4000}{275000}\cdot 1.05\right) = 1320\ \text{MPa} \tag{5.3}$$

$$F_{1t,\text{ETSL}} = 1450\ \text{MPa} \tag{5.4}$$

Thus, the Abaqus simulation output database was thoroughly examined. It was found that the normal traction outputs S22 of the longitudinal fibers' cohesive elements were systematically exceeding the maximum traction $t^o = 5000$ MPa, and thus not obeying the provided material traction separation law.

Therefore, a simplified model was created to remove as much external influences as possible (figure 5.20a). The model featured two CPE3 elements joined by a COH2D4 zero thickness cohesive element. Moreover, a vertical displacement boundary condition is imposed in node 6, and node 1 is pinned. The material properties used were the same ones used in the regular models (§4.2.7, §4.2.8), thus $G_f = 7500$ N/mm, $E_{\text{COH}} = 10^9$ MPa, $\delta_0 = 5\cdot 10^{-6}$ mm and $\delta_f = 0.003$ mm.

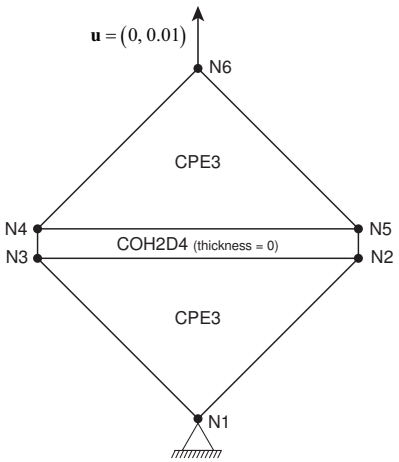

(a) Simplified troubleshoot model

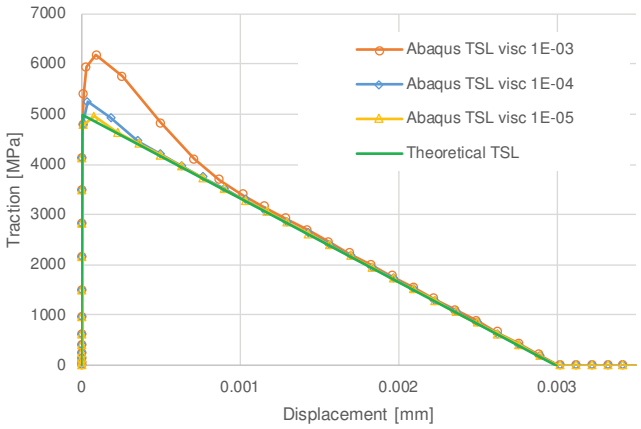

(b) Theoretical TSL and simplified model output TSL.

Figure 5.20: Damage variable deviation investigation plots.

After running the simulation, an "erroneous" increment featuring a cohesive normal traction S22 > 5000 MPa was searched. Once one was found, the displacements and damage variable SDEG were probed at that timeframe. The normal opening was found to be $\delta = 9.55\cdot 10^{-5}$mm and the damage variable SDEG = 0.433. The application of relation (4.6) with the provided values, results in $t = 5406$ MPa, exactly the same value reported

by Abaqus. However, the application of equation (4.7) results in a theoretical $\mathtt{SDEG}_{calc} = 0.477$, which turns into $t_{calc} = 4992$ MPa (TSL compliant).

Several potential causes for this deviation were studied. The time step of the simulation was refined, with no success. The non-linear convergence criterion was made stricter, with no success. E_{COH} and G_f were updated to the new properties (see chapter §7), but the deviation persisted. The damage initiation tolerance was reduced, with no success.

Finally, although the viscous effects were initially discarded due to the low energy contribution (zero) of ALLCD and ALLSD at the studied frame, a change of the viscosity parameter from $\eta = 10^{-3}$ to $\eta = 10^{-5}$ solved the problem. Moreover, $\eta = 10^{-4}$ also resulted in an incorrect response ($\approx$ 250 MPa, 5% error), as seen in figure 5.20b. It is thus concluded that "high" viscous regularization parameter ($\eta > 10^{-5}$ with the here used material properties) can lead to errors in the Abaqus cohesive damage variable calculation and thus the TSL response.

The application of $\eta = 10^{-5}$ to the larger problem resulted in a peak traction of $F_{1t} = 1325$ MPa, similar to the estimations in equations (5.2) and (5.3), which can be seen in figure 5.21.

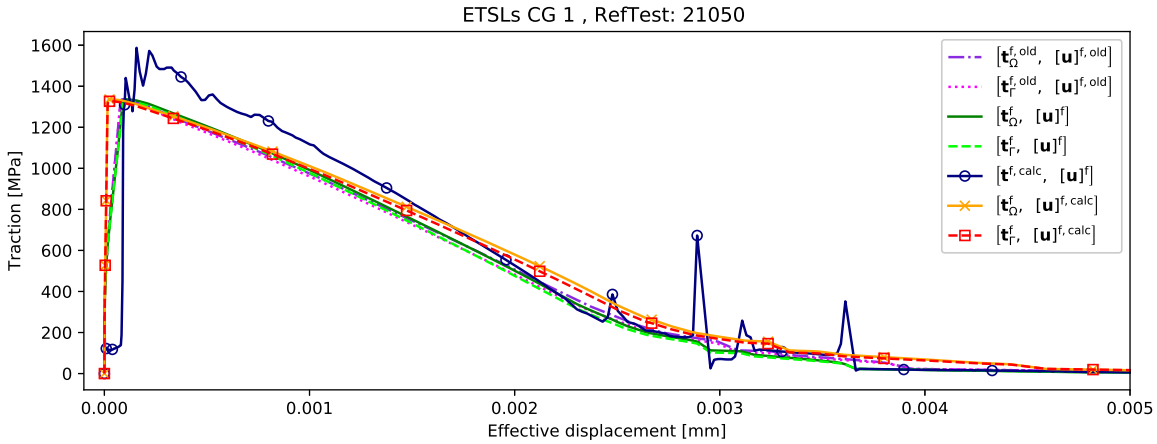

Figure 5.21: ETSL test #21050 with $\eta = 10^{-5}$. Uniaxial loading.

6

Verification

In this section, verification of the theory is performed and convergence studies are presented. First, the Hill-Mandel condition is verified. Then, three factors are studied. The first one (§6.3) investigates the convergence behavior when refining the grid size. The second check (§6.2) aims to verify that the results are similar for several test repetitions with different fiber distributions, thus not being strongly tied to the randomly generated geometry. Thirdly, the size of the domain is changed (§6.4), thus convergence is aimed to be found as the RVE is made larger. While several loading modes are used to test the Hill-Mandel compliance, the presented mesh and RVE convergence study are performed exclusively with uniaxial loading cases. Finally, the dependence of the crack propagation on the periodic boundary conditions and the domain size is discussed in §6.9.

6.1. Hill-Mandel verification

This section showcases the validity of the homogenization methods discussed from an inter-scale energy conservation standpoint. The objective is to guarantee the effective properties exchange the same amount of power in the micro-domain and the macroscopic one. This is performed by verifying the Hill-Mandel condition both for the global domain and the crack domain. The section extends the discussion in §5.5, providing new test cases and loading modes. From the post-processing it is possible to observe the Hill-Mandel condition is fulfilled in all the results: for uniaxial cases (figures 6.1 and 6.2), for shear (figure 6.3) and mixed mode (figure 6.4).

In the presented plots, there are several interesting details that can be addressed. For example, in figures 6.1 and 6.2, the two peaks correspond to each of the two longitudinal fibers breaking. Moreover, in figure 6.2 (45° uniaxial tensile case), it is interesting to highlight the peak of $P_{\Gamma_1}^{\text{f,old}}$ and $P_{\Gamma_1}^{\text{f,nocalc}}$ at $t = 0.14s$, caused by a mix of a large effective opening and high tractions due to crack opening in the matrix without fiber cracks (which do not occurr until $t = 0.18$). This deviation is consistent with what was covered in section §3.5.1.

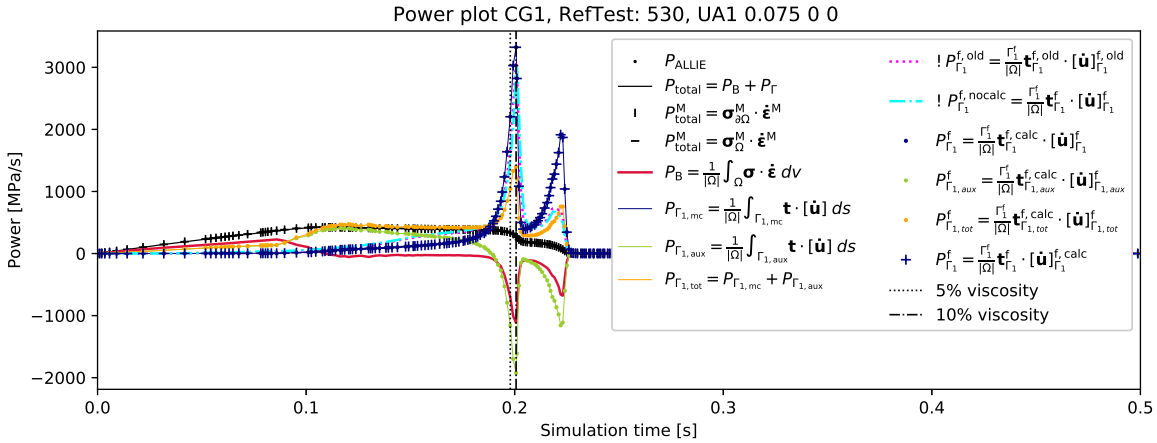

Figure 6.1: Power plot, test #530, uniaxial tensile loading 0° with respect to $\boldsymbol{e}_1$

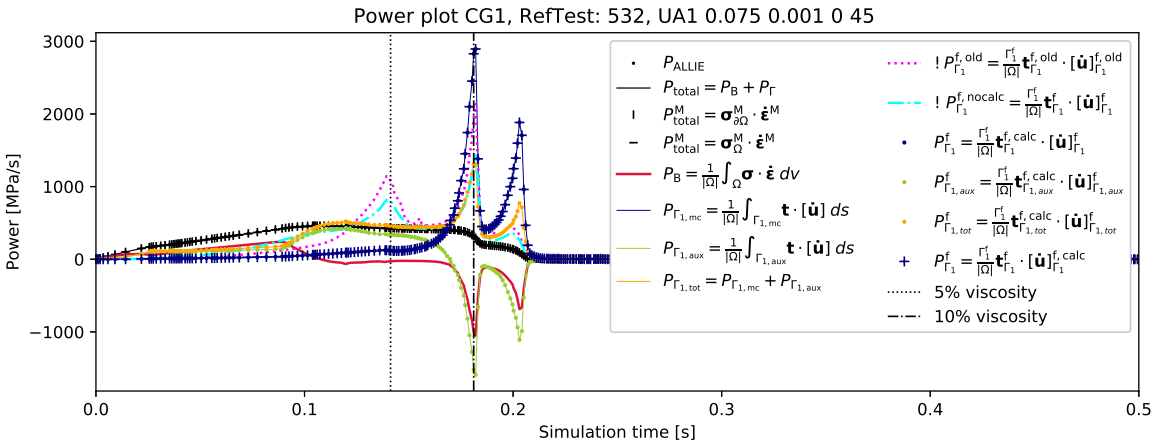

Figure 6.2: Power plot, test #532, uniaxial tensile loading 45° with respect to $\boldsymbol{e}_1$

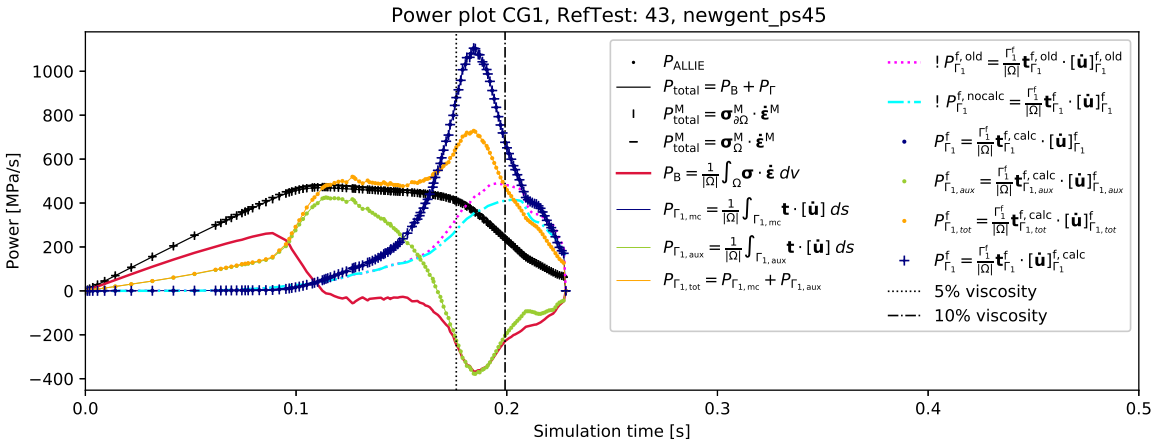

Figure 6.3: Power plot, test #43, pure shear 45°

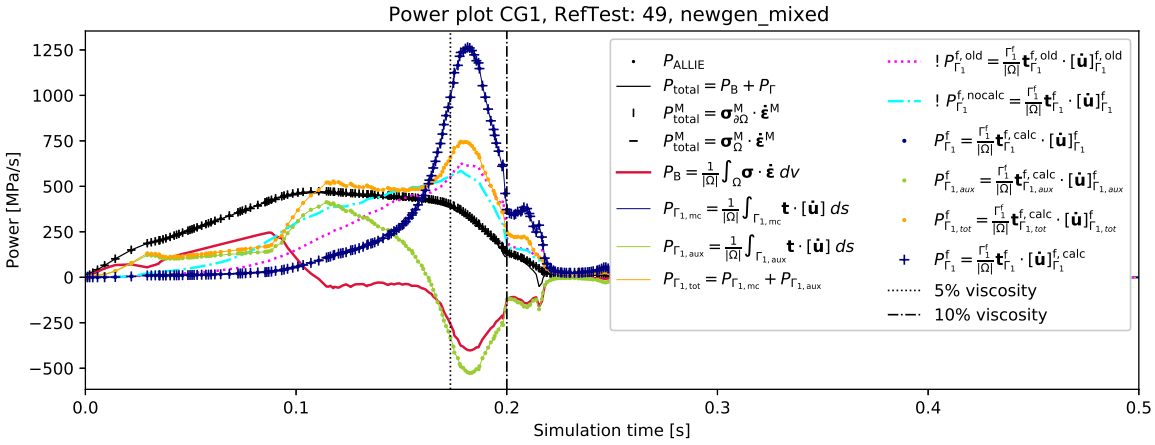

Figure 6.4: Power plot, test #49, mixed mode

6.2. Mesh convergence

Several analyses were performed to test convergence when changing the grid size of the mesh. Grid sizes of 0.5, 1, 2 and 3 μm were used. The mesh convergence study is performed for four squared domains with edge lengths 25 μm, 50 μm, 75 μm and 100 μm. For the larger domains (75 μm and 100 μm), the gridsize 0.5 μm is excluded due to computational cost. The used meshed domains can be seen in figures 6.5, 6.6, 6.7 and 6.8.

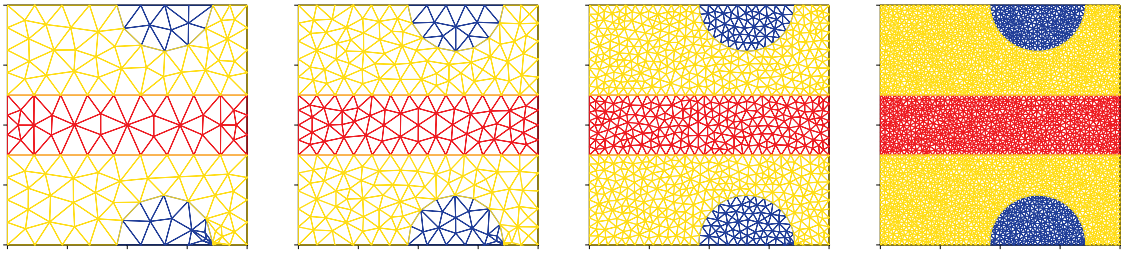

Figure 6.5: Domain size: 25 x 25 μm. Gridsizes: 3, 2, 1, 0.5 μm

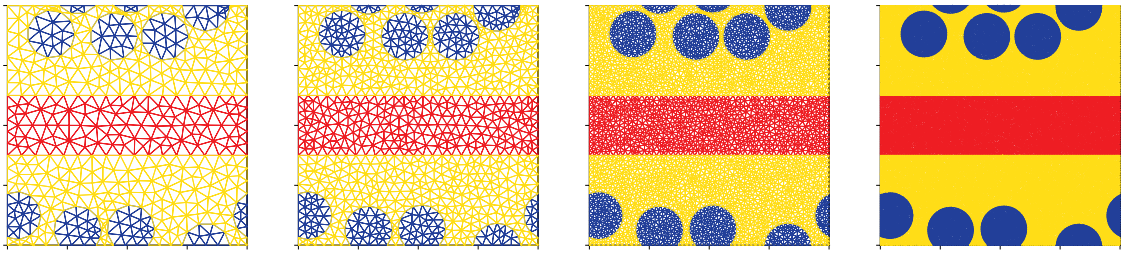

Figure 6.6: Domain size: 50 x 50 μm. Gridsizes: 3, 2, 1, 0.5 μm

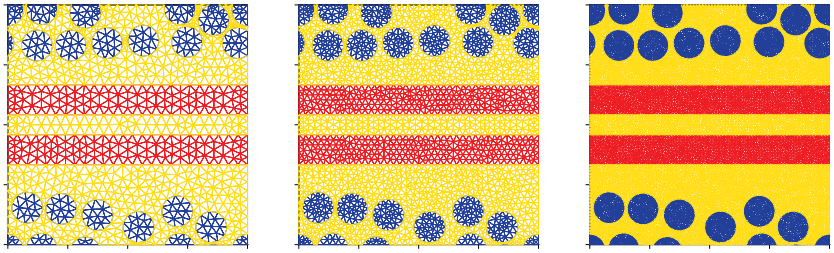

Figure 6.7: Domain size: 75 x 75 μm. Gridsizes: 3, 2, 1 μm

Figure 6.8: Domain size: 100 x 100 μm. Gridsizes: 3, 2, 1 μm

The mesh convergence study was performed for horizontal uniaxial loading cases. The following figures compare the effective traction-separation laws (both displacement and traction calculated) for the different grid sizes, extracted as discussed in section §6.3. Moreover, the crack fracture energy is also plotted.

For the displacement calculated curves, reasonable convergence can be seen in the estimation of the ETSL peak stress for all RVE sizes. Good ETSL general convergence is obtained for the smaller domains sizes (25 μm and 50 μm). For the larger domains (25 mum and 50 μm), fair convergence is observed on the first part of the curve, which deteriorates as it progresses towards the 5% viscosity limit. Convergence above this

point is deficient, and it worsens as more viscous energy is required. Moreover, it must be remarked that the results displayed for the 25 μm and 50 μm domains correspond to smaller RVEs with simpler fracture behavior and fewer cohesive elements (and thus less viscosity and artificial compliance). Hence, their superior convergence.

In the case of traction calculated curves, convergence cannot be found. The cohesive elements have an impact on the artificial compliance and the complexity of the fracture pattern. This heavily influences the behavior of the traction calculated curves. The branches and additional segments (more numerous in larger domains) contribute towards the opening of their crack group. Numerical instabilities can also be appreciated in these curves in the form of sudden sparks (no filtering is used).

The energy curves show good convergence for the 25 μm and 50 μm domains. Their convergence worsens as the domain is enlarged.

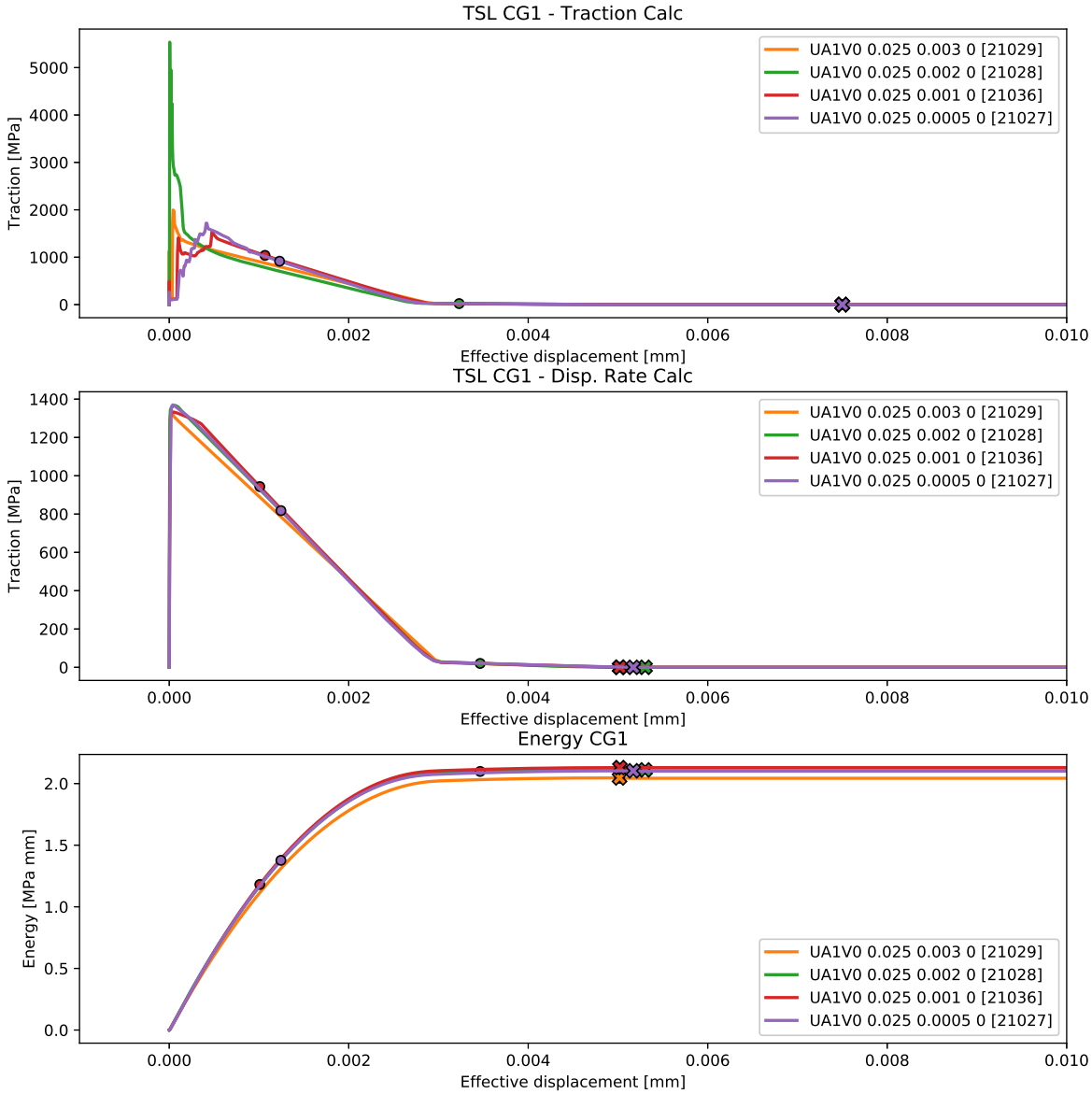

Figure 6.9: Mesh convergence plot for domain size 25μm, gridsizes 0.5, 1, 2 and 3 μm.

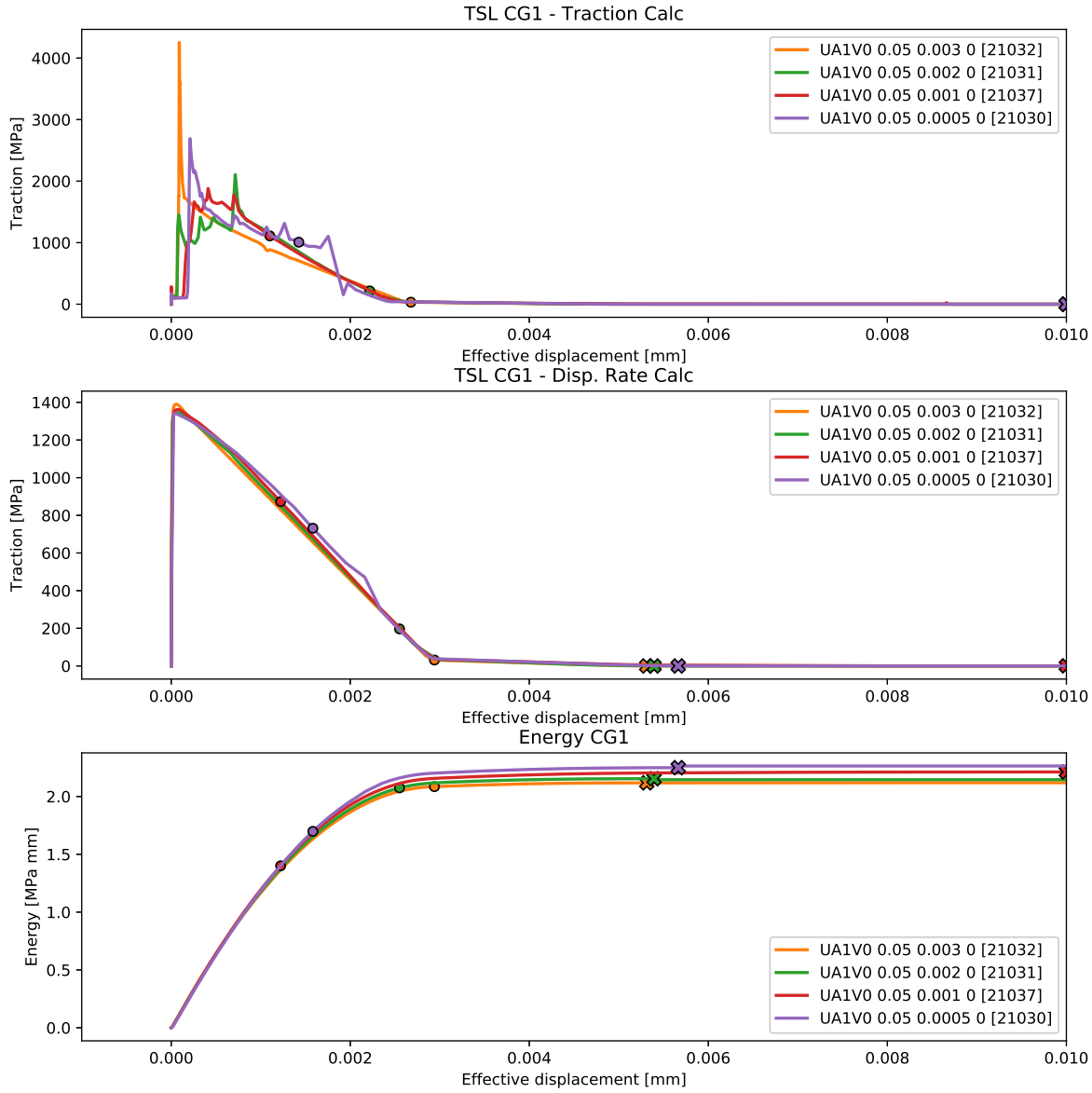

Figure 6.10: Mesh convergence plot for domain size 50μm, gridsizes 0.5, 1, 2 and 3 μm.

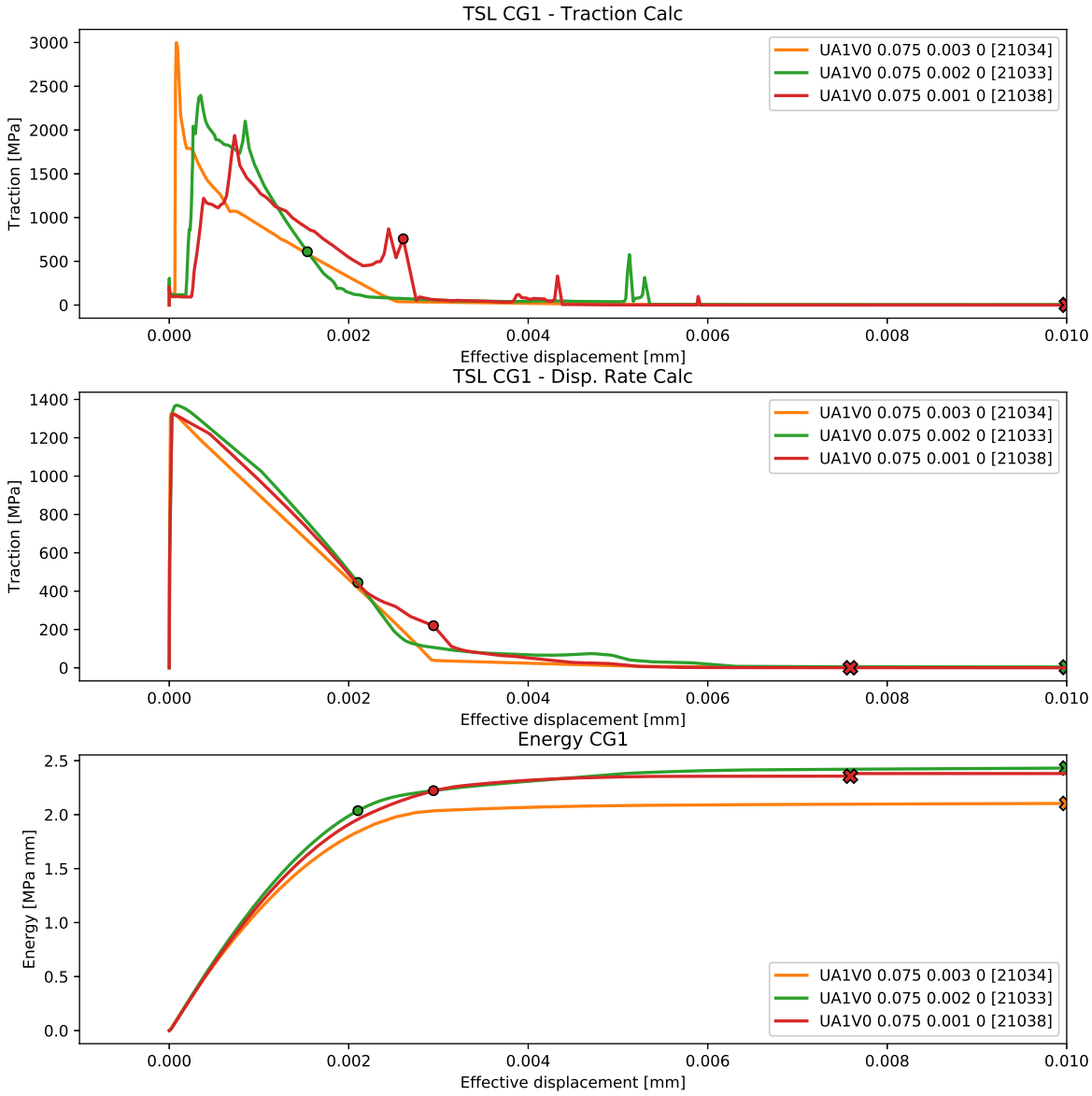

Figure 6.11: Mesh convergence plot for domain size 75μm, gridsizes 1, 2 and 3 μm.

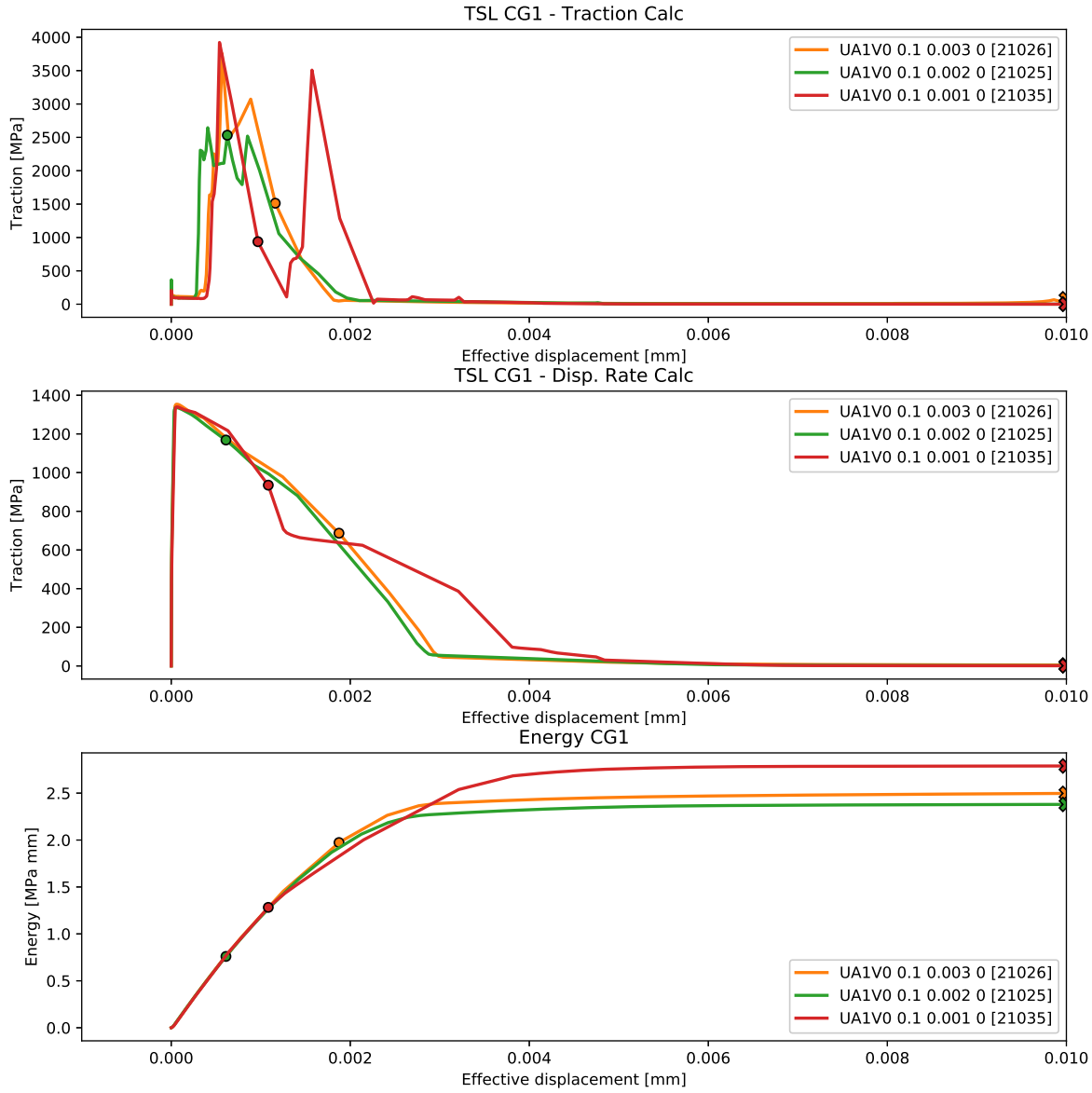

Figure 6.12: Mesh convergence plot for domain size 100μm, gridsizes 1, 2 and 3 μm.

6.3. Geometry generation statistical convergence

In chapter §4, it was described how the RVE geometry is randomly generated. This has an impact on the results and in the crack path due to the different mesh discretization. Therefore, tests are required to verify that the results are similar for different statistical repetitions, thus not being strongly tied to the randomly generated geometry. Each test is simulated between 4 and 5 times with different fiber distributions and meshes. While 5 repetitions are acknowledged as insufficient to perform a textbook statistical analysis, the cluster and processing time limit the possible number of statistical realizations.

The following figures display the results of each test repetition with dots, the average TSL with a continuous line, and the statistical deviation is represented by a shadow. Moreover, the large circle marker represents the most conservative 5% viscosity limit of all the repetitions, and the cross marker represents the displacement at the first simulation completion/exit time. In general, the plots show a small standard deviation among the simulations for the calculated displacement curves (traction-based, $\left[\mathbf{t}^{\mathrm{f}},\ [\![\dot{\mathbf{u}}]\!]^{\mathrm{f,calc}}\right]$), thus indicating close agreement between statistical repetitions. This is not the case of the traction calculated curves (displacement based, $\left[\mathbf{t}^{\mathrm{f,calc}},\ [\![\dot{\mathbf{u}}]\!]^{\mathrm{f}}\right]$), much more sensitive to the mesh geometry and numerical instabilities.

The small/reasonable deviation among tests in the case of the displacement calculated curves stays similar for larger RVE domains. In these tests, the statistical deviation remains negligible within the $< 5\%$ viscosity energy domain. However, the traction calculated curves retain and worsen their erratic behavior, and clear convergence cannot be obtained. Additionally, the values and shape of these curves change as the domain is enlarged. The convergence in RVE size is covered in §6.4.

When comparing the anisotropic case [0,90,0] against a more isotropic one [0] (figure 6.15), it is possible to observe that convergence improves for the latter one. Moreover, the traction and displacement calculated curves almost overlap. This is caused due to the crack propagating only through the matrix and interface, which have really similar properties.

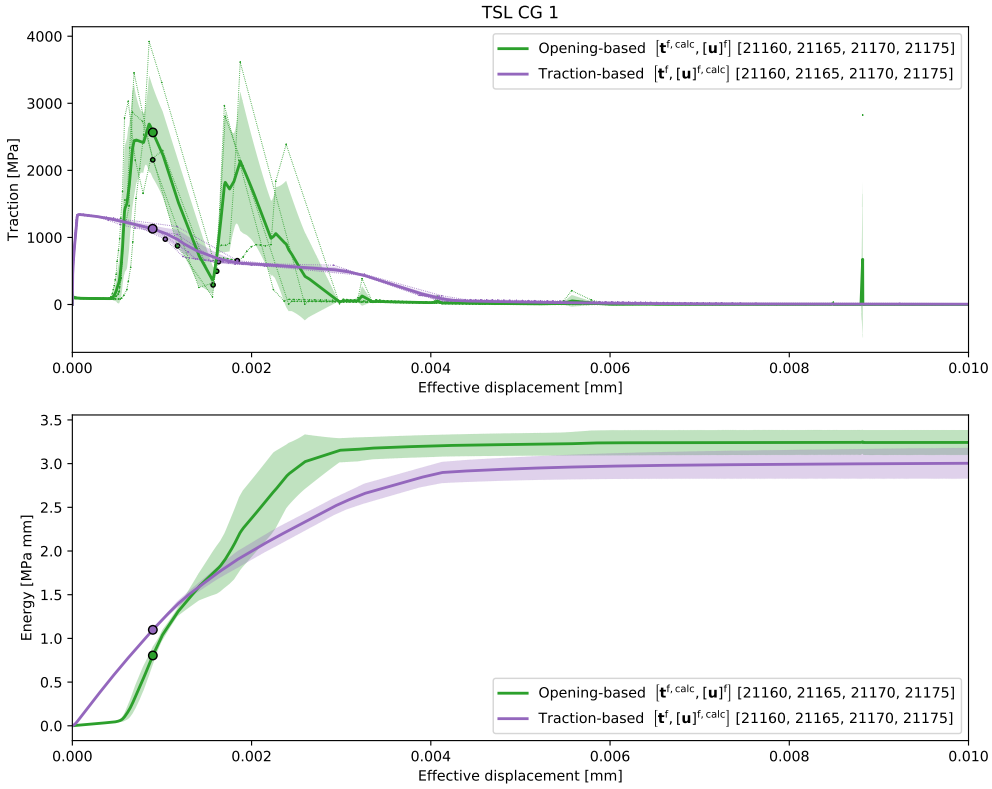

Figure 6.13: Geometry generation statistical convergence tests # 21100, 21105, 21110, 21115. Domain size 25 μm, gridsize 1 μm.

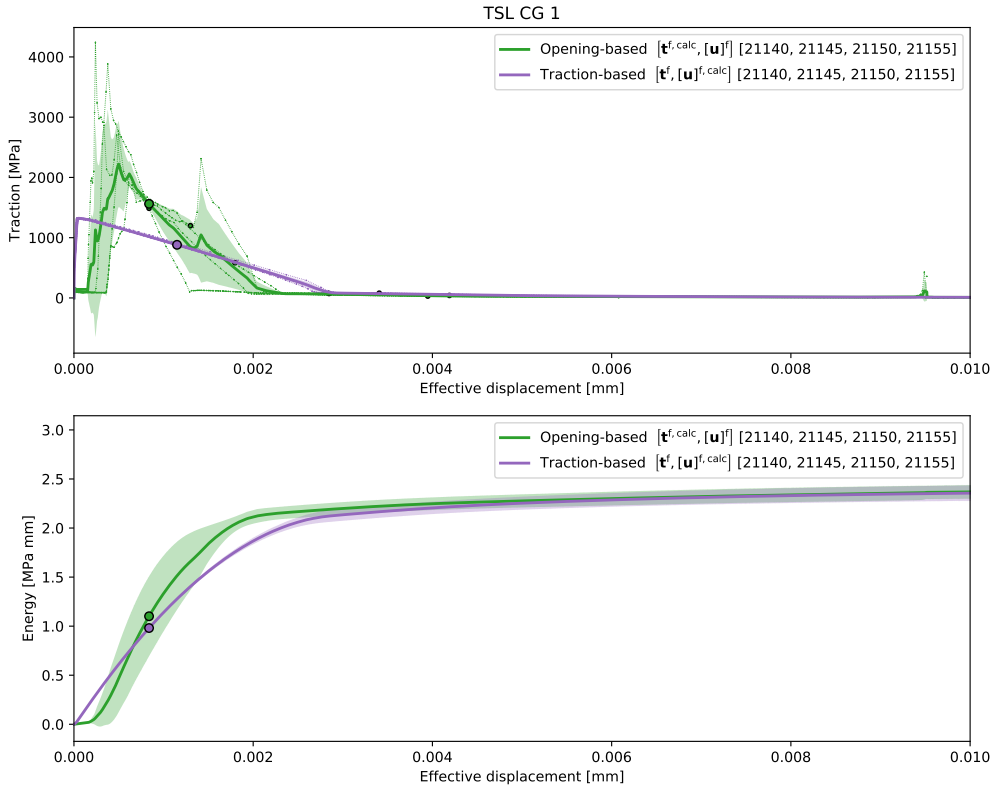

Figure 6.14: Geometry generation statistical convergence tests # 21140, 21145, 21150, 21155. Domain size 75 μm, gridsize 1 μm.

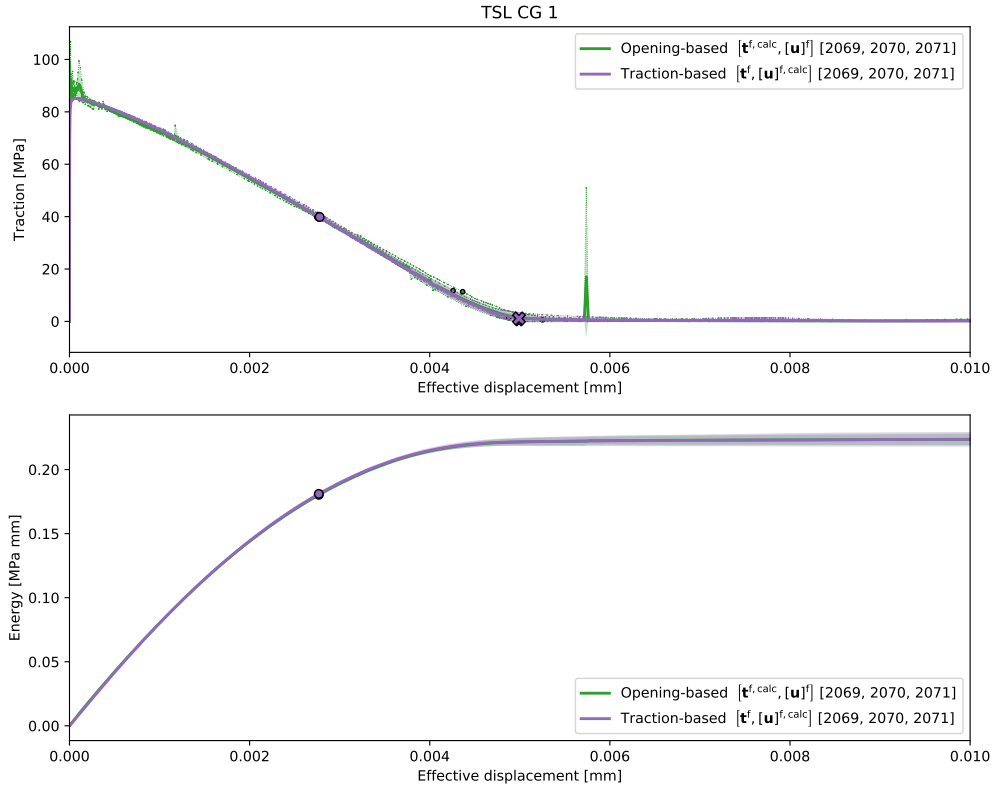

Figure 6.15: Geometry generation statistical convergence tests # 2069, 2070, 2071. Domain size 75 μm, gridsize 1 μm.

6.4. RVE convergence

Figure 6.16 presents the RVE size convergence study for the case of uniaxial loading in the horizontal direction. The traction calculated curves do not converge directly. These curves are affected by the appearance of artificial compliance and the opening of branches and secondary cracks. Thus, direct convergence cannot be expected when changing the RVE size. By normalizing by the domain size, it is possible to obtain a closer match between the curves before the localization of the crack. After fracture, artificial compliance does not play a role, and therefore this normalization is not required. Detailed information on RVEs' convergence and can be found in the paper by Nguyen et al. [71].

The behavior of the displacement calculated curves show agreement on the point of fracture initiation. Besides, convergence is achieved for sizes lower and equal to 75 μm. However, the 100 μm shows severe divergence. This is explained by the difficult convergence of these larger and more complex simulations, which forces Abaqus to use significant (> 5%) viscous damping in the early stages of opening of the crack. Furthermore, the more complex and different fracture patterns which, combined with the artificial viscosity, provoke a larger statistical deviation in the curves.

No convergence is found on the energy curves above the 5% viscosity limit. The injected viscous energy (ALLCD and ALLSD), makes energy convergence not possible. This issue worsens for larger domains, specially for the 100 μm.

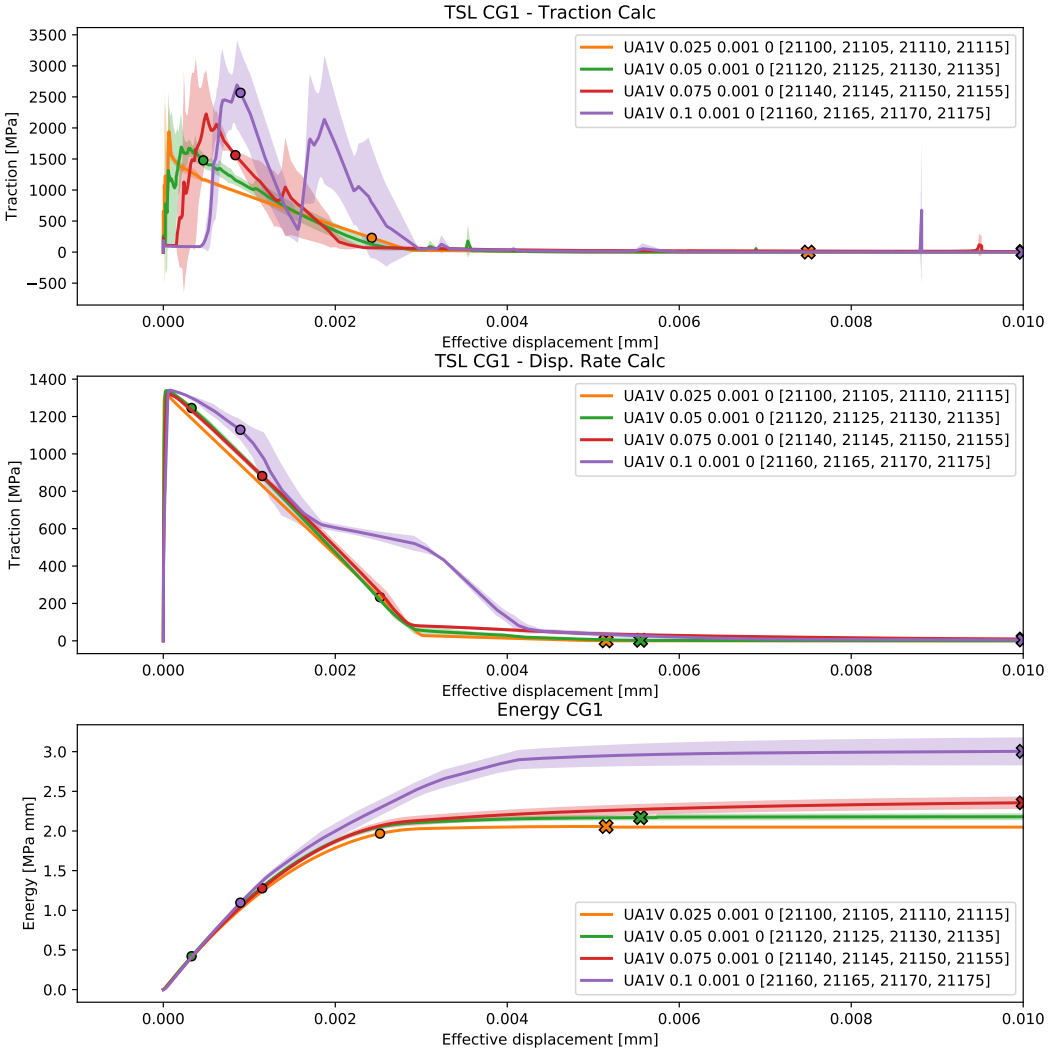

Figure 6.16: RVE convergence plot for UA1 [0,90,0], domain sizes 25, 50, 75 and 100 μm, and gridsize 1 μm.

It is interesting to observe the contrast between the anisotropic case [0,90,0] (figure 6.16) and the isotropic one [0] (6.17). The results from the [0] RVE, featuring matrix-interface fracture, look better than the [0,90,0] from an RVE convergence standpoint. It is important to remark that the 5% viscosity limit appears at a later point in the curve than in the [0,90,0] case. Moreover, it was observed that in the [0,90,0] case the 10% limit was located next to the 5% limit, while in the [0] case this limit appeared in the lower end of the TSL. This shows a much higher use of viscous regularization and automatic stabilization, which are coherent with the much more violent behavior of the simulation.

Moreover, the lower fracture strengths lead to a minimal effect of the artificial compliance. This, coupled to the almost simultaneous opening of the full crack path, contribute to making the traction calculated curve similar to the displacement calculated TSL. Numerical instabilities lead to the sparks in the curves.

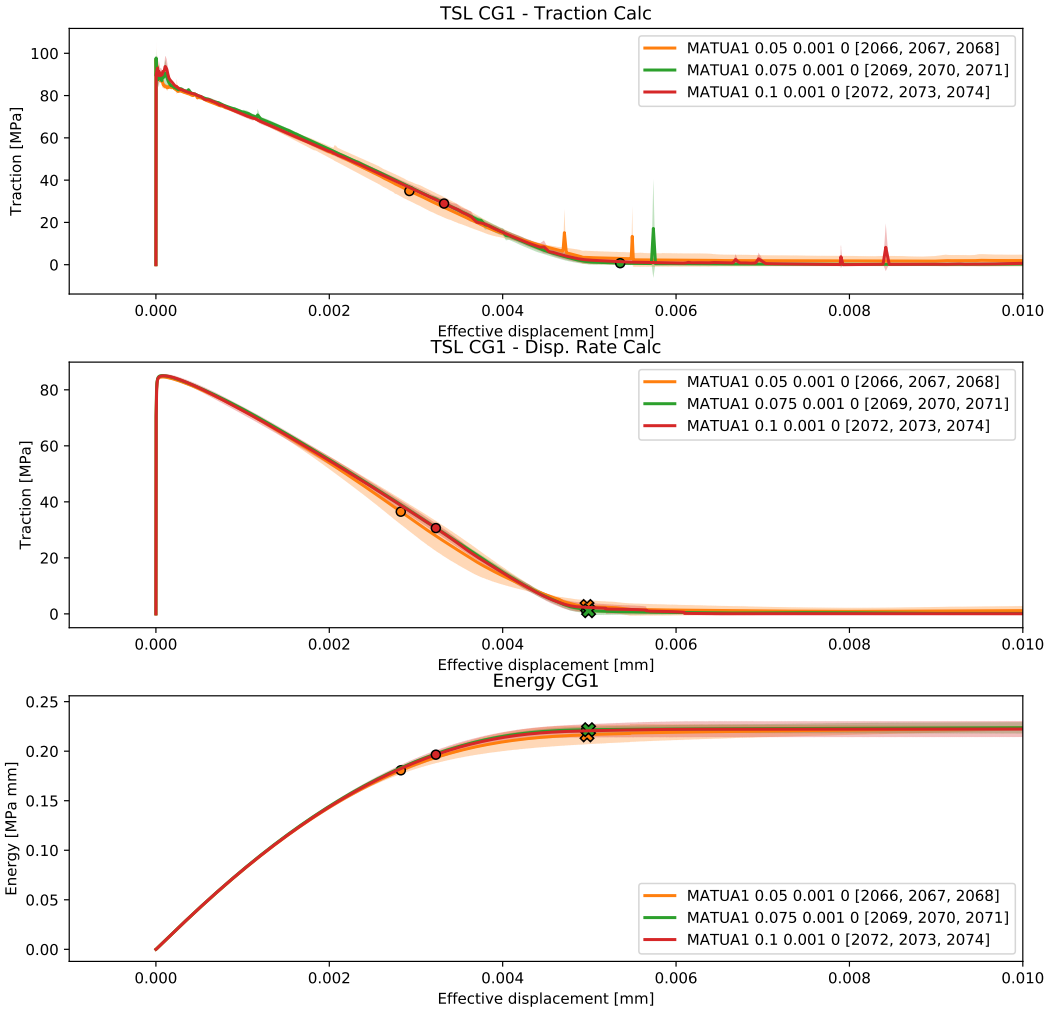

Figure 6.17: RVE convergence plot for UA1 [0], domain sizes 50, 75 and 100 μm, and gridsize 1 μm.

6.5. Energy comparison

The observation of the different energies and the dissipation percentages provides information about the fracture energy, the fracture process and the convergence of the analysis. The [0,90,0] cases display a very high influence of the numerical artifacts after the onset of fracture in the fibers. Figures 6.18 and 6.19 display the energy curves for two uniaxial tests featuring viscosity $\eta = 10^{-5}$, and domain sizes 50 μm and 100 μm respectively. In these cases, the large influence of the automatic stabilization ALLSD is observable after the onset of fracture. Moreover, it is interesting to compare these energy curves with the older cases featuring a larger viscosity $\eta = 10^{-3}$ (figures 6.20 and 6.21). In the latter ones, it is observable how the viscous regularization component ALLCD is more prominent.

Furthermore, the influence of the artificial viscosity grows as the domain is enlarged. This can be seen by comparing the dissipation percentage of test #21120 (figure 6.18) with test #21160 (figure 6.19). The same behavior applies for the $\eta = 10^{-3}$ cases, and can be observed by comparing tests #515 (figure 6.20) and #550 (figure 6.21).

Moreover, the [0] case in figure 6.22 (matrix/interface fracture) displays limited viscous influence (< 10% over the whole fracture process), mostly in the form of automatic stabilization. The anisotropic cases [0,90,0] show a much stronger influence of viscosity, with a quick raise over 10%, which aggravates in the cases using $\eta = 10^{-5}$.

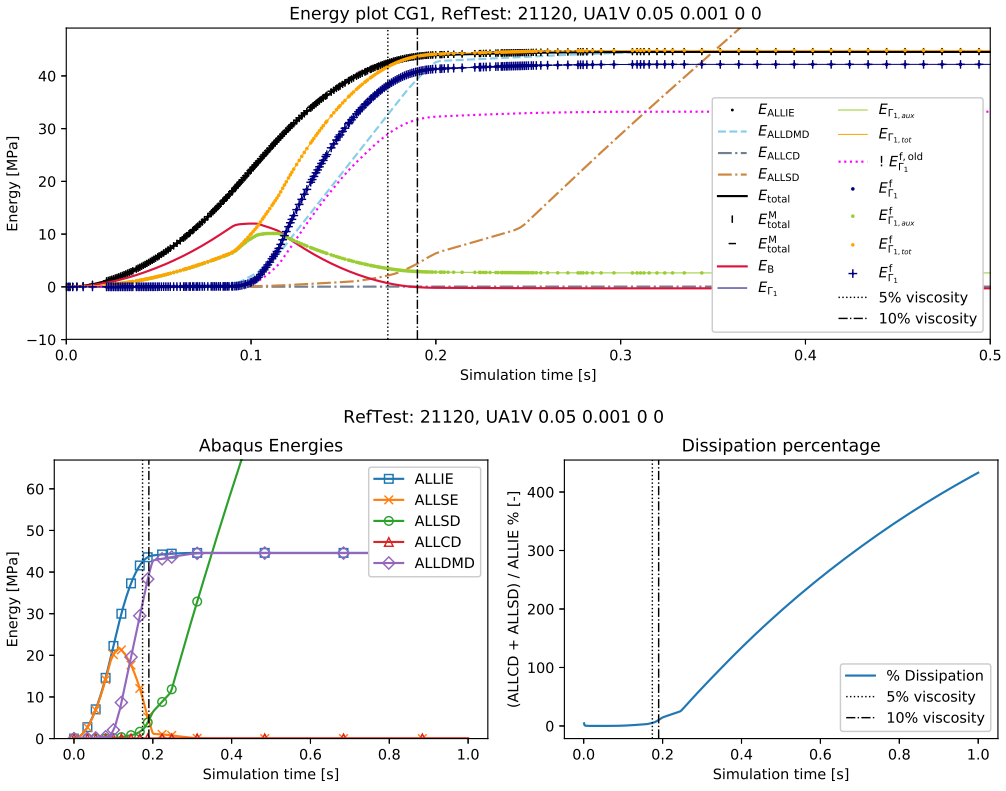

Figure 6.18: Energy plot test #21120 (UA1V with domain size 50 μm, gridsize 1 μm).

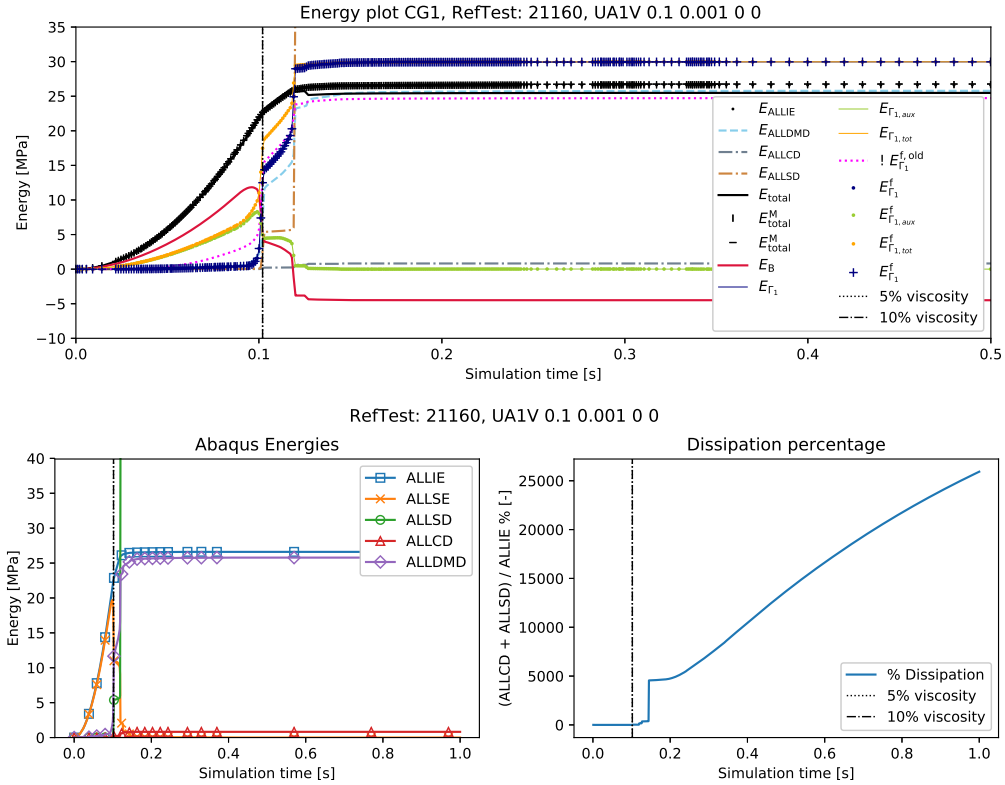

Figure 6.19: Energy plot test #21160 (UA1V with domain size 100 μm, gridsize 1 μm).

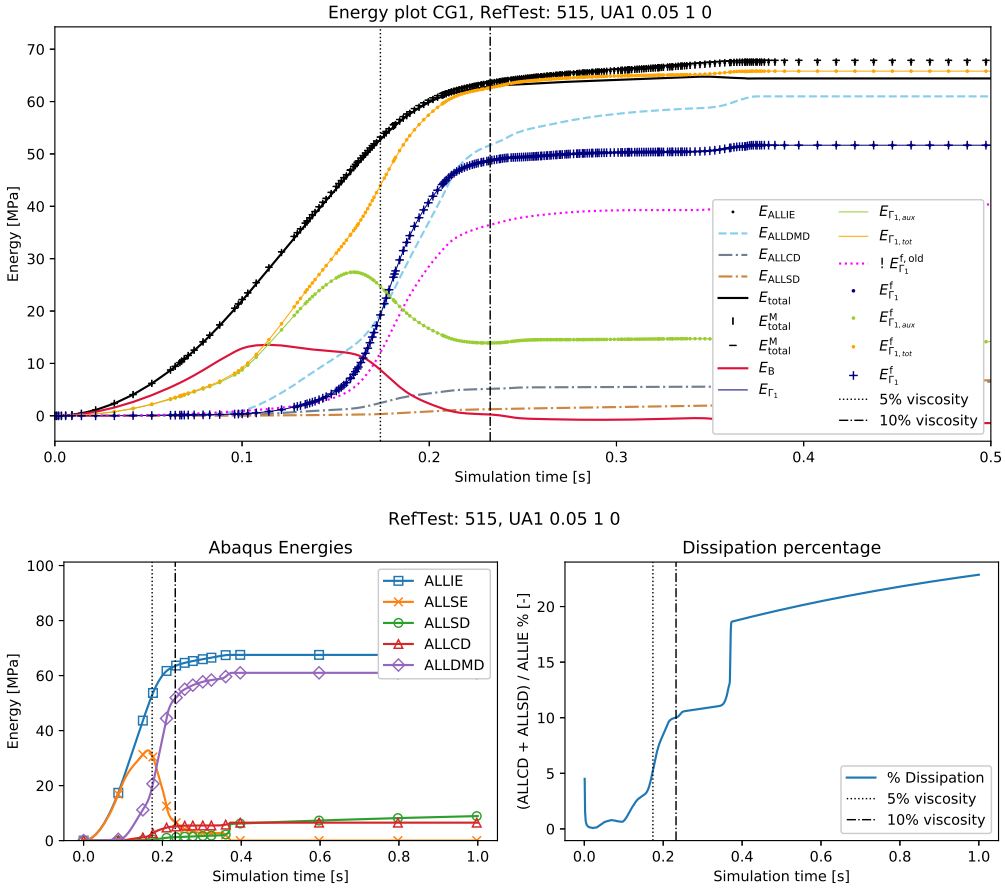

Figure 6.20: Energy plot test #515 (UA1 with domain size 50 μm, gridsize 1 μm).

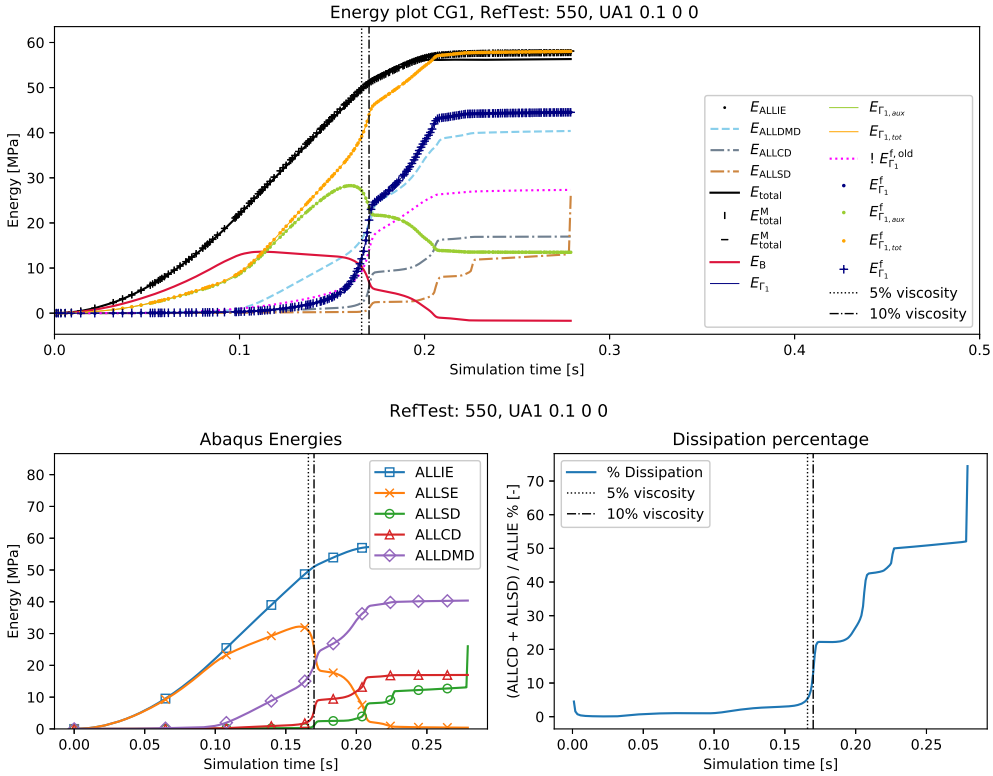

Figure 6.21: Energy plot test #550 (UA1 with domain size 100 μm, gridsize 1 μm). Analysis stop at $t = 0.29s$.

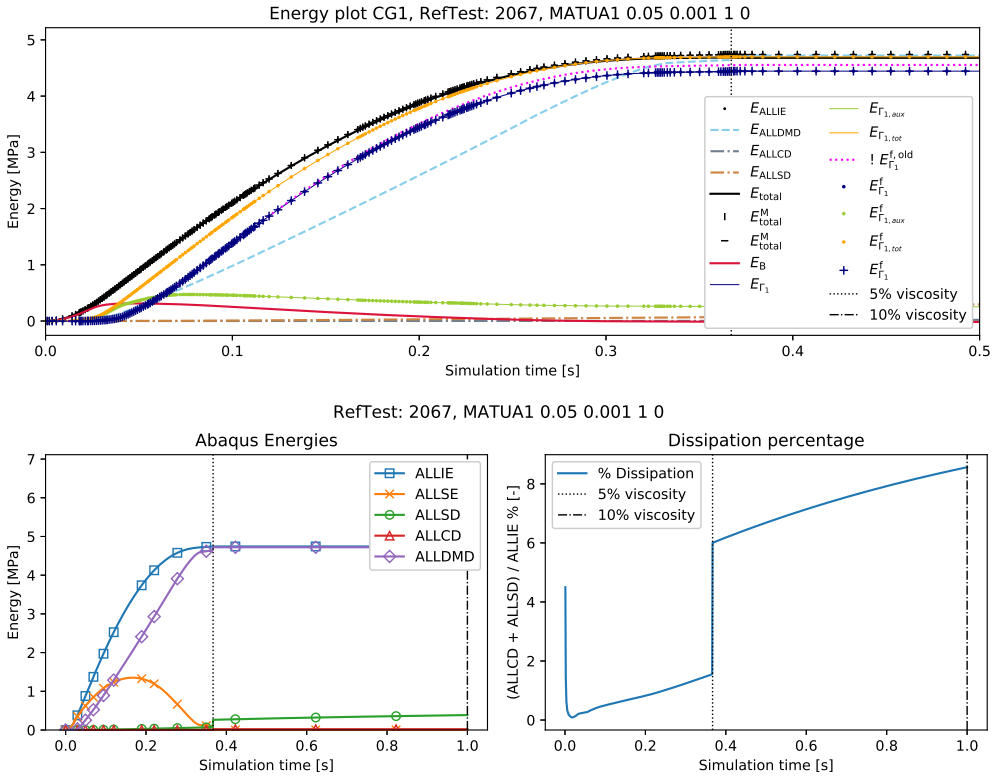

Figure 6.22: Energy plot test #2067 (MATUA1 with domain size 50 μm, gridsize 1 μm).

6.6. Multi-crack TSLs for biaxial loading

In section §4.3.2, it was described that the new algorithm could detect individually propagating cracks in domains displaying multiple differentiated cracks. This detection is possible in biaxial loading modes, where the two propagating cracks have clear and distinct orientations.

Using the previously shown test #32 featuring biaxial loading (crack recognition in figure 4.19), two power curves and ETSLs can be extracted. In both plots, it is possible to appreciate how the vertical crack CG2, which goes through the longitudinal fibers, is the one dissipating the most energy. In comparison, crack CG1 (horizontal crack going through matrix and interface) dissipates a small quantity of power. This difference among cracks is reflected as well in the ETSLs, where CG2 opens at a much higher traction level. As the quantity plotted in the *y* axis corresponds to the norm of the traction vector, it is important to remark that the orientation of the tractions is very similar to the orientation of the normal vectors of the cracks.

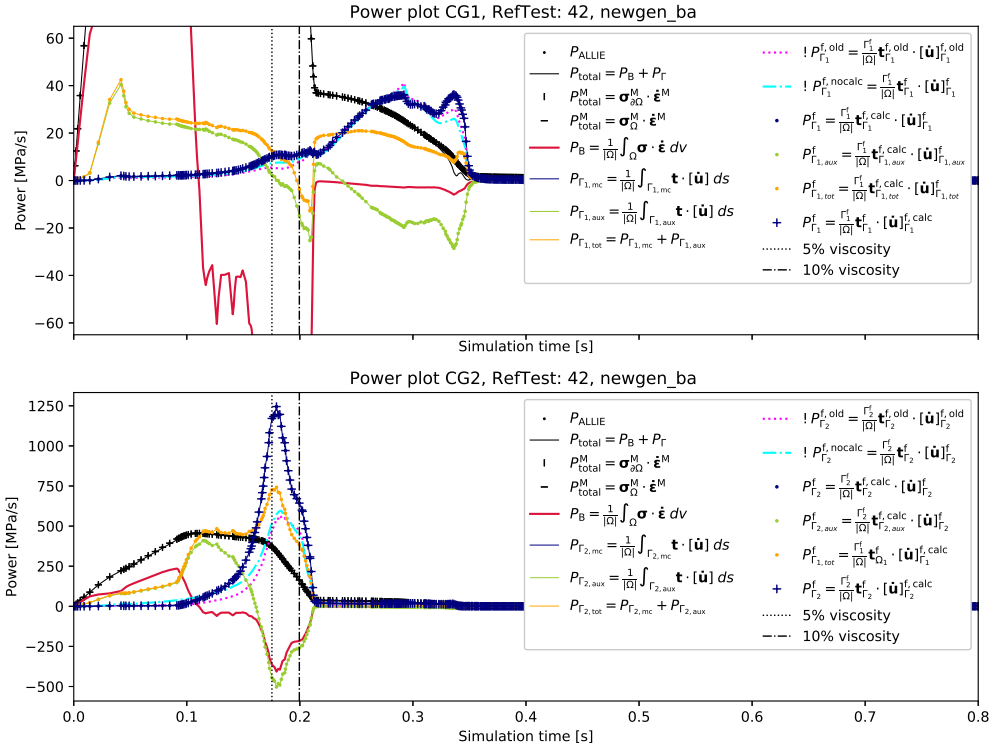

Figure 6.23: Power plots test #42 (biaxial loading). The diagram on top is magnified to see the power contributions of crack group 1 (CG1), which are very small in comparison with the total power and the crack group 2 (CG2, going through the [90] fibers) power.

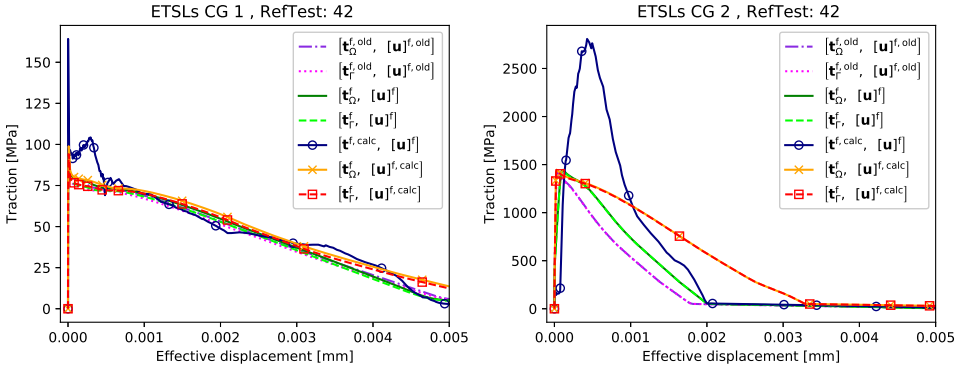

Figure 6.24: ETSLs test #42 (biaxial loading), presenting the individual ETSLs for CG1 (matrix crack) and CG2 (crack through the fibers).

6.7. Verification remarks

From the obtained results it is considered that the displacement calculated curves (effective set $\left[\mathbf{t}^{\mathrm{f}},\ [\![\dot{\mathbf{u}}]\!]^{\mathrm{f,calc}}\right]$) would be more reasonable, simple and stable for the macro-scale implementation. These curves are not as sensitive to the occurring artificial compliance and present less numerical problems. This conclusion may not be valid for other frameworks not featuring a cohesive intrinsic implementation.

Additionally, several problems hinder the obtention of valid results. From a numerical point of view, convergence is difficult to achieve. It is identified that the large contributions of viscous energy required to conduct the analysis prevent convergence over the full scope of the TSL. From a modeling point of view, the application of PBCs may not be suitable to study crack propagation and fracture energies.

6.8. Multi-angle TSLs for uniaxial loading

By combining the average ETSLs for different angles, it is possible to obtain an anisotropic ETSL for uniaxial loading. This can be seen in figure 6.25. Linear interpolation has been used between the ETSLs.

It can be appreciated how the maximum tensile stresses decrease as the force orientation approaches 90°. The sudden drop in the 77.5° case is explained by the creation of a crack not going through the fibers but parallel to them. Tests with loading orientation 67.5° were considered. In these cases, two cracks were formed: one through the fibers and one parallel to them. However, due to the opening sequence, the cracks could not be separated automatically into crack groups 1 and 2.

Moreover, a closer analysis of the averaged ETSLs for the 22.5° and 77.5° angles revealed an inconsistency on the final orientation of the cracks. This issue is covered in section §6.9.

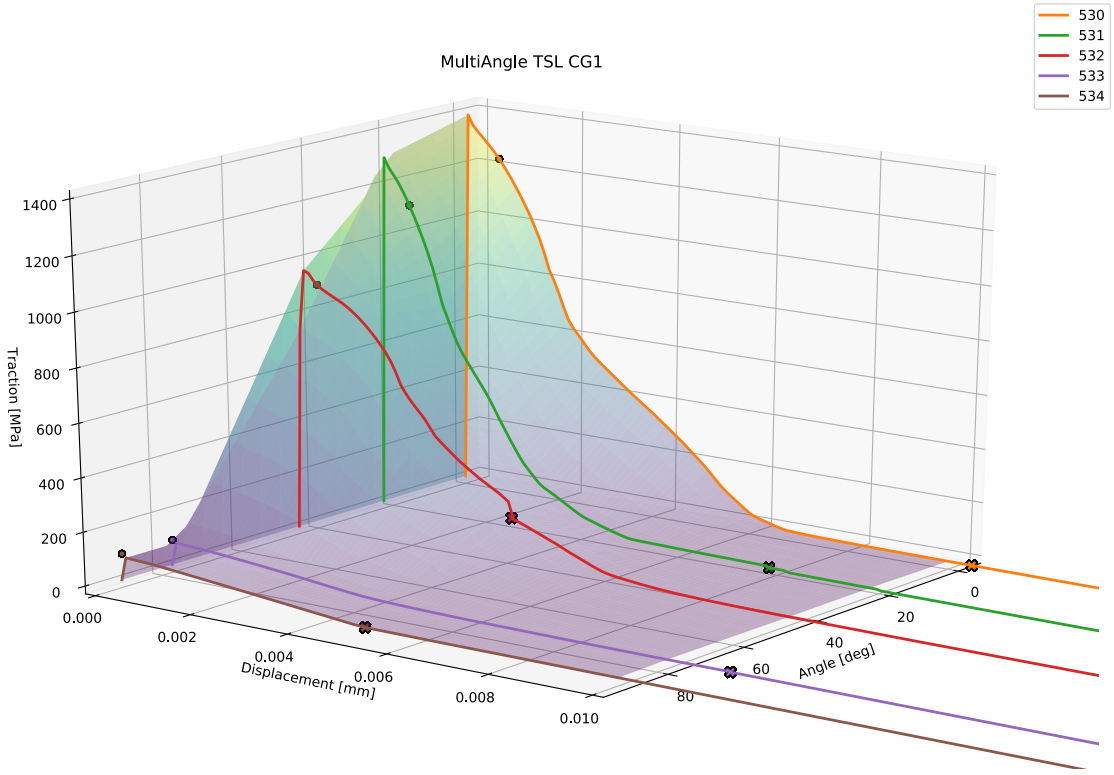

Figure 6.25: Multi-angle TSL. The averaged ETSLs are shown for uniaxial tension under several angles: $\theta = 0°,\ 22.5°,\ 45°, 77.5°, 90°$.

6.9. Crack orientation dependence on RVE dimensions and PBCs

In previous works [94], periodic boundary conditions have been considered to allow sufficient freedom to enable crack nucleation and propagation in arbitrary orientations. While this is applicable for the nucleation, it may not be so for the propagation. Simulations confirm that the crack nucleation and initial propagation occurs in the arbitrary direction most favored by the geometry and the loading conditions. However, results also show that PBCs tend to favor orientations that result in periodicity, which are dependent on the dimensions of the RVE. For instance, in the case of squared domains, 0°, 45° and 90° orientations are promoted.

The presence of longitudinal fibers ([90] phase) under loading modes not aligned with the orthotropic directions of the material highlight the dependency of the crack orientation with the RVE dimensions due to the application of PBCs. Simulations showed that fibers do not break twice in different points. Thus, under specific loads/orientations, "natural" fully periodic cracks may never be obtained.

Tests featuring 22.5° uniaxial tension are used to show the RVE and PBC crack path dependency. In figure 6.26, the UA1 22.5° tests used for the multi-angle TSL are plotted for a domain size of 100 μm. In the four repetitions of the test, it can be seen how two generate a full periodic crack in the promoted direction (0°), and how the other two generate a 22.5° not fully periodic crack. In smaller domains, the promoted direction has even more influence.

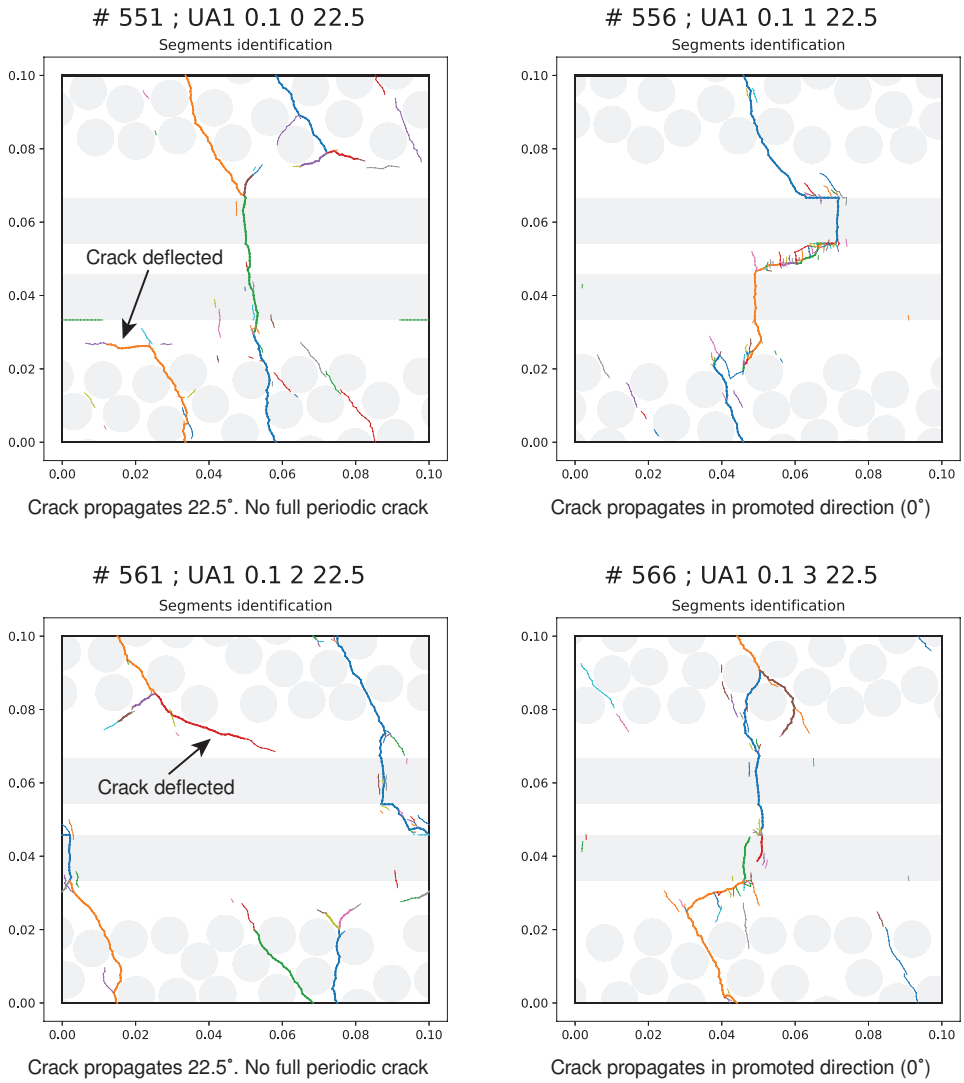

Figure 6.26: Uniaxial 22.5° tests #551, #556, #561, #566. Four repetitions with different fiber distributions are performed.

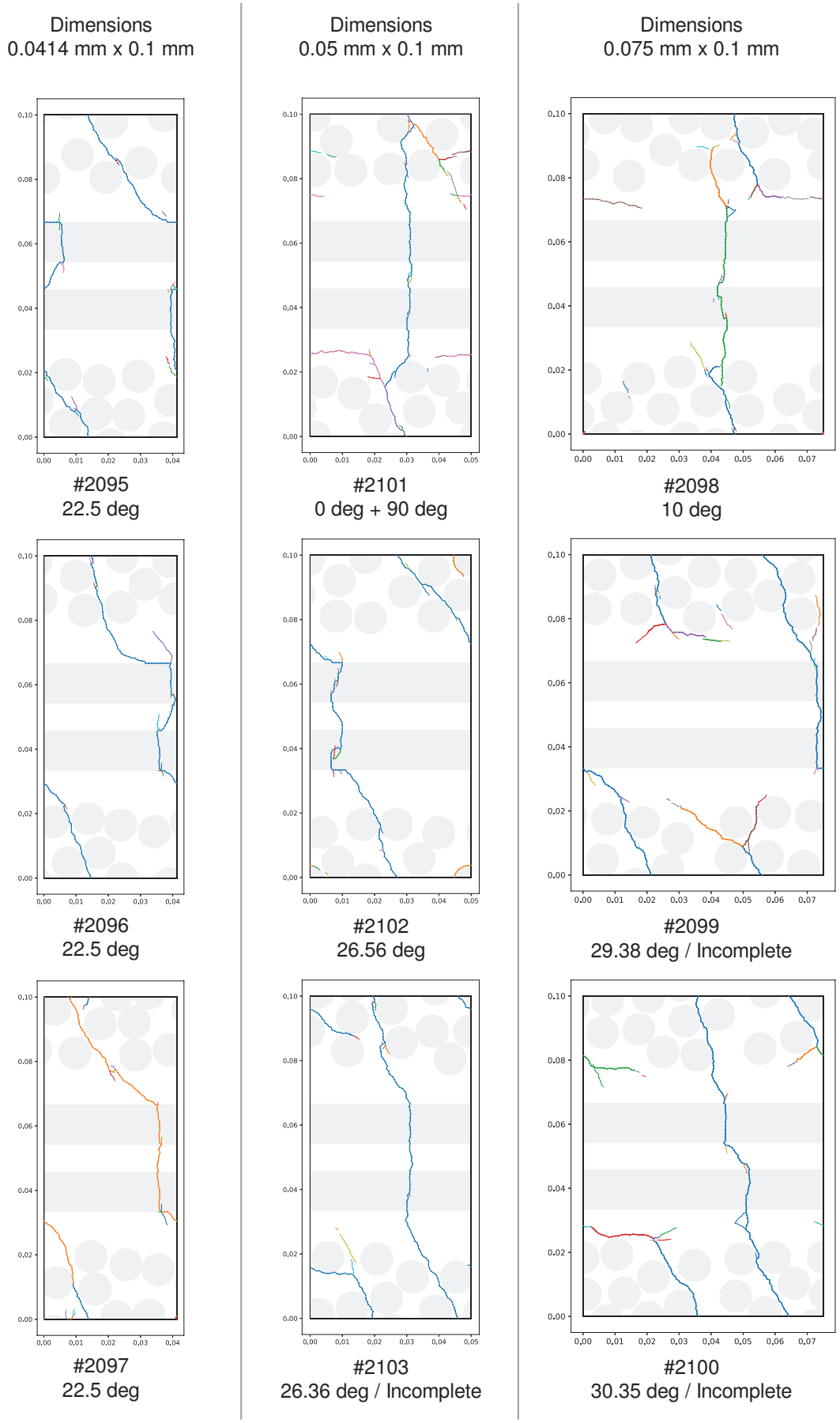

Figure 6.27: Uniaxial 22.5° tests with different RVE aspect ratios.

The influence of the aspect ratio of the RVE in the crack orientation and length can be seen in figure 6.27, where more UA 22.5° cases are presented. The leftmost column displays RVEs with dimensions specially tailored to favor the propagation of a 22.5° crack, which the loading conditions favor (UA 22.5°). In the middle column, however, the RVE dimensions give preference to the 0°, 90° and 26.56° orientations. This is seen in the crack patterns: test #2101 features a complete vertical 0° crack plus a horizontal 90° incomplete crack. Tests #2102 and #2103 display cracks in the favored direction. Finally, in the rightmost column, it is possible to observe a vertical 0° crack (#2098), and incomplete periodic cracks (#2099, #2100) deflected upon the second fiber crossing. From these results, dependency can be found on the aspect ratio of the RVE.

Moreover, similarly to the visualizations presented in [94], in figure 6.28 the domain (A) has been decomposed to show two equivalent crack domains (B, C). In the diagrams, it can be seen how the effective crack domain fails to represent a full periodic crack. Moreover, in (B) the deflection of the crack when approaching the top and bottom fibers is evident. This is problematic, as the lack of a proper full periodic crack under arbitrary loads compromises the argumentation to use PBCs after fracture localization.

These results show that the introduction of micro-fluctuations in the domain borders does not entail per se that the domain is periodic from a fracture point of view. Although the periodic boundary conditions introduce stresses in the domain due to their multi-point constraints, they do not introduce a stress field in the domain that yields in a consistent and natural periodic fracture pattern under arbitrary loading. Instead, the PBCs alter the orientation of the crack and create artificial periodic crack openings, thus distorting the averaging of the quantities by effectively enlarging the crack path and thus the weight of the [0] phase.

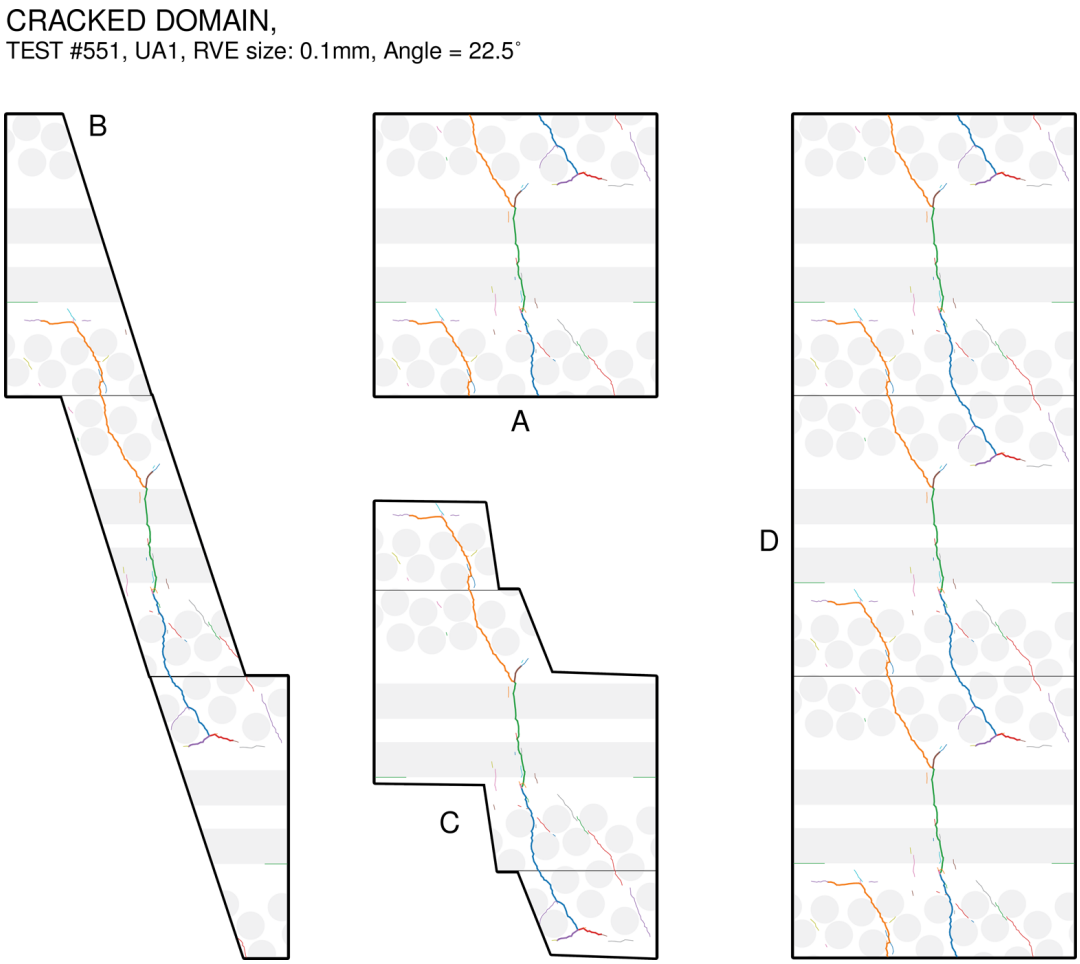

Figure 6.28: A: Original cracked domain. B and C: equivalent crack domains. D: stacked RVEs.

The phenomenon was then tested using homogeneous matrix domains ($V_f = 0\%$) to isolate the influence of the longitudinal fibers ([90] phase) and the heterogeneity of the [0] phase. The results, shown in figure 6.29 reflect a clear alignment of the cracks towards the PBC promoted orientations (0°, 90°, 45° for the squared domains). This is visible in tests #20994 (UA1 10°) and #20998 (UA1 40°), where the cracks are attracted towards the 0° and 45° promoted orientations respectively.

The tests #20995 (UA1 20°), #20996 (UA1 26.56°), #20997 (UA1 30°) produce a more complex crack pattern, but follow the same principle. In the cases #20996 and #20997, more complex pattern origins, but the multiplication of the periodic domain, shown in figure 6.30, clearly shows that the crack aligns with the 45° and 0° orientations, finally forming a 45° periodic crack.

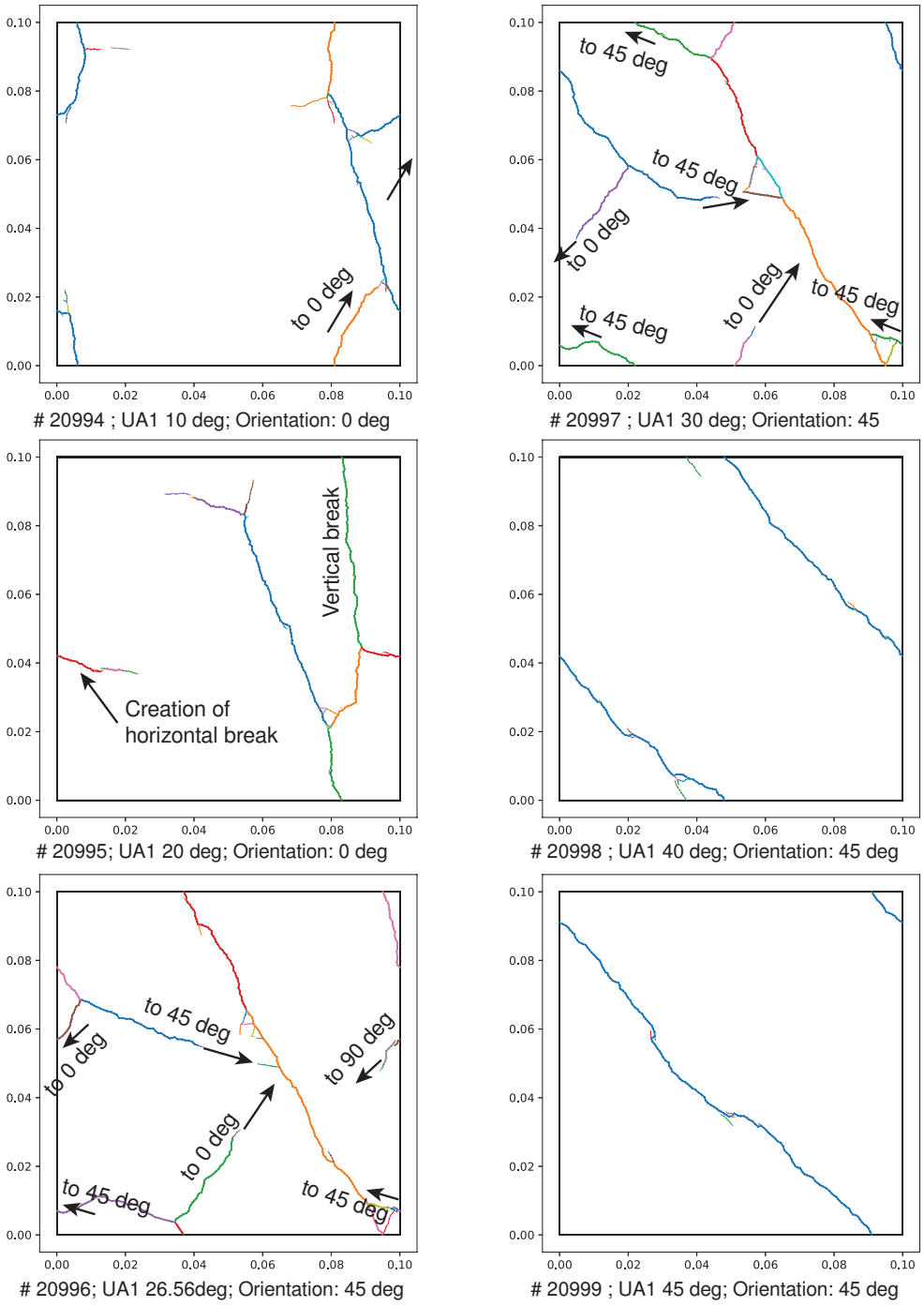

Figure 6.29: Uniaxial test with variable angle loading for a homogeneous matrix domain.

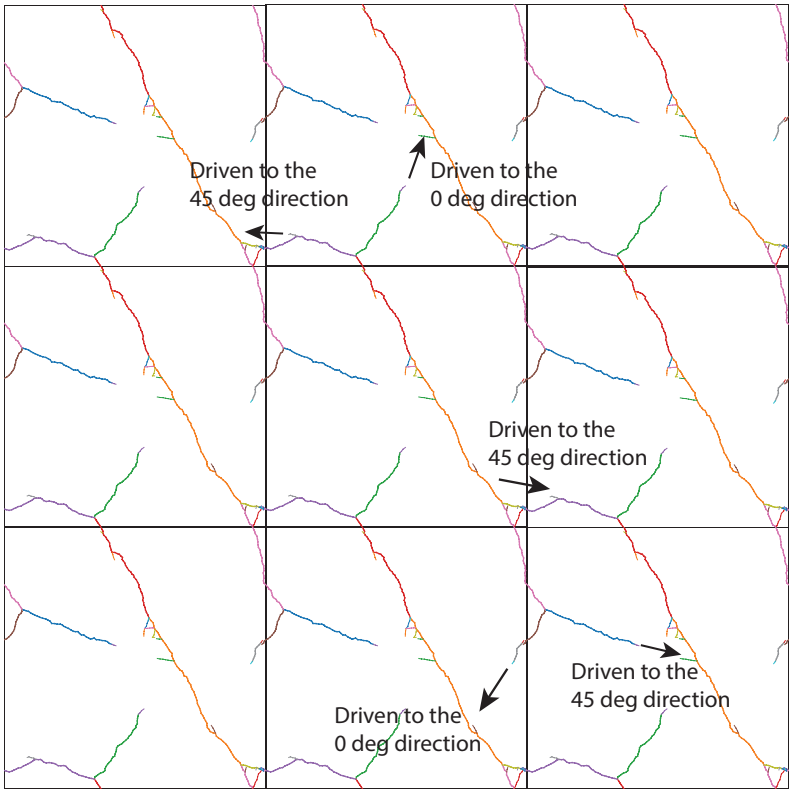

Figure 6.30: Test #20996 (UA1 26.56°). Periodic fractured domain.

The crack propagation dependence on the periodic boundary conditions (PBCs) and the domain aspect ratio has several implications on the current and past work. Overall, results indicate that PBCs, as implemented here, influence and constrain the crack propagation orientations. Their application results in cracks propagating in a set of promoted orientations, which vary in function of the domain aspect ratio. As far as simulations show, and under the current implementation, PBCs should not be used upon damage localization under arbitrary loads and domain geometries, as natural cracks are not obtained in general cases.

The problem lies not in the creation of parallel cracks, but on the loss of loading after the localization of the first fracture plane. This hinders the creation of a full periodic crack in the natural orientation. This observation is consistent with the remark about PBCs in [67]. The simulation of a periodic domain under PBCs as here implemented will not deliver such a crack for cases involving multiple fracture planes and arbitrary domain sizes.

Overall, the absence of a full periodic crack compromises the applicability of the post-processing methodology. It is important to remark that the post-processing methodology is considered to remain entirely valid. However, the post-processing methodology relies on the input of a fully periodic crack, this is an essential condition for its applicability. The complete set of effects of this evidence in the theory has not been fully explored, as the crack orientation dependence was studied at the end of the project. Yet, this issue would invalidate the analysis in those cases in which the crack normal is not 90°, 45° or 0° (in squared RVEs). Furthermore, the current modeling of the fibers does not include a statistical description of its defects. If this was to be modeled, the PBCs could affect the crack propagation through the matrix by introducing artificial crack paths connecting the periodic boundary crossings, even in the 0° case.

Most of the given examples in this thesis correspond to uniaxial tension in which the crack orientation coincides with the orientation promoted by the PBCs. These results are not expected to be highly influenced by this phenomenon. Again, the post-processing methodology is considered still entirely valid, although the implementation built for feeding it with fully periodic cracks is considered compromised. Still, many of the developed methods covered in the methodology and the numerical implementation can be useful in other situations and applied with other kinds of BCs enforced.

7

New Material Properties

As part of the study, an extensive effort has been made to gather and use material properties which are representative of the material. With this objective, several material properties have been extensively searched in the literature. While some information in this regard was available from the previous studies, several of the properties used in previous research had a relative nature, this is, had been selected to provide a qualitative behavior. Moreover, other material properties, like the fiber fracture energy were two orders of magnitude higher than values reported in the literature. While these choices simplify the development and interpretation of results, they hinder the validation process by providing results which cannot be contrasted with any experiments.

The materials chosen for the study are HexTow IM7 carbon fibers and HexPly 8552 epoxy matrix. This combination is chosen as it is a common combination and common material and experimental data are readily available in the literature. It must be remarked that all the material properties here gathered are obtained from material specifications or journal articles. No experimental material characterization has been performed as part of this research, and such exercise is not envisioned within the scope of this thesis.

7.1. New material parameters

7.1.1. Carbon Fibers: HexTow IM7

The material properties for the IM7 carbon fibers are summarized in table 7.1. The elastic properties are taken from [10, 37]. Fracture properties were much more difficult to obtain, as the fracture toughness and the strain energy release of single carbon fibers are extremely difficult to measure. Since the strain energy release rate of a single IM7 fiber could not be found, this property is evaluated based on the literature.

Herráez et al. [35] investigates fracture toughness in different structural fibers my means of the focused ion beam (FIB) technique, obtaining $K_{Ic} = 2.12\ \text{MPa}\,\text{m}^{1/2}$ and $G_{Ic} = 52\ \text{J/m}^2$ for AS4 carbon fibers. The strain energy release rate is obtained via a numerical J-integral along the crack contour in a FEM model. These fracture toughness values are in the same order to the ones presented by Naito [65] ($K_{Ic} = 1.82\ \text{MPa}\,\text{m}^{1/2}$ for IMS60 carbon fibers, $K_{Ic} = 1.91\ \text{MPa}\,\text{m}^{1/2}$ for T1000GB carbon fibers). Moreover, Naito [65] suggests a linear relationship between the tensile modulus E_1 and the fracture toughness K_{Ic}. Based on this, a $K_{Ic} = 1.8$ is selected for the IM7 fibers. By using the relation by Sih et al. [82] (7.1)[1], the strain energy release rate can be calculated for an orthotropic solid. This results in a strain energy release rate for IM7 fibers $G_f = 24.4\ \text{J/m}^2$, as showed in table 7.1. This value is more than two orders of magnitude lower than the previously used value $G_f = 7500\ \text{J/m}^2$.

$$G_{I(\text{orthotropic})} = K_I^2 \sqrt{\left(\frac{a_{11}a_{22}}{2}\right)\left(\sqrt{\frac{a_{11}}{a_{22}}} + \frac{2a_{12}+a_{66}}{2a_{22}}\right)} \tag{7.1}$$

$$a_{11} = \frac{1-\nu_{12}\nu_{21}}{E_1} \qquad a_{22} = \frac{1-\nu_{21}\nu_{12}}{E_2} \qquad a_{12} = -\frac{\nu_{21}\,(1-\nu_{23})}{E_1} \qquad a_{66} = \frac{1}{G_{12}} \tag{7.2}$$

[1] Relation as written in [35, 40]. It is suspected that the material indexes used in [65] are switched and result in a large overestimation.

Table 7.1: **IM7 fiber properties**. Material properties obtained from [10, 37]. Fracture properties obtained from [37] and calculated based on the data and methods in [35, 65].

ρ (g/cm^3)	E_1 (GPa)	E_2 (GPa)	E_3 (GPa)	ν_{12}	ν_{13}	ν_{23}	G_{12} (GPa)	G_{13} (GPa)	G_{23} (GPa)
1.78	276	19	19	0.2	0.2	0.35	27.6	27.6	27.6

$\varnothing$ (µm)	t_{ult} (MPa)	G_f (J/m^2)	d_f (mm)	E_{coh} (GPa)
5.2	5150	24.4	1.679×10^{-6}	1×10^6

7.1.2. Matrix: HexPly 8552 Epoxy Resin

The HexPly 8552 Epoxy Resin material properties are obtained from the manufacturer specifications [36]. However, the fracture strain energy release rate presented in the specification raises doubts: no information is available about the testing method used, and the value is six times higher than others found in the literature [68]. Moreover, this parameter is only given in the US version of the specification, and cannot be found in the EU/metric version. A review of the literature shows a large range (40 to 400 J/m^2) of values for this parameter for different epoxy resins [4, 41, 68]. Thus, it is chosen to take $G_f = 100$ J/m^2 as presented in [64, 68].

Table 7.2: HexPly 8552 properties. Obtained from [36]

ρ (g/cm^3)	E (GPa)	ν	t_{ult} (MPa)	G_f (J/m^2)	d_f (mm)	E_{coh} (GPa)
1.3	4670	0.35	121	100	5.61×10^{-3}	1×10^6

7.1.3. Interface: IM7/8552

Since experimentally obtained properties could not be found for IM7/8552, AS4/8552 properties are used. Fracture in the interface is modelled using the Benzeggagh-Kenane (BK) criterion. Thus, fracture energies are different for normal and shear loading, but both contribute towards the damage evolution. The material properties are obtained from [68].

Table 7.3: Interface AS4/8552 properties. Obtained from [68].

t_n (MPa)	t_s (MPa)	$E_{coh,n}$ (GPa)	$E_{coh,s}$ (GPa)	$G_{f,n}$ (J/m^2)	$G_{f,s}$ (J/m^2)	η_{BK}
42	64	100	100	2	100	1.2

7.2. Parametric study to determine E_{COH} and η

In order to establish the cohesive stiffness (E_{COH}) and the artificial regularization parameter (η) for the new set of material properties, a parametric study was conducted (see table 7.4). As part of the study, the convergence, the number of iterations and the presence of numerical errors were evaluated.

Several values were tested to determine suitable values for the cohesive stiffness. Very high values ($E_{\mathrm{COH}} > 10^{11}$) resulted in errors in Abaqus (excesive distortion), coupled with an inability to carry the analysis on the larger domains. Besides, low values ($E_{\mathrm{COH}} < 10^9$) resulted as well in premature analysis stoppage. It was found that for the new material properties, the previous cohesive stiffness $E_{\mathrm{COH}} = 10^8$ was insufficient for the [0] fiber phase, since all the fracture energy was contained within the elastic region. In figure 7.1, the fracture energy stored before failure is highlighted in green, and can be calculated as (7.3). In order for the TSL to be consistent, $G_{f,\,\mathrm{undamaged}}$ shall be lower than the total fracture energy G_f, which in the case of the fiber phase can be expressed as (7.4). However, after solving (7.3) for condition (7.4), it is obtained that the cohesive stiffness E_{COH} shall be over $5.435 \cdot 10^8$ MPa. Thus, the previously used cohesive stiffness $E_{\mathrm{COH,old}} = 10^8$ MPa is unsuitable for the new material parameters.

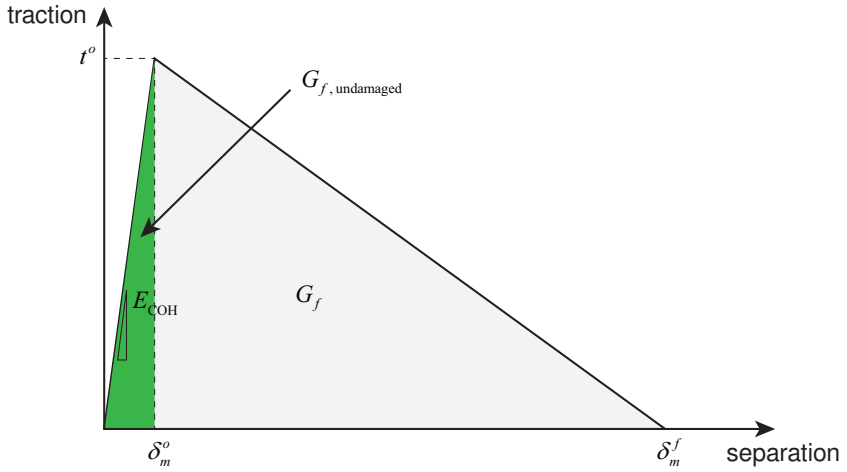

Figure 7.1: Material TSL, with the undamaged G_f highlighted.

$$G_{f,\text{undamaged}} = \frac{1}{2}\delta_m^o\, t^o = \frac{1}{2}\left(\frac{t^o}{E_{\text{COH}}}\right) t^o = \frac{1}{2}\cdot\left(\frac{5150}{E_{\text{COH}}}\right)\cdot 5150 \tag{7.3}$$

$$G_{f,\text{undamaged}} < 0.0244 \tag{7.4}$$

$$E_{\text{COH}} > 5.435\cdot 10^8 \tag{7.5}$$

Moreover, the parametric study also concluded that insufficient viscous regularization resulted in a higher number of increments required to complete the analysis, or in more extreme cases ($\eta < 10^{-6}$), in an inability to converge. An excess of viscous regularization ($\eta > 10^{-4}$) implied unrealistic results, thus having to be avoided as well.

Table 7.4: Parametric study to establish E_{COH} and η values for the new material parameters. Number of increments between parenthesis. Red = analysis failed. Green = analysis converged. Yellow = analysis converged with problems.

# Test	Status	Description	Size	Visc (η)	E_{COH}	
1035	Failed	UA1NM 0.025 0.001 3 0 EC2 NewECOHR3	0.025	1.00E-05	1.00E+08	SMALL E_{COH} Invalid Material TSL
1036	Failed	UA1NM 0.025 0.001 3 0 EC2 NewECOHR3 visc4	0.025	1.00E-04	1.00E+08	
1041	Failed	UA1NM 0.025 0.001 0 0 EC2 E9 v-4	0.025	1.00E-04	1.00E+09	
1042	Failed	UA1NM 0.025 0.001 0 0 EC2 E9 v-5	0.025	1.00E-05	1.00E+09	
1043	Failed	UA1NM 0.025 0.001 0 0 EC2 E9 v-5	0.025	1.00E-06	1.00E+09	
1039	**Good (1780)**	**UA1NM 0.025 0.001 0 0 EC2 E10 v-4**	**0.025**	**1.00E-04**	**1.00E+10**	
1028	**Good (1806)**	**UA1NM 0.025 0.001 3 0 EC2 NewECOHR2**	**0.025**	**1.00E-05**	**1.00E+10**	
1045	Failed	UA1NM 0.025 0.001 0 0 EC2 E10 v-5 NoAutoSta	0.025	1.00E-05	1.00E+10	
1040	Good (3458)	UA1NM 0.025 0.001 0 0 EC2 E10 v-6	0.025	1.00E-06	1.00E+10	
1044	Failed	UA1NM 0.025 0.001 0 0 EC2 E10 v-7	0.025	1.00E-07	1.00E+10	
1047	**Good (2.5 days)**	**UA1NM 0.075 0.001 0 0 EC2 E10 v-4**	**0.075**	**1.00E-04**	**1.00E+10**	
1046	**Good (2.5 days)**	**UA1NM 0.075 0.001 0 0 EC2 E10 v-5**	**0.075**	**1.00E-05**	**1.00E+10**	
1027	Good (9188)	UA1NM 0.025 0.001 3 0 EC2 NewECOHR1	0.025	1.00E-05	1.00E+11	
1034	Good (7244)	UA1NM 0.025 0.001 3 0 EC2 NewECOHR1 visc4	0.025	1.00E-04	1.00E+11	
1037	Failed - Distortion (21885)	UA1NM 0.075 0.001 0 0 EC2 NewECOHR1 visc4	0.075	1.00E-04	1.00E+11	
1020	Failed	UA1NM 0.025 0.001 3 0 EC2 NewECOH visc-10	0.025	1.00E-10	1.00E+12	HIGH E_{COH} Numerical Problems
1026	Failed	UA1NM 0.025 0.001 3 0 EC2 NewECOH visc-6	0.025	1.00E-06	1.00E+12	
1019	Good - Distortion at end	UA1NM 0.025 0.001 3 0 EC2 NewECOH	0.025	1.00E-05	1.00E+12	
1025	Good (9236)	UA1NM 0.025 0.001 3 0 EC2 NewECOH visc-4	0.025	1.00E-04	1.00E+12	
1021	Failed - Too much viscosity	UA1NM 0.025 0.001 3 0 EC2 NewECOH visc-2	0.025	1.00E-02	1.00E+12	

7.3. Discussion of the simulation results

From the parametric study, it was concluded that $E_{COH} = 10^{10}$ and $\eta \in [10^{-4}, 10^{-5}]$ rendered themselves as valid parameters (test references #1028, #1039, #1046 and #1047). Moreover, the new weaker interface properties promoted the natural appearance of delaminations, visible in figure 7.3.

The simulations, however, presented multiple difficulties. Firstly, it must be remarked that the label "good" in table 7.4 does not indicate full analysis completion, but completion until a point after the fracture process has occurred (crack initiated and opened). For instance, most of the carried "good" simulations did not go over 40% of the analysis time. Secondly, the new fiber fracture energy $G_f = 0.024$, two orders of magnitude smaller than the previously used value [39], entailed a much more violent failure behavior. Besides, this violence involved an immediate enormous contribution of ALLSD (automatic stabilization) over 2000% of the total energy ALLIE. Thirdly, the simulations had large computational cost (≈2.5 days, 4 cores) when compared to the same domain size but using the previous material properties (≈8 hours, 4 cores).

All these reasons, coupled with the fact these new material properties were gathered in the latter stages of the research, lead to demonstrate the new post-processing algorithms and capabilities using the by the time already carried simulations using the previous material properties. Nevertheless, these results constitute a wake-up call which may serve as starting point for an evaluation of the applicability of the present multiscale strategy, or the reformulation of its current implementation for the simulation of very brittle materials.

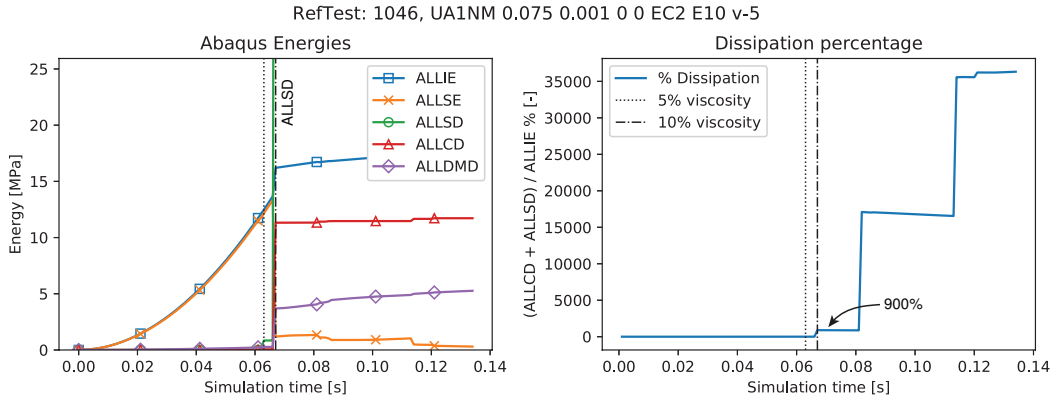

Figure 7.2: Abaqus energies and viscous dissipation for test #1046. Markers displayed for line identification.

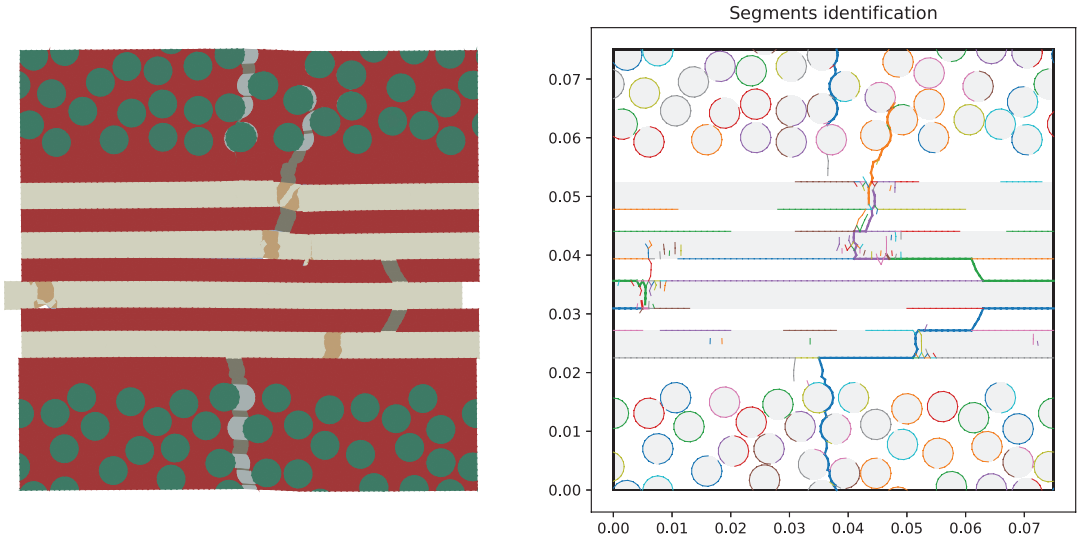

Figure 7.3: Test #1046 fracture pattern and crack recognition. The new material properties showcase delaminations and fiber/matrix debonding.

8

Conclusions and Recommendations

8.1. Conclusions

The use of multiscale simulations provides a natural and seamless way to study composites while avoiding phenomenological approaches and reducing experimental testing. By modeling fracture physics at their relevant scale, valuable understanding of how cracks initiate and propagate can be obtained. This knowledge, in the long term, will become essential for the design of damage tolerant aerostructures, and critical to realize the full potential of composite materials, leading to major weight and cost savings, and environmental benefits for society.

This thesis presents an extension of the multiscale framework by Turteltaub et al. [94] for its application in the study of fracture involving combined failure mechanisms in anisotropic microstructural domains, and for the determination of effective traction-separation laws (ETSLs). The method generates effective macroscopic quantities by homogenizing microscopic volume elements experimenting fracture, while complying with the Hill-Mandel condition, thus keeping energy and power equilibrium between scales.

The microstructural geometries are generated in Python and later meshed using Gmsh. A new subroutine was written in Gmsh to efficiently apply the PBCs without the need of calculating all the intersections between the fibers and the domain edges. With the mesh ready, cohesive elements are embedded in between all the elements to simulate the potential crack surfaces, allowing arbitrary crack nucleation and propagation through the domain. Additionally, this scheme also models the coalescence and branching of the cracks. Subsequently, FEM analyses are performed using Abaqus (standard), and the post-processing is executed using Python and the Abaqus scripting interface. Products are ETSLs, fracture patterns, and power and energy dissipation plots.

A revision of the methodology and its implementation was performed. New post-processing algorithms have been developed that supersede the Singular Value Decomposition (SVD) method and the method of projection of normals. The proposed algorithms detect and group the crack segments, and consistently reorientate their normal vectors. Multiple crack identification has been achieved, thus allowing ETSLs generation for each crack. Additionally, a new relation is proposed for the calculation of the effective opening of the crack, which results in a geometrically accurate opening value.

Moreover, the development of new homogenization algorithms allowed a critical assessment of the previous relations. It was found that previous effective parameters, based solely on averaging and scaling of the crack quantities, do not precisely comply with Hill-Mandel in general cases. The non-compliance aggravates in the case of anisotropic domains. Thus, two different ways to generate ETSLs while satisfying the Hill Mandel condition have been proposed and compared: traction-based and opening-based homogenization. Results show that in isotropic-like domains (involving fracture in only the matrix and the interface) both approaches yield similar values. However, in anisotropic domains (involving fiber fracture) both ETSLs calculation approaches diverge. Based on the observations, fixing the tractions and calculating the displacements using the Hill-Mandel energy balance (traction-based homogenization), is deemed as the most reasonable way to obtain ETSLs for the macro scales.

A verification and convergence study was carried. The proposed homogenization methods were success-

fully verified for Hill-Mandel compliance under uniaxial, shear, biaxial and mixed loading cases. Furthermore, a mesh and RVE size convergence study was performed for the uniaxial loading case. Results show a limited convergence of the [0,90,0] models in uniaxial tension as a result of the massive quantities of viscous artificial energy used by Abaqus. This problem aggravates as the domain size is enlarged. Moreover, comparisons show a worse convergence behavior of the highly anisotropic [0,90,0] domains with respect to models uniquely displaying matrix/interface fracture (e.g. [0] domains).

Finally, the study of the fracture patterns under different angles and conditions raised doubts about the application of periodic boundary conditions in the framework. Simulation results pointed to the periodic boundary conditions influencing the orientation of the crack paths, driving them to the promoted directions by the domain geometry. This compromises the multiscale framework since the post-processing methodology requires fully periodic cracks which cannot be delivered using the current implementation.

8.2. Recommendations

Several milestones have been achieved during this thesis; however several issues remain open and shall be addressed in the future. Thus, the following recommendations are issued:

R1: Reconsider the applicability of periodic boundary conditions in the current multiscale framework: the first and most important activity shall study more in depth the influence of periodic boundary conditions on the results, and explore possible alternatives to the present situation described in section §6.9. This may include changing the boundary conditions, modifying the post-processing, or revising the framework, choosing for another kind of scheme (e.g., concurrent).

R2: Correct the overlapping of crack surfaces: currently contact is lost when a large tangential displacement occurs between the cohesive elements' faces. This should be fixed by defining a contact relation in the whole crack front. Moreover, friction between the crack surfaces could be added at this point.

R3: Reduce the required viscous dissipation: when fibers break, the injected amount of viscous energy by the automatic stabilization and the viscous regularization is huge. If the results are intended to be quantitatively valid, the contribution of this energy should be reduced below 5%. This is especially critical if the "new" material properties presented in chapter §7 are to be used.

R4: Improve the crack identification algorithm: the newly built crack identification algorithm still needs to be perfected to recognize very complex crack patterns. The use of machine learning methods or more advanced algorithms may be interesting to improve the crack recognition.

R5: Explore other damage initiation and evolution models: currently, simple damage initiation and evolution models are chosen. Other models should be explored and compared (e.g., QUADS for damage initiation, and BK for mode-dependent damage evolution).

Further research topics that would be interesting to address would be:

R6: Validation activities: so far, validation with experiments has not been performed yet. Such a comparison would be useful to raise the confidence level of the framework and refine the material properties and models.

R7: Investigate and model fiber pullout correctly. So far, fiber pullout occurs in certain simulations, triggered by mesh considerations and not by a statistical modeling of the fibers' imperfections. Thus, proper modeling of the fibers defects together with a larger number of fibers would allow modeling fiber pullout correctly.

R8: Extend the framework to 3D. This would allow a more realistic modeling of the transversal phase. Moreover, the composite failure sequence and mechanisms could be captured with more accuracy. However, this is highly dependent on the unlocking of **R1** and the definition of proper boundary conditions for the three-dimensional domain.

Bibliography

[1] F. F. Abraham, D. Brodbeck, W. E. Rudge, J. Q. Broughton, D. Schneider, B. Land, D. Lifka, J. Gerner, M. Rosenkrantz, J. Skovira, and H. Gao. Ab initio dynamics of rapid fracture. *Modelling and Simulation in Materials Science and Engineering*, 6(5):639–670, September 1998.

[2] M. V. C. Alfaro, A. S. J. Suiker, and R. de Borst. Multiscale Modelling of the Failure Behaviour of Fibre-Reinforced Laminates. In R. de Borst and E. Ramm, editors, *Multiscale Methods in Computational Mechanics: Progress and Accomplishments*, pages 233–259. Springer Netherlands, Dordrecht, 2011. ISBN 978-90-481-9809-2.

[3] T. L. Anderson. *Fracture mechanics: Fundamentals and Applications*. CRC Press, 3rd edition, 2005. ISBN 9781420058215.

[4] E. H. Andrews and A. Stevenson. Fracture energy of epoxy resin under plane strain conditions. *Journal of Materials Science*, 13(8):1680–1688, August 1978. ISSN 0022-2461.

[5] G. I. Barenblatt. The Mathematical Theory of Equilibrium of Crack in Brittle Fracture. *Adv. Appl. Mech.*, 7:55–129, 1962. ISSN 0065-2156.

[6] B. Budiansky and N. A. Fleck. Compressive failure of fibre composites. *Journal of the Mechanics and Physics of Solids*, 41(1):183–211, 1993. ISSN 0022-5096.

[7] P. P. Camanho and C. G. Davila. Mixed-Mode Decohesion Finite Elements for the Simulation of Delamination in Composite Materials. Technical report, NASA Langley Research Center, Hampton, June 2002.

[8] L. P. Canal, C. González, J. Segurado, and J. LLorca. Intraply fracture of fiber-reinforced composites: Microscopic mechanisms and modeling. *Composites Science and Technology*, 72(11):1223–1232, June 2012. ISSN 02663538.

[9] L. P. Canal Casado. *Experimental and computational micromechanical study of fiber-reinforced polymers*. PhD thesis, UPM, 2011.

[10] S. Choi and B. V. Sankar. Micromechanical Analysis of Composite Laminates at Cryogenic Temperatures. *Journal of Composite Materials*, 40(12):1077–1091, June 2006. ISSN 0021-9983.

[11] M. V. Cid Alfaro, A. S. J. Suiker, and R. De Borst. Transverse failure behavior of fiber-epoxy systems. *Journal of Composite Materials*, 44(12):1493–1516, 2010. ISSN 00219983.

[12] A. Cornec, I. Scheider, and K. H. Schwalbe. On the practical application of the cohesive model. *Engineering Fracture Mechanics*, 70(14):1963–1987, 2003. ISSN 00137944.

[13] B. Cox and Q. Yang. In quest of virtual tests for structural composites. *Science (New York, N.Y.)*, 314 (5802):1102–7, November 2006. ISSN 1095-9203.

[14] I. M. Daniel and O. Ishai. *Engineering Mechanics of Composite Materials*. Oxford University Press, 2006. ISBN 9780195150971.

[15] Dassault Systèmes Simulia Corp. *Abaqus 6.10 documentation*. Providence, 2010.

[16] R. de Borst. Numerical aspects of cohesive-zone models. *Engineering Fracture Mechanics*, 70(14):1743–1757, 2003. ISSN 00137944.

[17] G. de Jong. *Multiscale Modeling of the effect of sub-ply voids on the failure of composites: A progressive failure model*. MSc thesis, TU Delft, 2018.

[18] E. de Souza Neto, P. Blanco, P. Sánchez, and R. Feijóo. An RVE-based multiscale theory of solids with micro-scale inertia and body force effects. *Mechanics of Materials*, 80:136–144, January 2015. ISSN 01676636.

[19] W. Drugan and J. Willis. A micromechanics-based nonlocal constitutive equation and estimates of representative volume element size for elastic composites. *Journal of the Mechanics and Physics of Solids*, 44(4):497–524, April 1996. ISSN 00225096.

[20] D. Dugdale. Yielding of steel sheets containing slits. *Journal of the Mechanics and Physics of Solids*, 8 (2):100–104, May 1960. ISSN 00225096.

[21] M. Elices, G. Guinea, J. Gómez, and J. Planas. The cohesive zone model: advantages, limitations and challenges. *Engineering Fracture Mechanics*, 69(2):137–163, 2002. ISSN 00137944.

[22] F. Feyel and J. L. Chaboche. FE2 multiscale approach for modelling the elastoviscoplastic behaviour of long fibre SiC/Ti composite materials. *Computer Methods in Applied Mechanics and Engineering*, 183 (3-4):309–330, March 2000. ISSN 00457825.

[23] J. Fish. Multiscale Computations: Boom or Bust. *IACM Expressions*, 22(January), 2008.

[24] J. Fish. Multiscale Modeling and Simulation of Composite Materials and Structures. In Y. W. Kwon, D. H. Allen, and R. Talreja, editors, *Multiscale Methods in Computational Mechanics*, pages 215–231. Boston, MA, 2011. ISBN 978-0-387-36318-9.

[25] M. G. D. Geers, V. G. Kouznetsova, K. Matouš, and J. Yvonnet. Homogenization Methods and Multiscale Modeling: Nonlinear Problems. In *Encyclopedia of Computational Mechanics Second Edition*, pages 1–34. John Wiley & Sons, Ltd, Chichester, UK, July 2017. ISBN 9781119176817.

[26] M. Geers, V. Kouznetsova, and W. Brekelmans. Multi-scale computational homogenization: Trends and challenges. *Journal of Computational and Applied Mathematics*, 234(7):2175–2182, 2010. ISSN 03770427.

[27] J. Geiser. *Multicomponent and Multiscale Systems*. Springer International Publishing, Cham, 2016. ISBN 978-3-319-15116-8.

[28] P. H. Geubelle and J. S. Baylor. Impact-induced delamination of composites: a 2D simulation. *Composites Part B: Engineering*, 29(5):589–602, September 1998. ISSN 13598368.

[29] C. Geuzaine and J.-F. Remacle. Gmsh: A 3-D finite element mesh generator with built-in pre- and post-processing facilities. *International Journal for Numerical Methods in Engineering*, 79(11):1309–1331, September 2009. ISSN 00295981.

[30] S. Ghosh, J. Bai, and P. Raghavan. Concurrent multi-level model for damage evolution in microstructurally debonding composites. *Mechanics of Materials*, 39(3):241–266, March 2007. ISSN 01676636.

[31] I. Gitman, H. Askes, and L. Sluys. Representative volume: Existence and size determination. *Engineering Fracture Mechanics*, 74(16):2518–2534, November 2007. ISSN 00137944.

[32] C. González and J. LLorca. Multiscale modeling of fracture in fiber-reinforced composites. *Acta Materialia*, 54(16):4171–4181, September 2006. ISSN 13596454.

[33] C. González and J. LLorca. Mechanical behavior of unidirectional fiber-reinforced polymers under transverse compression: Microscopic mechanisms and modeling. *Composites Science and Technology*, 67(13):2795–2806, 2007. ISSN 02663538.

[34] A. A. Griffith. The Phenomena of Rupture and Flow in Solids. *Philosophical Transactions of the Royal Society of London A: Mathematical, Physical and Engineering Sciences*, 221(582-593), 1921.

[35] M. Herráez, A. Fernández, C. S. Lopes, and C. González. Strength and toughness of structural fibres for composite material reinforcement. *Philosophical transactions. Series A, Mathematical, physical, and engineering sciences*, 374(2071):20150274, July 2016. ISSN 1471-2962.

[36] Hexcel Corporation. HexPly® 8552 Product Data Sheet (US Version), 2016. URL https://www.hexcel.com/user_area/content_media/raw/HexPly_8552_us_DataSheet.pdf.

[37] Hexcel Corporation. HexTow® IM7 Product Data Sheet, 2016. URL https://www.hexcel.com/user_area/content_media/raw/IM7_HexTow_DataSheet.pdf.

[38] P. J. Hine, H. Rudolf Lusti, and A. A. Gusev. Numerical simulation of the effects of volume fraction, aspect ratio and fibre length distribution on the elastic and thermoelastic properties of short fibre composites. *Composites Science and Technology*, 62(10-11):1445–1453, August 2002. ISSN 02663538.

[39] C. Hirsch. *Multiscale mixed-mode fracture analysis and deduction of effection traction-sepataion relations for anisotropic composites*. Diplomarbeit, Technische Universität Dresden, 2017.

[40] K. Honjo. Fracture toughness of PAN-based carbon fibers estimated from strength–mirror size relation. *Carbon*, 41(5):979–984, January 2003. ISSN 0008-6223.

[41] T. Hsieh, A. Kinloch, K. Masania, A. Taylor, and S. Sprenger. The mechanisms and mechanics of the toughening of epoxy polymers modified with silica nanoparticles. *Polymer*, 51(26):6284–6294, December 2010. ISSN 0032-3861.

[42] IMDEA Materials. VIPER (VIrtual Ply propERty). URL http://materials.imdea.org/research/simulation-tools/viper/.

[43] C. Inglis. Stresses in a plate due to the presence of cracks and sharp corners. *Transactions of the Institute of Naval Architects*, 55:219–230, 1913.

[44] G. Irwin. Fracture Dynamics. In *Fracturing of Metals*, pages 147–166, Cleveland, 1947. ASM.

[45] G. Irwin. Onset of Fast Crack Propagation in High Strength Steel and Aluminum Alloys. Technical report, Naval Research Laboratory, Washington, D.C., 1956.

[46] G. Irwin. Analysis of Stresses and Strains near the End of a Crack Traversing a Plate. *Journal of Applied Mechanics*, 24:361–364, 1957.

[47] M. Janssen, J. Zuidema, and R. Wanhill. *Fracture mechanics*. Delft University Press, Delft, 2nd edition, 2002. ISBN 90-407-2221-8.

[48] Z.-H. Jin and C. Sun. Cohesive zone modeling of interface fracture in elastic bi-materials. *Engineering Fracture Mechanics*, 72(12):1805–1817, August 2005. ISSN 00137944.

[49] Z.-H. Jin and C. Sun. A comparison of cohesive zone modeling and classical fracture mechanics based on near tip stress field. *International Journal of Solids and Structures*, 43(5):1047–1060, 2006. ISSN 00207683.

[50] A. Jumahat, C. Soutis, F. Jones, and A. Hodzic. Fracture mechanisms and failure analysis of carbon fibre/toughened epoxy composites subjected to compressive loading. *Composite Structures*, 92(2):295–305, January 2010. ISSN 0263-8223.

[51] T. Kanit, S. Forest, I. Galliet, V. Mounoury, and D. Jeulin. Determination of the size of the representative volume element for random composites: statistical and numerical approach. *International Journal of Solids and Structures*, 40(13-14):3647–3679, June 2003. ISSN 00207683.

[52] V. Kouznetsova, W. A. M. Brekelmans, and F. P. T. Baaijens. An approach to micro-macro modeling of heterogeneous materials. *Computational Mechanics*, 27(1):37–48, January 2001. ISSN 0178-7675.

[53] V. Kouznetsova. *Computational homogenization for the multi-scale analysis of multi-phase materials*. PhD thesis, Technische Universiteit Eindhoven, January 2002.

[54] V. Kouznetsova, M. Geers, and W. Brekelmans. Multi-scale second-order computational homogenization of multi-phase materials: a nested finite element solution strategy. *Computer Methods in Applied Mechanics and Engineering*, 193(48-51):5525–5550, December 2004. ISSN 00457825.

[55] J. Lee and G. L. Fenves. Plastic-Damage Model for Cyclic Loading of Concrete Structures. *Journal of Engineering Mechanics*, 124(8):892–900, August 1998. ISSN 0733-9399.

[56] J. Llorca, C. González, and J. Segurado. Finite element and homogenization modelling of materials. In *Multiscale Materials Modelling*, pages 121–147. Woodhead Publishing, 2007. ISBN 9781845690717.

[57] J. LLorca, C. González, J. M. Molina-Aldareguía, J. Segurado, R. Seltzer, F. Sket, M. Rodríguez, S. Sádaba, R. Muñoz, and L. P. Canal. Multiscale Modeling of Composite Materials: a Roadmap Towards Virtual Testing. *Advanced Materials*, 23(44):5130–5147, November 2011.

[58] S. Loehnert and T. Belytschko. A multiscale projection method for macro/microcrack simulations. *International Journal for Numerical Methods in Engineering*, 71(12):1466–1482, September 2007. ISSN 00295981.

[59] C. S. Lopes, C. González, O. Falcó, F. Naya, J. LLorca, and B. Tijs. Multiscale virtual testing: the roadmap to efficient design of composites for damage resistance and tolerance. *CEAS Aeronautical Journal*, 7(4): 607–619, December 2016. ISSN 1869-5582.

[60] J. Lubliner, J. Oliver, S. Oller, and E. Oñate. A plastic-damage model for concrete. *International Journal of Solids and Structures*, 25(3):299–326, 1989. ISSN 00207683.

[61] P. Maimí, P. P. Camanho, J. A. Mayugo, and C. G. Dávila. A continuum damage model for composite laminates: Part I – Constitutive model. *Mechanics of Materials*, 39(10):897–908, 2007. ISSN 01676636.

[62] K. Matous, M. Kulkarni, and P. Geubelle. Multiscale cohesive failure modeling of heterogeneous adhesives. *Journal of the Mechanics and Physics of Solids*, 56(4):1511–1533, April 2008. ISSN 00225096.

[63] C. McCarthy and T. Vaughan. 14 – Micromechanical failure analysis of advanced composite materials. In *Numerical Modelling of Failure in Advanced Composite Materials*, pages 379–409. 2015. ISBN 9780081003329.

[64] A. Melro, P. Camanho, F. Andrade Pires, and S. Pinho. Micromechanical analysis of polymer composites reinforced by unidirectional fibres: Part II – Micromechanical analyses. *International Journal of Solids and Structures*, 50(11-12):1906–1915, June 2013. ISSN 0020-7683.

[65] K. Naito. Stress analysis and fracture toughness of notched polyacrylonitrile (PAN)-based and pitch-based single carbon fibers. *Carbon*, 126:346–359, January 2018. ISSN 0008-6223.

[66] National Research Council. *Accelerated Aging of Materials and Structures*. The National Academies Press, Washington, D.C., January 1996.

[67] F. Naya, C. Lopes, C. González, and J. LLorca. Computational micromechanics strategies for the analysis of failure in unidirectional composites. In *Numerical Modelling of Failure in Advanced Composite Materials*, pages 411–433. Elsevier, 2015. ISBN 9780081003329.

[68] F. Naya, C. González, C. Lopes, S. Van der Veen, and F. Pons. Computational micromechanics of the transverse and shear behavior of unidirectional fiber reinforced polymers including environmental effects. *Composites Part A: Applied Science and Manufacturing*, 92:146–157, January 2017. ISSN 1359835X.

[69] A. Needleman. A Continuum Model for Void Nucleation by Inclusion Debonding. *Journal of Applied Mechanics*, 54(3):525, 1987. ISSN 00218936.

[70] V. P. Nguyen. An open source program to generate zero-thickness cohesive interface elements. *Advances in Engineering Software*, 74:27–39, August 2014. ISSN 09659978.

[71] V. P. Nguyen, O. Lloberas-Valls, M. Stroeven, and L. J. Sluys. Homogenization-based multiscale crack modelling: From micro-diffusive damage to macro-cracks. *Computer Methods in Applied Mechanics and Engineering*, 200(9-12):1220–1236, February 2011. ISSN 00457825.

[72] V. P. Nguyen, O. Lloberas-Valls, M. Stroeven, and L. J. Sluys. Computational homogenization for multiscale crack modeling. Implementational and computational aspects. *International Journal for Numerical Methods in Engineering*, 89(2):192–226, January 2012.

[73] V. P. Nguyen, M. Stroeven, and L. J. Sluys. Multiscale failure modeling of concrete: Micromechanical modeling, discontinuous homogenization and parallel computations. *Computer Methods in Applied Mechanics and Engineering*, 201-204:139–156, January 2012. ISSN 00457825.

[74] M. I. Okereke, A. I. Akpoyomare, and M. S. Bingley. Virtual testing of advanced composites, cellular materials and biomaterials: A review. *Composites Part B: Engineering*, 60:637–662, 2014. ISSN 13598368.

[75] E. Orowan. Notch brittleness and the strength of metals. *Transactions of The Institution of Engineers and Shipbuilders in Scotland*, 89:165–215, 1945.

[76] M. Ortiz and A. Pandolfi. Finite-deformation irreversible cohesive elements for three-dimensional crack-propagation analysis. *International Journal for Numerical Methods in Engineering*, 44(9):1267–1282, March 1999. ISSN 0029-5981.

[77] K. Park and G. H. Paulino. Cohesive Zone Models: A Critical Review of Traction-Separation Relationships Across Fracture Surfaces. *Applied Mechanics Reviews*, 64(6):060802, February 2013. ISSN 0003-6900.

[78] D. Perić, E. A. de Souza Neto, R. A. Feijóo, M. Partovi, and A. J. C. Molina. On micro-to-macro transitions for multi-scale analysis of non-linear heterogeneous materials: unified variational basis and finite element implementation. *International Journal for Numerical Methods in Engineering*, 87(1-5):149–170, July 2011. ISSN 00295981.

[79] S. A. Ponnusami, S. Turteltaub, and S. van der Zwaag. Cohesive-zone modelling of crack nucleation and propagation in particulate composites. *Engineering Fracture Mechanics*, 149:170–190, November 2015. ISSN 00137944.

[80] J. R. Rice. A Path Independent Integral and the Approximate Analysis of Strain Concentration by Notches and Cracks. *Journal of Applied Mechanics*, 35(2):379, June 1968. ISSN 00218936.

[81] E. Saether, V. Yamakov, D. R. Phillips, and E. H. Glaessgen. An Overview of the State of the Art in Atomistic and Multiscale Simulation of Fracture. Technical report, National Aeronautics and Space Administration, February 2009.

[82] G. Sih, P. Paris, and G. Irwin. On cracks in rectilinearly anisotropic bodies. *International Journal of Fracture Mechanics*, 1(3):189–203, September 1965. ISSN 0020-7268.

[83] M. Silani, S. Ziaei-Rad, H. Talebi, and T. Rabczuk. A semi-concurrent multiscale approach for modeling damage in nanocomposites. *Theoretical and Applied Fracture Mechanics*, 74:30–38, December 2014. ISSN 01678442.

[84] V. Šmilauer, C. G. Hoover, Z. P. Bažant, F. C. Caner, A. M. Waas, and K. W. Shahwan. Multiscale simulation of fracture of braided composites via repetitive unit cells. *Engineering Fracture Mechanics*, 78(6):901–918, April 2011. ISSN 00137944.

[85] G. Soni, R. Singh, M. Mitra, and B. G. Falzon. Modelling matrix damage and fibre–matrix interfacial decohesion in composite laminates via a multi-fibre multi-layer representative volume element (M2RVE). *International Journal of Solids and Structures*, 51(2):449–461, January 2014. ISSN 00207683.

[86] C. T. C.-T. Sun and Z.-H. Jin. *Fracture mechanics*. Academic Press, 2012. ISBN 9780123850010.

[87] S. Swaminathan, S. Ghosh, and N. J. Pagano. Statistically Equivalent Representative Volume Elements for Unidirectional Composite Microstructures: Part I - Without Damage. *Journal of Composite Materials*, 40(7):583–604, April 2006. ISSN 0021-9983.

[88] E. B. Tadmor, M. Ortiz, and R. Phillips. Quasicontinuum analysis of defects in solids. *Philosophical Magazine A*, 73(6):1529–1563, June 1996. ISSN 0141-8610.

[89] H. Talebi, M. Silani, S. P. A. Bordas, P. Kerfriden, and T. Rabczuk. A computational library for multiscale modeling of material failure. *Computational Mechanics*, 53(5):1047–1071, May 2014. ISSN 0178-7675.

[90] H. Talebi, M. Silani, and T. Rabczuk. Concurrent multiscale modeling of three dimensional crack and dislocation propagation. *Advances in Engineering Software*, 80:82–92, February 2015. ISSN 09659978.

[91] R. Talreja. Physical modelling of failure in composites. *Philosophical transactions. Series A, Mathematical, physical, and engineering sciences*, 374(2071):20150280, July 2016. ISSN 1471-2962.

[92] J. R. Tarpani, M. T. Milan, D. Spinelli, and W. W. Bose. Mechanical performance of carbon-epoxy laminates. Part I: quasi-static and impact bending properties. *Materials Research*, 9(2):115–120, June 2006. ISSN 1516-1439.

[93] D. Trias, J. Costa, A. Turon, and J. Hurtado. Determination of the critical size of a statistical representative volume element (SRVE) for carbon reinforced polymers. *Acta Materialia*, 54(13):3471–3484, August 2006.

[94] S. Turteltaub, N. van Hoorn, W. Westbroek, and C. Hirsch. Multiscale analysis of mixed-mode fracture and effective traction-separation relations for composite materials. *JMPS (preprint)*, 2017.

[95] V. Tvergaard and J. W. Hutchinson. The influence of plasticity on mixed mode interface toughness. *Journal of the Mechanics and Physics of Solids*, 41(6):1119–1135, June 1993. ISSN 00225096.

[96] N. van Hoorn. *Multiscale Fracture Simulations for Composite Materials*. MSc thesis, TU Delft, 2016.

[97] T. Vaughan and C. McCarthy. A combined experimental–numerical approach for generating statistically equivalent fibre distributions for high strength laminated composite materials. *Composites Science and Technology*, 70(2):291–297, February 2010.

[98] T. Vaughan and C. McCarthy. A micromechanical study on the effect of intra-ply properties on transverse shear fracture in fibre reinforced composites. *Composites Part A: Applied Science and Manufacturing*, 42(9):1217–1228, September 2011. ISSN 1359835X.

[99] C. V. Verhoosel, J. J. C. Remmers, M. A. Gutiérrez, and R. de Borst. Computational homogenization for adhesive and cohesive failure in quasi-brittle solids. *International Journal for Numerical Methods in Engineering*, 83(8-9):1155–1179, August 2010. ISSN 00295981.

[100] T. Vogler, S.-Y. Hsu, and S. Kyriakides. Composite failure under combined compression and shear. *International Journal of Solids and Structures*, 37(12):1765–1791, 2000. ISSN 00207683.

[101] A. Wells. Unstable Crack Propagation in Metals: Cleavage and Fast Fracture. In *Proceedings of the Crack Propagation Symposium*, pages Vol. 1, Paper 84, Cranfield, 1961.

[102] W. Westbroek. *Multiscale Modeling of Fracture in Composites: A Progressive Failure Model for Cryogenic Applications*. 2017.

[103] H. Westergaard. Bearing pressures and cracks. *Journal of Applied Mechanics*, 6:A49–A53, 1939.

[104] S. Xiao and T. Belytschko. A bridging domain method for coupling continua with molecular dynamics. *Computer Methods in Applied Mechanics and Engineering*, 193(17-20):1645–1669, May 2004. ISSN 00457825.

[105] M. Xu. Concurrent Coupling of Atomistic and Continuum Models. In *Multiscale Methods*, pages 93–133. Oxford University Press, October 2009.

[106] X.-P. Xu and A. Needleman. Numerical simulations of fast crack growth in brittle solids. *Journal of the Mechanics and Physics of Solids*, 42(9):1397–1434, September 1994. ISSN 00225096.

[107] M. Yekani Fard. Nonlinear Inelastic Mechanical Behavior Of Epoxy Resin Polymeric Materials. 2011.

[108] B. Zhang, Z. Yang, X. Sun, and Z. Tang. A virtual experimental approach to estimate composite mechanical properties: Modeling with an explicit finite element method. *Computational Materials Science*, 49 (3):645–651, September 2010. ISSN 09270256.

A

Analysis inputs

The analysis input entries required and stored in the main database are here described.

Entry	Description	Entry	Description
ref	Unique reference number	nu13_f	Fiber Poisson's ratio 13
status	Status along the processing flow	nu23_f	Fiber Poisson's ratio 23
description	Description of the test	G12_f	Fiber Shear modulus
id_group	ID of the test group it belongs	G13_f	Fiber Shear modulus
grid_size	Mesh grid size	G23_f	Fiber Shear modulus
R	Statistic repetition number	rho_m	Matrix density
angle	Angle of rotation of the strain tensor	nu_m	Matrix Poisson's ratio
viscreg	Viscous regularization parameter	E_m	Matrix modulus of elasticity
lastframe	*Output: last converged frame time*	dam_init_cf	Fiber damage initiation criteria (Default: MAXS)
mesh_path	Relative path of the .msh file	dam_evol_cf	Fiber damage evolution crtieratia (Default: ENERGY)
RVE_phases	Phases of the RVE (e.g [C], [C,T,C], [C,T,C,T,C])	t_ult_cf	Fiber ultimate traction
RVE_w	Width of the RVE	G_f_cf	Fiber fracture energy
RVE_h	Height of each of the RVE phases - Array [h1, h2, h3]	d_f_cf	Fiber failure opening
RVE_V_f	Fiber volume fraction of the RVE	E_coh_cf	Fiber cohesive element fracture energy
RVE_f_diameter	Diameter of the fibers	dam_init_cm	Matrix damage initiation criteria (Default: MAXS)
RVE_V_f_real_out	*Output: real volume fraction after geometry generation*	dam_evol_cm	Matrix damage evolution crtieratia (Default: ENERGY)
RVE_bc	RVE geometry boundary conditions (by default all periodic ['P', 'P', 'P', 'P'])	t_ult_cm	Matrix ultimate traction
INP_bc	Boundary conditions for the analysis (by default all periodic ['P', 'P', 'P', 'P'])	G_f_cm	Matrix fracture energy
e11	Input macroscopic strain tensor 11 component	d_f_cm	Matrix failure opening
e22	Input macroscopic strain tensor 22 component	E_coh_cm	Matrix cohesive element fracture energy
e12	Input macroscopic strain tensor 12 component	dam_init_ci	Interface damage initiation criteria (Default: MAXS)
e21	Input macroscopic strain tensor 21 component	dam_evol_ci	Interface damage evolution crtieratia (Default: ENERGY)
rho_f	Fiber density	t_ult_ci	Interface ultimate traction
E1_f	Fiber Longitudinal (1) modulus of elasticity	G_f_ci	Interface fracture energy
E2_f	Fiber Transverse (2) modulus of elasticity	d_f_ci	Interface failure opening
E3_f	Fiber Transverse (3) modulus of elasticity	E_coh_ci	Interface cohesive element fracture energy
nu12_f	Fiber Poisson's ratio 12	author	Test submission author

Reference	Mesh	Abaqus .INP	Material properties

B

Gmsh .geo file structure

The structure and sintaxis of the Gmsh geometry input file .geo is hereby described.

```
SetFactory("OpenCASCADE");

// RVE DIMENSIONS - Set gridsize, width and height
gridsize = 0.001;
w = 0.05;
h = 0.05;

// PBC ENFORCE OPTIONS - Enable/Disable PBC in the Bottom/Top and Left/Right borders
enforce_PBC_BottomTop = 1;
enforce_PBC_LeftRight = 1;

// PHYSICAL GROUPS - Define groups to classify the geometric features
CFiberGroup = {};
TFiberGroup = {};

// GEOMETRICAL ENTITIES - The fibers and other features are drawn here
// Circle Type - Creates the [0] fiber geometry and adds it to the CFiber group.
// idx_l: line index, idx_ll: line loop index, idx_fg: fiber geometry index
idx_l = newl  ; Circle(idx_l) = {x_coord, y_coord, z_coord, radius, 0, 2*Pi};
idx_ll = newll ; Line Loop(idx_ll) = {idx_l};
idx_fg = newreg; Plane Surface(idx_fg) = {idx_ll};
CFiberGroup += {idx_fg};
...

// Rectangle Type - Creates the [90] fiber geometry and adds it to the TFiber group.
idx_fg = newreg; Rectangle(idx_fg) = {x_coord, y_coord, z_coord, width, height, 0};
TFiberGroup += {idx_fg};
...

// SUBROUTINE - See appendix C [...]

// MESH COMMANDS AND SAVE OPTIONS
Mesh.Algorithm=5;
Mesh.Smoothing=10;
Mesh.CharacteristicLengthMin=gridsize/2;
Mesh.CharacteristicLengthMax=gridsize;
Mesh 2;
Coherence Mesh;
SetOrder 1;

Save "38.msh";
Save "mesh.eps";
Exit;
```

C

Gmsh PBC subroutine

The subroutine in charge of performing the boolean operations, the contour detection and the creation of PBC relations within the .geo file is hereby described.

```
// COMMON CODE ============================================================================
// RVE MESH GENERATOR FOR PERIODIC BOUNDARY CONDITIONS ====================================
// AUTHOR: RUBEN SUAREZ MILLAN
// TU DELFT 2018. REFERENCE ACCORDINGLY.

// RVE RECTANGLE - OUTER CONTOUR
// Define corner nodes p_i, edge lines l_i, and the RVE surface

p1 = newp ; Point(p1) = {0, 0, 0, 1.0};
p2 = newp ; Point(p2) = {w, 0, 0, 1.0};
p3 = newp ; Point(p3) = {w, h, 0, 1.0};
p4 = newp ; Point(p4) = {0, h, 0, 1.0};

l1 = newl ; Line(l1) = {p1, p2};
l2 = newl ; Line(l2) = {p2, p3};
l3 = newl ; Line(l3) = {p3, p4};
l4 = newl ; Line(l4) = {p4, p1};

ll1 = newll ; Line Loop(ll1) = {l4, l1, l2, l3};
RVESurface = newreg ; Plane Surface(RVESurface) = {ll1};

// CFIBERS GROUP >>
// Intersects the CFibersGroup with the RVESurface to eliminate the fiber portions outside the
   ↪  domain dimensions. Extract the boundaries of the resulting domain.

s_c_fibers = BooleanIntersection{ Surface{CFiberGroup()}; Delete; }{ Surface{RVESurface}; };
s_c_fibers_b = Unique[Abs[Boundary{ Surface{s_c_fibers()};}]];
Printf("C-Fiber boundaries: ",s_c_fibers_b());

Physical Surface ("CFIBERS" , 111 ) = { s_c_fibers() };

// TFIBERS GROUP >>
// Intersects the TFibersGroup with the RVESurface to eliminate the fiber portions outside the
   ↪  domain dimensions. Extract the boundaries of the resulting domain.

s_t_fibers = BooleanIntersection{ Surface{TFiberGroup()}; Delete; }{ Surface{RVESurface}; };
s_t_fibers_b = Unique[Abs[Boundary{ Surface{s_t_fibers()};}]];
Printf("T-Fiber boundaries: ",s_t_fibers_b());

Physical Surface ("TFIBERS" , 222 ) = { s_t_fibers() };

// MATRIX GROUP >>
```

```
// Extracts the portion of the domain belonging to the matrix by a) selecting the whole domain if there are no fibers. b) Taking the difference between the RVESurface and the fibers surfaces.

If ((#s_c_fibers_b() == 0) && (#s_t_fibers_b() == 0))
        s_matrix() = RVESurface;

ElseIf ((#s_c_fibers_b() != 0)  (#s_t_fibers_b() != 0))
        s_matrix() = BooleanDifference{ Surface{RVESurface}; Delete;}{ Surface{s_c_fibers()}; Surface{s_t_fibers()}; } ;

EndIf

s_matrix_b() = Unique[Abs[Boundary{ Surface{s_matrix()};}]];
Printf("Matrix boundaries: ",s_matrix_b());

Physical Surface ("MATRIX" , 999) = {s_matrix()};

// OUTER CONTOUR >>
// Takes the outer contour of the RVE Rectangle after the intersection operations. The contour is obtained by identifying common edges between the fibers and matrix group, and substracting this common edges from all the edges.

If ((#s_c_fibers_b() == 0) && (#s_t_fibers_b() == 0))
        contour() = s_matrix_b();
        Printf("Common edges: no common edges as only matrix is present");
        Printf("Contour: ",contour());

ElseIf ((#s_c_fibers_b() != 0)  (#s_t_fibers_b() != 0))
        common_edges() = Unique[BooleanIntersection{Line{s_c_fibers_b()}; Line{s_t_fibers_b()};}{Line{s_matrix_b()};}];
        all_edges() = Unique[BooleanUnion{Line{s_c_fibers_b()}; Line{s_t_fibers_b()};}{Line{s_matrix_b()};}];
        contour() = BooleanDifference{ Line{all_edges()}; }{ Line{common_edges()}; };
        Printf("Common edges: ",common_edges());
        Printf("Contour: ",contour());

EndIf

// PERIODIC BOUNDARIES LIST INITIALIZATION
// Initialize the lists to store the boundary domains

PBC_L = {};
PBC_B = {};

PBC_T = {};
PBC_R = {};

// GEOMETRICAL TOLERANCE - Sometimes requires to be adjusted
// geo_tolerance = 1e-10

// IDENTIFY AND CLASSIFY THE OUTER BOUNDARIES L,R,B,T
// Loops over the contour lines and classifies them into Left Right Bottom and Top edges based on their endpoints having a common coordinate equal to the edge's axis.

For i In {0:#contour()-1}

        line_i_boundary = Boundary{ Line{ contour(i) }; };

        Point_0 = Point{line_i_boundary(0)};
        Point_1 = Point{line_i_boundary(1)};

```

```
95          // VERTICAL SEGMENTS
96
97          If ((Abs[Point_0[0]] < geo_tolerance) && (Abs[Point_1[0]] < geo_tolerance))
98                  PBC_L += {contour(i)};
99
100         ElseIf ((Abs[Point_0[1]] < geo_tolerance) && (Abs[Point_1[1]] < geo_tolerance))
101                 PBC_B += {contour(i)};
102
103         // HORIZONTAL SEGMENTS
104
105         ElseIf ((Abs[Point_0[0]] > w - geo_tolerance) && (Abs[Point_1[0]] > w - geo_tolerance))
106                 PBC_R += {contour(i)};
107
108         ElseIf ((Abs[Point_0[1]] > h - geo_tolerance) && (Abs[Point_1[1]] > h -
            ↪  geo_tolerance))
109                 PBC_T += {contour(i)};
110
111         EndIf
112
113 EndFor
114
115 Printf("PBC_B",PBC_B());
116 Printf("PBC_L",PBC_L());
117
118 // ENFORCE PERIODIC BOUNDARY CONDITIONS IN THE MESH
119 // Runs two for loops, one for each contour list of the each of the opposed edges. If the contour_i
    ↪  and contour_j have equivalent coordinates, creates a Periodic Line relation, which creates a
    ↪  periodic mesh over that contour pair.
120
121 If (enforce_PBC_BottomTop == 1)
122         For i In {0:#PBC_B()-1}
123                 For j In {0:#PBC_T()-1}
124
125                         B_i = Boundary{ Line{ PBC_B(i) }; };
126                         T_i = Boundary{ Line{ PBC_T(j) }; };
127
128                         Point_B0 = Point{B_i(0)};
129                         Point_B1 = Point{B_i(1)};
130
131                         Point_T0 = Point{T_i(0)};
132                         Point_T1 = Point{T_i(1)};
133
134                         If ((Abs[Point_B0[0] - Point_T0[0]] < geo_tolerance) && (Abs[Point_B1[0] -
                            ↪  Point_T1[0]] < geo_tolerance))
135                                 Periodic Line {PBC_T(j)} = {PBC_B(i)};
136
137                         ElseIf ((Abs[Point_B0[0] - Point_T1[0]] < geo_tolerance) &&
                            ↪  (Abs[Point_B1[0] - Point_T0[0]] < geo_tolerance))
138                                 Periodic Line {PBC_T(j)} = {-PBC_B(i)};
139
140                         EndIf
141
142                 EndFor
143         EndFor
144 EndIf
145
146 If (enforce_PBC_LeftRight == 1)
147         For i In {0:#PBC_L()-1}
148                 For j In {0:#PBC_R()-1}
149
150                         L_i = Boundary{ Line{ PBC_L(i) }; };
```

```
151                         R_i = Boundary{ Line{ PBC_R(j) }; };
152
153                         Point_L0 = Point{L_i(0)};
154                         Point_L1 = Point{L_i(1)};
155
156                         Point_R0 = Point{R_i(0)};
157                         Point_R1 = Point{R_i(1)};
158
159                         If ((Abs[Point_L0[1] - Point_R0[1]] < geo_tolerance) && (Abs[Point_L1[1] -
                            ↪  Point_R1[1]] < geo_tolerance))
160                                 Periodic Line {PBC_R(j)} = {PBC_L(i)};
161
162                         ElseIf ((Abs[Point_L0[1] - Point_R1[1]] < geo_tolerance) &&
                            ↪  (Abs[Point_L1[1] - Point_R0[1]] < geo_tolerance))
163                                 Periodic Line {PBC_R(j)} = {-PBC_L(i)};
164
165                         EndIf
166
167                 EndFor
168         EndFor
169 EndIf
```

D

Abaqus input .inp file structure

A description of the `.inp` file is here given. The file starts by defining the job name in the heading and certain options related with the reporting of the analysis. After the heading, the RVE part is generated by defining its nodes, elements, sets, orientations and section assignments. The definition of the nodes and elements is based on the processing of the mesh file `.msh`. The notation `(...)` indicates there are multiple entries with the same structure (e.g. line 5 indicates that are n node entries with the same structure as line 4).

```
1  *Heading
2  ** Job name: job_name Model name: model_name
3  ** Generated by:  Multiscale gen_inp.py for Abaqus/CAE 6.14-2
4  *Preprint, echo=NO, model=NO, history=NO, contact=NO
5  **
6  ** PARTS
7  *Part, name= RVE
8  *Node
9  node index, x coordinate, y coordinate
10 ...
11 *Element, type=CPE3
12 element ID, node 1 index, node 2 index, node 3 index
13 ...
14 *Element, type=COH2D4
15 element index, node 1 index, node 2 index, node 3 index, node 4 index
16 ...
```

Element sets are defined for the cross sectional fibers `CFIBERS`, the longitudinal fibers `TFIBERS`, the matrix and the interfaces between these phases. These element sets are used later to create the sections.

```
17 *Elset, elset=CFIBERS
18 element index
19 ...
20 *Elset, elset=TFIBERS
21 ...
22 *Elset, elset=MATRIX
23 ...
24 *Elset, elset=BULK_ELEMENTS
25 ...
26 *Elset, elset=COHESIVE_CFIBERS_CFIBERS
27 ...
28 *Elset, elset=COHESIVE_CFIBERS_MATRIX
29 ...
30 *Elset, elset=COHESIVE_TFIBERS_TFIBERS
31 ...
32 *Elset, elset=COHESIVE_TFIBERS_MATRIX
33 ...
34 *Elset, elset=COHESIVE_MATRIX_MATRIX
```

```
...
*Elset, elset=COH_ELEMENTS
...
```

Moreover, orientations are enforced to ensure consistency. In this case, no rotations are applied, as for simplicity two materials are defined for CFIBER and TFIBER. In principle, this can also be done using one material and applying a rotation.

```
*ORIENTATION, NAME=TFIBERS, DEFINITION=COORDINATES
 1., 0., 0., 0., 1., 0.
 3, 0
*ORIENTATION, NAME=CFIBERS, DEFINITION=COORDINATES
 1., 0., 0., 0., 1., 0.
 3, 0
*ORIENTATION, NAME=MATRIX, DEFINITION=COORDINATES
 1., 0., 0., 0., 1., 0.
 3, 0
```

Section assignments link the element sets with the materials, controls and orientations. Solid and cohesive sections are created. Moreover, the materials and controls (not yet defined) are already assigned. This ends the geometry of the RVE.

```
 **
 ** SECTION ASSIGNMENTS
 **
 **Section: CFIBERS
 *Solid Section, elset=CFIBERS, controls=EC-2, material=CFIBERS, ORIENTATION = CFIBERS
 ,
 **Section: TFIBERS
 *Solid Section, elset=TFIBERS, controls=EC-2, material=TFIBERS, ORIENTATION = TFIBERS
 ,
 **Section: MATRIX
 *Solid Section, elset=MATRIX, controls=EC-2, material=MATRIX, ORIENTATION = MATRIX
 ,
 **Cohesive Section: COHESIVE_CFIBERS_CFIBERS
 *Cohesive Section, elset=COHESIVE_CFIBERS_CFIBERS, controls=EC-2,
  ↪ material=COHESIVE_CFIBERS_CFIBERS, response=TRACTION SEPARATION
 ,
 **Cohesive Section: COHESIVE_CFIBERS_MATRIX
 *Cohesive Section, elset=COHESIVE_CFIBERS_MATRIX, controls=EC-2, material=COHESIVE_CFIBERS_MATRIX,
  ↪ response=TRACTION SEPARATION
 ,
 **Cohesive Section: COHESIVE_TFIBERS_TFIBERS
 *Cohesive Section, elset=COHESIVE_TFIBERS_TFIBERS, controls=EC-2,
  ↪ material=COHESIVE_TFIBERS_TFIBERS, response=TRACTION SEPARATION
 ,
 **Cohesive Section: COHESIVE_TFIBERS_MATRIX
 *Cohesive Section, elset=COHESIVE_TFIBERS_MATRIX, controls=EC-2, material=COHESIVE_TFIBERS_MATRIX,
  ↪ response=TRACTION SEPARATION
 ,
 **Cohesive Section: COHESIVE_MATRIX_MATRIX
 *Cohesive Section, elset=COHESIVE_MATRIX_MATRIX, controls=EC-2, material=COHESIVE_MATRIX_MATRIX,
  ↪ response=TRACTION SEPARATION
 ,
 **
 *End Part
```

The dummy nodes discussed in previous sections §4.2.5 are now created as new parts. For convenience, the

dummies' position is at 1.2 times the width and height of the RVE, not having this choice any influence on the simulation.

```
*Part, name=DUMMY_LR
*Node
index DLR, 1.2*w_RVE ,  0,
*End Part
*Part, name=DUMMY_TB
*Node
index DTB,  0, 1.2*h_RVE,
*End Part
```

With all parts defined, the assembly is performed. The three previously defined parts (`RVE`, `DUMMY_LR`, `DUMMY_TB`) are added as instances.

```
** ASSEMBLY
*Assembly, name=Assembly
**
*Instance, name=RVE, part=RVE
*End Instance
**
*Instance, name=DUMMY_LR-1, part=DUMMY_LR
*End Instance
**
*Instance, name=DUMMY_TB-1, part=DUMMY_TB
*End Instance
**
```

Moreover, node sets are defined for dummy nodes, the corner nodes (`NODE_CORNER_i`), and also for those nodes connected by periodic boundary conditions (`LEFT_NODE_i`, `RIGHT_NODE_i`, `BOTTOM_NODE_i`, `TOP_NODE_i`).

```
*Nset, nset=DUMMY_LR, instance = DUMMY_LR-1
index DLR
*Nset, nset=DUMMY_TB, instance = DUMMY_TB-1
index DBT
*Nset, nset=ALL_NODES, instance = RVE
node index
...
*Nset, nset=NODE_CORNER_i, instance = RVE
corner node i index
...
*Nset, nset=LEFT_NODE_i, instance = RVE
left node i index
...
*Nset, nset=RIGHT_NODE_i, instance = RVE
right node i index
...
*Nset, nset=BOTTOM_NODE_i, instance = RVE
bottom node i index
...
*Nset, nset=TOP_NODE_i, instance = RVE
top node i index
...
```

The periodic boundary conditions are applied as described in §4.2.5 for the top-bottom and the left-right couplings. Two equations are applied per PBC, one per coordinate. This ends the assembly.

```
** Top-Botttom PBC equations
*Equation
3
TOP_NODE_i,1,1, BOTTOM_NODE_j,1,-1, DUMMY_TB,1,-1
*Equation
3
TOP_NODE_i,2,1, BOTTOM_NODE_j,2,-1, DUMMY_TB,2,-1
...
** Left-Right PBC equations
*Equation
3
RIGHT_NODE_i,1,1, LEFT_NODE_j,1,-1, DUMMY_LR,1,-1
3
RIGHT_NODE_i,2,1, LEFT_NODE_j,2,-1, DUMMY_LR,2,-1
...
*End Assembly
```

Next, the element controls and material properties are added. The defined EC-2 control does not remove the fully damaged cohesive elements and applies the viscous regularization parameter.

```
** ELEMENT CONTROLS
**
*Section Controls, name=EC-2, ELEMENT DELETION=NO, VISCOSITY=viscous_regularization_parameter
1., 1., 1.
```

The material properties are now defined. In accordance to the models and properties described in section §4.2.8, the materials are defined as follows.

```
*Material, name=MATRIX
*Density
 1.31e-06
*Elastic
 4000, 0.35


*Material, name=COHESIVE_CFIBERS_CFIBERS
*Damage Initiation, criterion=MAXS
 5000.0, 5000.0, 5000.0
*Damage Evolution, type=ENERGY
 7.5
*Elastic, type=TRACTION
 1000000000, 1000000000, 1000000000


*Material, name=COHESIVE_TFIBERS_TFIBERS
*Damage Initiation, criterion=MAXS
 5000.0, 5000.0, 5000.0
*Damage Evolution, type=ENERGY
 7.5
*Elastic, type=TRACTION
 1000000000, 1000000000, 1000000000


*Material, name=COHESIVE_MATRIX_MATRIX
*Damage Initiation, criterion=MAXS
 80, 80, 80
*Damage Evolution, type=ENERGY
 0.2
*Elastic, type=TRACTION
 100000000, 100000000, 100000000
```

```
*Material, name=COHESIVE_CFIBERS_MATRIX
*Damage Initiation, criterion=MAXS
 85, 85, 85
*Damage Evolution, type=ENERGY
 0.2
*Elastic, type=TRACTION
 100000000, 100000000, 100000000


*Material, name=COHESIVE_TFIBERS_MATRIX
*Damage Initiation, criterion=MAXS
 85, 85, 85
*Damage Evolution, type=ENERGY
 0.2
*Elastic, type=TRACTION
 100000000, 100000000, 100000000
```

The boundary conditions for the left corner node are enforced as defined in §4.2.5.

```
** BOUNDARY CONDITIONS
** Name: BC_NODE_C1B Type: Displacement/Rotation
*BOUNDARY
NODE_C1B, 2
** Name: BC_NODE_C1L Type: Displacement/Rotation
*BOUNDARY
NODE_C1L, 1
```

The loading step and displacement conditions are enforced to the dummy nodes. Moreover, the maximum number of cutbacks for an increment (by default set in Abaqus to 5) is changed to 50. This enables to continue the analysis in situations with high discontinuities.

```
** STEP: LOAD_STEP
*Step, name=LOAD_STEP, nlgeom=YES, inc=5000
*Static, stabilize, allsdtol=0.05, continue=YES
 0.001, 1, 1e-13, 0.01, 1
**
** LOAD CONDITIONS
** Name: PBC_DUMMY_TB Type: Displacement/Rotation
*BOUNDARY, TYPE=DISPLACEMENT
 DUMMY_TB , 1 , 1 , 0.0
 DUMMY_TB , 2 , 2 , 0.0
** Name: PBC_DUMMY_LR Type: Displacement/Rotation
*BOUNDARY, TYPE=DISPLACEMENT
 DUMMY_LR , 1 , 1 , 0.015000000000000027
 DUMMY_LR , 2 , 2 , 0.0
**
** CONTROLS
*Controls, ANALYSIS=DISCONTINUOUS
*Controls, parameters=time incrementation
, , , , , , , 50, , ,
```

Finally, the desired field and history outputs are specified, together with their frequency. This finished the input file.

```
** OUTPUT REQUESTS
*Restart, write, frequency=0
**
```

```
** FIELD OUTPUT: F-Output-1
*Output, field, time interval=0.001, time marks=NO
*Node Output, GLOBAL=YES
 U, VF, TF, COORD
*Element Output, directions=YES
 E, LE, EE, ER, S, MISES, EVOL, STATUS, SDEG
*Contact Output
 CSDMG, CSMAXSCRT, CSMAXUCRT
**
** HISTORY OUTPUT: H-Output-1
*Output, history, time interval=0.001, time marks=NO
*Node Output, nset=NODE_i
 U, TF, VF
*Energy Output
 ETOTAL, ALLIE, ALLSD, ALLCD, ALLSE, ALLWK, ALLDMD, ALLVD
*Contact Output
 CSDMG, CSMAXSCRT, CSMAXUCRT
**
*End Step
```